
Computational characterization of flow and turbulence in IC engine-relevant cooling channels

An LES- and Reynolds-stress-modeling study

Zur Erlangung des akademischen Grades Doktor-Ingenieur (Dr.-Ing.)

Genehmigte Dissertation von Sebastian Wegt aus Darmstadt

Tag der Einreichung: 22. Oktober 2021, Tag der Prüfung: 15. Dezember 2021

1. Gutachten: apl. Prof. Dr.-Ing. habil. Suad Jakirlić
2. Gutachten: Prof. Dr.-Ing. Jeanette Hussong
3. Gutachten: Prof. Dr.-Ing. habil. Michael Breuer
Darmstadt



TECHNISCHE
UNIVERSITÄT
DARMSTADT

Mechanical Engineering
Department

Institute for Fluid
Mechanics and
Aerodynamics (SLA)

Modelling and Simulation
of Turbulent Flows

Computational characterization of flow and turbulence in IC engine-relevant cooling channels
An LES- and Reynolds-stress-modeling study

Accepted doctoral thesis by Sebastian Wegt

1. Review: apl. Prof. Dr.-Ing. habil. Suad Jakirlić
2. Review: Prof. Dr.-Ing. Jeanette Hussong
3. Review: Prof. Dr.-Ing. habil. Michael Breuer

Date of submission: 22. Oktober 2021

Date of thesis defense: 15. Dezember 2021

Darmstadt

Bitte zitieren Sie dieses Dokument als:

URN: urn:nbn:de:tuda-tuprints-203537

URL: <http://tuprints.ulb.tu-darmstadt.de/20353>

Dieses Dokument wird bereitgestellt von tuprints,
E-Publishing-Service der TU Darmstadt
<http://tuprints.ulb.tu-darmstadt.de>
tuprints@ulb.tu-darmstadt.de

CC-BY-SA 4.0

Erklärungen laut Promotionsordnung

§8 Abs. 1 lit. c PromO

Ich versichere hiermit, dass die elektronische Version meiner Dissertation mit der schriftlichen Version übereinstimmt.

§8 Abs. 1 lit. d PromO

Ich versichere hiermit, dass zu einem vorherigen Zeitpunkt noch keine Promotion versucht wurde. In diesem Fall sind nähere Angaben über Zeitpunkt, Hochschule, Dissertationsthema und Ergebnis dieses Versuchs mitzuteilen.

§9 Abs. 1 PromO

Ich versichere hiermit, dass die vorliegende Dissertation selbstständig und nur unter Verwendung der angegebenen Quellen verfasst wurde.

§9 Abs. 2 PromO

Die Arbeit hat bisher noch nicht zu Prüfungszwecken gedient.

Darmstadt, 22. Oktober 2021

S. Wegt

Abstract

The present work provides an insight into the flow topology of common pipe structures with the newly designed Water Spider Geometry (WSG) as a generic flow guidance of an Internal Combustion (IC) engine cooling channel, which includes flow deflection (90°-pipe bend), division (T-junction) and confluence (reverse T-junction). Therefore, a cost-efficient Large-Eddy Simulation (LES) framework for pipe structures is elaborated, which satisfies the well-known quality criteria defined in literature. The associated flow discussions enable an application-oriented assessment of the pipe structures with the focus on critical wall-abrasive flow conditions. Positions of pronounced surface degradation within the WSG detected by complementary conducted experiments (see Klink et al., 2019, and Klink and Wegt, 2021) could be attributed to the flow topology and appropriate countermeasures postulated. As a special feature, the vortex identification methodology according to Graftieux et al. (2001) is applied to the flow discussions, which enables the identification of characteristic vortex topologies and their formation mechanisms.

For further investigations within the WSG framework, an ω_h -based elliptic-blending-related Reynolds-stress model (EBM) is formulated, calibrated and validated with a multitude of well-known benchmark cases. The formulation is based on the suggestions of Manceau and Hanjalić (2002) and Jakirlić and Maduta (2015) and combines the advantageous elliptic blending procedure for the pressure redistribution with the homogeneous specific dissipation rate concept. Furthermore, the phenomenon 'backbending' could be reliably avoided within the considered benchmark cases by a reformulation of the Simple Gradient Diffusion Hypothesis (SGDH). The extensive validation study including the WSG demonstrates the capability of the EBM to reproduce a variety of flow phenomena and confirms its suitability for further investigations.

Zusammenfassung

Die vorliegende Arbeit gewährt Einblicke in die Strömungstopologie gängiger Rohrstrukturen basierenden auf der neu entwickelten Wasser Spinnen Geometrie (WSG). Diese repräsentiert eine generische Kühlkanalgeometrie eines Verbrennungsmotors und beinhaltet Strömungsumlenkung (90° -Rohrkrümmer), Strömungsteilung (T-Abzweigung) und Strömungszusammenfluss (umgekehrte T-Abzweigung). Die Basis bilden ressourcenschonende Grobstruktursimulationen (LES) innerhalb der Rohrstrukturen, die die in der Literatur anerkannten LES-Qualitätskriterien erfüllen. Die Strömungsdiskussion ermöglicht eine anwendungsorientierte Bewertung der Strömungstopologie mit Blick auf kritische wandabtragende Strömungszustände. Positionen ausgeprägter Oberflächen-degradation der WSG, die in komplementär durchgeführten Experimenten detektiert wurden (siehe Klink et al., 2019, und Klink and Wegt, 2021), sind der Strömungstopologie zugeordnet und entsprechende Gegenmaßnahmen postuliert worden. Als Besonderheit ist die Wirbelidentifikationsmethodik nach Graftieaux et al. (2001) in die Strömungsdiskussion integriert, was die Identifizierung von charakteristischen Wirbelformationen sowie deren Entstehungsmechanismen ermöglicht.

Für weiterführende Untersuchungen innerhalb der WSG ist ein ω^h -basiertes, "elliptic-blending" relevantes Reynoldsspannungsmodell (EBM) formuliert, kalibriert und mit einer Vielzahl von bekannten Testfällen validiert worden. Die Formulierung orientiert sich an den Vorschlägen von Manceau and Hanjalić (2002) sowie Jakirlić and Maduta (2015) und kombiniert die vorteilhafte elliptische Prozedur für die Druckumverteilung mit dem homogenen spezifischen Dissipationsratenkonzept. Des Weiteren ist das Phänomen 'Backbending' in den betrachteten Testfällen durch eine Umformulierung der einfachen Gradientendiffusionshypothese (SGDH) zuverlässig vermieden worden. Die umfangreiche Validierungsstudie unter Einbeziehung der WSG demonstriert die Fähigkeit des EBM, eine Vielzahl von Strömungsphänomenen zu erfassen

und bestätigt seine Eignung für weiterführenden Untersuchungen.

Acknowledgement

The present work was created during my work as a research assistant at the Institute of Fluid Mechanics and Aerodynamics (SLA), Technical University of Darmstadt in the period April, 2018 to December, 2021. First and foremost, my thanks goes to Prof. Dr.-Ing. Jeanette Hussong, Prof. Dr.-Ing. Cameron Tropea and apl. Prof. Dr.-Ing. habil. Suad Jakirlić for the opportunity to do a doctorate. Furthermore, a special thanks to my supervisor, apl. Prof. Dr.-Ing. habil. Suad Jakirlić, for the trust and confidence in my abilities and for supporting me with advice and assistance whenever necessary.

A productive and supportive work environment is fundamental for a successful doctorate for which my former and current office colleagues Dr.-Ing. Benjamin Krumbein, Dr.-Ing. Felix Gerlach, Maximilian Bopp and Ivan Joksimovic have contributed significantly, thank you very much! A special thanks for their tireless perseverance in countless discussions I would like to express to Dr.-Ing. Robert Maduta, Dr.-Ing. Johannes Kissing and Dr.-Ing. Markus Schremb, which allowed me to see solutions and contributed to my progress. For all administrative activities and beyond, I could always rely on the support and advice of Birgit Neuthe, for which I am very grateful! In the process of writing this dissertation, Dr.-Ing. Johannes Kissing, Dr.-Ing. Felix Gerlach, Maximilian Bopp, Mark Gloerfeld, Louis Reitter, Dr.-Ing. Rüdiger Reitz and Artur Klink have thankfully proofread parts of it and thus contributed to the successful completion of my doctorate, many thanks!

The inter-institutional cooperation within the project 'Flow Erosion I' was characterized by an exceptionally loyal and productive way of working and therefore I would like to thank Artur Klink, Dr.-Ing. Rüdiger Reitz and Dr.-Ing. Tom Engler from the Center for Structural Materials (MPA-IfW).

In addition, I would also like to thank the Research Association for Combustion Engines (FVV) for its financial support as well as the Lichtenberg High Performance Computer of TU Darmstadt for providing the necessary

computational resources.

Last but not least, I heartily thank my family for their unwavering support during a very exciting and also turbulent time.

Contents

Abstract	v
Zusammenfassung	vii
Acknowledgement	ix
1. Introduction	1
1.1. Motivation	2
1.2. Outline	5
2. Theoretical background	9
2.1. The motion of Newtonian fluids: The Navier-Stokes equations .	10
2.2. Fundamental concepts of turbulence and modeling approaches .	11
2.2.1. Energy cascade and the life cycle of turbulent structures	11
2.2.2. Reynolds-Averaged Navier-Stokes (RANS) equation and second moment closure	14
2.2.3. Large-Eddy Simulation (LES)	16
2.2.4. Smagorinsky Subgrid-Scale (SGS) model	18
2.2.5. Dynamic Smagorinsky Subgrid-Scale (SGS) model . . .	19
2.2.6. Wall-Adapting Local Eddy-viscosity (WALE) Subgrid- Scale (SGS) model	20
2.3. Finite-Volume Method (FVM)	21
2.3.1. Spatial discretization	22
2.3.2. Temporal discretization	25
2.3.3. Under-relaxation	27

3. IC-engine-relevant cooling channel configuration: Water Spider Geometry (WSG)	29
3.1. Experimental conditions	31
3.1.1. Geometric dimensions of the WSG	31
3.1.2. Working fluid: 50/50 vol.% MEG/(deionized) water . .	32
3.1.3. Flow conditions	35
3.2. Computational framework	37
3.3. Preliminary LES investigations	38
3.3.1. Pipe grid optimization: Cross-section cell arrangement .	39
3.3.2. Pipe grid optimization: Streamwise-to-spanwise grid-cell ratio	43
3.3.3. Pipe grid optimization: Pipe section length	45
3.3.4. Feasibility check & subgrid-scale model	48
3.3.5. Conclusions	56
3.4. WSG-related pipe configurations	58
3.5. Flow in an isolated 90°-pipe bend	61
3.5.1. Introduction	61
3.5.2. Computational domain	64
3.5.3. Discussion: LES validation through experimental com- parison	66
3.5.4. Discussion: 90°-pipe bend flow topology	67
3.5.5. Discussion: Vortex topology	72
3.5.6. Discussion: Wall-abrasive flow effects	77
3.5.7. Discussion: Turbulence evolution	79
3.5.8. Discussion: Evolution of the Dean vortex circulation . .	84
3.5.9. Conclusions & Outlook	87
3.6. Flow in a symmetric pipe T-junction: Inflow division	89
3.6.1. Introduction	89
3.6.2. Computational domain	92
3.6.3. Discussion: First impression	94
3.6.4. Discussion: Impingement and vortex tube pair formation	97
3.6.5. Discussion: Flow detachment and formation of a recir- culation zone	103
3.6.6. Discussion: Outlet section	106
3.6.7. Conclusion and outlook	113

3.7.	Flow in a symmetric pipe T-junction: Confluence of two streams	115
3.7.1.	Introduction	115
3.7.2.	Computational domain	117
3.7.3.	Discussion: First impression	119
3.7.4.	Discussion: Saddle point and roll-up	124
3.7.5.	Discussion: Double symmetric vortex topology	128
3.7.6.	Discussion: Flow separation	132
3.7.7.	Conclusion and outlook	136
3.8.	Water Spider Geometry (WSG)	139
3.8.1.	Introduction	139
3.8.2.	Computational domain	140
3.8.3.	Discussion: First impression	142
3.8.4.	Discussion: WSG inflow	144
3.8.5.	Discussion: T-junction	147
3.8.6.	Discussion: Surface degradation upstream of the second deflection	149
3.8.7.	Discussion: Reverse T-junction	161
3.8.8.	Conclusion and outlook	171
3.9.	Conclusions and outlook	174
4.	Development of an ω_h-based elliptic-blending-related Reynolds-stress model	179
4.1.	Introduction	180
4.2.	Model formulation	185
4.2.1.	Pressure redistribution model term Φ_{ij}	187
4.2.2.	Stress-dissipation correlation model term ε_{ij}^h	190
4.2.3.	Specific dissipation rate equation $D\omega^h/Dt$	192
4.2.4.	Turbulent diffusion model terms D_{ij}^t and $D_{\omega^h}^t$	193
4.2.5.	Reynolds stress tensor blending in momentum equation	196
4.3.	Channel flow	201
4.4.	Pipe flow	208
4.5.	Zero pressure gradient boundary layer	213
4.6.	Flow past a rounded step - APG flow	218
4.7.	Flow past Backward-facing step (BFS)	226
4.8.	Flow past a periodically arranged 2D hill	232
4.9.	Flow in a 3D-diffuser	239

4.10. Flow in the WSG	247
4.11. Conclusion and outlook	255
5. Conclusions and outlook	259
A. EBM - Model Specification	265
B. Instability-Sensitive Elliptic-Blending-related Reynolds Stress Model	269
Bibliography	273
Acronyms	289
List of Symbols - Latin letters	293
List of Symbols - Greek letters	305
List of Indices - subscripted	309
List of Indices - superscripted	313
List of Figures	315
List of Tables	335

1. Introduction

The multitude of available fluids and the combination of them enables the adjustment of almost any desired fluid property combination and can provide a tailor-made solution, especially for technical applications. The range of applications for liquids is nearly unlimited, whether as energy source in engines or coolant in reactors and engines, as prominent technical examples, with the latter application being closely followed in the present study. Therefore, the preparation and/or reprocessing of the fluid is essential to provide fluid conditions (temperature, pressure, volume flux etc.) appropriate for the individual application. The specified fluid conditions have to be maintained from the point of preparation/reprocessing to the point of application, which requires the fluid to be transported through pipe systems. The usually compact design of technical applications prevents a direct pipe connection and a pipe system adapted to the available construction space is inevitable. Subsequently, a multitude of flow deflections, divisions and confluences are mostly unavoidable and the design of such arbitrary pipe systems is a highly complex engineering task especially with respect to a fluid transport that is as loss-free as possible.

Isothermal flow conditions are usually the exception in technical applications. The vast majority are thermally stressed and exhibits a pronounced non-isothermal flow characteristic, which can significantly complicate the design of such pipe systems. Apart from the temperature-dependent fluid properties and a possible impairment of the application functionality, an increased temperature can favor electrochemical corrosion of the flow configuration as well as provoking a potential phase change event whether it is of a cavitative and/or thermal nature. Apart of the cavitative bubble implosion, the surface-degradative effect of a thermally induced phase change event should not be underestimated. Under particularly critical conditions, the thermally-induced phase change can cause a dewetting of the wall and the formation of a wall-isolating vapor layer. The consequence is an increase in the wall temperature, which can lead to the

so-called 'boiling crises' and cause pronounced thermal stresses in the wall (see Behnke, 2009). Furthermore, the wall shear of the flow has to be included in a wall-degradative observation, especially with an abrasive medium having contaminated the fluid. Such contamination can be caused by manufacturing (e.g. molding residues of lost molds) or surface-degradative flow mechanism (e.g. cavitation) and can significantly increase the surface degradation potential of the flow. The listed phenomena usually have a localized effect and can cause a pronounced surface degradation, which can reduce the functionality (e.g. due to a deviating flow topology) up to a total failure of the technical application (e.g. breakthrough of the flow configuration wall).

Besides the flow conditions (volume flux, pressure, temperature), the expected flow phenomena and the corresponding surface degradation are closely related to the flow guidance and its shape in regions of pronounced streamline deflection. Such regions can usually be found in the vicinity of flow deflections, wall impingements or flow confluences. Knowledge of the expected flow topology within common flow guidance and the corresponding critical points with respect to the expected flow phenomena can provide significant advantages in the failure-proof construction of technical applications.

1.1. Motivation

Engineers have to deal with the above-described situation especially in the design of cooling systems, where the focus is not primarily on maintaining the flow conditions rather on the heat absorption process of the fluid/coolant within the heat exchanger. Due to the combination of unfavorable flow guidance and increased heat input, thermally critical conditions can arise, which can exceed the functional limits of the coolant and can lead to a decomposition of the coolant followed by a total failure of the cooling system. The automotive industry is also confronted with this situation in the design of the cooling systems of its Internal Combustion (IC) engines. The concurrent increase in the performance of IC engines coupled with the more stringent emission requirements imposed by the European union (Heibel, 2009, and Gruden, 2008) lead to an increase of thermal stresses on the cooling system by methods such as downsizing (van Basshuysen, 2013) and intelligent thermomanagement (Lunanova, 2009).

In order to ensure the functional reliability of the cooling system under the

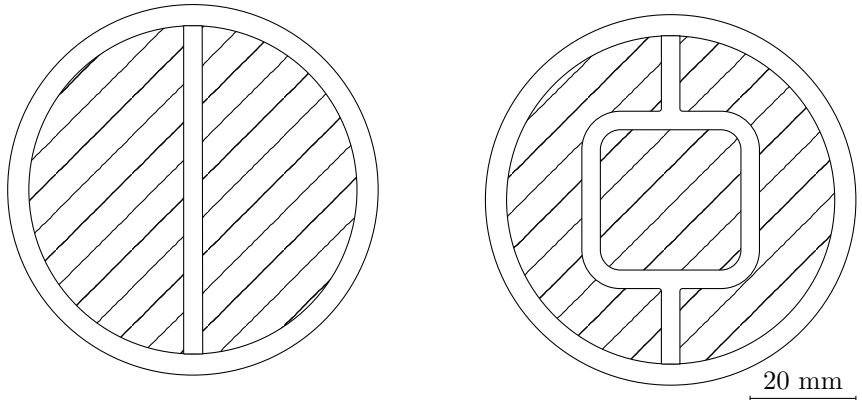


Figure 1.1.: Schematic illustration of the straight pipe reference test sample (left) and the newly designed reference test sample, denoted as Water Spider Geometry (WSG) (right). Both illustrations are published in Wegt et al. (2002).

application-oriented conditions, it is essential to understand the flow conditions within the cooling system, especially in regions of enhanced heat input. For this purpose, complementary experimental and numerical investigations have been carried out within the framework of a Bundesministerium für Wirtschaft und Energie (BMWi) project (Klink and Wegt, 2021) with the focus on flow conditions in pipe structures. These pipe structures represent generic geometries, which are highly suitable for experimental access and have a strong relevance to practical applications, see both test samples in Fig. 1.1. The latter configuration (Fig. 1.1, right) represents a new design of a reference test sample integrated within a modified version of the so-called Modulare Heißtestanlage (MHTA) (see Klink et al., 2019). Unlike flat reference test samples (not shown here), representing a gap flow between two circular plates as designed by Diehl (2006) and established by Kaiser (2009), the new reference sample (denoted as WSG) exhibits a large variety of simultaneously occurring, highly turbulent flow phenomena, as encountered in realistic cooling channels of IC engines and illustrated in Fig. 1.2. These include alternating flow decelerations and accelerations within stagnation and confluence regions as well as multiple

wall-bounded separation and reattachment regions affected eventually by a relevant pressure variation due to geometry deflection.

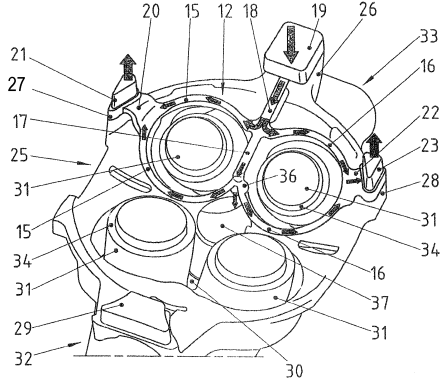


Figure 1.2.: Cooling channel configurations in the cylinder head of a realistic internal combustion engine accommodating the valve seat rings according to Reustle (2012) (United States Patent No. US 8,151,743 B2). Interested readers are referred to the original reference (downloadable from <https://patents.google.com/patent/US8151743B2/en>) for the explanation of individual positions.

Knowledge of the flow topology of the WSG is essential for the experimental evaluation of the flow guidance/coolant interaction as well as the development of constructive improvements to avoid critical flow conditions. The limited experimental accessibility and the completely unknown flow topology due to the newly designed flow guidance of the WSG predestines the employment of Computational Fluid Dynamics (CFD) for the fundamental characterization of the flow topology within the WSG. Although the experimentally defined flow conditions causes a pronounced phase change characteristics, the focus is set on the isothermal flow conditions in the following to obtain a meaningful insight into the flow topology of the WSG.

1.2. Outline

An efficient numerical setup for the consideration of pipe systems within well-resolved, highly comprehensive LES is elaborated and applied to the newly designed WSG as well as its, computed in an isolated manner, constitutive elements (straight sections as well as bend, bifurcation and confluence segments) with special focus on detecting the flow localities exhibiting increased potential for surface degradative flow mechanisms. Herewith, uniquely detailed instantaneous and time-averaged flow fields have been created, representing an indispensable reference for future modeling activities. Furthermore, a relevant Elliptic-Blending Model (EBM) proposal, utilizing the advantageous features of the Reynolds-stress models of turbulence by Manceau and Hanjalić (2002) and Jakirlić and Maduta (2015), is formulated within the RANS framework and evaluated by means of computing a number of relevant benchmark flow configurations. The particular attention is devoted to the asymptotically correct behavior of the Reynolds stress components when approaching the solid wall. Furthermore, the appropriate detection of flow separation due to an adverse pressure gradient (APG) was in the foreground of the RANS-model derivation, remedying at the same time the frequently encountered anomalous backbending of the mean dividing streamline around the flow reattachment. This issue was of crucial importance with respect to the correct capturing of the flow topology within the WSG.

An overview of the relevant theoretical background with the fluid mechanical consideration of turbulent flows and the numerical realization is provided in [Chapter 2](#). Apart of the governing equations of fluid dynamics, the fundamental concepts of turbulence modeling in the framework of the RANS- and LES-based methodologies are examined and the applied subgrid-scale (SGS) models are briefly introduced. The numerical realization based on the Finite-Volume Method (FVM) framework including relevant discretization methods is introduced, tailored appropriately to the present work.

A detailed flow discussion within the newly designed WSG and its constituting geometries follows in [Chapter 3](#) within well-resolved, highly comprehensive LES. After the geometrical properties (shapes and dimensions) and experimental conditions are described in [Chapter 3.1](#), a numerically efficient setup for pipe systems is elaborated in [Chapter 3.3](#). A feasibility study of the WSG-related pipe configurations ([Chapter 3.4](#)) precedes the flow discussions

in its separately considered geometrical components (90°-pipe bend (Chapter 3.5), T-junction (Chapter 3.6) and reverse T-junction (Chapter 3.7)) with the insights contributing correspondingly to the flow discussion of the WSG in Chapter 3.8. Particular attention was paid to the comparative assessment of the flow features encountered in the entire WSG and its relevant elements. Although the physical rationale of the general degradative flow mechanisms are in the foreground of the flow discussions, special attention is given to the experimentally detected regions of increased tendency to surface degradation. Accordingly, detailed three-dimensional velocity and pressure fields as well as those of turbulent quantities within the WSG have been provided, accessible for future numerical parameter studies. The latter is accompanied with in-depth analyses of the structural flow properties. Especially worth mentioning is the vortical flow characterization based on the three-dimensional mapping of the vortex position and its circulation.

The focus of Chapter 4 is on the further development of a Reynolds-stress model of turbulence (termed Elliptic-Blending Model - EBM) including its interactive validation and subsequent applications. The governing equations in terms of the transport equations of the homogeneous part of the specific dissipation rate ω^h and the Reynolds stress tensor $\overline{u_i u_j}$ are introduced and the modeling approaches for the individual terms are presented. The model formulation is interactively guided by selected channel flow configurations, serving as an important flow representative for studying the near-wall turbulence. Special attention is paid to the non-linear (in terms of the Reynolds-stress anisotropy tensor) modeling of the pressure redistribution process and of the turbulent diffusion mechanisms in both Reynolds stress and dissipation equations. A specific definition of the relevant characteristic lengthscales within the diffusion coefficients, accounting for both turbulent energy-containing scales and the viscosity-affected scales, was of crucial importance. The resulting model, modified appropriately towards the numerical robustness increase, represents a wall-reflection-term-free formulation. For the validation of the developed EBM formulation, several well-known benchmark cases are applied, whereby the greatest possible variety of flow phenomena has been ensured. The benchmark cases include some canonical two-dimensional flow configurations (fully developed channel (Chapter 4.3) and pipe flows (Chapter 4.4)), developing flows (a zero-pressure gradient boundary layer (Chapter 4.5) and a high Reynolds number APG boundary layer (Chapter 4.6)), flow separation from sharp-

edged (backward-facing step (BFS), Chapter 4.7) and continuous curved walls (periodic hill, Chapter 4.8) as well as three-dimensional, geometry-sensitive flow separation in differently configured 3D diffuser configurations (Chapter 4.9). Finally, the EBM is applied to the WSG and its suitability for near-industry flow configurations is discussed.

Chapters 3-~~r~~ 4 end up each with a relevant concluding section emphasizing most important achievements from the viewpoint of the computational methodology applied and flow physics captured.

Chapter 5 concludes the work by a general summary of the findings in the context of the WSG configuration simulation and relevant modeling activity, culminating in the EBM development. Furthermore, suggestions for possible further investigations are adequately specified.

2. Theoretical background

The chapter 'Theoretical background' provides an insight into the theoretical foundations relevant to the present work. The intention of this chapter is not to give an all-encompassing explanation of the individual topics, but rather to provide a focused excerpt and to draw the reader's attention to the main subjects.

With regard to the fluid mechanical observation of Internal Combustion (IC)-engine-relevant cooling channels, the governing equations of fluid mechanics are presented with the technically relevant assumption of an incompressible Newtonian fluid. Furthermore, one of the fundamental fluid mechanical dimensionless numbers, denoted as Reynolds number Re , is introduced, which is essential for characterizing the flow nature and comparability of different flow configurations.

The turbulent character of the flow within IC-engine-relevant cooling channels requires the integration of turbulence into the fluid mechanical considerations. The fundamental ideas of turbulence are outlined in terms of the life cycle of turbulent eddies and the smallest turbulent structures. Two relevant modeling strategies (Reynolds-Averaged Navier-Stokes (RANS) and Large-Eddy Simulation (LES)) are briefly introduced and relevant closure concepts for the governing equations are presented. Subsequently, well-known and in the present work applied subgrid-scale (SGS) models within the LES framework are discussed.

The concluding part introduces the numerical practicability of the governing equations and the spatial/temporal discretization methodology within the Finite-Volume Method (FVM). An excerpt of the discretization practice employed in the present work is presented and an important technique for stabilizing the numerics is introduced.

2.1. The motion of Newtonian fluids: The Navier-Stokes equations

The numerical consideration of fluid mechanical problems is usually based on a set of differential equations, the Navier-Stokes equations, which are the governing equations (mass and momentum balance) for Newtonian fluids with the continuum hypothesis and the Euler concept being applied. The continuum hypothesis allows the fluid to be considered as a continuous medium with the functional dependencies of its properties being continuous in space x_i and in time t . For the description of the continuum, the Euler concept is applied, since in an application-oriented consideration of a fluid mechanical problem, the motion of individual molecular particles is usually not of interest, but rather the flow variables at a certain location x_i and at a certain instant in time t (Spurk and Aksel, 1989). The fluids considered in the present work are of incompressible nature and the Cartesian index notation for tensors with the Einstein summation convention ($i, j = 1, 2, 3$) is applied. The incompressible Navier-Stokes equations are written as:

$$\frac{\partial U_i}{\partial x_i} = 0 \quad (2.1)$$

$$\frac{\partial U_i}{\partial t} + U_j \frac{\partial U_i}{\partial x_j} = -\frac{1}{\varrho} \frac{\partial p}{\partial x_i} + \frac{\partial}{\partial x_j} \left(\nu \frac{\partial U_i}{\partial x_j} \right) \quad (2.2)$$

$p(x_i, t)$ denotes the pressure and $U_i(x_i, t)$ the velocity of the fluid at a certain location in space x_i and at a certain instant in time t , as well as ϱ the density and ν the kinematic viscosity of the fluid. For the characterization of a flow configuration, the Reynolds number Re is a suitable fluid mechanical parameter. The Reynolds number relates to the ratio of the inertial to viscous forces and allows a statement about the flow regime, i.e., whether the flow acts laminar or turbulent. It is defined as

$$\text{Re} = \frac{\mathcal{U}\mathcal{L}}{\nu} \quad (2.3)$$

with a characteristic velocity \mathcal{U} and length \mathcal{L} adjusted to the given flow configuration. For a pipe flow, which is in the focus of interest in the present work, the characteristic velocity represents the bulk velocity of the flow U_b ,

i.e., the average velocity over the cross-section, and the characteristic length corresponds to the diameter of the pipe D .

2.2. Fundamental concepts of turbulence and modeling approaches

Turbulent flows are characterized by an apparently chaotic behavior superimposed on the mean flow, which is expressed in spatial and temporal fluctuations of the flow quantities. In our everyday lives, turbulent flows are omnipresent, which can be observed, for example, at a water tap, but is also one of the decisive factors in arriving at work in the morning by car. The latter is related to the increased mixing capability of turbulent flows compared to the laminar regime, which is advantageous for the mixing of matter, heat or momentum as described by Pope (2000). This distinguishes turbulent flow conditions for a variety of technical applications and is one of the motivations of the intensive research efforts in the field of turbulence in the last decades. The most fundamental concept of turbulence and the modeling approaches relevant to the present work are discussed below.

2.2.1. Energy cascade and the life cycle of turbulent structures

A well-known concept of turbulent flows was introduced by Richardson (1922) and further developed by Kolmogorov (1941), in which turbulent flows are described as a superposition of eddies with different sizes l and velocities $u(l)$. Kinetic energy is supplied to the turbulence by its production process in the form of the largest eddies, which are in the order of magnitude of the characteristic length of the flow configuration (see Eq. (2.3), \mathcal{L}). The characteristic Reynolds number of the largest eddies is sufficiently great ($\text{Re}_0 = u_0 l_0 / \nu$) that viscous effects are negligible. The largest eddies of turbulence are of unstable nature and continuously decay into smaller eddies, transferring the energy to them without any losses. The decay of the eddies continues until a stable state is reached, which corresponds to the state of the smallest eddies. The smallest eddies do not decay further, instead dissipate due to the increasing viscous effects. The decay and dissipation process of the turbulent

eddies is called energy cascade, where a direct relation is established between the production process of the largest eddies and the dissipation of the smallest eddies ε .

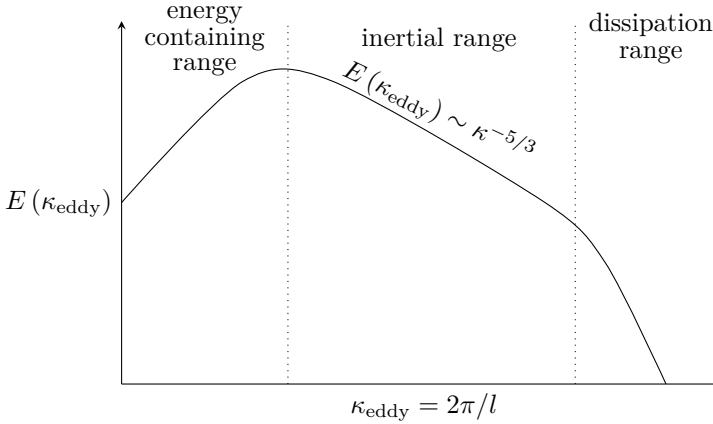


Figure 2.1.: Schematic illustration of the energy spectrum with the eddy energy $E(\kappa_{\text{eddy}})$ depicted over the eddy wave number $\kappa_{\text{eddy}} = 2\pi/l$.

The concept of the energy cascade is illustrated in Fig. 2.1 with the energy spectrum of an isotropic turbulent state. The energy spectrum of a turbulent state is classically depicted double logarithmic with the energy $E(\kappa_{\text{eddy}})$ over the wavenumber of the associated eddies $\kappa_{\text{eddy}} = 2\pi/l$. The three states of the turbulent eddy life cycle with the production process (energy-containing range), the decay and energy transfer to smaller eddies (inertial subrange) and the dissipation of the smallest eddies (dissipation range) are highlighted in Fig. 2.1, where the energy transfer within the inertial subrange can be described by a power law with a power of $-5/3$. The energy spectrum can be employed to describe the energetic state of the turbulence, which corresponds to the area enclosed by the energy spectrum according to Eq. (2.4) and is denoted as the turbulent kinetic energy k .

$$k = \int_0^{\infty} E(\kappa_{\text{eddy}}) d\kappa_{\text{eddy}} \quad (2.4)$$

The smallest, dissipative eddies within a turbulent state are statistically isotropic and have an universal character according to the explanations of Kolmogorov (1941). Any information about the flow topology and its boundaries, which determines the formation and shape of the largest eddies, is lost within the smallest eddies as a result of the cascading process. Due to the universal character of the smallest eddies, their characteristics in terms of length, velocity and time scale can be described by the kinematic viscosity ν and the viscous dissipation ε . These characteristics are denoted as Kolmogorov scales (length η , velocity u_η and timescale τ_η of the smallest eddies) and are defined as:

$$\eta = (\nu^3/\varepsilon)^{1/4} \quad u_\eta = (\varepsilon\nu)^{1/4} \quad \tau_\eta = (\nu/\varepsilon)^{1/2} \quad (2.5)$$

The knowledge of the characteristics of the smallest turbulent scales by the Kolmogorov scales forms the basis for a wide range of modeling approaches for turbulent processes. A well-known example are the considerations of Durbin (1991) for modeling the size of the turbulent eddies L with superimposing the turbulent lengthscale $L_L \sim k^{3/2}/\varepsilon$ and the Kolmogorov lengthscale $L_\eta \sim \eta$ by a 'max' function to correctly capture the near-wall behavior of the dissipation (see Eq. (2.6)). For adjusting the switch between both lengthscales according to the theoretical considerations of Durbin, the lengthscales are factorized with constants defined as $C_L = 0.17$ and $C_\eta = 80$. Analogous considerations are introduced by Durbin (1991) for the timescale of turbulent eddies T (see Eq. (2.7)), where the factorization of the Kolmogorov timescale is done with $C_T = 6$. The choice of constants has been modified by various authors, as well as the superposition method of the individual scales by Durbin (1996) with the geometric mean for example. A summary of modeling strategies and choices of constants is given by Billard and Laurence (2012).

$$L = C_L \max\left(k^{3/2}/\varepsilon, C_\eta (\nu^3/\varepsilon)^{1/4}\right) \quad (2.6)$$

$$T = \max\left(k/\varepsilon, C_T (\nu/\varepsilon)^{1/2}\right) \quad (2.7)$$

The modeling of turbulent flows can be achieved by different modeling strategies, which can be classified by the amount of modeled to total turbulent kinetic energy. The classical strategies include the Direct Numerical Simulation (DNS), Large-Eddy Simulation (LES) and Reynolds-Averaged Navier-Stokes

(RANS)-based strategies. Within the Direct Numerical Simulation (DNS) framework, the Navier-Stokes equations are solved directly without any modeling approaches, which involves an enormous amount of computational effort. This method is not applied in the present work and interested readers are referred to Pope (2000), for example. The remaining two strategies (RANS and LES) are relevant to the present work and are described in the following sections.

2.2.2. Reynolds-Averaged Navier-Stokes (RANS) equation and second moment closure

For most technical applications, the apparently chaotic behavior of turbulent flows is of secondary importance and the determination of the underlying time-averaged flow field is of primary interest. One of the first who described this behavior was Reynolds (1895), who proposed a decomposition of the turbulent flow quantities $\Theta_i(x_i, t)$ into a (partially) time-averaged $\overline{\Theta}_i(x_i, t)$ and a fluctuating part $\theta_i(x_i, t)$ (see Eq. (2.8)). The time-averaged part can still be time-dependent, for example for periodic flow phenomena.

$$\Theta_i(x_i, t) = \overline{\Theta}_i(x_i, t) + \theta(x_i, t) \quad (2.8)$$

For the determination of the mean quantities of a turbulent flow, the Reynolds decomposition is applied to the governing equations for incompressible Newtonian fluids, the Navier-Stokes equations (Equations (2.1) and (2.2)). The velocity $U_i(x_i, t)$ and pressure field $p(x_i, t)$ within the Navier-Stokes equations are decomposed according to Reynolds and the entire system of equations is time-averaged. The resulting system of equations (Equations (2.9) and (2.10)) represents the governing equations for the mean velocity $\overline{U}_i(x_i, t)$ and pressure field $\overline{p}(x_i, t)$ and is known as Reynolds-Averaged Navier-Stokes (RANS) equations.

$$\frac{\partial \overline{U}_i}{\partial x_i} = 0 \quad (2.9)$$

$$\frac{\partial \overline{U}_i}{\partial t} + \overline{U}_j \frac{\partial \overline{U}_i}{\partial x_j} = -\frac{1}{\rho} \frac{\partial \overline{p}}{\partial x_i} + \frac{\partial}{\partial x_j} (2\nu \overline{S}_{ij} - \overline{u_i u_j}) \quad (2.10)$$

From the time-averaging procedure of the RANS equations (Eq. (2.10)), an additional term on the right-hand side arises, the so-called Reynolds stress tensor $\overline{u_i u_j}$. The Reynolds stress tensor is a symmetrical tensor of second order and represents the momentum transfer by the fluctuating velocity field according to Pope (2000). Thus, the RANS equations contain ten unknowns, the mean pressure \overline{p} , velocity \overline{U}_i and Reynolds stress field $\overline{u_i u_j}$, compared to four equations, which causes an underdetermined system of equations. Consequently, the RANS equations cannot be solved without further effort, which is known as the closure problem of turbulence.

A well-known approach for closing the RANS equations was proposed by Boussinesq (1877) with modeling the momentum transfer of the fluctuating velocity field by means of the mean rate of strain $\overline{S}_{ij} = 0.5 (\partial \overline{U}_i / \partial x_j + \partial \overline{U}_j / \partial x_i)$ and a scalar, the so-called turbulent viscosity ν_t . The corresponding modeling approach for the Reynolds stress tensor, known as turbulent-viscosity hypothesis, is defined in Eq. (2.16) with the Kronecker delta δ_{ij} being 1 for equal and 0 for unequal indices. By applying this hypothesis to the RANS equations, the Reynolds stress tensor with its six unknowns is reduced to the unknown turbulent viscosity.

$$\overline{u_i u_j} = -2\nu_t \overline{S}_{ij} + \frac{2}{3} k \delta_{ij} \quad (2.11)$$

The unknown turbulent viscosity requires a modeling approach for closing the equation system, which is classified by the number of additional differential equations employed. A variety of modeling approaches has been developed in the past decades, such as the algebraic mixing length model according to Prandtl (1925), the two-equation $k - \omega$ Shear Stress Transport (SST) model according to Menter (1992), or the four-equation $k - \varepsilon - \zeta - f$ model proposed by Hanjalić et al. (2004). As the present work focuses on the Second-Moment Closure (SMC) approach, the turbulent-viscosity hypothesis is not discussed in detail and reference is made to the literature accordingly.

Another possibility for closing the RANS equations is to derive the governing equation of the Reynolds stress tensor. Therefore, the momentum balance of the Navier-Stokes equation I_i (Eq. (2.2)), the momentum balance of the RANS equations \overline{I}_i (Eq. (2.10)) and the momentum balance of the fluctuations $I'_i = I_i - \overline{I}_i$ are combined as $\overline{u_i I'_j} + \overline{u_j I'_i} = 0$. The governing equation of the Reynolds stress tensor is presented in Eq. (2.12) with the production P_{ij} ,

the viscous dissipation ε_{ij} , the pressure redistribution Φ_{ij} and the diffusion D_{ij} . The latter can be divided from left to right into turbulent diffusion D_{ij}^t , molecular diffusion D_{ij}^v and pressure diffusion D_{ij}^p . The pressure diffusion is classically neglected within turbulence modeling. Except the production of the Reynolds stress tensor, all terms on the right-hand side of Eq. (2.12) are unknown and require model approaches to solve the Reynolds stress transport equation.

$$\begin{aligned}
 \frac{\partial \overline{u_i u_j}}{\partial t} + \overline{U}_k \frac{\overline{u_i u_j}}{\partial x_k} &= \underbrace{-\overline{u_i u_k} \frac{\partial \overline{U}_j}{\partial x_k} - \overline{u_j u_k} \frac{\partial \overline{U}_i}{\partial x_k}}_{\text{production } P_{ij}} + \underbrace{2\nu \frac{\partial \overline{u_i}}{\partial x_k} \frac{\partial \overline{u_j}}{\partial x_k}}_{\text{dissipation } \varepsilon_{ij}} \\
 + \underbrace{\frac{p}{\rho} \left(\frac{\partial u_i}{\partial x_j} + \frac{\partial u_j}{\partial x_i} \right)}_{\text{pressure redistribution } \Phi_{ij}} &+ \underbrace{\frac{\partial}{\partial x_k} \left[-\overline{u_i u_j u_k} + \nu \frac{\partial \overline{u_i u_j}}{\partial x_k} - \frac{p}{\rho} (\delta_{ki} u_j + \delta_{kj} u_i) \right]}_{\text{diffusion } \mathcal{D}_{ij}}
 \end{aligned} \tag{2.12}$$

Superficially, the derivation of the Reynolds stress transport equation has merely added new unclosed terms compared to the turbulent-viscosity hypothesis. However, the fundamental advantage in the application of the Reynolds stress transport equation is the consideration of the anisotropic character of the Reynolds stresses, which is largely lost within the turbulent-viscosity hypothesis.

For closing the Reynolds stress transport equation, numerous modeling approaches for the individual unclosed terms are present in literature. A detailed discussion of these approaches is omitted at this point and reference is made to Chapter 4, in which the approaches are discussed in the context of the modeling concept of the ω_h -based elliptic-blending-related Reynolds-stress model (EBM).

2.2.3. Large-Eddy Simulation (LES)

In contrast to the RANS-based models, a part of the turbulent motion is directly resolved within the Large-Eddy Simulation (LES) framework, namely the largest eddies. Unlike the smallest eddies, the largest eddies do not have an isotropic character and contribute significantly to the flow characteristics.

Classically, a well-resolved, highly comprehensive LES is characterized by the modeled part of the turbulent kinetic energy of the underlying subgrid-scale (SGS) model being less than 20% of the total amount ($k_{\text{SGS}}/k < 0.2$), according to Pope (2000). However, the quality criteria of LES are discussed in detail in Chapter 3.3.4. The following LES discussion has already been published in Wegst et al. (2002).

For the detection of the largest eddies, a spatial, low-pass filter is applied to the flow quantities to decompose them into a filtered $\widetilde{\Theta}_i(x_i, t)$ and a residual component $\theta'_i(x_i, t)$, the SGS component. The filter-based decomposition of an arbitrary flow quantity $\Theta_i(x_i, t)$ is presented in Eq. (2.13), where the filtered components are marked with $\widetilde{(\cdot)}$ and the residual with $(\cdot)'$.

$$\Theta_i(x_i, t) = \widetilde{\Theta}_i(x_i, t) + \theta'_i(x_i, t) \quad (2.13)$$

For the determination of the governing equations of the filtered flow quantities, the procedure presented in Eq. (2.13) is applied to the velocity $U_i(x_i, t)$ and pressure fields $p(x_i, t)$ contained in the Navier-Stokes equation (see Equations (2.1) and (2.2)) and the resulting system of equations is again spatially filtered. The resulting spatially filtered system of equations represents the spatially filtered Navier-Stokes equations and has the following form:

$$\frac{\partial \widetilde{U}_i}{\partial x_i} = 0 \quad (2.14)$$

$$\frac{\partial \widetilde{U}_i}{\partial t} + \frac{\partial \widetilde{U}_j(\widetilde{U}_i)}{\partial x_j} = -\frac{1}{\rho} \frac{\partial \widetilde{p}}{\partial x_i} + 2\nu \frac{\partial \widetilde{S}_{ij}}{\partial x_j} - \frac{\partial \tau_{\text{SGS},ij}}{\partial x_j} \quad (2.15)$$

$\widetilde{U}_i(x_i, t)$ and $\widetilde{p}(x_i, t)$ denote the filtered velocity and pressure fields, whereby the tilde-operator denotes a three-dimensional filtering in space with a filter width Δ as already mentioned and $\widetilde{S}_{ij} = 0.5 (\partial \widetilde{U}_i / \partial x_j + \partial \widetilde{U}_j / \partial x_i)$ is the strain-rate tensor of the filtered velocity. The SGS stress tensor $\tau_{\text{SGS},ij} = \widetilde{U}_i \widetilde{U}_j - \widetilde{U}_i \widetilde{U}_j$ represents the non-resolved residual turbulence for which an adequate closure model is required. The relevant filter width, interpreted actually as the representative grid spacing within the implicit filtering strategy, is calculated by the cubic root of the grid-cell volume $\Delta = V_{\text{cell}}^{1/3}$.

Similar to the turbulent-viscosity hypothesis, the residual-stress tensor $\tau_{\text{SGS},ij}$ is modeled by using the Boussinesq correlation in analogy to the molecular viscous stress:

$$\tau_{\text{SGS},ij} - \frac{1}{3}\delta_{ij}\tau_{\text{SGS},kk} = -2\nu_{\text{SGS}}\tilde{S}_{ij} \quad (2.16)$$

The strategies for modeling the unknown SGS viscosity ν_{SGS} applied in this work, namely the standard Smagorinsky model (Smagorinsky, 1963), its dynamic version (Germano et al., 1991, and Lilly, 1992) and the Wall-Adapting Local Eddy-viscosity (WALE) model (Nicoud and Ducros, 1999), are briefly described in the following sections. For a more detailed specification, the reader is referred to the original papers.

2.2.4. Smagorinsky Subgrid-Scale (SGS) model

A well-known model formulation, based on the local equilibrium between the production and dissipation of the unresolved turbulence structures, is postulated by Smagorinsky (1963). The resulting relationship for incompressible flows describes the proportionality of the relevant turbulent viscosity to a characteristic length scale of the subgrid scales Δ_{SGS} and the filtered strain rate tensor \tilde{S}_{ij} :

$$\nu_{\text{SGS}} = (C_s\Delta_{\text{SGS}})^2\sqrt{2\tilde{S}_{ij}\tilde{S}_{ij}} \quad (2.17)$$

with the Smagorinsky constant $C_s = C_k^{3/4}/C_\varepsilon^{1/4} \approx 0.168$; $C_k = 0.094$ and $C_\varepsilon = 1.048$. To ensure the zero wall-value of the SGS viscosity when approaching the solid wall, an empirical damping function proposed by Van Driest (1956) has to be taken into account. It is considered by a procedure blending between the representative grid-spacing-dependent filter width Δ and the van Driest formulation including the von Kármán constant $\kappa = 0.41$ and the model constant $A^+ = 26$:

$$\Delta_{\text{SGS}} = \min \left\{ \frac{\kappa y}{C_s} [1 - \exp(-y^+/A^+)], \Delta \right\} \quad (2.18)$$

The associated subgrid-scale fractions of the kinetic energy k_{SGS} and its dissipation rate ε_{SGS} are defined as follows:

$$k_{\text{SGS}} = \frac{C_k}{C_\varepsilon} \Delta_{\text{SGS}}^2 \widetilde{S}_{ij} \widetilde{S}_{ij} \quad (2.19)$$

$$\varepsilon_{\text{SGS}} = C_\varepsilon k_{\text{SGS}}^{3/2} / \Delta_{\text{SGS}} \quad (2.20)$$

2.2.5. Dynamic Smagorinsky Subgrid-Scale (SGS) model

Germano et al. (1991) proposed a dynamic procedure in which the Smagorinsky constant is calculated as a field variable depending on the flow conditions. The procedure was extended by Lilly (1992). In this regard, another filtering operator, denoted by $\widehat{(\cdot)}$, is applied to Equations (2.14) and (2.15), resulting in the 'test-filtered' Navier-Stokes equations accounting for the subtest-scale stress tensor T_{ij} in analogy to the SGS stress tensor $\tau_{\text{SGS},ij}$. The resolved turbulent motion characterized by the scales ranging between the filter width Δ , coping with the underlying grid resolution, and the subtest-scale filter width $\widehat{\Delta} = 2\Delta$ is represented by the tensor L_{ij} ($= T_{ij} - \tau_{\text{SGS},ij}$) and can be connected to the subtest-scale and SGS stress tensors by its deviatoric components as follows:

$$L_{ij} - \frac{1}{3} \delta_{ij} L_{kk} = -2C_s^2 M_{ij} \quad (2.21)$$

with

$$M_{ij} = \widehat{\Delta}^2 \widehat{S}_{ij} |\widehat{S}| - \Delta^2 \left(\widehat{S}_{ij} |\widehat{S}| \right) \quad (2.22)$$

By an error estimation of Eq. (2.22) a dynamic calculation procedure for the Smagorinsky "constant" is formulated and the turbulent viscosity of the subgrid scales can be calculated:

$$C_s^2 = -0.5 \frac{L_{ij} M_{ij}}{M_{kl} M_{kl}} \quad (2.23)$$

$$\nu_{\text{SGS}} = (C_s \Delta)^2 \sqrt{2 \widetilde{S}_{ij} \widetilde{S}_{ij}} \quad (2.24)$$

The formulations defining the SGS fractions of the turbulence kinetic energy k_{SGS} and its dissipation rate ε_{SGS} in the dynamic Smagorinsky framework read:

$$k_{\text{SGS}} = \frac{0.5 \left(|\widehat{\widetilde{U}_i \widetilde{U}_i}| - |\widetilde{U}_i \widetilde{U}_i| \right) \left(\widehat{\Delta} |\widehat{\widetilde{S}}| |\widehat{\widetilde{S}}| - \Delta |\widetilde{S} \widetilde{S}| \right)}{\left(\widehat{\Delta} |\widehat{\widetilde{S}}| |\widehat{\widetilde{S}}| - \Delta |\widetilde{S} \widetilde{S}| \right)^2} \quad (2.25)$$

$$\varepsilon_{\text{SGS}} = C_\varepsilon k_{\text{SGS}}^{3/2} / \Delta \quad (2.26)$$

2.2.6. Wall-Adapting Local Eddy-viscosity (WALE) Subgrid-Scale (SGS) model

In order to correctly capture the asymptotic near-wall behavior of the SGS viscosity ν_{SGS} and to avoid empirical damping functions, such as the one described by Van Driest (1956), the filtered vorticity-rate tensor $\widetilde{\Omega}_{ij} = 0.5(\partial \widetilde{U}_i / \partial x_j - \partial \widetilde{U}_j / \partial x_i)$ is included in the model formulation in addition to the filtered strain-rate tensor \widetilde{S}_{ij} within the framework of the Wall-Adapting Local Eddy-viscosity (WALE) SGS model proposed by Nicoud and Ducros (1999). The relevant operator $(\mathcal{S}_{ij}^d \mathcal{S}_{ij}^d)^{3/2} \sim y^3$ exhibits the targeted near-wall behavior without inclusion of any empirical damping functions, whereby \mathcal{S}_{ij}^d (Eq. (2.28)) corresponds to the traceless symmetric part of the square of the velocity gradient tensor. The formulation of the subgrid-scale viscosity ν_{SGS} in the WALE framework is defined according to Eq. (2.27), where, for reasons of non-dimensioning and numerical stability, the operator $(\mathcal{S}_{ij}^d \mathcal{S}_{ij}^d)^{3/2}$ is normalized by $(\widetilde{S}_{ij} \widetilde{S}_{ij})^{5/2} + (\mathcal{S}_{ij}^d \mathcal{S}_{ij}^d)^{5/4}$. The previously defined filter width Δ can be used directly as the characteristic length scale of the SGS on the basis of the modeling strategy described above.

$$\nu_{\text{SGS}} = (C_w \Delta)^2 \frac{(\mathcal{S}_{ij}^d \mathcal{S}_{ij}^d)^{3/2}}{(\widetilde{S}_{ij} \widetilde{S}_{ij})^{5/2} + (\mathcal{S}_{ij}^d \mathcal{S}_{ij}^d)^{5/4}} \quad (2.27)$$

with

$$\mathcal{S}_{ij}^d = \widetilde{S}_{ik} \widetilde{S}_{kj} + \widetilde{\Omega}_{ik} \widetilde{\Omega}_{kj} - \frac{1}{3} \delta_{ij} [\widetilde{S}_{mn} \widetilde{S}_{mn} + \widetilde{\Omega}_{mn} \widetilde{\Omega}_{mn}] \quad (2.28)$$

The choice of the WALE constant C_w is subject of Chapter 3.3.4. Whereas Nicoud and Ducros (1999) proposed the value laying in the range $C_w = 0.5$ to 0.6 , the value $C_w = 0.325$ is suggested in conjunction with the OpenFOAM® code application. The SGS kinetic energy k_{SGS} and its dissipation rate ε_{SGS} are defined by the following equations with $C_k = 0.094$ and $C_\varepsilon = 1.048$:

$$k_{\text{SGS}} = \frac{\nu_{\text{SGS}}^2}{\Delta^2 C_k^2} \quad (2.29)$$

$$\varepsilon_{\text{SGS}} = C_\varepsilon k_{\text{SGS}}^{3/2} / \Delta \quad (2.30)$$

2.3. Finite-Volume Method (FVM)

The transformation of the above presented equations determining the flow motion into the numerical procedure of the Finite-Volume Method (FVM) requires a spatial and temporal discretization of the equations to apply them to the control volumes (CVs) into which the flow configuration is decomposed. For the illustrative description of the discretization procedure, the incompressible Navier-Stokes equations (Eq. (2.1) and (2.2)) are unsuitable due to their complex form. Instead and following Schäfer (2006), the procedure of the spatial discretization is carried out on the basis of a general stationary transport equation of an arbitrary, time-independent scalar field $\phi(x_i)$ (Eq. (2.31)) and afterwards extended to the general time-dependent transport equation with $\phi(x_i, t)$ for explanation of the time discretization (Eq. (2.40)). The terms of Eq. (2.31) on the left-hand side describe the convective and diffusive flux of ϕ with the diffusion coefficient α_{Diff} . On the right-hand side, the volume sources and sinks of ϕ are summarized in f .

$$\frac{\partial}{\partial x_i} \left(\rho U_i \phi - \alpha_{\text{Diff}} \frac{\partial \phi}{\partial x_i} \right) = f \quad (2.31)$$

The discretization procedure is described on a simplified, quadrilateral two-dimensional grid with a homogeneous cell distribution and a cell-orientated arrangement of nodes (cell center \equiv computational node), as illustrated in Fig. 2.2. The considered CV is highlighted in gray, its node is denoted by P and has the surface areas S_c as well as the volume V . The nodes C as well as the midpoints of the faces c around the observed CV (node P) are denoted

according to the labeling of a compass with $C = N, E, S, W$ and $c = n, e, s, w$. The normal vectors on the faces of the CV are denoted by n_c and the corresponding face lengths by δS_c .

The present Chapter 2.3 'Finite-Volume Method (FVM)' is guided by the explanations of Schäfer (2006) and represents an excerpt relevant to the present work. For more detailed information, please refer to Schäfer (2006).

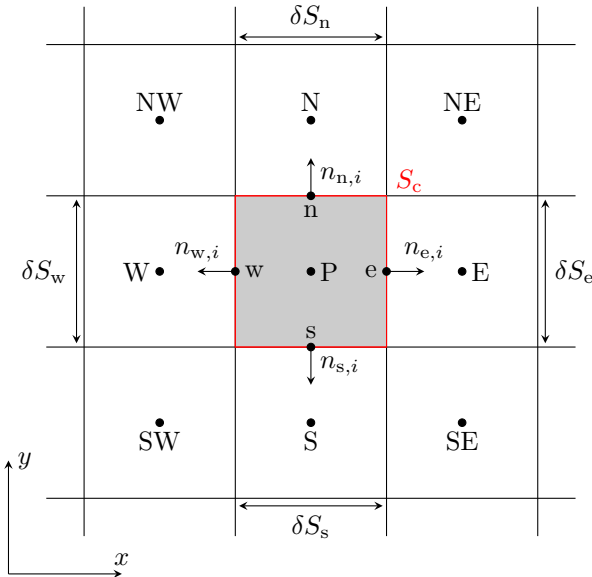


Figure 2.2.: Schematic illustration of a simplified, quadrilateral two-dimensional grid with a homogeneous distribution and a cell-oriented arrangement of nodes with the considered cell volume (CV) highlighted in gray. The node and face denotation follows the labeling of a compass.

2.3.1. Spatial discretization

For the spatial discretization of Eq. (2.31), the integral form has to be derived with the help of the integral theorem of Gauß, whereby the surface integral

can be written as the sum over the surface S_c . The integral form of the general stationary transport equation (Eq. (2.32)) contains surface integrals including the convective and diffusive fluxes over the CV borders as well as volume integrals of the source and sink terms. Both have to be approximated in terms of CV nodes ϕ_C for spatial discretization.

$$\sum_c \int_{S_c} \left(\rho U_i \phi - \alpha_{\text{Diff}} \frac{\partial \phi}{\partial x_i} \right) n_i \, dS_c = \iiint_V f \, dV \quad (2.32)$$

The approximation of the surface and volume integrals are carried out with the so-called midpoint rule, which approximates an integral by the center value of the integrand multiplied with the length, area or volume spanned by the integral limits. Applying the midpoint rule on Eq. (2.32) with the assumptions of constant density ρ and velocity U_i over S_c leads to

$$\sum_c \dot{m}_c \phi_c - \sum_c \alpha_{\text{Diff}} n_{ci} \delta S_c \left(\frac{\partial \phi}{\partial x_i} \right)_c = f_P \delta V, \quad (2.33)$$

which is an integral-free, discretized form of Eq. (2.31) and is formulated as a function of the face midpoint values ϕ_c and their spatial derivatives. Within the FVM framework, only the values of ϕ at the nodes of the CV (ϕ_C) are known, which prevents direct application of Eq. (2.33) to the numerical solution framework. Rather, an approximation of Eq. (2.33) and its terms has to be done in dependence of the CV nodes (P, N, E, S, W).

Discretization of convective fluxes

In the case of convective flux, the face mid-points ϕ_c have to be approximated in terms of CV nodes. A possibility is the linear interpolation between the nodes of the considered CV P with the corresponding neighbor C, which is known as Central Difference Scheme (CDS) and has a second-order interpolation error. The corresponding approximation of ϕ_e according to the CDS is presented in Eq. (2.34) with the interpolation factor $\gamma_e = (x_e - x_P)/(x_E - x_P)$ with x_e , x_E and x_P denote the position of the nodes along the x -axis according to Fig. 2.2.

$$\phi_e \approx \gamma_e \phi_E + (1 - \gamma_e) \phi_P \quad (2.34)$$

Another way of approximating ϕ_c is the Upwind Difference Scheme (UDS), which, in its simplest form, approximates ϕ_c as a step function depending on the mass flux \dot{m}_c according to Eq. (2.35) (exemplary for ϕ_e). The interpolation error of the described UDS is of first-order and the resulting error is called numerical diffusion due to the similar form of the leading error term to the diffusion term.

$$\phi_e \approx \phi_P, \quad \text{if } \dot{m}_e > 0; \quad \phi_e \approx \phi_E, \quad \text{if } \dot{m}_e < 0 \quad (2.35)$$

CDS is characterized by a high level of accuracy, whereby numerical instabilities can occur due to a lack in robustness. In contrast, UDS has a clear higher level of robustness compared to CDS, but with significant losses in accuracy due to the first-order interpolation error. To combine the advantages of different flux approximations, Khosla and Rubin (1974) introduced the concept of the flux-blending, in which two schemes are linearly combined with the flux blending factor β_{flux} . For the flux blending of CDS and UDS, the approximation of ϕ_e results in Eq. (2.36) with β_{flux} between 0 and 1, whereby $\beta_{\text{flux}} = 0$ corresponds to full UDS and $\beta_{\text{flux}} = 1$ to full CDS.

$$\phi_e \approx (1 - \beta_{\text{flux}}) \phi_e^{\text{UDS}} + \beta_{\text{flux}} \phi_e^{\text{CDS}} \quad (2.36)$$

Discretization of diffusive fluxes

The diffusive flux requires an approximation of the surface normal derivative of ϕ in terms of CV nodes. Assuming ϕ is a linear function between P and C, the application of the CDS for $c = e$ leads to:

$$\left(\frac{\partial \phi}{\partial x} \right)_e \approx \frac{\phi_E - \phi_P}{x_E - x_P} \quad (2.37)$$

The interpolation error of this approximation depends on the grid. For an equidistant grid, the interpolation error is of second-order. With increasing deviation from $(x_E - x_e) / (x_e - x_P) = 1$, the interpolation error tends to first-order.

Linear equation system

The application of the described approximation methods to Eq. (2.33) results in a general, node depending form presented in Eq. (2.38) with the corresponding

prefactors summarized in a_P , a_N , a_E , a_S , a_W and b_P .

$$a_P\phi_P = a_N\phi_N + a_E\phi_E + a_S\phi_S + a_W\phi_W + b_P. \quad (2.38)$$

An expansion of the approximation methods to the remaining $(N - 1)$ CV within the grid of the computational domain results in a linear system of N -equations. This can be summarized to:

$$a_P^i\phi_P^i - \sum_c a_c^i\phi_c^i = b_P^i \quad \text{with } i = 1 \dots N \quad \text{and } c = N, E, S, W \quad (2.39)$$

The numerical solution procedure of linear equation systems is a well-known topic in literature and a detailed description would go beyond the scope of this discussion. Interested readers are recommended to Hirsch (1988), Ferziger et al. (2002), Schäfer (2006) or Versteeg and Malalasekera (2007), for example.

2.3.2. Temporal discretization

Fluid mechanical problems are in most cases of a transient nature, i.e., the consideration of the temporal dimension is essential. To extend the preceding discussion to a transient consideration, the steady-state transport equation presented in Eq. (2.31) is extended to its transient form (Eq. (2.40)) including the temporal derivative of $\phi(x_i, t)$, which is now a function of its location x_i and time t .

$$\frac{\partial(\varrho\phi)}{\partial t} + \frac{\partial}{\partial x_i} \left(\varrho U_i \phi - \alpha_{\text{Diff}} \frac{\partial \phi}{\partial x_i} \right) = f \quad (2.40)$$

The temporal discretization is preceded by a spatial discretization, where the methods presented in Chapter 2.3.1 can be applied.

Summing the now time-dependent prefactors according to Eq. (2.38) and assuming a time-independent density and CV volume ($\varrho, \delta V \neq f(t)$), leads to the following ordinary differential equation:

$$\frac{\partial \phi_P}{\partial t} = \frac{1}{\varrho \delta V} \left[-a_P(t)\phi_P + \sum_C a_C(t)\phi_C + b_P(t) \right] \quad \text{with } c = N, E, S, W \quad (2.41)$$

Considering the number of CVs of the computational domain, a coupled system of N ordinary differential equations has to be solved in the transient case. Eq. (2.41) is summarized as Eq. (2.42) in the following, to ensure clarity with $\vec{\phi}$ being the sum of the unknown N functions in vectorial form and $\vec{L}(\vec{\phi})$ representing the right-hand side of Eq. (2.41).

$$\frac{\partial \vec{\phi}}{\partial t} = \vec{L}(\vec{\phi}) \quad (2.42)$$

In the numerical solution procedure, the observed time interval ΔT is decomposed into discrete moments t^n with a temporal distance of Δt^n , which can be non-equidistant:

$$t^{n+1} = t^n + \Delta t^n \quad n = 0, 1, 2, \dots \quad (2.43)$$

Time is always directed towards the future and is consequently constantly increasing, which means that the present time step t^{n+1} can only be influenced by previous ones. The methods for time discretization can be subdivided into two groups, the explicit methods, where only the preceding time steps are considered ($\phi^{n+1} = F(\phi^n, \phi^{n-1}, \dots)$) and the implicit methods, where the current time step is additionally taken into account ($\phi^{n+1} = F(\phi^{n+1}, \phi^n, \phi^{n-1}, \dots)$).

Explicit methods

A well-known representative of the explicit methods is the explicit Euler method. In the context of the explicit Euler method, the time derivative of $\vec{\phi}$ is approximated by a forward differencing scheme. For the time step t^n , this results in

$$\frac{\partial \vec{\phi}}{\partial t}(t^n) \approx \frac{\vec{\phi}^{n+1} - \vec{\phi}^n}{\Delta t^n} = \vec{L}(\vec{\phi}^n) \quad (2.44)$$

Transformed to the unknown $\vec{\phi}^{n+1}$ of the new time step

$$\vec{\phi}^{n+1} = \vec{\phi}^n + \vec{L}(\vec{\phi}^n) \Delta t^n \quad (2.45)$$

results in a right-hand side which depends only on known quantities from the past time step. Consequently, the coupled system of N ordinary differential

equations is completely decoupled and each can be solved separately. The explicit Euler method is of first-order accuracy in time.

Implicit methods

For the discretization in the framework of the implicit methods, Eq. (2.42) is approximated by a first-order backward differencing scheme, resulting in Eq. (2.46) for the time step t^{n+1} .

$$\frac{\partial \vec{\phi}}{\partial t}(t^{n+1}) \approx \frac{\vec{\phi}^{n+1} - \vec{\phi}^n}{\Delta t^n} = \vec{L}(\vec{\phi}^{n+1}) \quad (2.46)$$

In contrast to the explicit Euler method (Eq. (2.44)), the right-hand side now depends on the new time step t^{n+1} resulting in a coupled system of equations. The solution of the coupled system of equations requires a higher computational and memory effort compared to the explicit Euler method, but the size of the chosen time step is not bounded, which mostly compensates the former. The accuracy is equal to the explicit Euler method and is of first-order.

To increase the accuracy of the time discretization, arbitrary numbers of previous time steps can be considered in the approximation. A compromise between accuracy and stability is the second-order backward differencing scheme, in which the current time step and the two preceding ones are taken into account. The approximation of Eq. (2.42) thus results in:

$$\frac{\partial \vec{\phi}}{\partial t}(t^{n+1}) \approx \frac{3\vec{\phi}^{n+1} - 4\vec{\phi}^n + \vec{\phi}^{n-1}}{2\Delta t^n} = \vec{L}(\vec{\phi}^{n+1}) \quad (2.47)$$

2.3.3. Under-relaxation

To allow convergence of stationary but also transient cases, a well-known possibility is the under-relaxation method proposed by Baliga and Patankar (1980), where the change of a field quantity is reduced within an iteration/time step. As an example, the under-relaxation applied to Eq. (2.39) results in

$$\phi_P^{k+1} = \alpha_\phi \frac{\sum_C \alpha_C \phi_C^{k+1} + b_P}{a_P} + (1 - \alpha_\phi) \phi_P^k \quad (2.48)$$

with k describing the iteration step and α_ϕ the under-relaxation factor of ϕ . The under-relaxation factor can take values between > 0 and 1, whereby the smaller α_ϕ , the stronger the change of ϕ between the iterations is reduced. For stationary problems the usage of under-relaxation is unproblematic, for transient scale-resolving problems a decoupling of the equation system and consequently an unwanted influence on the result can occur. In the latter case, the choice of the under-relaxation has to be chosen carefully.

3. IC-engine-relevant cooling channel configuration: Water Spider Geometry (WSG)

A newly designed generic Internal Combustion (IC)-engine-relevant cooling channel configuration, denoted as Water Spider Geometry (WSG), is investigated within a Bundesministerium für Wirtschaft und Energie (BMWi) project in a complementary numerical and experimental cooperation (see Klink and Wegt, 2021) and the numerical determination of the isothermal flow topology within the WSG is subject of the present chapter. A requirement for detailed knowledge of the isothermal flow condition within the WSG has arisen from the experimental side in order to assess the various flow phenomena caused, among other things, by the thermal conditions and leading to regions of pronounced surface degradation. In practice, pronounced surface degradation has occurred around the inlet of the second deflection and the inner radius of the reverse T-junction for thermally critical conditions (high inlet temperature in conjunction with low volume flux). An isothermal flow analysis provides a reliable statement of the fundamental flow topology by using a highly accurate numerical environment with respect to the turbulence modeling approach (Large-Eddy Simulation (LES) framework) and applied numerical grid. A direct consideration of the expected flow phenomena (boiling, cavitation, particle erosion, surface degradation) is not advisable due to the unknown flow topology within the WSG configuration, because a superimposed consideration of the listed flow phenomena complicates a targeted assessment of the individual one.

The WSG combines several standard geometrical components with flow division (T-junction), flow deflections (90°-pipe bend) and flow confluence (reverse T-junction) as denoted in Fig. 3.1 left. The spatial distance between the isolated geometrical components is less than five pipe diameters (see Fig. 3.1

right), suggesting superimposed flow effects of the geometrical components according to Baehr and Stephan (2006), which assumes a fully developed pipe flow after 60 pipe diameters. Due to the mutual influence, a targeted flow discussion of the WSG is complicated without detailed knowledge of the flow topology within the isolated geometrical components. Consequently, the WSG flow discussion is preceded by a segment-by-segment discussion of the isolated geometrical components (90°-pipe bend, T-junction and reverse T-junction), focusing on potentially critical regions with regard to abrasive flow conditions, thermal stress as well as possible thermal and/or cavitative driven phase changes.

Within the present chapter, the experimental conditions regarding the geometrical dimensions of the WSG, the coolant and the flow conditions are firstly presented (Chapter 3.1). Then, the numerical framework is briefly described (Chapter 3.2), followed by a detailed grid study regarding the most efficient meshing of pipe sections and the choice of SGS model within the LES framework (Chapter 3.3). The feasibility check of the pipe configurations relevant for the present work with common quality criterion for LES is performed in Chapter 3.4, followed by the segment-by-segment flow discussion of the 90°-pipe bend (Chapter 3.5), the T-junction (Chapter 3.6) and the reverse T-junction (Chapter 3.7). Finally, the analysis of the entire WSG follows focusing on the cause of experimentally identified locations of pronounced surface degradation (Chapter 3.8).

Note that the contents of Chapter 3.3, 3.4 and 3.5 are published in Wegt et al. (2002).

3.1. Experimental conditions

3.1.1. Geometric dimensions of the WSG

The WSG represents a triple symmetrical flow guidance with a circular cross-section of diameter $D = 3.5$ mm milled on a circular aluminium (AlSi6Cu4) sample disc with diameter $l_{\text{WSG}} = 62$ mm. The WSG does not have any sharp edges, which is designed to mimic real cooling ducts in view of the casting manufacturing process of IC engine blocks. In particular, the transition region between the pipe segments within the T-junction and reverse T-junction is designed with an inner radius of $R_{\text{inner}} = 0.5$ mm, along which the cross-section shape always remains circular with the constant diameter D . Both 90° deflections within the WSG have the similar curvature radius of $R_c = 1.58 D$, which is selected in accordance with the existing literature and has been investigated in a similar flow configuration by Röhrig et al. (2015), for example. The geometric dimensions of the WSG are illustrated in Fig. 3.1 right and summarized in Table 3.1.

The assurance of defined inlet conditions within the WSG is of primary importance due to the first complementary experimental and numerical investigations within the framework of the so called Modulare Heißtestanlage (MHTA) (see Klink et al., 2019). Without defined inlet conditions, a comparison between the experimental and numerical investigations is only conditionally permissible because of a basically different flow topology in the inlet section of the WSG. The defined inlet conditions are achieved by a continuous transition between the sample inlet/outlet and the sample holder as well as a well-defined pre-inlet section upstream of the sample holder with an appropriate length of $l_{\text{WSG,inlet}} = 340$ mm $> 60 D_{\text{outer}}$. The latter guarantees a fully developed pipe flow entering the geometry according to Baehr and Stephan (2006). The continuous transition around the sample holder corresponds to a construction-related variation of the pipe diameter upstream and downstream the WSG with an outer diameter of $D_{\text{outer}} = 4$ mm and a necking length of $l_{\text{WSG,necking}} = 0.5$ mm. Within the experimental setup, the WSG is composed of two half-samples, which are fixed and pressed together by the sample holder during the experiment. The gap between the half-samples has been given special attention in the design of the test rig in order to avoid unwanted gap flow. Due to an increased design effort, the gap could be reduced to a minimum and thus gap flow could be avoided. Subsequently, no necessity exists to observe

3. IC-engine-relevant cooling channel configuration: Water Spider Geometry (WSG)

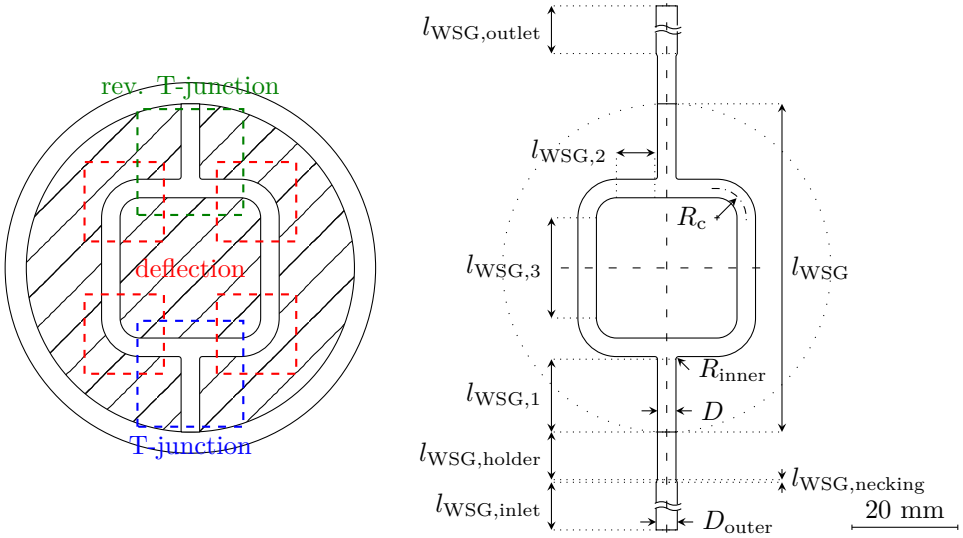


Figure 3.1.: Schematic illustrations of the WSG, left: sample half with the individual geometries color-coded, right: spatial dimensions of the WSG including inlet section and outlet section. The associated dimensions are listed in Table 3.1.

the WSG as half-samples with a gap within the numerical framework and the consideration of a full-sample flow guidance is sufficient. The pressure level within the WSG is experimentally controlled and the corresponding pressure sensor is located at a distance of $l_{\text{WSG,outlet}}$ downstream of the necking in the outlet section at which the outlet pressure p_{outlet} is present. The selected pressure level has to satisfy practical requirements without leading to any experimental disadvantages, such as the mentioned gap flow.

3.1.2. Working fluid: 50/50 vol.% MEG/(deionized) water

The working fluid applied within the experimental and numerical setup is related to coolants of water-cooled IC engines, which are usually composed of

D_{outer}	D	R_{inner}	R_c
4 mm	3.5 mm	0.5 mm	5.53 mm
l_{WSG}	$l_{\text{WSG,necking}}$	$l_{\text{WSG,inlet}}$	$l_{\text{WSG,holder}}$
62 mm	0.5mm	340 mm $>$ 60 D_{outer}	9 mm
$l_{\text{WSG,1}}$	$l_{\text{WSG,2}}$	$l_{\text{WSG,3}}$	$l_{\text{WSG,outlet}}$
13.75 mm	7.25 mm	18.94 mm	60.5 mm

Table 3.1.: Summary of the geometric dimensions of the WSG illustrated in Fig. 3.1 right.

70 to 50 vol.% water and 30 to 50 vol.% coolant additive. Coolant additives serve to specifically influence the properties of the coolant and common ones are antifreeze additives such as monoethylene glycol (MEG), potential hydrogenii (pH)-buffers and a number of corrosion inhibitors. Additives are not just used to influence the coolant advantageously, rather to compensate the disadvantages of individual coolant components. Although the fluid properties of water in terms of heat capacity and conductivity are beneficial with regard to the transport of heat within a cooling system, the associated freezing and boiling limits of water are critical for application in an IC engine. The aim in IC engines is to keep the cylinder wall temperatures below 200° C (see Basshuysen and Schäfer, 2015, Dörnenburg et al., 2010, and Stoffregen, 2009), which would increase the risk of boiling and could cause a critical boiling state within the cooling system if pure water is applied. The coolant additive MEG has significantly more favorable freezing and boiling limits with respect to IC engines, which in mixture with water leads to a significant increase of the boiling point (up to 135° C) and decrease of the freezing point (see Duchardt et al., 2015). Besides the unfavorable boiling and freezing limits of water, the dissolved oxygen in water is also critical with regard to the corrosion protection of the coolant. The dissolved oxygen interacts with most metallic surfaces and can cause a corrosive effect. The latter causes a local deterioration of the heat transfer and can lead to surface abrasive effects onto the flow guidance of the cooling system. The application of inhibitors within the coolant suppresses the reaction of the dissolved oxygen with the metallic materials and thus increases the corrosion protection (Schmitt and Fässler, 1990).

3. IC-engine-relevant cooling channel configuration: Water Spider Geometry (WSG)

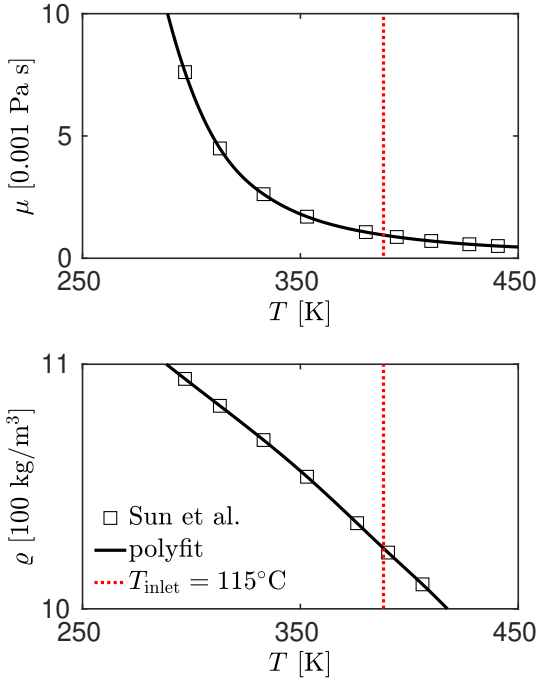


Figure 3.2.: Thermal response of the dynamic viscosity μ (top) and density ρ (bottom) of MEG/water 50/50 vol.% (squares) according to Sun and Teja (2003). For the interpolation of the experimental data, a polyfit (black solid line) is applied to capture the relevant fluid properties at the reference point $T_{\text{inlet}} = 115^\circ\text{C}$ (red dotted line).

The coolant is required to resist various external influences during its life cycle without losing its functionality. High thermal stresses as well as the contact of MEG with the environment can cause the coolant additive MEG to decompose into different carboxylic acids (Claeys and Lievens, 2006) and influence its pH-value. The alteration of the pH-value leads to a deterioration of the corrosion protection, which is prevented by the addition of pH-buffers, for example. pH-buffers ensure long-term preservation of the initial pH-value

and thus guarantee the specified corrosion protection. Due to the large number of different and highly polydisperse coolants with different fluid properties, a simplified coolant composed of a MEG/water mixture with a mixing ratio of 50/50 vol. % is employed as working fluid in the experiment characterized over a wide temperature range by Sun and Teja (2003). The study is remarkable for its fluid properties data above 100 °C, which is crucial for the thermal conditions present in the experiments. The relevant fluid properties for the isothermal consideration are depicted in Fig. 3.2 with the dynamic viscosity μ (top) and density ρ (bottom) for MEG/water 50/50 vol. %.

3.1.3. Flow conditions

The selected flow conditions are defined in close cooperation with a committee of industry representatives and are based on practice-relevant flow conditions within cooling systems of water-cooled IC engines including the inlet volume flux \dot{V} , the inlet temperature T_{inlet} , the outlet pressure p_{outlet} and the heat flux \dot{Q} . The selected volume flux \dot{V} is chosen in accordance with the minimum and maximum velocities within IC cooling systems. An unofficial survey of industry representatives revealed a maximum velocity of up to 4 m/s within common IC cooling systems. In order to capture different engine conditions, a variation of the volume flux is required, resulting in the selected volume fluxes of $\dot{V} = 2.2$ l/min, 3.2 l/min and 4.3 l/min. The volume flux at which the experimentally detected locations of pronounced surface degradation occurred and thus is of primary relevance to the present work, is $\dot{V} = 2.2$ l/min. The coolants of IC engines are operated according to Braess and Seiffert (2011) at an average temperature of 90 and 110 °C with a pressure of 1.5 bar, whereas an unofficial survey of industry representatives indicates an average coolant temperature of up to 125 °C in conjunction with a system pressure of up to 5 bar. In order to cover the entire thermal range, the inlet temperatures to be investigated are selected as $T_{\text{inlet}} = 95$ °C, 105 °C and 115 °C, whereby only the latter is relevant for the present work due to the mentioned topic of surface degradation. The fluid properties of the considered MEG/water mixture matching the inlet temperature of $T_{\text{inlet}} = 115$ °C are highlighted by a red dotted line in Fig. 3.2. For the pressure condition, a compromise is made between the experimental feasibility with regard to unwanted gap flows between the half-samples and the practice-oriented conditions. An outlet

3. IC-engine-relevant cooling channel configuration: Water Spider Geometry (WSG)

pressure of $p_{\text{outlet}} = 1.5$ bar has satisfied both, within the range of realistic pressure conditions while avoiding gap flows. The heat flux is of secondary importance for the isothermal consideration in the present work and is only listed for completeness. It is experimentally applied one-sided via a block heater with a total power of $\dot{Q} = 3200$ W.

The resulting bulk Reynolds numbers at the inlet of the WSG $\text{Re}_b = U_b D / \nu$, in the outer section $\text{Re}_{\text{outer}} = U_{b,\text{outer}} D_{\text{outer}} / \nu$ and in the deflections $\text{Re}_{\text{deflection}} = 0.5 U_b D / \nu$, taking into account the fluid properties of MEG/water 50/50vol. % at $T_{\text{inlet}} = 115$ °C, are summarized in Table 3.2. The bulk velocity is derived from the corresponding volume flux and pipe diameter with $U_b = \dot{V} / (0.25\pi D^2)$ and $U_{b,\text{outer}} = \dot{V} / (0.25\pi D_{\text{outer}}^2)$. From the listed Reynolds numbers in Table 3.2, a fully turbulent character of the flow topology within the considered flow guides can be assumed, which requires the appropriate modeling of the turbulence.

\dot{V}	2.2 l/min	3.2 l/min	4.3 l/min
Re	14400	21000	28000
Re_{outer}	12600	18300	24600
$\text{Re}_{\text{deflection}}$	7200	10500	14000

Table 3.2.: Complete listing of present pipe Reynolds numbers within the WSG for $T_{\text{inlet}} = 115$ °C considering the selected volume fluxes \dot{V} . $\text{Re}_b = U_b D / \nu$ denotes the Reynolds number at the WSG inlet, $\text{Re}_{\text{outer}} = U_{b,\text{outer}} D_{\text{outer}} / \nu$ in the outer section and $\text{Re}_{\text{deflection}} = 0.5 U_b D / \nu$ in the deflections.

3.2. Computational framework

To avoid a multiple repetition of the numerical framework within the present chapter, the numerical framework is explained in detailed here representative for all following Large Eddy Simulations (LES). The equations governing the flow motion within the LES computational framework are implemented in the finite-volume based open-source toolbox OpenFOAM® version 19.12, with which all simulations have been performed. With respect to the discretization procedure introduced in Chapter 2.3, the temporal (second-order backward differencing scheme, see Eq. (2.47)) and the spatial discretization (Central Difference Scheme (CDS), see Eq. (2.34)) applied to the governing equations within the LES framework are of second-order accuracy. The adopted temporal resolution ensures the Courant number Co being smaller than $Co < 1$ in the entire solution domain. The meshes required for the numerical simulations are generated with OpenFOAM's meshing tool 'blockMesh' and have a fully hexahedral block-structured cell arrangement. The low Reynolds character of the LES framework is satisfied by a dimensionless wall distance of the cell closest to the wall smaller than $y^+ < 1$, allowing the consideration of the entire viscous sublayer.

3.3. Preliminary LES investigations

The mesh generation of pipe cross-sections is usually realized by utilizing the so-called O -grid arrangement as illustrated in Fig. 3.3. The circular cross-section is discretized by a mesh consisting of five blocks, one of which is centrally located in the middle of the pipe, whereas the other four encircle it, thus enabling the circular shape to be achieved. Although the O -grid is a common meshing strategy applied in case of circular pipe configurations, the grids can significantly differ in the cell arrangement. Some important questions arise here: what shape and relative size the inner block should have in relation to the pipe radius - R_{block}/R , what cell-face ratio in the mean flow direction is most suitable - $\Delta z^+/\Delta \varphi^+$, and how long a corresponding precursor pipe (l_{pre}) should be so that turbulent structures can develop undisturbed. The general validity of the following considerations is ensured by adopting a Reynolds number range as large as possible. The considered bulk Reynolds numbers range from $\text{Re}_b = U_b D/\nu = 5300$ to 39000 , respectively, the friction Reynolds numbers from $\text{Re}_\tau = u_\tau R/\nu = 180$ to 1000 . This is selected in line with available DNS studies of fully developed pipe flows performed by Fukagata and Kasagi (2002) ($\text{Re}_\tau = 180$), El Khoury et al. (2013) ($\text{Re}_\tau = 360, 550$ and 1000) and Wu and Moin (2008) ($\text{Re}_\tau = 685$). The corresponding grid study is carried out by applying the WALE SGS model (with $C_w = 0.325$).

For the sake of computational resource affordability and keeping in mind an intensive simulation campaign to be performed, no grid resolutions corresponding strictly to the LES standards are used. Such a procedure is anyhow regarded to be more appropriate, because the resulting trends from the following grid study will be increasingly emphasized, enabling a clear conclusion. In the case of following closely the relevant quality criteria by performing a well-resolved LES, the results obtained by varying the above-listed grid parameters would not be sufficiently insightful. The credibility of this grid optimization study, also in conjunction with different SGS models, will be adequately checked in Chapter 3.3.4. The overall goal of this preliminary investigation is to determine the most suitable cell arrangement for a pipe flow, that is appropriate for the turbulent structures to be captured with as few cells as possible. The assessment is based on the predicted near-wall behavior in terms of the friction Reynolds number Re_τ , the time-averaged flow quantities but also the required computational time, if reasonably detectable.

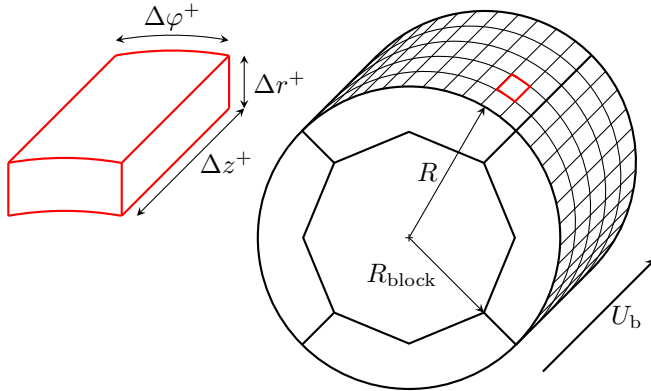


Figure 3.3.: Schematic of the grid structure of a pipe flow configuration according to the so-called O -grid arrangement with an octagon-shaped central block.

Various shapes of the inner block have been previously studied (not shown here). The previous study includes a square, an octagon, a hexagon and a rounded square, but did not lead to significant differences in the computational results. Under the condition that the distance between the wall-closest cells and the wall itself remains as constant as possible over the entire pipe perimeter and, at the same time, the corner cells of the inner block do not become too skew, the octagon shape is adopted as the best compromise.

3.3.1. Pipe grid optimization: Cross-section cell arrangement

The relative size of the inner block in relation to the pipe radius R_{block}/R determines the distribution of the cells in the pipe cross-section, i.e., the number of cells in the radial as well as in the circumferential direction. The larger the inner block is selected, the more cells have to be provided across the pipe cross-section in circumferential direction in order to ensure a uniform cell distribution. The relative influence of the inner block size on the flow as well as on the computational effort is investigated by computing the pipe flow at the afore-mentioned five Reynolds numbers. The ratio of the inner

3. IC-engine-relevant cooling channel configuration: Water Spider Geometry (WSG)

block size is varied in terms of the relevant radius to the pipe radius in the range of $R_{\text{block}}/R = 0.5 - 0.9$. The cell ratio in the mean flow direction ($\Delta z^+/\Delta\varphi^+ = 3$) and the length of the precursor pipe ($l_{\text{pre}} = 2.5 D$) are kept constant, as well as the number of cells in the entire pipe section for each considered Reynolds number, see Table 3.3.

Re_τ	180	360	550	685	1000
n_{total}	100 k	200 k	400 k	600 k	1000 k
n_{cores}	8	16	32	48	192

Table 3.3.: Total number of grid cells n_{total} ($\text{k} \equiv 10^3$) and computer cores n_{cores} used for computing the pipe flow at five considered friction Reynolds numbers Re_τ .

The influence of the inner block ratio R_{block}/R can be assessed by analyzing the computationally obtained friction Reynolds number (depending on the wall shear stress) relative to its reference DNS value $\text{Re}_\tau/\text{Re}_{\tau,\text{DNS}}$, as well as the corresponding calculation time normalized by the calculation time for the case $R_{\text{block}}/R = 0.5$. The corresponding outcomes are illustrated in Fig. 3.4. The calculated Reynolds number ratio $\text{Re}_\tau/\text{Re}_{\tau,\text{DNS}}$ (Fig. 3.4 top) reveals a tendency that is qualitatively independent of the considered Reynolds number. The ratio $\text{Re}_\tau/\text{Re}_{\tau,\text{DNS}}$ exhibits a linear increase with the inner block ratio R_{block}/R up to a value of 0.8. From this value onwards, the calculated friction Reynolds number ratio flattens out, apart of a certain drop for $\text{Re}_\tau = 180$. In addition, it can be seen that the influence of the inner block ratio increases with increasing Reynolds number. It is also noticeable that the outcome corresponding to $\text{Re}_\tau = 180$ comes closest to the reference DNS. This is in line with the grid resolution of 100000 cells, which can be considered as approximately appropriate for such a low Reynolds number. The influence of the comparably coarse grids applied onto the present study is clearly visible for increasing Reynolds numbers, where a somewhat enhanced departure from the DNS data is documented. The latter is, as expected, mostly emphasized at the highest Reynolds number $\text{Re}_\tau = 1000$.

A similar behavior can be observed with respect to the required calculation time (Fig. 3.4 bottom), which also exhibits a tendency qualitatively independent of the considered Reynolds number. With the exception of the outlier

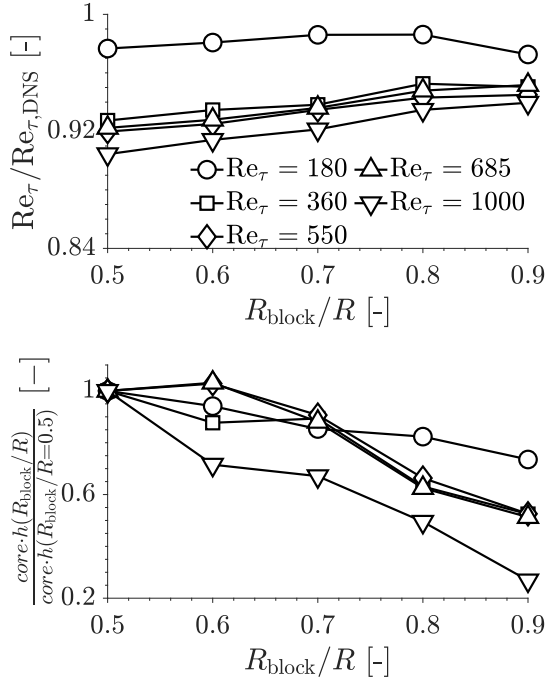


Figure 3.4.: Computationally obtained friction Reynolds number in relation to its reference DNS value $Re_\tau/Re_{\tau,DNS}$ (top) and calculation time used in relation to calculation time required for the radius ratio $R_{block}/R = 0.5$ (bottom) over the inner block size ratio R_{block}/R for the pipe flow over the considered Reynolds number range.

detected at $Re_\tau = 550$ and 685 for the inner block ratio of $R_{block}/R = 0.6$, an inversely proportional dependency between the calculation time and the inner block ratio can be observed. The higher the Reynolds number, the more pronounced is the decrease of the relative calculation time, with a maximum reduction of almost 80% at $Re_\tau = 1000$.

The influence of the inner block size ratio can further be illustrated by directly analyzing the flow fields obtained. Fig. 3.5 displays, exemplary at

3. IC-engine-relevant cooling channel configuration: Water Spider Geometry (WSG)

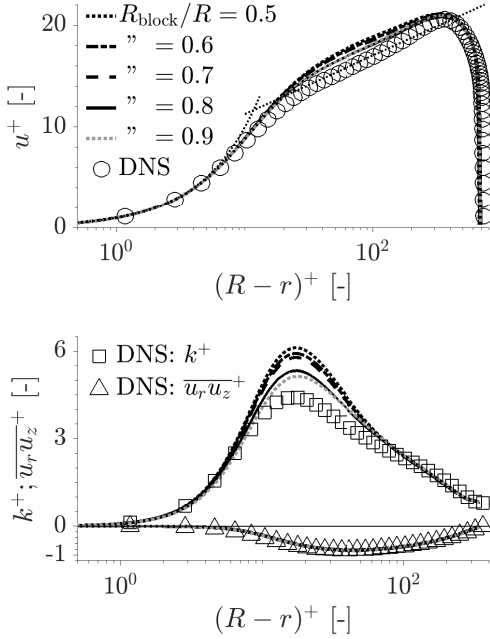


Figure 3.5.: Semi-log profiles of the non-dimensional streamwise velocity u^+ (top) as well as the non-dimensional turbulent kinetic energy k^+ and $\overline{u_r u_z}^+$ (bottom) over the non-dimensional wall distance $(R-r)^+$ for different inner block size ratios R_{block}/R for $\text{Re}_\tau = 360$ compared to the reference DNS data by El Khoury et al. (2013).

$\text{Re}_\tau = 360$, the semi-log plots of the streamwise velocity u^+ (Fig. 3.5 top), the turbulent kinetic energy k^+ and the shear stress component $\overline{u_r u_z}^+$ (Fig. 3.5 bottom). The velocity and turbulent kinetic energy profiles demonstrate an improved behavior with increasing the inner block size ratio in comparison with the reference DNS data by El Khoury et al. (2013). A profile match is observed after the radius ratio of $R_{\text{block}}/R = 0.8$ has been reached, whereas the $\overline{u_r u_z}^+$ -profiles are entirely unaffected by the inner block size ratio. However, the

profiles match can be directly related to that of the calculated friction Reynolds numbers (see Fig. 3.4 top), since both the velocity and turbulent quantities are normalized by the friction velocity u_τ . Consequently, the improvement of the results with increasing inner block size ratio is clearly evident.

A suitable choice of the inner block size ratio R_{block}/R can both improve the results and reduce calculation time. It can be generalized that a larger inner block size ratio is advantageous, which further implies that the number of grid cells in the circumferential direction is more important than in the radial direction for a pipe flow configuration. A ratio of $R_{\text{block}}/R = 0.8$ is found to be the best compromise for the relevant Reynolds numbers within the WSG ($\text{Re}_b < 14400$) with respect to the predicted near-wall characteristics in terms of friction Reynolds number. This ratio will be used in the following numerical computations.

3.3.2. Pipe grid optimization: Streamwise-to-spanwise grid-cell ratio

A suitable grid arrangement is required for successful detection of the turbulent elongated structures in a pipe flow, especially with respect to a corresponding extent of the cells in the streamwise flow direction. Therefore, the ratio of the cell extension in streamwise to circumferential direction of the wall-closest cell $\Delta z^+/\Delta\varphi^+$ is considered and its influence analyzed. The ratio $\Delta z^+/\Delta\varphi^+ = 1$ corresponds to a uniform cell distribution over the pipe surface and a ratio of $\Delta z^+/\Delta\varphi^+ = 5$ denotes the cell extension in streamwise direction by a factor of 5. This study is carried out with an inner block size ratio of $R_{\text{block}}/R = 0.8$ and a pipe section length of $l_{\text{pre}} = 2.5 D$ with the number of cells in the cross-sectional area remaining constant. Accordingly, the total number of cells in the pipe segment will vary depending on their extension ratio.

In Fig. 3.6, the calculated friction Reynolds number ratio $\text{Re}_\tau/\text{Re}_{\tau,\text{DNS}}$ is plotted against the streamwise-to-spanwise grid-cell ratio $\Delta z^+/\Delta\varphi^+$ for different pipe Reynolds numbers. A Reynolds number independent tendency can be observed with a maximum for $\Delta z^+/\Delta\varphi^+ = 3$ and decreasing for smaller and larger streamwise-to-spanwise grid-cell ratios. As expected, the insufficient grid resolution is reflected in a more pronounced deviation from the reference DNS values increasing with the Reynolds number which is in line with the discussion related to Fig. 3.4 top. An analysis of the required calculation

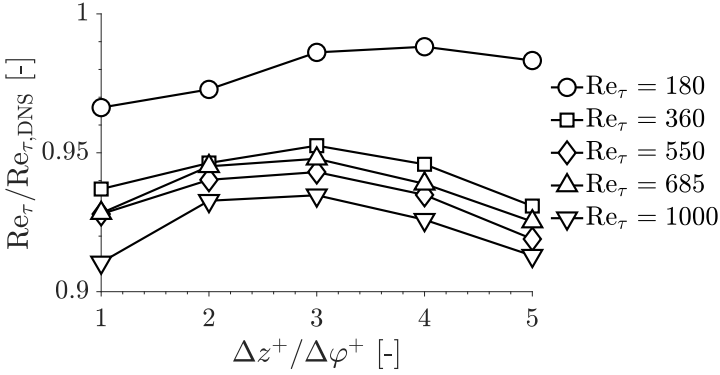


Figure 3.6.: Computationally obtained friction Reynolds number in relation to its reference DNS value $Re_\tau/Re_{\tau,DNS}$ over the streamwise-to-spanwise grid-cell ratio $\Delta z^+/\Delta \varphi^+$ for the pipe flow over the considered Reynolds number range.

time is difficult to perform here, since the influence of parallelization and the number of cells per core is too dominant due to the varying number of cells for each streamwise-to-spanwise grid-cell ratio.

In contrast to the calculated friction Reynolds number, a possibly small streamwise-to-spanwise grid-cell ratio is advantageous in view of capturing the radial distributions of the flow velocity and the turbulence kinetic energy. A direct comparison to the reference DNS data is illustrated in Fig. 3.7 for $Re_\tau = 360$, revealing the closest agreement for the grid-cell ratio greater than $\Delta z^+/\Delta \varphi^+ > 2$. Since the influence of the streamwise-to-spanwise grid-cell ratio on the required calculation time can not be determined accurately and the results depend strongly on the total cell number within the flow domain, a grid-cell ratio of $\Delta z^+/\Delta \varphi^+ = 3$ is adopted for future calculations as a best compromise. This is also chosen with respect to the fact that the results will be appropriately improved when the number of cells is increased (see Chapter 3.3.4).

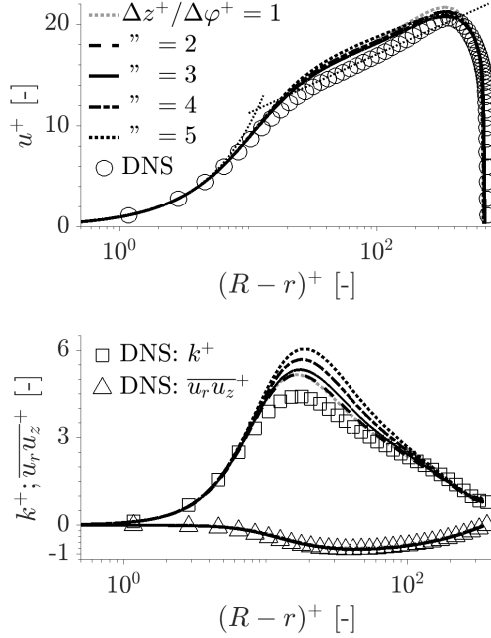


Figure 3.7.: Semi-log profile of the non-dimensional streamwise velocity u^+ (top) as well as non-dimensional turbulent kinetic energy k^+ and $\overline{u_r u_z^+}$ (bottom) over the non-dimensional wall distance $(R-r)^+$ for different streamwise-to-spanwise grid-cell ratios $\Delta z^+/\Delta \varphi^+$ for $\text{Re}_\tau = 360$ compared to the reference DNS data by El Khoury et al. (2013).

3.3.3. Pipe grid optimization: Pipe section length

The necessary length of the solution domain within a pressure-driven precursor pipe flow (l_{pre} ; compare for example Fig. 3.49) aiming at obtaining a fluctuating, fully developed flow field, which is not influenced by the inflow and outflow, is the subject of the present subsection. If the domain length is chosen too short, a spatial periodicity of the flow structures can be indeed achieved, but with

very probable deviation from the inherent physics of a turbulent flow. For a fixed inner block ratio of $R_{\text{block}}/R = 0.8$ and the streamwise-to-spanwise grid-cell ratio of $\Delta z^+/\Delta \varphi^+ = 3$, the pipe section length is varied in the range of $l_{\text{pre}}/D = 1$ to 5, implying also that the grid cell distribution within the cross-section as well as the number of cells per diameter in the mean flow direction are kept constant for each considered Reynolds number.

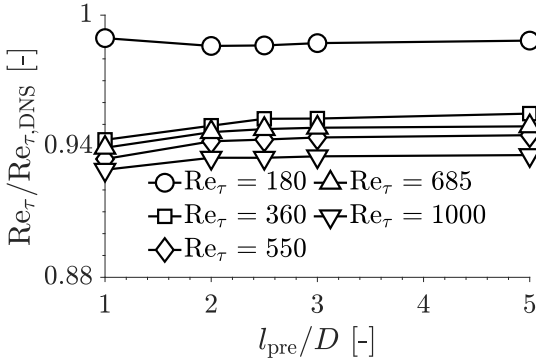


Figure 3.8.: Computationally obtained friction Reynolds number in relation to its reference DNS value $\text{Re}_\tau/\text{Re}_{\tau,\text{DNS}}$ for different non-dimensional pipe section lengths l_{pre}/D for the pipe flow over the considered Reynolds number range.

The influence of the pipe section length l_{pre} on the friction Reynolds number ratio $\text{Re}_\tau/\text{Re}_{\tau,\text{DNS}}$ as well as on the radial distribution of the flow velocity u^+ , the turbulent kinetic energy k^+ and the Reynolds shear stress component $\overline{u_r u_z^+}$, is depicted in Figures 3.8 and 3.9, respectively. As an outcome, an almost constant Reynolds number ratio $\text{Re}_\tau/\text{Re}_{\tau,\text{DNS}}$ can be observed over the entire pipe length variation, independent of the bulk Reynolds number. A very slight deviation from this trend can only be seen for a pipe section length of $l_{\text{pre}} = 2 D$ and shorter. A similar behavior can also be observed at the profiles of the flow velocity and the turbulent quantities illustrated in Fig. 3.9 for $\text{Re}_\tau = 360$. The deviations are visible only with respect to the peak of the turbulent kinetic energy, which is correspondingly overestimated compared to the DNS reference for a pipe section length of $l_{\text{pre}} = 1 D$. The

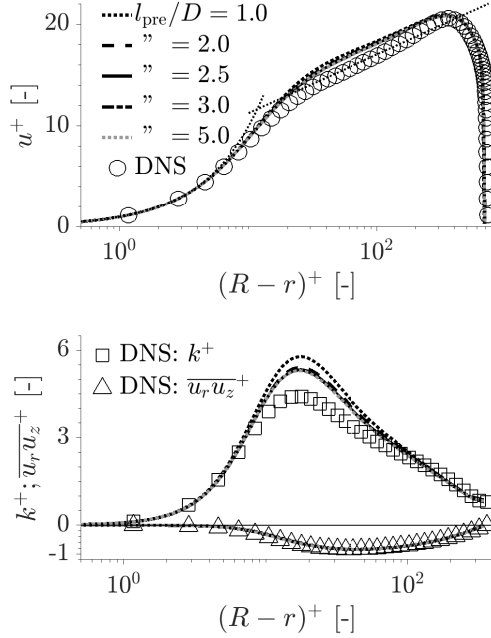


Figure 3.9.: Semi-log profile of the non-dimensional streamwise velocity u^+ (top) as well as non-dimensional turbulent kinetic energy k^+ and $\overline{u_r u_z}^+$ (bottom) over the non-dimensional wall distance $(R-r)^+$ for different non-dimensional pipe section lengths l_{pre}/D for $\text{Re}_\tau = 360$ compared to the reference DNS data by El Khoury et al. (2013).

velocity distribution reveals an almost non-noticeable deviation over the entire pipe section length range.

In summary, a pipe section length of $l_{\text{pre}} = 2.5 D$ in this pressure-driven precursor simulation can be regarded as sufficient to generate a fully developed pipe flow with turbulent fluctuations unaffected by the inlet/outlet periodicity. The fluctuating turbulence content, from the physical point of view, will be adequately highlighted in the following subsection.

3.3.4. Feasibility check & subgrid-scale model

In order to elaborate the influences of the coarser grids from the previous study in comparison with a proper LES grid, the pipe flow at $Re_\tau = 360$ is simulated here repeatedly, but adopted a grid resolution satisfying the LES-quality constraints. The obtained results are compared with the corresponding unresolved LES from the previous subsections, as well as with the reference DNS by El Khoury et al. (2013). The corresponding grid parameters are listed in Table 3.4. In addition, the choice of the WALE model constant C_w is analyzed by comparing the results obtained with $C_w = 0.325$, proposed within the OpenFOAM[®] Code, and $C_w = 0.5$ proposed originally by Nicoud and Ducros (1999). Furthermore, the predictive performance of the two widely-used SGS models, named Smagorinsky model and its dynamic counterpart, are comparatively assessed. Whereas the interpretation of the results concentrated exclusively on the time-averaged flow quantities in the previous subsections, it is here extended towards the SGS turbulence properties and unsteady flow features (including for instance turbulence spectra presentation) in accordance with the LES quality criteria measures.

Re_τ	n_{total}	n_{cs}	$\Delta r_{\text{min...max}}^+$	$\Delta\varphi^+$	Δz^+
360	200 k	5.2 k	0.5, ..., 15.0	14.7	44.5
360	3210 k	31.5 k	0.3, ..., 5.9	5.8	17.5

Table 3.4.: Grid characteristics for simulating the pipe flow at friction Reynolds number $Re_\tau = 360$ with respect to the cell numbers ($k \equiv 10^3$) - in total and within the cross-section, n_{total} and n_{cs} , respectively - and the dimensionless grid spacings in radial $\Delta r_{\text{min...max}}^+$, circumferential $\Delta\varphi^+$ and flow direction Δz^+ .

The radial profiles of the streamwise velocity u^+ , normalized by the friction velocity u_τ , obtained by different SGS models are presented in Fig. 3.10 exhibiting very good agreement with the DNS data. Only the WALE model used in conjunction with the coarse grid overestimates the velocity (dotted blue line), specifically for the buffer and logarithmic regions, caused by an underestimation of the wall shear stress represented by u_τ and consequently of the corresponding friction Reynolds number Re_τ . The latter result represents a common outcome in LES simulations when using coarse grids. Apart from

this slight overshoot, this result can also be regarded as reasonable in view of a significantly coarser grid.

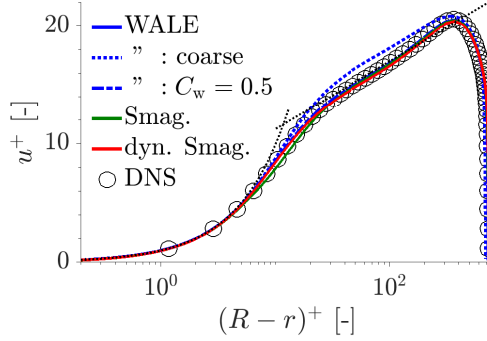


Figure 3.10.: Semi-log profiles of the non-dimensional streamwise velocity u^+ over the non-dimensional wall distance $(R-r)^+$ for $Re_\tau = 360$ predicted by different SGS models - **WALE**, **Smagorinsky** and **dynamic Smagorinsky** models - compared with reference DNS data by El Khoury et al. (2013). In the case of the WALE model, the solid line and the dash-dotted line represent the results obtained at the fine grid by using the constant values $C_w = 0.325$ and $C_w = 0.5$, respectively; the dotted line relates to the coarse-grid LES performed with $C_w = 0.325$.

Contrary to this, the differences in the predictive capabilities of different SGS models applied are much more emphasized when analyzing the Reynolds stress tensor components $\overline{u_i u_j}^+$ displayed in Fig. 3.11. This is especially visible at the behavior of the streamwise stress component $\overline{u_z u_z}^+$. Here, only the dynamic Smagorinsky model and the WALE model, utilizing both C_w -constant values and in conjunction with the fine grid result in an outcome comparing well with the DNS data. The maximum value related to the WALE constant of $C_w = 0.5$ is somewhat closer to the reference DNS peak value. The streamwise stress profile predicted by the Smagorinsky model is characterized by a maximum position being shifted further away from the wall. This is strictly in relation with the two remaining normal stress components depicted

3. IC-engine-relevant cooling channel configuration: Water Spider Geometry (WSG)

in Fig. 3.11 bottom. The corresponding profiles exhibit a similarly stretched shape featured by a certain underestimation of their maximum values. As it is typical for an under-resolved LES, the WALE model applied in conjunction with a coarser grid resolution results in a significant overprediction of the $\overline{u_z u_z}^+$ peak value as well as in a corresponding underprediction of both radial ($\overline{u_r u_r}^+$) and circumferential ($\overline{u_\varphi u_\varphi}^+$) stress components.

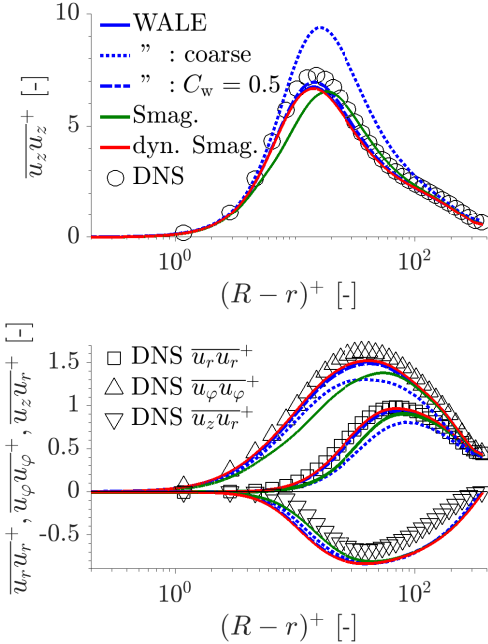


Figure 3.11.: Semi-log profiles of the non-dimensional Reynolds stress components $\overline{u_i u_j}^+$ over non-dimensional wall distance $(R-r)^+$ for $Re_\tau = 360$ predicted by different SGS models - **WALE**, **Smagorinsky** and **dynamic Smagorinsky** models - compared with reference DNS data by El Khoury et al. (2013). See caption of Fig. 3.10 for further information.

The turbulence level depicted in Fig. 3.11 is in close correlation with the

total viscous dissipation rate ε^+ illustrated in Fig. 3.12. Both, the dynamic Smagorinsky and WALE (with $C_w = 0.325$) models applied on the fine grid quantitatively predict the dissipation profile characterized by the maximum value at the wall itself, its negative near-wall gradient and a specific wavy shape at the position around $(R - r)^+ \approx 10$ in close accordance with the DNS data. The Smagorinsky model seriously overestimates the dissipation rate and predicts a global maximum around $(R - r)^+ \approx 8$. This behavior has a suppressing effect on the corresponding turbulence level, which is reflected in the underestimation of the associated Reynolds stresses, Fig. 3.11. Probably the cause of the depicted Smagorinsky results can be attributed to the choice of the Smagorinsky constant C_s . The WALE model in conjunction with the coarse grid slightly underestimates the dissipation rate within the same region, following closely the streamwise stress overestimation. Despite this deviation, a reasonable prediction of the dissipation on the clearly coarser grid is remarkable, which is particularly related to the near-wall region. Somewhat surprising is the profile development characterizing the WALE model application by utilizing the model constant $C_w = 0.5$, which, apart of the wall vicinity, clearly overestimates the dissipation level in the remainder of the cross-section up to the pipe center. In the corresponding region, the SGS fraction of the dissipation rate calculated by the WALE model in combination with the higher constant has a magnitude overweighting the resolved fraction (compare with Fig. 3.13 bottom), which possibly explains the proposed reduction of the WALE model constant by the OpenFOAM[®] developers.

A widely used criterion to characterize the quality of a LES outcome is the consideration of the ratio of the SGS fraction of turbulent kinetic energy to its total intensity k_{SGS}/k , which according to Pope (2000) should not exceed 20% for a well-resolved LES. The relevant ratio is depicted in Fig. 3.13 top. The corresponding ratio related to the WALE models, regardless of which version is considered, is well below the mentioned limit of $k_{\text{SGS}}/k = 0.2$ over the entire pipe radius. A local increase can be observed for the standard and dynamic Smagorinsky-type model version. The result related to the standard Smagorinsky model exceeds the limit in the region of significant turbulence production, which suggests an inappropriate grid resolution with respect to the above-defined criterion. On the other hand, the outcome of the dynamic Smagorinsky model clearly exceeds the 20 %-limit in the region of the immediate wall vicinity. The reason can be presumably found in the

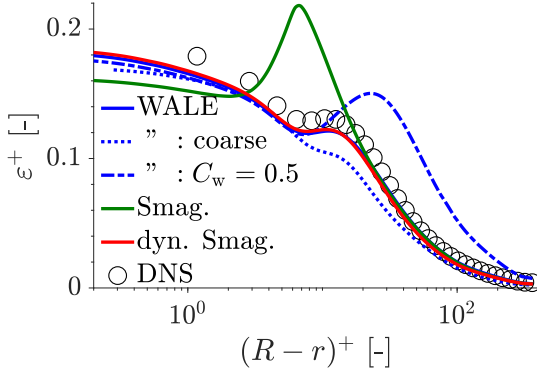


Figure 3.12.: Semi-log profiles of the non-dimensional dissipation rate ε^+ over non-dimensional wall distance $(R - r)^+$ for $Re_\tau = 360$ predicted by different SGS models - **WALE**, **Smagorinsky** and **dynamic Smagorinsky** models - compared with reference DNS data by El Khoury et al. (2013). See caption of Fig. 3.10 for further information.

dynamic procedure of the Smagorinsky constant determination and represents a characteristic of the model implementation, which has also been observed by Krumbein (2019). Looking at the behavior of the WALE model applied on a coarse grid, it seems that the criterion does not universally apply, keeping in mind the grid resolution which is far below an LES-compliant one. Accordingly, it seems reasonable, especially in the context of the WALE modeling concept, to use additionally some further criteria to assess the quality of the simulation.

One possibility, analogous to the previous criterion, is to use the dissipation rate of the SGS fraction to its total amount $\varepsilon_{SGS}/\varepsilon$, as illustrated in Fig. 3.13 bottom. The relative behavior of the dissipation ratio related to individual SGS models corresponds qualitatively to the turbulence kinetic energy ratio. The only exception is that a steep increase in the turbulence kinetic energy ratio towards the wall characterizing the dynamic Smagorinsky model is not correspondingly followed by the dissipation ratio. Admittedly, it is uncertain what should be the quantitative physical limit for the ratio $\varepsilon_{SGS}/\varepsilon$, but the profiles related to the dynamics Smagorinsky and WALE (with $C_w = 0.325$) models (exhibiting both the most consistent behavior in the previous analysis),

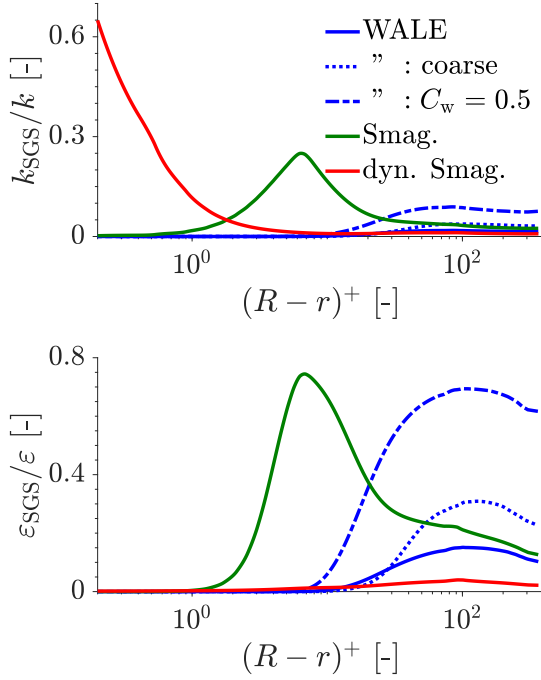


Figure 3.13.: Modeled-to-total turbulence kinetic energy ratio k_{SGS}/k (top) and modeled-to-total dissipation rate ratio $\varepsilon_{SGS}/\varepsilon$ (bottom) over non-dimensional wall distance $(R-r)^+$ for $\text{Re}_\tau = 360$ characterizing the results obtained by different SGS models (WALE, Smagorinsky and dynamic Smagorinsky).

indicate fairly small values, clearly under 0.2.

A further criterion for the mesh resolution suitability, also postulated by Pope (2000), considers the ratio of a representative grid width Δ to the smallest (dissipative) vortex structures represented by the Kolmogorov length scales $\eta = (\nu^3/\varepsilon)^{1/4}$. The relevant ratio should be at least in the range of $\Delta/\eta \approx 10$ to 12 or lower. The latter estimation relates actually to the homogeneous isotropic turbulence, which approximately corresponds to the flow situation encountered

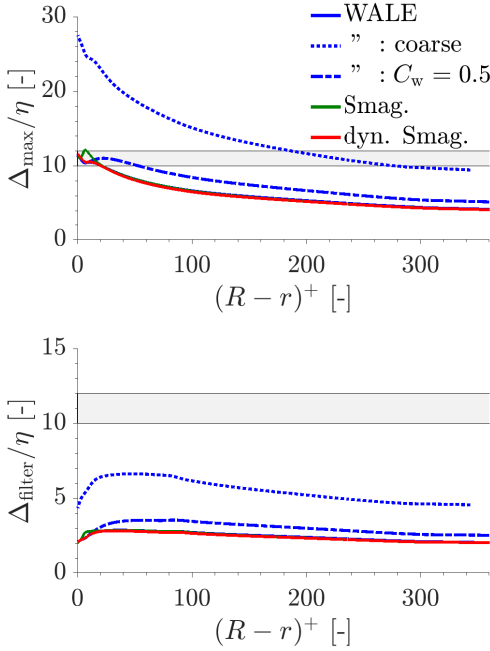


Figure 3.14.: Profiles of the ratio $\Delta_{\text{filter}}/\eta$ (top) and Δ_{\max}/η (bottom) over the non-dimensional wall distance $(R-r)^+$ for $\text{Re}_\tau = 360$ characterizing the results obtained by different SGS models (WALE, Smagorinsky and dynamic Smagorinsky). See caption of Fig. 3.10 for further information.

around the pipe center. Both the volume grid cell width Δ_{filter} ($\equiv \Delta = V_{\text{cell}}^{1/3}$) and the largest cell face dimension Δ_{\max} can be adopted as a characteristic grid spacing, with the latter representing a somewhat more rigorous criterion. The corresponding Δ/η profiles are presented in Fig. 3.14. A comparison between the results obtained by different SGS models and with respect to both criteria reveals similar qualitative behavior, with the substantially higher values pertinent to the Δ_{\max}/η ratio. In the case of adopting the volume

grid cell width as the representative grid width (Fig. 3.14 bottom), all results comply with above-postulated limit, whereas the criterion utilizing the largest cell face length Δ_{\max} as a characteristic grid width indicates clearly the coarser grid resolution ($n_{\text{total}} = 200000$) not conforming with the well-resolved LES constraints. The latter definition offers as a more rigorous criterion and will be exclusively used in the following consideration.

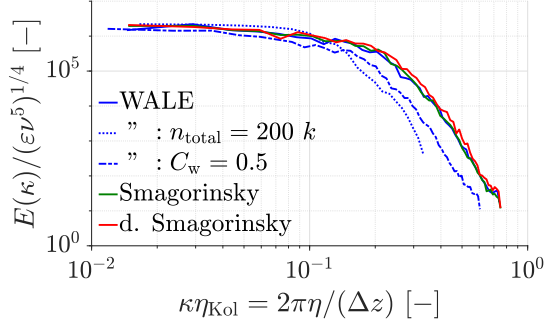


Figure 3.15.: Normalized energy spectrum of the streamwise velocity component $E(\kappa_{\text{eddy}})/(\varepsilon\nu^5)^{1/4}$ over normalized wavenumber $\kappa_{\text{eddy}}\eta$ for $\text{Re}_\tau = 360$ characterizing the results obtained by different SGS models (WALE, Smagorinsky and dynamic Smagorinsky). See caption of Fig. 3.10 for further information.

Fig. 3.15 depicts the energy spectrum pertinent to the u_z velocity component at the location coinciding with the pipe center over two decades of the dimensionless wavenumber $\kappa_{\text{eddy}}\eta$. The energy spectrum for each SGS model has been evaluated for several time steps (up to 20 and more) and subsequently averaged. The spectra related to the dynamic Smagorinsky, WALE (fine grid, $C_w = 0.325$) and standard Smagorinsky models show a close mutual agreement, whereas the WALE model utilizing the coarser grid results in a corresponding shortening of the spectrum range. The latter outcome is, as expected, strictly in line with the improper modeling of unresolved scales complying with a substantially coarser grid. The offset between the spectra related to different WALE models is also due to the normalization, especially with respect to the calculated dissipation rate in the pipe center (and subsequently the Kolmogorov length), which is for instance overestimated by the fine-grid LES

employing the WALE model with $C_w = 0.5$ (see Fig. 3.12).

In view of a significant inconsistency of the results related to the standard Smagorinsky model employment (Figures 3.11 to 3.13) and of a strong near-wall increase of the modeled turbulent kinetic energy obtained by using the dynamic Smagorinsky model (Fig. 3.13 top), the WALE model has been proved to be the best compromise to be applied for the following highly-resolved LES study. Furthermore, the originally proposed WALE constant of $C_w = 0.5$ has been shown to result in an overestimated dissipation rate in the entire off-wall domain. The value adopted within the OpenFOAM[®]-framework ($C_w = 0.325$) demonstrated a more consistent behavior compared to the reference data and is recommended.

3.3.5. Conclusions

Preliminary computational investigations of pipe flow configurations with focus on grid arrangement and appropriate SGS models in the LES framework are carried out aiming at achieving optimal reproduction of the flow dynamics. The grid study resulted in a most resource-effective cell arrangement in the context of the 'O-grid' arrangement following the necessary requirements for correct capturing of the fluctuating flow structures. Accordingly, the number of cells distributed in the circumferential direction proved to be of decisive importance. Therefore, the finest possible resolution should be provided here. With respect to the cross-sectional grid topology, the ratio of the inner block size to the pipe radius of $R_{\text{block}}/R = 0.8$ is recommended. Furthermore, a streamwise-to-spanwise grid cell ratio of $\Delta z^+/\Delta \varphi^+ = 3$ and a (precursor) straight pipe section length of $l_{\text{pre}} = 2.5 D$ have proven to be adequate for the correct representation of the fluctuating flow characteristics. A comparative assessment of the most adequate SGS models demonstrated that the WALE model by Nicoud and Ducros (1999) proved to be an advantageous formulation. It correctly captures the flow physics, especially within the near-wall region, while showing excellent results for the entire parameter range investigated. However, in the WALE framework, the quality criterion concerning the ratio of the subgrid-to-total turbulent kinetic energy ($k_{\text{SGS}}/k < 0.2$, according to Pope (2000)), is not applicable in a straightforward manner. This constraint is often satisfied even with coarser grid resolution. Here, the ratio of characteristic grid width to Kolmogorov lengthscale Δ/η as well as the subgrid-to-total viscous

dissipation rate ($\varepsilon_{\text{SGS}}/\varepsilon$) proved to be more suitable.

3.4. WSG-related pipe configurations

The solution domain size and grid arrangement representing the outcome of Chapter 3.3: $R_{\text{block}}/R = 0.8$, $\Delta z^+/\Delta\varphi^+ = 3.0$ and $l_{\text{pre}} = 2.5 D$ - have been adopted as a basis for simulating the precursor fully developed pipe flow at the three deflection Reynolds numbers (see Table 3.2). The respective results obtained, serving as the inflow into the WSG and its isolated geometrical components, are marked in the following by the colors **blue** ($\text{Re}_{\text{deflection}} = 7200$), **green** ($\text{Re}_{\text{deflection}} = 10500$) and **red** ($\text{Re}_{\text{deflection}} = 14000$). The results of the latter are also applied to the inflow Reynolds number of $\text{Re}_b = 14400$, which is justified by the small deviations between the two Reynolds numbers ($\Delta\text{Re} = \text{Re}_b (\dot{V} = 2.2 \text{ l/min}) - \text{Re}_{\text{deflection}} (\dot{V} = 4.3 \text{ l/min}) = 400$). Accordingly, the grid resolution parameters (representing the results of a preliminary grid-dependence study; not shown here) for which a detailed study on quality assessment measures have been provided in line with the previously performed analysis, are listed in Table 3.5. The wall-resolved simulations utilizing the WALE model have been performed with a minimum wall-nearest cell size of $\Delta r_{\text{min}}^+ = 0.3$, enabling the correct capturing of the structural characteristics of the viscous sublayer in its entirety.

$\text{Re}_{\text{deflection}}$	n_{total}	n_{cs}	$\Delta r_{\text{min}, \dots, \text{max}}^+$	$\Delta\varphi^+$	Δz^+
7200	1740 k	20480	0.3, ..., 4.7	4.6	13.8
10500	2650 k	27540	0.3, ..., 5.8	5.6	16.8
14000	3600 k	34000	0.3, ..., 6.7	6.6	19.7

Table 3.5.: Grid characteristics ($k \equiv 10^3$) for the three pipe Reynolds numbers $\text{Re}_{\text{deflection}} = 7200, 10500, 14000$ in terms of the total and cross-section cell numbers, n_{total} and n_{cs} , respectively, and the dimensionless grid resolution parameters in the radial $\Delta r_{\text{min}, \dots, \text{max}}^+$, circumferential $\Delta\varphi^+$ and mean flow directions Δz^+ .

The resulting profiles of the mean velocity u^+ , Reynolds stress components $\overline{u_i u_j}^+$ and viscous dissipation rate of the turbulent kinetic energy ε^+ are presented in Fig. 3.16. The depictions of the resulting flow quantities will not be discussed further and is presented here for the sake of completeness with regard to the inflows of the WSG and its isolated geometrical components.

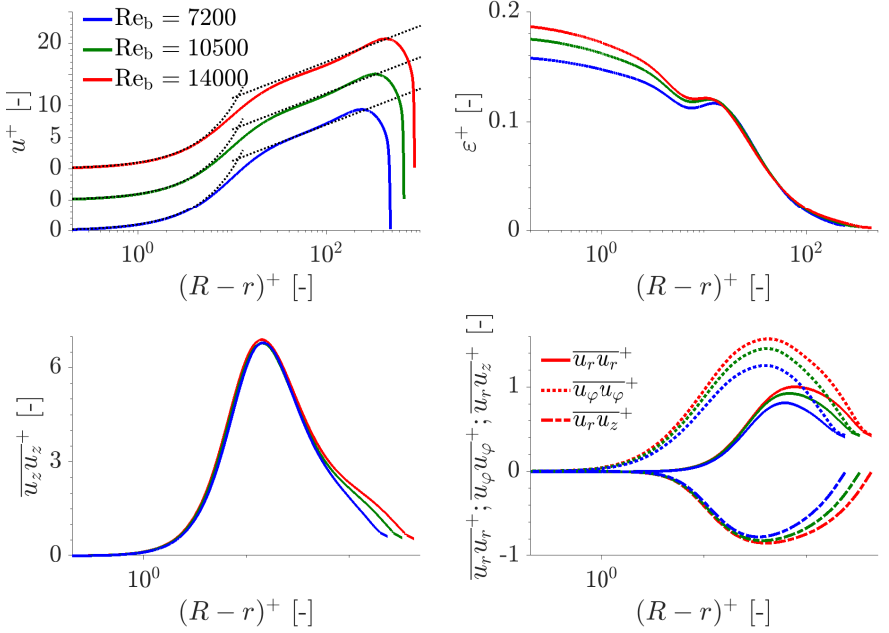


Figure 3.16.: Semi-log plot of the non-dimensional streamwise velocity component u^+ (top left), non-dimensional Reynolds stress components $\overline{u_i u_j}^+$ (bottom left & right) and viscous dissipation rate of the turbulent kinetic energy ε^+ (top right) over non-dimensional wall distance $(R-r)^+$ for the Reynolds numbers $Re_{\text{deflection}} = 7200, 10500$ and 14000 , respectively, friction Reynolds numbers $Re_\tau = 238, 331$ and 428 .

For assessing the quality of the pipe flow simulations for the given grid resolution (Table 3.5), the LES quality parameters discussed in Chapter 3.3.4 are here also evaluated, specifically the modeled-to-total turbulent kinetic energy ratio k_{SGS}/k (Fig. 3.17 top left), the corresponding ratio of the modeled-to-total viscous dissipation rate $\varepsilon_{\text{SGS}}/\varepsilon$ (Fig. 3.17 top right), the ratio of the

3. IC-engine-relevant cooling channel configuration: Water Spider Geometry (WSG)

largest cell dimension to the Kolmogorov lengthscale Δ_{\max}/η (Fig. 3.17 bottom left) and the energy spectra (Fig. 3.17 bottom right). Accordingly, the well-known criteria with respect to all evaluated quality assessment measures are clearly satisfied.

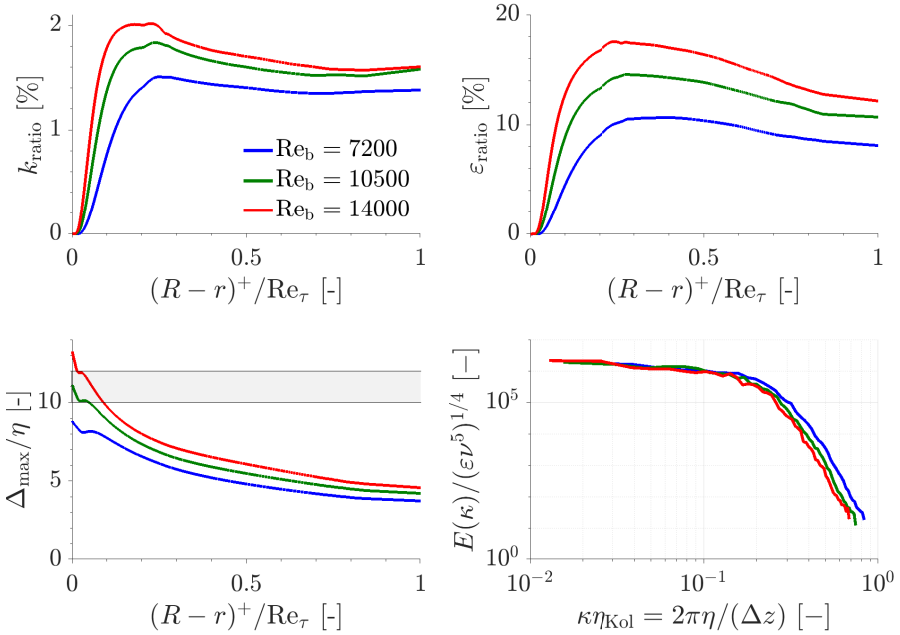


Figure 3.17.: Modeled-to-total turbulent kinetic energy ratio k_{SGS}/k (top left), modeled-to-total viscous dissipation rate ratio $\epsilon_{\text{SGS}}/\epsilon$ (top right) and ratio Δ_{\max}/η over the non-dimensional wall distance $(R-r)^+/\text{Re}_\tau$ (bottom left) for the Reynolds numbers $\text{Re}_{\text{deflection}} = 7200$, 10500 and 14000, respectively, friction Reynolds numbers $\text{Re}_\tau = 238$, 331 and 428. The normalized energy spectrum of the streamwise velocity component $E(\kappa_{\text{eddy}})/(\epsilon\nu^5)^{1/4}$ over normalized wavenumber $\kappa_{\text{eddy}}\eta$ are also depicted for the considered Reynolds numbers (bottom right).

3.5. Flow in an isolated 90°-pipe bend

3.5.1. Introduction

The flow conditions inside a curved pipe are typically characterized by the so-called Dean number De in addition to the Reynolds number Re_b based on the bulk velocity U_b and the pipe diameter D . The Reynolds number globally relates to the ratio of the inertial to viscous forces enabling a statement about the flow regime, i.e., whether the flow behaves as turbulent or laminar. The Dean number accounts for the influence of both the longitudinal (denoted by the curvature radius of the pipe bend R_c) and the transverse curvature (represented by the pipe diameter D) of the pipe section on the flow. The latter parameter quantifies the formation and intensity of curvature-induced counter-rotating vortices within and downstream of the flow deflection, the so-called Dean vortices. According to W. R. Dean (1928), such structures can arise when $De > 54$, which have their origin in the momentum balance fulfillment implying the centrifugal forces acting on the faster core flow and thereby displacing the faster fluid towards the outer radius of the curved pipe. The flow present at the outer radius escapes the faster flow core and is deflected along the cross-sectional pipe curvature. As a result of the arising shear effects, two mutually rotating vortices are created and convected downstream by the main flow, the Dean vortices. The Dean number is defined by Eq. (3.1) in terms of the bulk Reynolds number Re_b as

$$De = Re_b \sqrt{\frac{D}{2R_c}} \quad \text{with} \quad Re_b = \frac{U_b D}{\nu} . \quad (3.1)$$

The flow in curved pipe segments and the associated flow dynamics have been subject of numerous experimental and numerical studies due to its wide range of applications in science and industry especially considering its passive mixing effects. An early review article by Berger et al. (1983) provides an in-depth insight into the relevant flow characteristics. A detailed overview of the variety of investigations in the field of flow deflection, in terms of deflection angles, relative radius of curvature and flow regimes is given in Kalpakli Vester et al. (2016). Röhrig et al. (2015) performed a complementary numerical work to the experimental investigations of Kalpakli et al. (2012) and Kalpakli and Örlü (2013), by applying a LES utilizing the dynamic Smagorinsky model to

investigate the flow in a 90° -pipe bend. Comparative assessment has also been provided with the results obtained by a widely-used low Reynolds number $k - \varepsilon$ model due to Launder and Sharma (1974) and a near-wall Reynolds Stress Model (RSM) by Jakirlić and Maduta (2015) in the framework of the OpenFOAM® code. An early LES work on the flow in a pipe bend by Rütten et al. (2001) concentrated primarily on the frequency analysis in relation to the vortex shedding arising at the inner pipe wall in correlation with the Dean vortices. The simulations have been performed over a range of Reynolds numbers up to $Re_b = 27000$ and two relative curvatures, $R/R_c = 1/6$ and 0.5 . A relevant work from the same group followed by Rütten et al. (2005). The influence of the Dean vortical structures originating from an elbow positioned upstream of a T-junction configuration on the thermal mixing and a possible pipe wall fatigue has been investigated by Tunstall et al. (2016) by using a LES employing the dynamic Smagorynski model. Furthermore, a DNS of a relevant 90° -pipe bend at a lower Reynolds number of $Re_b = 5300$ and a relative curvature of $R/R_c = 0.4$ was carried out by Wang et al. (2018) by using the high-order spectral element method code Nek5000. The study focused primarily on the flow oscillations downstream of the deflection by employing a relatively long outlet pipe. The solution domain with the inlet pipe length of $l_{inlet} = 12.5 D$ and outlet pipe length of $l_{outlet} = 40 D$ was meshed by a grid comprising 105 million cells arranged appropriately to provide the non-dimensional resolution corresponding to $\Delta z^+ = 3.03 - 9.91$, $\Delta r^+ = 0.14 - 4.36$ and $\Delta \varphi^+ = 1.51 - 4.93$. Note that this DNS solution domain and grid properties served to a certain extent as a reference starting point for the target grid arrangement in the present LES study. Subsequent DNS investigations of the same group (Lupi et al., 2020) focus on a global stability analysis on the threshold detection indicating the transition from the steady to the periodically unsteady regime. The flow in a pipe bend with the relative curvature of $R/R_c = 1/3$ at Reynolds numbers in the range between $Re_b = 2000$ and 3000 has been selected for this analysis. Di Liberto et al. (2013) performed a DNS of differently curved pipes - from a straight pipe to a 180° -turned pipe - investigating the influence of the curvature radius on the budget of the equation governing the turbulent kinetic energy. They conclude that the convection enhancement correlated with the strengthening of the secondary currents is represented by the Dean vortices.

The relevant research is in general not focused only on the isolated flow

dynamics within a pipe deflection, but also on the underlying multi-phase flow characteristics. For instance, the curved cooling channels in IC engines are subjected to a great diversity of different simultaneously occurring phenomena. One phenomenon of decisive importance is the flow-induced abrasive degradation of the wall surface. The erosive behavior of a correspondingly generated, by the wall material removal, particle-laden flow within and downstream of a pipe deflection represents a prominent research field. Adequate background is encountered in the oil industry and oil production. Well-known studies in the field of surface degradation due to an abrasive medium within the particle-laden flow (typically air-sand mixture) are those of X. Chen et al. (2004), Solnordal et al. (2015) and Vieira et al. (2016). All three studies investigate the surface degradation due to a sand-air mixture within a pipe deflection at different Reynolds numbers. Especially, the detection and numerical prediction of the correct particle-wall interaction with multiple impacts and subsequent erosion is a challenging task described in detail by, e.g., Sommerfeld and Huber (1999). An overview of most-widely used particle erosion models and their predictive capabilities is given in Vieira et al. (2016) and Wegt et al. (2020). Furthermore, the increased passive mixing behavior due to a deflection is of particular interest in the context of heat exchanger design and possible boiling effects. Studies investigating boiling in deflections are limited to a very small number. The investigations by Z. Yang et al. (2008) should be mentioned who studied the boiling behavior inside meandering 180° deflections.

The present chapter is primarily concerned with a well-resolved, highly comprehensive LES study of the topological features of the single-phase flow within a 90°-pipe bend relevant to the IC-engine cooling channel configurations, in terms of corresponding geometrical properties and Reynolds number range. The results are interpreted with regard to the time-averaged flow characteristics including mean velocity and turbulence statistics as well as vortex topology and evolution applying the vortex identification methodology according to Graftieaux et al. (2001). Subsequently, a detailed three-dimensional mapping of the wall shear-stress and pressure distributions are provided representing suitable indicators for the flow-induced forces the fluid exerts on the wall in relation to a potential erosion tendency and associated processes. Finally, the peculiarity of the Dean's vortical events in view of their formation and structural behavior is analyzed by means of their spatial tracking as well as circulation evolution within the flow field.

3.5.2. Computational domain

The computational domain of the presently investigated 90°-pipe bend configuration is schematically illustrated in Fig. 3.18, representing a part of the afore-presented WSG (red marked region of Fig. 3.1). The considered volume fluxes, practically encountered in cooling systems of IC-engines according to Table 3.2 with $Re_b = Re_{\text{deflection}} = 7200, 10500$ and 14000 , indicate a fully-turbulent flow regime. The 90°-pipe bend configuration is the exception, where the three volume fluxes from Table 3.2 are considered within the present work, since the present reference data situation is suitable for the evaluation of the performed LES.

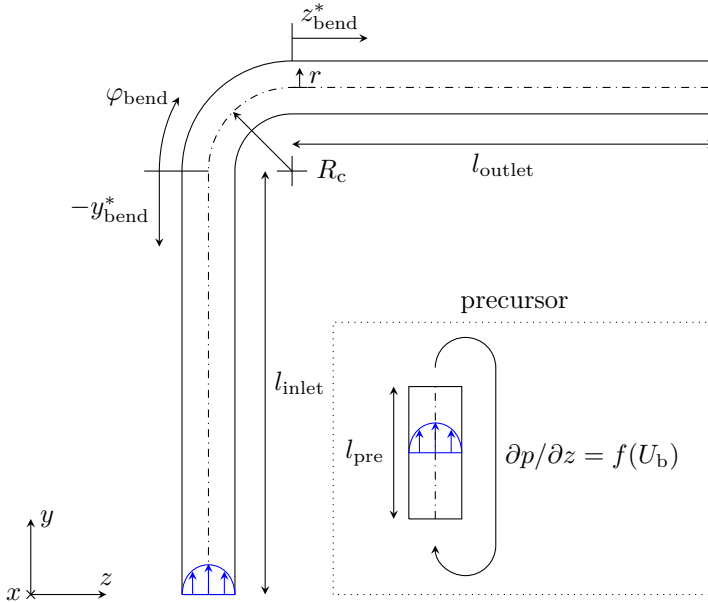


Figure 3.18.: Schematic illustration of the computational domain including the main and precursor regions as well as the dimensionless coordinates $y^*_{\text{bend}} = y_{\text{bend}}/D$, φ_{bend} and $z^*_{\text{bend}} = z_{\text{bend}}/D$.

The computational domain consists of two regions with the 90°-pipe bend and a preceding region representing the so-called precursor. The adopted relative curvature corresponds to $R/R_c = 0.316$, with R_c denoting the curvature radius of the pipe centerline. The smaller the relative curvature, the stronger its influence on the streamline topology due to the deflection. The considered bulk Reynolds numbers lead to Dean numbers of $De = 4050, 5900$ and 7876 according to Eq. (3.1). Consequently, the formation of counter-rotating twin vortices in the cross-sectional area will form as $De > De_{crit} = 54$. The main computational domain is preceded by an $l_{pre} = 2.5 D$ long straight pipe segment (so-called precursor, see Fig. 3.18) to provide a fully developed flow at the inlet of the main computational domain. The simulation within the precursor is performed utilizing periodic inlet/outlet boundary conditions underlying an iteratively predicted pressure gradient associated with the relevant Reynolds numbers Re_b . The resulting instantaneous flow field is mapped onto the inlet of the main domain. The characteristics of the grid in terms of the cell-face ratio and cross-sectional arrangement elaborated in Chapter 3.3 are straightforwardly adopted for simulating the 90°-pipe bend flow. An exception is the streamwise-to-spanwise grid cell ratio within the pipe bend itself, which has been fixed towards $\Delta z^+ / \Delta \varphi^+ = 1.0$. This corresponds to a homogeneous cell distribution at the pipe bend surface which has been shown to be advantageous in various grid studies. Furthermore, appropriate lengths of the inlet and outlet regions are elaborated to provide a flow situation being undisturbed by the flow in adjacent pipe segments. Accordingly, the length of inlet and outlet straight pipe sections of $l_{inlet} = l_{outlet} = 8 D$ proved to be suitable. The resulting grid resolution in terms of the total number of cells n_{total} meshing the entire configuration, including also the corresponding precursor as shown in Fig. 3.18, is listed in Table 3.6 for all three considered Reynolds numbers.

Re_b	7200	10500	14000
De	4050	5900	7876
n_{total}	28 mio.	42 mio.	56.5 mio.

Table 3.6.: Number of grid cell n_{total} (including also the precursor region), for the respective Reynolds Re_b and Dean number De combinations.

3.5.3. Discussion: LES validation through experimental comparison

A validation of the LES results in the 90°-pipe bend flow is performed by comparing them directly to the available reference measurements from Kalpakli Vester et al. (2016) and Sattarzadeh Shirvan (2011) (see also Vester et al. (2016)). Due to the lack of corresponding data, this comparison is limited to the bulk Reynolds number of $Re_b = 14000$. It should also be noted that the experimentally available data correspond to the relative curvatures of $R/R_c = 0.33$ (Kalpakli Vester et al. (2016)) and $R/R_c = 0.43$ (Sattarzadeh Shirvan (2011)) deviating slightly from the presently investigated one - $R/R_c = 0.316$. The relevant comparison is depicted in Fig. 3.19 which includes the mean streamwise velocity u_z/U_b and the related turbulence intensity $u_{z,RMS}/U_b$ at two locations downstream of the pipe bend denoted by $z_{bend}^* = z_{bend}/D = 0.67$ and 1.5 (see Fig. 3.18 for notations).

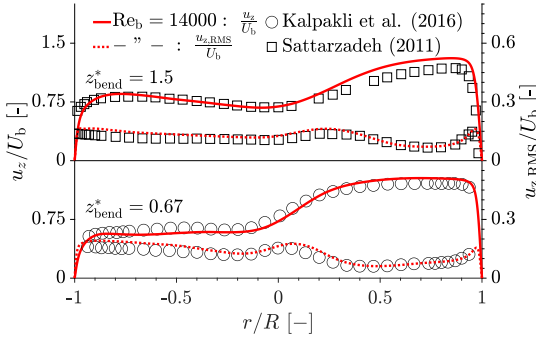


Figure 3.19.: Streamwise velocity u_z/U_b and turbulence intensity $u_{z,RMS}/U_b$ at $z_{bend}^* = z_{bend}/D = 0.67$ and 1.5 for $Re_b = 14000$ compared to the experimental data by Kalpakli Vester et al. (2016) and Sattarzadeh Shirvan (2011).

The velocity profiles resemble an asymmetrical shape typical for a flow influenced by the varying sign change of longitudinal gradients correlated with the formation of a shear layer: global velocity decrease due to flow deceleration along the inner surface and velocity increase due to flow acceleration at the

outer surface. Correspondingly, the turbulence intensity exhibits a local maximum in the core flow coinciding with the shear layer location interfacing the slower inner stream and the somewhat faster outer stream. It should be noticed that such a variation is typical for the flow region downstream of the bend. Within the bend itself, the flow is characterized by an alternating switching between the faster and slower streams (see Chapter 3.5.4). The numerical and experimental results with regards to both quantities, velocity and root-mean-square of the streamwise Reynolds stress components, coincide very well especially in view of the above-mentioned deviations in the relative curvature and thus in the Dean number. It is valid for the near-wall region, but also for the central region characterized by the high velocity gradient and appropriately intensive turbulence production. Both are reproduced qualitatively and quantitatively well at both positions downstream of the deflection. Only in the case of the velocity maximum related to the outer region at $z_{\text{bend}}^* = 1.5$, a slight overestimation can be recognized. However, the deviation can be explained by a somewhat lower relative curvature (implying a larger curvature radius R_c) and thus slower reorientation of the flow with respect to flow acceleration-deceleration changeover.

3.5.4. Discussion: 90°-pipe bend flow topology

In technical applications involving pipe flows with deflections, as encountered for instance in the cooling channels of IC engines, the flow conditions at the pipe wall dominate the boiling and erosive processes and are therefore of key interest. Accordingly, the topological features of the flow based on the three-dimensional mapping of the time-averaged flow fields and respective vortical structures, will be linked to flow conditions at the wall. These will provide a basis for adequate future modifications of the flow geometry towards controlling and suppression of possible wall material degradation due to enhanced wall shear strength in relation to potentially emerging boiling and erosive processes. Additionally, underlying mechanisms specifically responsible for the topological flow field evolution will be elaborated. In the following, the flow topology will be discussed interactively due to a very close correlation of the velocity (Figures 3.20, 3.21 and 3.22) and pressure fields (Figures 3.22 and 3.23) in their entirety as well as those of the turbulence quantities (Figures 3.20, 3.25 and 3.26).

3. IC-engine-relevant cooling channel configuration: Water Spider Geometry (WSG)

The time-averaged velocity magnitude U/U_b and turbulent kinetic energy fields k/U_b^2 for $Re_b = 7200$ are illustrated exemplary in Fig. 3.20 by their iso-contours and mean velocity streamlines within the $y-z$ -symmetry plane as well as at selected cross-sections. This enables a detailed insight into the three-dimensional flow topology within the pipe bend and the straight outlet pipe segment downstream. Vortex centers are marked by magenta crosses, squares and circles within the selected cross-sections. They are detected by utilizing the methodology proposed by Graftieaux et al. (2001), where the maxima of the Γ_1 scalar field are considered as the center-determining quantity. For current investigations within the 90° -pipe bend configuration, a threshold of $\Gamma_1 = 0.55$ is applied to extract vortex center locations. The search window size is set to 11. The vortex center tracking throughout the flow domain will be interactively discussed in the following text.

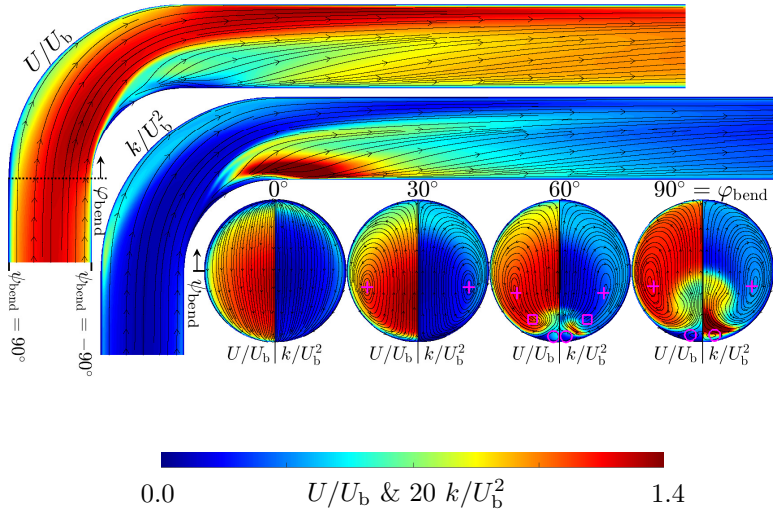


Figure 3.20.: Time-averaged velocity magnitude U/U_b (upper or left) and turbulent kinetic energy k/U_b^2 (lower or right) within the $y-z$ -symmetry plane and selected cross-sections for $Re_b = 7200$. The visualized data are derived from averaging over the symmetry planes.

The corresponding development of the time-averaged mean velocity profile in the vertical $y-z$ -symmetry plane and in the vertical plane coinciding with the pipe symmetry axis ($r = 0$, Fig. 3.18) is depicted in Fig. 3.21 for all three Reynolds numbers considered. To allow a detailed investigation of interacting flow effects, the velocity profile development is analyzed by presenting both the streamwise (longitudinal) u_z and the curvature-radial, normal-to-wall component u_{cr} . The velocity components are depicted in both perpendicular-to-each-other planes enabling an insight into the three-dimensionality of the profiles within the inlet pipe segment, pipe bend and straight outlet pipe. Here, $r/R = -1$ ($\psi_{\text{bend}} = -90^\circ$) represents the inner wall and $r/R = 1$ ($\psi_{\text{bend}} = 90^\circ$) the outer wall. The lower part of Fig. 3.21 shows the corresponding profile plots starting from the pipe center $r/R = 0$ towards the pipe wall denoted by $r/R = -1$ ($\psi_{\text{bend}} = 0^\circ$), perpendicular to the $y-z$ -symmetry plane. Only one half is displayed here due to the completely symmetrical flow picture. The region of the pipe deflection ($\varphi_{\text{bend}} = 0^\circ$ to 90°) is colored in gray for clarity. Also visible in these plots are the trajectories of the above-mentioned vortex centers denoted by symbols.

The flow in the vertical inlet pipe segment ($y_{\text{bend}}^* = -1$ in Fig. 3.21) represents the inflow into the 90°-pipe bend. The inflow is unidirectional in mean and corresponds to a fully developed turbulent pipe flow. It is characterized by a perfectly symmetrical streamwise velocity profile and zero value of the radial velocity component. The flow stream entering the pipe bend resembles a high-momentum jet skewing smoothly in accordance with the geometry-related flow guidance and hitting subsequently the outer wall. A strong longitudinal streamline curvature in the $y-z$ -symmetry plane is the consequence. The flow experiences a weak acceleration in the inner-wall proximity and deceleration in the upper half of the cross-section. Latter it is characterized by the streamwise velocity profile getting a slightly asymmetrical shape with the maximum shifted towards the lower wall (see Fig. 3.21 top). The profile asymmetry is also reflected in different magnitudes of the velocity gradients, with an alternating increasing-decreasing tendency at the lower wall and an opposite behavior at the upper wall. Some quantitative differences can be observed at velocity profiles in relation to different Reynolds numbers. For instance, the u_z -velocity gradient at the deflection inner radius becomes slightly stronger with the Reynolds number increase. The corresponding variation of the skin-friction coefficient at both inner ($r/R = -1$) and outer ($r/R = 1$)

3. IC-engine-relevant cooling channel configuration: Water Spider Geometry (WSG)

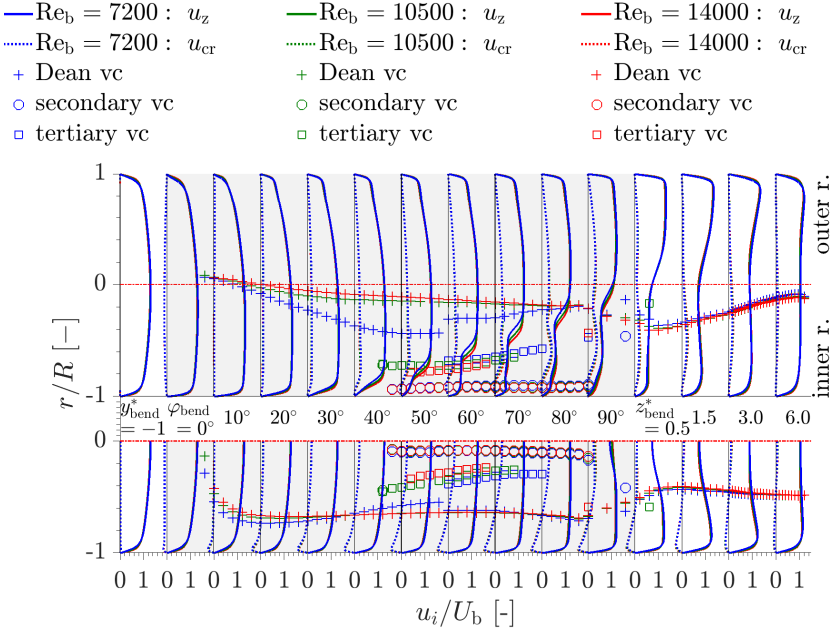


Figure 3.21.: Time-averaged streamwise u_z/U_b and curvature-radial u_{cr}/U_b velocity at selected positions within the $y - z$ -symmetry plane (top) and in the perpendicular plane, which coincides with the pipe symmetry axis $r/R = 0$ (bottom) for the considered Reynolds numbers. The spatial evolution of the vortex centers are presented by symbols and the pipe bend region is highlighted in gray. The pipe center is marked by a red dash-dotted line.

wall contours, illustrated in Fig. 3.24, will be discussed later. Right at the inlet of the pipe bend, the streamline curvature and the corresponding pressure reduction towards the inner deflection radius (see Fig. 3.23) lead to a negative curvature-radial velocity component ($u_{cr}(\varphi_{bend} = 0^\circ) < 0$, Fig. 3.21). This corresponds to a cross-sectional flow in the direction of the negative pressure gradient and is consistent with observations in Fig. 3.20. Such a negative

curvature-radial velocity component, acting over the entire cross-section, can only be observed at the pipe bend inlet and not for deflection angles exceeding $\varphi_{\text{bend}} = 20^\circ$.

As afore-mentioned, the longitudinal skewness of the flow within the 90°-pipe bend is clearly evident from the cross-sectional pressure gradient visible in the $y-z$ -symmetry plane depicted in Fig. 3.23. The surface pressure distribution, represented by its coefficient, reveals a negative pressure region towards the inner radius of the deflection, correlated with the flow acceleration, and a positive pressure in the upper flow part complying with the flow deceleration. This denotes in sum a positive pressure gradient over the cross-section from $r/R = -1$ ($\psi_{\text{bend}} = -90^\circ$) to $r/R = 1$ ($\psi_{\text{bend}} = 90^\circ$). It is valid not only at the pipe bend surface, but also in the flow core, implying an almost zero pressure gradient in the planes normal to the $y-z$ -symmetry plane over the entire cross-section as can be seen in Fig. 3.22 top. This behavior holds qualitatively within the pipe bend in its entirety and is identical for all three considered Reynolds numbers.

The flow acceleration in the $y-z$ -symmetry plane is also indicated by the streamlines concentration in the direction of the inner deflection radius as can be observed in Fig. 3.20. The streamline closest to the inner deflection radius, which departs from the inner deflection radius as the deflection proceeds, separates the faster flow in the upper half and the slower flow in the lower half of the curved pipe section. It visualizes the shear layer formation. The narrowing of the space between the streamlines toward the upper wall illustrates the spatial switch of the accelerating flow regions. This is also noticeable at the streamwise velocity profiles indicated an enhanced magnitude in the upper half of the pipe relative to that in the lower half for $\varphi_{\text{bend}} > 50^\circ$. The shear layer formation is closely connected to the APG effect over the cross-section causing a flow deceleration within and underneath this region (Fig. 3.23). Accordingly, the low velocity region observed in the $y-z$ -symmetry plane shifts increasingly towards the pipe center. The flow topology reveals a strong three-dimensional structure with the inplane motion in the cross-section playing an important role, superposed to the main flow stream. Apart of the cross-section flow at $\varphi_{\text{bend}} = 0^\circ$ with the streamlines showing into negative vertical direction (see $u_{\text{cr}} < 0$ in Fig. 3.21), the strengthening of the longitudinal flow curvature causes the re-orientation of the inplane streamlines (see $u_{\text{cr}} > 0$ for $\varphi_{\text{bend}} > 0^\circ$ in Fig. 3.21). Consequently, a pair of symmetrical

counter-rotating vortices arises for $\varphi_{\text{bend}} > 9, 10^\circ$, as can be recognized by the vortex centers marked in Fig. 3.20 and known as Dean vortices (W. R. Dean, 1928), representing a typical feature of the flow in a curved pipe. These vortical structures represent the consequence of the associated centrifugal force according to the flow acceleration along the deflection (see Fig. 3.20). The relevant acceleration is formulated in terms of the streamwise velocity component $\rightarrow u_z^2/R_c$. The centrifugal force is driving the fluid elements from the lower convex wall ($r/R = -1$; $\psi_{\text{bend}} = -90^\circ$) towards the upper concave wall ($r/R = 1$; $\psi_{\text{bend}} = 90^\circ$) in terms of the positive curvature-radial velocity component u_{cr} in $y - z$ -symmetry plane in Fig. 3.21. This upward cross-sectional inplane stream bifurcates after reaching the upper wall. The divided flow streams towards the inner radius of the deflection at both side walls and is supported by the surface pressure gradient (see Fig. 3.23). This behavior is characterized by the negative radial velocity component u_{cr} at the side walls of the pipe and can be seen in Fig. 3.21 bottom. The onset of the negative curvature-radial velocity at the wall locality is observed at a position denoted by $\varphi_{\text{bend}} = 10^\circ$ indicating the spatial origin of the Dean vortices and coincide with the depicted vortex centers starting at $\varphi_{\text{bend}} = 8^\circ$ to 9° . The vortex-induced effects influence the evolution of the curvature-radial velocity with an increase within the $y - z$ -symmetry plane (Fig. 3.21 top, $r/R \approx -0.8$) and a decrease in the side wall proximity (Fig. 3.21 bottom, $r/R \approx -0.95$).

3.5.5. Discussion: Vortex topology

The Dean vortices with their origin in the arising centrifugal forces within the 90° -pipe bend develop for deflection angles of $\varphi_{\text{bend}} > 9^\circ$ to 10° . They extend gradually over the entire cross-section as visualized for instance at the location $\varphi_{\text{bend}} = 30^\circ$ by closed streamlines in Fig. 3.20. Up to the location at $\varphi_{\text{bend}} = 60^\circ$, an elongation of the Dean vortex and a specific twisting towards the inner radius occurs. A magnified cross-sectional view of the time-averaged velocity field together with the corresponding mean pressure coefficient field C_p for the deflection angle of $\varphi_{\text{bend}} = 60^\circ$ in Fig. 3.22 top enables a more detailed insight into the flow evolution in terms of the vortex topological properties. For this purpose, multiple vortex centers are marked by magenta symbols, which are identified by maxima of the Γ_1 -scalar field. The vortex elongation implies narrowing of the inplane streamlines followed by the radial

velocity enhancement visible also in Fig. 3.21 between the locations denoted by $\varphi_{\text{bend}} = 50^\circ$ to 90° . A specific bump-shaped maximum of the u_{cr} velocity can be observed in the lower half of the $y - z$ -symmetry plane, indicating an intensified confluence of the two downward streams flowing at the side walls. This event is accompanied by emergence of a region of low velocity at the most inner radius of the pipe bend at $\psi_{\text{bend}} = -90^\circ$ in Fig. 3.22 top. Another vortex can be identified which rotates in opposite direction to the Dean vortex. It is denoted as secondary vortex and marked by a magenta circle. Simultaneously, a second Dean vortex center, highlighted by a magenta square, with the same rotating direction as the main Dean vortex emerges. This tertiary vortex splits off the main Dean vortex and its location coincides with the lower extreme of the mostly elongated inplane streamline.

The cross-sectional convection and elongation of the Dean vortices are caused by their self-induced velocity with respect to the pipe wall. It can be described by considering the potential theory solution for an infinitely long straight vortex, which induces the velocity $|\vec{u}_{\text{vortex}}| = \Gamma/(2\pi a)$ at a location with a distance a vertical to the vortex tube. In the case of the Dean vortex the distance a is on the one hand the distance to its twin vortex and on the other hand twice the distance from the vortex center to the wall. Accounting for the smaller distance of the Dean vortex center to the pipe wall relative to the $y - z$ -symmetry plane (see Fig. 3.20 $\varphi_{\text{bend}} = 30^\circ$), the induced velocity originated from the mirrored vortex by the pipe wall is stronger than that of its twin vortex. This causes consequently an induced velocity directed towards the inner deflection radius and subsequently the elongation of the Dean vortex. Note that a convection of the vortex center to the inner deflection radius with a constant vertical position causes the vortex center moving closer to the wall.

The increase in the velocity induced in the immediate wall vicinity due to the proximity of the Dean vortices, initiates the detachment of the flow from the wall at the inner most pipe bend location. This region immediately above the pipe wall accomodates the secondary vortex structure and it is characterized by a pressure minimum as visible in Fig. 3.22 top (see also Fig. 3.23). The formation of the secondary and tertiary vortex structures observed is due to an APG acting in the downward direction (negative radius direction) towards the inner deflection radius. This fairly weak APG towards the inner deflection radius between the tertiary and secondary vortices, which can be observed in Fig. 3.22 top, is clearly visible also in Fig. 3.23 for $\varphi_{\text{bend}} > 45^\circ$ between $\psi_{\text{bend}} = -45^\circ$

and -90° . For larger deflection angles, it decreases continuously until it vanishes at the bend outlet ($\varphi_{\text{bend}} = 90^\circ$). Both, the main Dean vortices and the associated secondary vortices, can also be identified at the outlet of the pipe bend ($\varphi_{\text{bend}} = 90^\circ$), but the elongation and bowing of the Dean vortices have slightly weakened (see Fig. 3.20). The latter process is reflected also in weakening of the u_{cr} -maximum as can be observed in the curvature-radial velocity evolution in Fig. 3.21. The reduction of the local APG mentioned above occurs concurrently with cessation of both secondary and tertiary vortex. Subsequently, the Dean vortex starts to gradually restore its initial shape which is clearly noticeable in Fig. 3.22 bottom. The corresponding depression of the streamwise velocity profile in the Dean vortex center is visible in the plane vertical to the $y - z$ -symmetry plane at $\varphi_{\text{bend}} = 90^\circ$ and immediately after, but gradually weakens downstream within the straight outlet pipe (see Fig. 3.21).

The spatial tracking of the characteristic vortex centers within the pipe bend is depicted by colored symbols ('+' Dean vortex, 'o' secondary vortex, '□' tertiary vortex) in Fig. 3.21 for all three flow Reynolds numbers in relation to the velocity field variation. The symbols denote the spatial positions of the vortex centers and their evolution. Taking into account both diagrams, the upper one displaying the velocity profiles within the $y - z$ -symmetry plane and the lower one showing them in the plane perpendicular to it, the exact center positions of all three characteristic vortex structures - main Dean vortex, secondary vortex and tertiary vortex - can be thoroughly followed. The dependence of the vortex centers trace on the turbulence field variability can be extracted from Fig. 3.26. The Dean vortices are the first to be detected and tracked by means of the vortex identification methodology according to Graftieaux et al. (2001)¹ from an angle of $\varphi_{\text{bend}} = 9^\circ - 10^\circ$. As observed in the cross-sectional presentation of the flow pattern (Fig. 3.20 and 3.22), the center of the main Dean vortex resides approximately at the position

¹Graftieaux et al. (2001) developed this method to track the center of the precessing vortex core in a swirling flow. The method has been subsequently applied to different vortex-dominated flows, as, e.g., to vortices formation and shedding from a pitch-up maneuver of a flat plate at a very low Reynolds number of oncoming flow by Huang and Green (2015) and to quantify the leading-edge vortex circulation and its spatially evolving center locations in moderately high Reynolds number flow over a flat plate undergoing simultaneous pitching and plunging motion by Kissing et al. (2020). Presently, it is for the first time applied to the Dean vortices characterization.

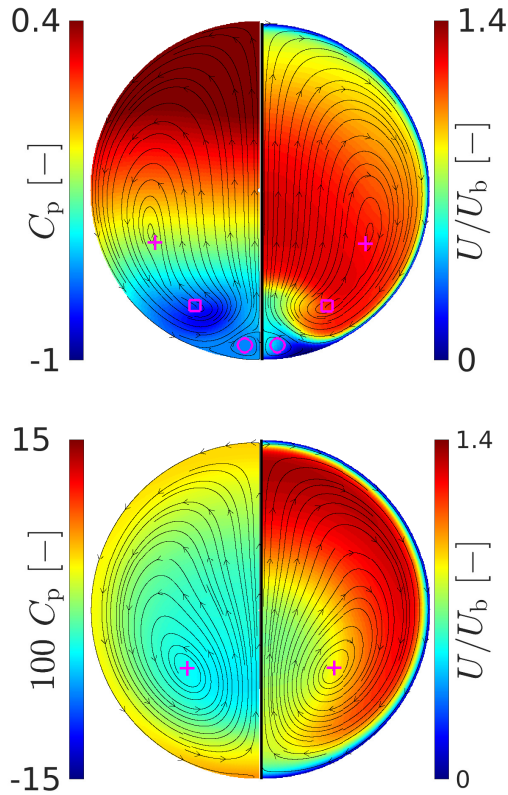


Figure 3.22.: Time-averaged iso-contours of the pressure coefficient $C_p = (p - p_{\text{mean}})/(0.5 \rho U_b^2)$ (left half) and velocity magnitude U/U_b (right half) with the streamlines within the pipe bend at $\varphi_{\text{bend}} = 60^\circ$ (top) and $z_{\text{bend}}^* = 1.5$ (bottom) for $\text{Re}_b = 7200$. p_{mean} is the mean pressure within the cross-section. The visualized data are derived from averaging over the symmetry planes.

around $r \approx 0$ (Fig. 3.21 top) convecting towards the side wall. The trace

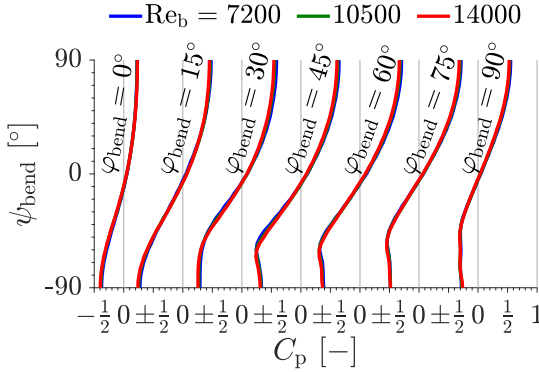


Figure 3.23.: Distribution of the surface pressure coefficient ($C_p = (p - p_{\text{mean}})/(0.5 \rho U_b^2)$) on the side pipe bend wall over the circumferential angle range from $\psi_{\text{bend}} = -90^\circ$ (corresponding to inner wall radius $r/R = -1$) to $\psi_{\text{bend}} = 90^\circ$ (corresponding to outer wall radius $r/R = 1$) for selected deflection angles φ_{bend} between $0^\circ - 90^\circ$ for the three Reynolds numbers considered. p_{mean} is the mean pressure averaged over the corresponding cross-section.

of the Dean vortices coincide with the positions denoted by the sign change of the curvature radial velocity u_{cr} in Fig. 3.21 bottom. The appearance of the secondary and tertiary vortex is detected at the location $\varphi_{\text{bend}} \approx 48^\circ$ independent of the bulk Reynolds number. As discussed previously, their occurrence is closely correlated with the APG towards the innermost deflection wall between $\psi_{\text{bend}} = -60$ to -90 (see $\varphi_{\text{bend}} = 45$ -depiction in Fig. 3.23), which acts beneficially towards the boundary layer detachment. The radial expansion of the secondary and tertiary vortices towards the pipe bend center causes the u_{cr} -velocity maximum within the $y - z$ -symmetry plane. The position of the u_{cr} -maximum coincides with the trace of the tertiary vortices, which is visible in the pipe bend between $\varphi_{\text{bend}} \approx 48^\circ$ and 80° (see Fig. 3.21 top). An appropriate weakening of the streamwise velocity component u_z within the $y - z$ -symmetry plane for $r/R < 0$ is the consequence.

The secondary and the tertiary vortices ultimately dissipate downstream of

the deflection at $z_{\text{bend}}^* > 0.1$, with only the main Dean vortex remaining. Their disappearance is accompanied by a continuous decrease of the curvature radial velocity component, visible in both coordinate planes. Slight differences in the vortex center location tracking are noticeable depending on the Reynolds number considered. First, in the case of $\text{Re}_b = 7200$, a differentiation of the Dean and tertiary vortex is only partially possible, which explains the deviation of the spatial position of the Dean vortex center and the reduced identification of the tertiary structures compared to the higher Reynolds numbers. Second, the vortex identification partially detects another vortex structure in addition to the Dean vortices downstream of $z_{\text{bend}}^* = 0.1$. This can be attributed to the spatial distortion of the Dean vortex and is not related to the secondary and tertiary structures for $z_{\text{bend}}^* < 0.1$. The spatial distortion of the Dean vortex is illustrated for example in Fig. 3.25 for $z_{\text{bend}}^* = 0.5$. The streamwise velocity component exhibits a specific profile shape variation across the boundary layer developing at the inner deflection radius and the shear layer region above. It is characterized by a lower-wall gradient, a subsequent flattened progression and the next velocity increase at the position denoting the transition between the shear layer and the fast flow stream within the upper half of the pipe cross-section. The Dean vortices are still observable downstream of the deflection throughout the outlet despite their dissipative nature, with the intensity of the vortices decreasing sharply, as will be discussed in Fig. 3.27.

3.5.6. Discussion: Wall-abrasive flow effects

An important aspect of the illustrated flow topology within the 90°-pipe bend is the variation of the near-wall velocity gradients, which affect the wall shear-stress $\tau_w = \mu \partial u_z / \partial x_n$ with x_n representing the normal-to-the-wall coordinate in terms of the friction coefficient $C_f = \tau_w / (0.5 \rho U_b^2)$. It is of particular relevance for technical applications, because the wall shear stress τ_w , and respectively the friction coefficient C_f , is a key indicator with respect to erosive processes and the structural safety of technical applications. Therefore, it will be discussed in the following in relation to observed flow field characteristics.

The friction coefficient C_f is depicted exemplary for the inner ($\psi_{\text{bend}} = -90^\circ$) and outer ($\psi_{\text{bend}} = 90^\circ$) deflection radius along the 90°-pipe bend in Fig. 3.24 for all three Reynolds numbers, including portions of the inflow and outflow straight pipes. The region of the deflection is highlighted by a gray shadow for

clarity. Upstream of the deflection ($y_{\text{bend}}^* < 0$), a continuous increase in the friction coefficient at the inner wall contour and a continuous reduction at the outer wall contour can be observed up to the 90° -pipe bend inlet. This behavior is in line with the local flow acceleration and deceleration when approaching the bend section being in obvious correlation with the strengthening and weakening of the wall-relevant velocity gradients. At the 90° -pipe bend inlet ($\varphi_{\text{bend}} > 0^\circ$), the developing tendency of the friction coefficient reverses. C_f decreases at the inner deflection radius and increases at the outer deflection radius. This alternating change is in relation to the centrifugal forces affecting the flow due to the continuous acceleration of the fluid bulk within the bend. The friction coefficient at the outer deflection radius increases steadily as long as the centrifugal force prevails, reaching its maximum at the exit of the pipe bend and decreasing continuously downstream of the bend towards the value corresponding approximately to the inflow pipe segment.

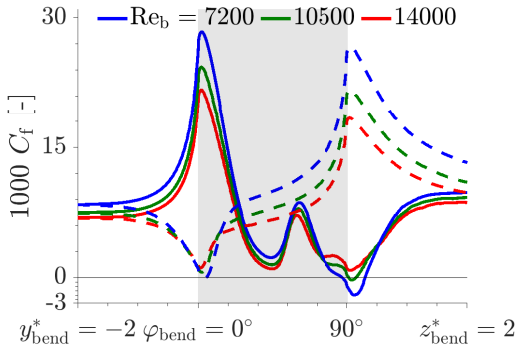


Figure 3.24.: Development of the friction coefficient $C_f = \tau_w / (0.5 \rho U_b^2)$ at the inner ($\psi_{\text{bend}} = -90^\circ$; solid lines) and outer ($\psi_{\text{bend}} = 90^\circ$, dashed lines) deflection radius within the pipe bend for all three considered Reynolds numbers.

The friction coefficient development at the inner deflection radius is additionally affected by various local flow field characteristics. After its decrease at the inner radius of the deflection ($\varphi_{\text{bend}} > 0^\circ$), the friction coefficient reaches a local minimum at $\varphi_{\text{bend}} = 45^\circ$, which coincides with the position of the

slight APG towards the inner wall contour (in the negative radius direction; see Fig. 3.23) correlated with the increasingly positive u_{cr} velocity component. Afterwards, the friction coefficient rises abruptly at $\varphi_{bend} = 45^\circ$ and reaches a local maximum at $\varphi_{bend} = 60^\circ$. The increasing characteristic up to the position of the local maximum coincides with the emergence of the secondary and tertiary vortices (at $\varphi_{bend} \approx 48^\circ$), where the peak friction value at $\varphi_{bend} = 60^\circ$ could be an indicator for the peak intensity of the secondary and tertiary vortices within the 90°-pipe bend. For deflection angles larger than $\varphi_{bend} = 60^\circ$ the intensity of secondary vortices seems to decrease gradually. Consequently, their effect on the friction coefficient at the inner deflection wall decreases, until the coefficient reaches its global minimum downstream of the exit of the deflection $z_{bend}^* = 0.1$. The global minimum is also characterized by its negative values for two lower Reynolds numbers indicating a local boundary layer separation. This highlights the effect of the vortex topology, the associated variation of the velocity gradients at the pipe wall and the corresponding shear-stress development. Downstream of the pipe bend the friction coefficient increases again until it takes the value equal to the one characterizing the outer deflection radius.

The overall skin-friction development is qualitatively similar for all three Reynolds numbers. With respect to a possible abrasive stress on the pipe wall and especially when contaminants are added to the fluid, special attention should be paid to the 90°-pipe bend inlet in the area of the inner radius and the 90°-pipe bend outlet in the area of the outer radius.

3.5.7. Discussion: Turbulence evolution

The decay of secondary and tertiary vortices towards the outlet of the 90°-pipe bend is accompanied by significant changes of the velocity profile shape relevant to both components, which is related to a high level of turbulence as can be seen in Fig. 3.20. This is assumed to be caused by strongly varying local velocity gradients due to vortex decay and its relationship with the turbulence production term $P_k = -\overline{u_i u_j} \partial u_i / \partial x_j$.

To further elaborate the turbulence production increase within the 90°-pipe bend in its lower cross-sectional area, the mean velocity field and the corresponding turbulence kinetic energy field are presented in Fig. 3.25 at $z_{bend}^* = 0.5$. At lower values of z_{bend}^* , both secondary and tertiary vortices

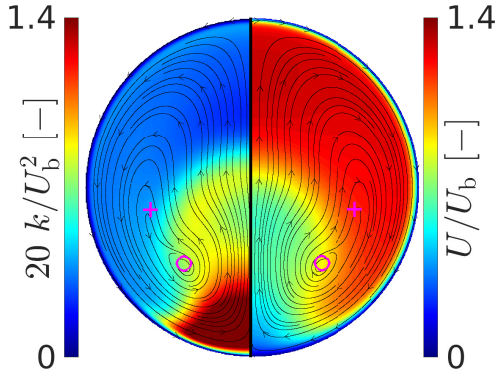


Figure 3.25.: Time-averaged turbulent kinetic energy k/U_b^2 (left half) and velocity magnitude U/U_b (right half) with the streamlines at the location $z_{\text{bend}}^* = 0.5$ for $Re_b = 7200$. The vortex center is highlighted by magenta-colored symbols. The visualized data are derived from averaging over the symmetry planes.

have already decayed. The velocity field and the relevant streamline pattern have been already discussed in detail in relation to Figures 3.20 and 3.22. The velocity field is generally characterized by the main Dean vortex (with the center marked by a magenta cross) and the low velocity region near the deflection inner radius, where the secondary and tertiary vortices have grown towards the pipe centre and decayed completely up to the depicted location. The lower velocity region in Fig. 3.25 at the bottom is characterized by a strong wall-related gradient and represents, in combination with a longitudinal pressure gradient, a mean source of turbulent kinetic energy. Its highest level is detected within the region closest to the inner deflection radius. Less pronounced, but still fostering an emphasized turbulent kinetic energy intensity, is the velocity gradient acting within the shear layer region. It represents the upper border of the low velocity region. Outside the weak velocity area, a horseshoe-shaped region of enhanced velocity magnitude spreading towards the pipe wall can be identified, characterized by a lower intensity of turbulence

production.

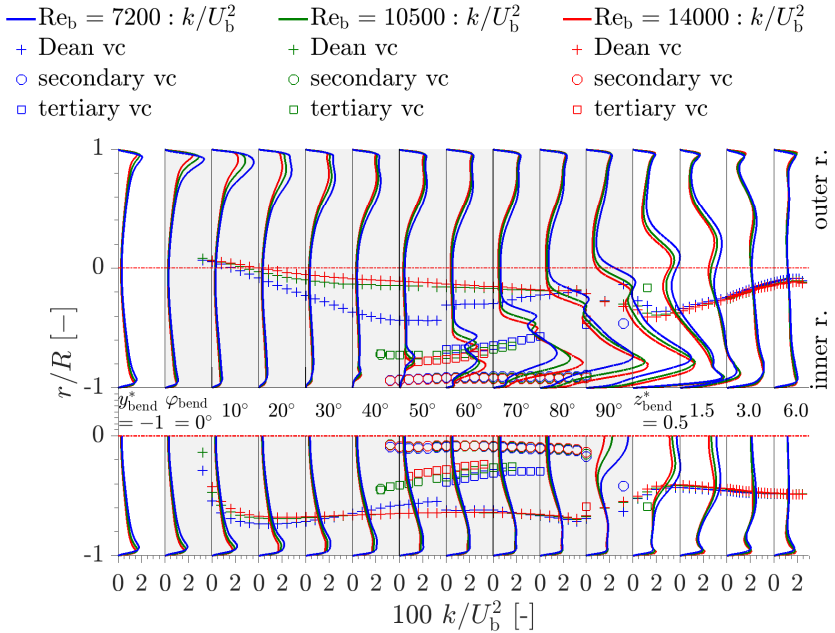


Figure 3.26.: Time-averaged turbulent kinetic energy k/U_b^2 at selected positions within the $y - z$ -symmetry plane (top) and in the plane perpendicularly, which coincides with the pipe symmetry axis $r/R = 0$ (bottom) for considered Reynolds numbers. The spatial evolution of the vortex centers are presented by symbols and the pipe bend region is highlighted in gray. The pipe center is marked by a red dash-dotted line.

In order to provide the basis for an in-depth discussion of the turbulent kinetic energy evolution with respect to the underlying vortex topology, Fig. 3.20 illustrates the evolution of the turbulent kinetic energy in the $y - z$ -symmetry plane as well as selected cross-sections. Complementary to the illustration, Fig. 3.26 depicts its profile development in the $y - z$ -symmetry plane (top)

and in the plane perpendicular to it (bottom), following the extraction scheme introduced with respect to Fig. 3.21. The kinetic energy is normalized by the square of the bulk velocity enabling a suitable mutual comparability of the results obtained at different Reynolds numbers.

The profile shapes are in a strong correlation with the development of the mean velocity field (Figures 3.20 and 3.21) and clearly reflect the effects of the underlying complex flow straining. Within the vertical straight pipe segment the profile exhibits a symmetrical shape featured by the near-wall peaks over the entire circumference, as it is typical for a fully developed pipe flow. The longitudinal curvature in the initial pipe bend portion up to $\varphi_{\text{bend}} \approx 30^\circ$ influences the profile shape of the turbulent kinetic energy with respect to the weak flow acceleration within its inner portion ($r/R = -1$) and deceleration within its outer portion occur ($r/R = 1$). It reflects a turbulence attenuation at the innermost pipe bend-wall and, concurrently, the peak enhancement related to the upper wall contour. This is in relation to the well-known effects of the longitudinal streamline curvature exerted on the flow from the 90° -pipe bend geometry. The rotation direction of the fluid elements concentrated closer to the lower bend wall (at $r/R = -1$) coincides with the global clockwise direction imposed to the flow by the 90° -pipe bend guidance. This so-called stabilizing curvature exercises a suppressing effect on the turbulence structures in this locality. Opposite to this behavior is the so-called destabilizing curvature originates from different rotating orientations between the global bend-relevant curvature and the counterclockwise rotation of the fluid elements populated closer to the outer bend-wall contour. It promotes the turbulence level intensification in this region. This enhancement can also be attributed to the centrifugal effects forcing the fluid elements towards the outer radius of the 90° -pipe bend resulting in a stagnation region with respect to the curvature-radial, normal-to-wall velocity component u_{cr} , which is in accordance with the formation process of the twin-like Dean vortex structures. The earlier discussed flow acceleration switch, whose onset coincides approximately with the shear layer formation at $\varphi_{\text{bend}} \approx 40^\circ$ (see Figures 3.20 and 3.21), implies the reversion of this flow situation. The presence of the longitudinal APG at the innermost wall contour (Fig. 3.23) additionally contributes to the incipient turbulence level increase.

The turbulent structures featured by the secondary and tertiary vortices and the correspondingly enhanced turbulence production is clearly visible from the

gradually rising peak of the turbulent kinetic energy within the $y-z$ -symmetry plane near the inner deflection radius ($r/R = -1$) (upper plot series in Fig. 3.26), downstream of the deflection angle of $\varphi_{\text{bend}} \approx 40^\circ - 50^\circ$. The spread of the shear layer region implies a continuous shift of the turbulent kinetic energy maximum towards the pipe-bend center with increasing deflection angle. At the 90°-pipe bend exit ($\varphi_{\text{bend}} = 90^\circ$), the profile maximum reaches the pipe center. This increase in turbulent kinetic energy is further visible at the relevant profiles within the plane running perpendicular to the pipe deflection along the bend symmetry axis ($r/R = 0$; lower scheme in Fig. 3.26), which is clearly in accordance with the axial velocity depression (Fig. 3.21). The position of the turbulent kinetic energy peak coincides with the spatial extension of the low velocity region, which is characterized by a strong velocity gradient within its fringe area as can be seen in Fig. 3.25. The line plots of the turbulent kinetic energy in the plane perpendicular to the $y-z$ -symmetry plane (lower scheme in Fig. 3.26) are characterized by a near-wall maximum (at $r/R = -1$), the plateau of which gradually spreads within the wall-proximity region. This area encompasses also the ring-shaped flow structure induced by the main Dean vortex appearing initially at the deflection angle of $\varphi_{\text{bend}} = 8 - 9^\circ$ according to the vortex identification methodology of Graftieaux et al. (2001).

The multilayered characteristics of the shear layer region, illustrated by an alternately varying cross-sectional velocity gradient, is furthermore demonstrated through the second peak at the turbulent kinetic energy profiles formed in the vicinity of the inner deflection radius at $\varphi_{\text{bend}} = 60^\circ$. This represents a consequence of the complex near-wall flow shearing representing the rationale of the turbulence production within this locality. The wall-related peak is significantly more pronounced than the turbulent kinetic energy peak situated within the core flow. The peak's radial position remains approximately constant and is near the vortex center of the secondary structure. The increase of this peak is accompanied by the local decrease of the friction coefficient related to the inner bend radius, which is associated with the gradual decay of secondary structures (see Fig. 3.24 and associated discussion). In correlation with the near-wall flow straining, the latter represents a driving mechanism for the turbulence enhancement. The turbulence activity intensification is mostly pronounced in the lowest Reynolds number case, which, indicated by the flow separation, exhibits the highest spreading rate of the shear layer domain. Contrary to that, the peak value of the lowest Reynolds number that

is located closer to the pipe center in Fig. 3.26 top and is related to the upper extent of the shear-layer region is somewhat lower.

3.5.8. Discussion: Evolution of the Dean vortex circulation

To conclude the discussion of the flow in the 90° -pipe bend, the circulation of the Dean vortex Γ_{Dean} will be considered in the following. The circulation of the vortex is obtained with the aid of the vortex identification methodology according to Graftieaux et al. (2001). With this methodology, the already discussed spatial evolution of the vortex structures is detected as shown in Figures 3.21 and 3.26. In accordance with the approach proposed by Graftieaux et al. (2001), the outer vortex boundary is identified by thresholding the Γ_2 scalar field with $\Gamma_2 = 2/\pi$. The search window size is set to 11, equal to Γ_1 -criterion. Subsequently, the circulation is obtained by integration of the circulation within the vortex boundary according to Stokes' theorem. The circulation evolution of the Dean vortex Γ_{Dean} is depicted in Fig. 3.27 top for the three considered Reynolds numbers over the deflection ($\varphi_{\text{bend}} = 0^\circ - 90^\circ$) and the outlet section ($z_{\text{bend}}^* > 0$). The life cycle of the secondary vortex structures, which are independent of the Reynolds number, is highlighted in gray, starting at $\varphi_{\text{bend}} \approx 48^\circ$ and disappearing at $z_{\text{bend}}^* \approx 0.1$.

The circulation within the deflection increases steadily from the first detection ($\varphi_{\text{bend}} \approx 9^\circ$ to 10°) and reaches a maximum in the range of $\varphi_{\text{bend}} \approx 80^\circ$, independent of the Reynolds number. A flattening of the increase can be seen with the appearance of the secondary vortex structures. Downstream of the maximum, the circulation decreases, which, according to the previous discussion, is consistent with the viscous dissipation of the Dean vortex, since the driving force of the circulation, the centrifugal force, is absent. The circulation evolution exhibits a consistent qualitative pattern independent of the Reynolds number. However, a proportionally higher circulation can be observed for higher Reynolds numbers. The considered Reynolds numbers differ only in the bulk velocity U_b , since the geometrical dimensions of the configurations are identical. Normalizing the circulation of the Dean vortex Γ_{Dean} with the associated bulk velocity U_b leads to coinciding curves (see dotted lines in Fig. 3.27 top), which indicates a direct proportionality of the Dean vortex circulation and the bulk velocity under the same geometrical conditions ($\Gamma_{\text{Dean}} \sim U_b$). Taking into account the proposed normalization

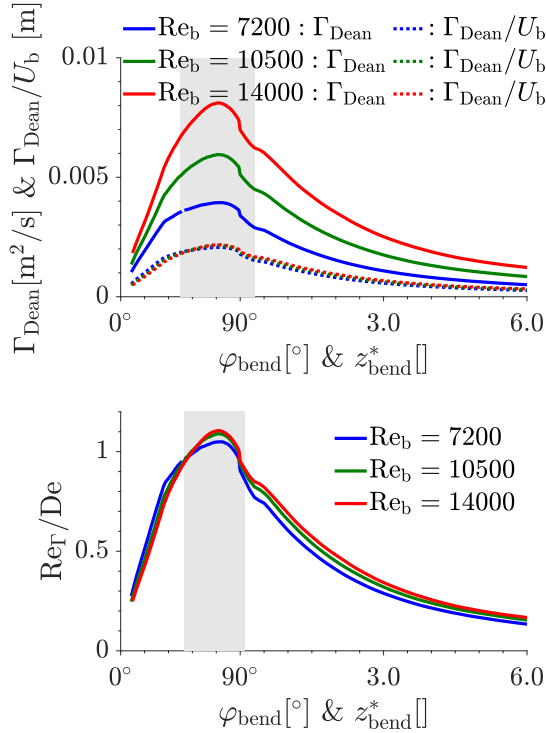


Figure 3.27.: Vorticity Γ_{Dean} (solid line) and a normlized vorticity by bulk velocity Γ_{Dean}/U_b (dotted line) of the Dean vortex (top) and vortex Reynolds number to Dean number ratio $\text{Re}_\Gamma/\text{De}$ (bottom) depicted over the deflection angle φ_{bend} and the outlet coordinate z_{bend}^* for the considered Reynolds numbers (color-coded). The spatial life-cycle of the secondary vortex structures are highlighted in gray.

Γ_{Dean}/U_b for the circulation evolution in comparison with the occurrence of the secondary vortex structures (highlighted in gray in Fig. 3.27), the initial formation of the secondary vortex structures is independent of the considered Reynolds number and can be observed for $\Gamma_{\text{Dean}}/U_b \approx 0.0019$. It should be noted that the proposed normalization with the bulk velocity leads to a

dimensional value, which presumably provides a sufficient normalization for the current study, but does not consider any geometric characteristics of the 90°-pipe bend nor does it allow for a geometrically generalized normalization. For a more general normalization, not only the bulk velocity U_b should be considered. The geometrical characteristics of the 90°-pipe bend with the pipe diameter D and the radius of curvature R_c should be taken into account as well. The Dean number De (see Eq. (3.1)) appears to be a suitable parameter, in which the geometric characteristics mentioned above as well as the pipe Reynolds number are combined. The circulation is usually normalized by the kinematic viscosity of the flow, which is denoted as vortex Reynolds number $Re_\Gamma = \Gamma/\nu$ in literature and allows to compare fluids of different viscosity with respect to vortex circulation. The ratio of the vortex Reynolds number to the Dean number Re_Γ/De seems to be a suitable normalization for the Dean vortex circulation evolution to satisfy the relevant flow characteristics and is depicted in Fig. 3.27 bottom for the considered three Reynolds numbers. A similar Reynolds number independent pattern can be observed as depicted by the dotted lines in Fig. 3.27 top. At a ratio of $Re_\Gamma/De = 0.95$, the origin of the secondary structures can be observed, which indicates the existence of a generalized threshold for the formation of secondary vortex structures in the present configurations. It should be mentioned explicitly that in the present study only the variation of the bulk velocity is investigated. In order to determine a possible general validity of the mentioned initiation threshold for secondary structure occurrence, an extension of the study with respect to geometric characteristics and fluid properties (kinematic viscosity ν) has to be carried out. An interpretation of the Re_Γ/De ratio is difficult due to the multitude of flow characteristics combined within the ratio. However, with respect to the formation mechanism of the secondary vortex structures and the detachment of the Dean vortex due to the arising circumferential APG, the ratio provides insights into the intensity of the emerging circumferential APG within the 90°-pipe bend configuration, where the flow seems to provoke a flow detachment and the formation of secondary vortex structures for $Re_\Gamma/De > 0.95$.

3.5.9. Conclusions & Outlook

The flow topology development within the isolated 90°-pipe bend has been investigated by applying well-resolved, highly comprehensive Large-Eddy Simulations (LES) over a range of bulk Reynolds numbers from $Re_b = 7200$ to 14000 with special focus on wall abrasive flow conditions and emerging vortex structures. The Γ_1 -criterion introduced by Graftieaux et al. (2001) was utilized to map the dynamics of vortices and track the vortex centers within the 90°-pipe bend. These studies were combined with analyses of the Γ_2 -criterion for circulation determination of the Dean vortex. Based on this, the origin of the formation of the vortices and their influence and relation to the flow's topological features were investigated and correspondingly related to technically relevant flow characteristics such as wall shear stress and turbulence intensity.

It was demonstrated that the aforementioned vortical motion, encompassing the mean Dean vortices and its associated tertiary vortices as well as a wall-bounded secondary vortices, affect the flow dynamics decisively within the 90°-pipe bend. Accordingly, this relates also to the near-wall characteristics of the flow, which are of direct relevance for erosive applications. The vortical topology is dominated by Dean vortices, which arise within the 90°-pipe bend due to the action of centrifugal forces. Within the bend, vortical structures gradually convect towards the side wall and the inner pipe wall due to a self-induced velocity, which intensifies progressively with the Dean vortices approaching the pipe wall. Subsequently, an APG develops at the wall eventually causing the flow separation in the inner bend region. The latter process is somewhat more pronounced in the lowest Reynolds number case. As a consequence of the wall-bounded separation, the secondary and tertiary vortices emerge at the inner deflection radius and disappear ultimately towards the 90°-pipe bend outlet. Qualitatively similar vortex topology evolution is observed for all three considered Reynolds numbers.

The application of the vortex identification methodology according to Graftieaux et al. (2001) also allowed a deeper insight into the vortex topology within the 90°-pipe bend in terms of the circulation evolution. The circulation evolution of the Dean vortex could be captured and discussed in detail, where a suitable normalization could be identified with respect to the Dean number and vortex Reynolds number. The developed normalization resulted in a comparable normalized circulation evolution for the present flow configurations,

where the emergence of the secondary vortex structures could be identified at a ratio of $Re_T/De = 0.95$ independent of the considered Reynolds number. This ratio has to be validated for geometric influences (pipe diameter D and the curvature radius R_c) and fluid properties (kinematic viscosity ν) in the future.

Keeping in mind the effects of the main Dean vortex and secondary vortices exert on the wall shear-stress and the close relationship to the flow topology, a minimization of erosion and boiling processes in relevant technical applications would be possible by an appropriate modification of the vortex topology. Besides the bulk velocity U_b and the pipe diameter D , the curvature radius R_c is a suitable choice for modifying the vortex topology in terms of altering the centrifugal force in the 90° -pipe bend. The proposed manipulation of the vortex and flow topology would require further investigations of the vortex properties to additionally quantify the underlying mechanisms, as, for example, enhanced turbulence generation within the deflection and increased passive mixing of the fluid are closely linked. Current considerations allowed to attribute the source of additional turbulence production to the decay of the secondary and tertiary vortical structures. Furthermore, a higher bulk Reynolds number is assumed to generate stronger vortical structures, leading to a comparatively higher turbulence production and to respective intensification of the passive mixing capability of the flow. A specific modification of vortex topology might also affect turbulence intensity and increase/decrease consequently the flow cooling rate.

3.6. Flow in a symmetric pipe T-junction: Inflow division

3.6.1. Introduction

The fluid flow guidance through arbitrarily configured pipe systems regularly encountered in technical practice is a highly complex engineering task, especially under non-isothermal conditions with respect to possible phase change events. The so-called burn-out effect can occur under critical thermal conditions and causes a high thermal load on the pipe walls resulting potentially in thermal fatigue cracking. Here, the driving force rationale for a phase change can have a cavitation or boiling background, as well as a mixed form of both. Furthermore, the flow straining in terms of wall shear stress has also to be taken into consideration, especially when an abrasive medium is present. These effects can strongly contribute to a wall degradation process reducing the pipe configuration functionality up to a total failure of the relevant technical applications. The provision of a fluid and its properties over a certain spatial area, as in heat exchangers, or the supply for simultaneously operating technical devices, as in the case of internal-combustion engines, requires a subtle division of a technical fluid into multiple streams continuing in different directions, which usually involves T-junction-shaped flow sections. The final constructive design of a T-junction configuration is mostly task-oriented and manufacturing-oriented, resulting in a diversity of technical configurations in terms of varying cross-sectional areas, regions of variably intersecting pipe segments and, subsequently, differently directed flow streams. Due to its high practical relevance, the flow structures in T-junction geometries have been subject of numerous past and current research studies. The focus of these investigations was rather on mixing of two flow streams than on the division of an inflow stream following its perpendicular impingement, as considered here in the following.

A commonly investigated T-junction configuration, reported intensively in the published literature, resembles the flow mixing within a straight pipe section, or a duct section, into which a fluid from a perpendicularly positioned supplying branch enters. Different T-junction configurations, in terms of flow rates, cross-sectional dimensions and structural flow properties, have been studied. For instance, a single-phase flow within a horizontal sharp-edged T-

junction with circular cross-section was experimentally investigated by Walker et al. (2009). A comparable configuration was observed numerically by Ayhan and Sökmen (2012) within a LES framework using different SGS models with focus on the thermal mixing characteristic of the flow topology. Adechy and Issa (2004) investigated the isothermal annular two-phase flow in a similar T-junction geometry, but with a continuous wall transition in the intersection from the secondary vertical branch into the main horizontal pipe characterized by a certain finite inner-wall radius, with the latter detail being existent also in the present work. An earlier work dealing with multiphase flow within T-junctions has been performed by Azzopardi and Whalley (1982), focusing on mixing characteristics depending on the two-phase flow pattern upstream of the T-junction. A more complex structure was observed by Tunstall et al. (2016), involving a 90°-pipe bend upstream of the T-junction. Flow and thermal fields, with the temperature regarded as a passive scalar, in T-junction configurations with rectangular cross-sections were the subject of the computational studies by Hattori et al. (2014) and Krumbein et al. (2018) by applying DNS and LES as well as a newly developed hybrid RANS/LES model, respectively.

The flow division within a T-junction-formed geometry is preceded by the flow impingement characterized by an intense flow-wall interaction, representing an alternating deceleration-acceleration event occurring under conditions of a strongly varying pressure gradient. Wall impingements are encountered in numerous engineering applications and a large number of experimental and computational works have been published. However, most of them consider single-jet impingement in a non-confined environment and provide detailed flow analysis. Manuscripts reviewing the research carried out on a single-jet impingement are contributed by Downs and James (1987), Jambunathan et al. (1992) and Webb and Ma (1995). An analytical study of the wall-shear stress response on an axis-symmetric jet-wall impingement onto a flat surface over a wide Reynolds number range was performed by Phares et al. (2000). Due to the circular flow cross-section considered in the present work, the flow impingement occurs on a concave surface. The influence of the complex three-dimensional streamline curvature effects on the flow topology representing the outcome of the impingement onto a concave-shaped wall has been studied by Gau and Chung (1991), G. Yang et al. (1999) and Sharif and Mothe (2010).

The investigations of a pipe-shaped T-junction with one inlet and two symmetrically arranged outlets are rare. The work of K. K. Chen et al. (2015)

has to be mentioned due to the similarity of the flow configuration compared with the T-junction configuration considered in the present chapter. They investigated the flow in a symmetric T-junction geometry with finite inner-wall radii, but with rectangular cross-section. Here, the inflow experiences an impingement and division towards the two symmetrically arranged outlets. The investigations were carried out at a inflow-based Reynolds number of $Re_b < 1000$ which is much lower than considered in the present chapter. Special attention is devoted in the paper to the influence of the finite inner-wall radius in comparison to configurations with sharp duct intersections. Furthermore, Bassett et al. (2001) discuss an analytically derived prediction of the pressure loss coefficient in differently shaped T-junction configurations with pipe-shaped cross-sections.

In contrast to the existing literature, the present study investigates a T-junction with a circular cross-section and finite inner-wall radii at the intersection regions. Thus, the symmetric division of a fully-developed pipe inflow along an edgeless smooth flow configuration is in the foreground of the consideration. For the present study, the structural topology of the flow and turbulence of an isothermal single-phase flow is studied within a pipe-constituted T-junction configuration relevant to cooling systems in IC engines with respect to the WSG, representing a corresponding reference test sample (see Fig. 3.1). The time-averaged flow characteristics including mean velocity and turbulence statistics are evaluated from the flow field obtained by a well-resolved, highly comprehensive LES. The interpretation of the results focuses on the three-dimensional mapping of the wall-shear and pressure distribution. Both represent suitable indicators for surface degradation effects as well as for possible thermal stresses. The latter is generally favored by low velocity regions acting beneficially towards a potential boiling onset. Accordingly, a fundamental understanding of the underlying flow structure is necessary with respect to the flow and vortex topology within the T-junction configuration. For this purpose, the vortex identification methodology according to Graftieaux et al. (2001) is applied, which allows for a comprehensive characterization of all vortical flow pattern and their development.

3.6.2. Computational domain

The T-junction configuration as the first geometrical component within the WSG is a double symmetric structure with an inlet and two outlets. The geometrical dimension of the T-junction corresponds to Table 3.1 with a pipe diameter of $D = 3.5$ mm and an inner radius in the transition between the individual pipe segments of $R_c = 0.5$ mm. A schematic illustration of the computational domain ($z - y$ - and $z - x$ -symmetry plane) can be seen in Fig. 3.28. In addition to the main region representing the T-junction, another separate region is provided, the precursor region. The precursor with length $l_{\text{pre}} = 2.5 D$ ensures a fully developed fluctuating pipe flow at the inlet of the T-junction. The fully developed fluctuating pipe flow is generated within the precursor via a periodic procedure, whereby the bulk flow is adjusted iteratively via the pressure gradient between the precursor inlet and outlet, and mapped instantaneously from the center section to the inlet of the T-junction. The inlet section of the T-junction as well as the outlet sections are provided with a length of $l_{\text{inlet}} = l_{\text{outlet}} = 8 D$, which has proven to be sufficient in an extensive grid study to ensure an undisturbed flow within the T-junction. For clarification, the cross-section shape along the T-junction's inner radius always remains circular along the inner radius with the pipe diameter D . Furthermore, in Fig. 3.28 three coordinates relevant for the flow discussion are defined with the angle along the inner radius φ_{TJ} , the outlet angle along the pipe curvature ψ_{TJ} and the corresponding outlet coordinate s_{TJ}^* . Quantities relevant for the T-junction are indexed with 'TJ'.

The flow conditions are related to the isothermal conditions within the cooling system of common IC engines as described in Chapter 3.1. The inlet conditions are set to $\text{Re}_b = U_b D/\nu = 14400$ with regard to the location of the T-junction within the WSG (see Fig. 3.1) and in accordance with Table 3.2. Considering the bi-section of the inlet volume flux and consequently of the Reynolds number in the outlet sections, a fully turbulent flow condition can be assumed within the entire computational domain.

The cell topology and its arrangement within the T-junction have a decisive influence on the quality of the results. A block-structured cell arrangement with a hexahedral cell topology is chosen due to its advantageous features within the numerical procedure. The entire computational domain including the precursor and the T-junction region consists of $n_{\text{total}} = 103564000$ cells, whereby attention is paid to a homogeneous cell structure within the T-junction.

3.6. Flow in a symmetric pipe T-junction: Inflow division

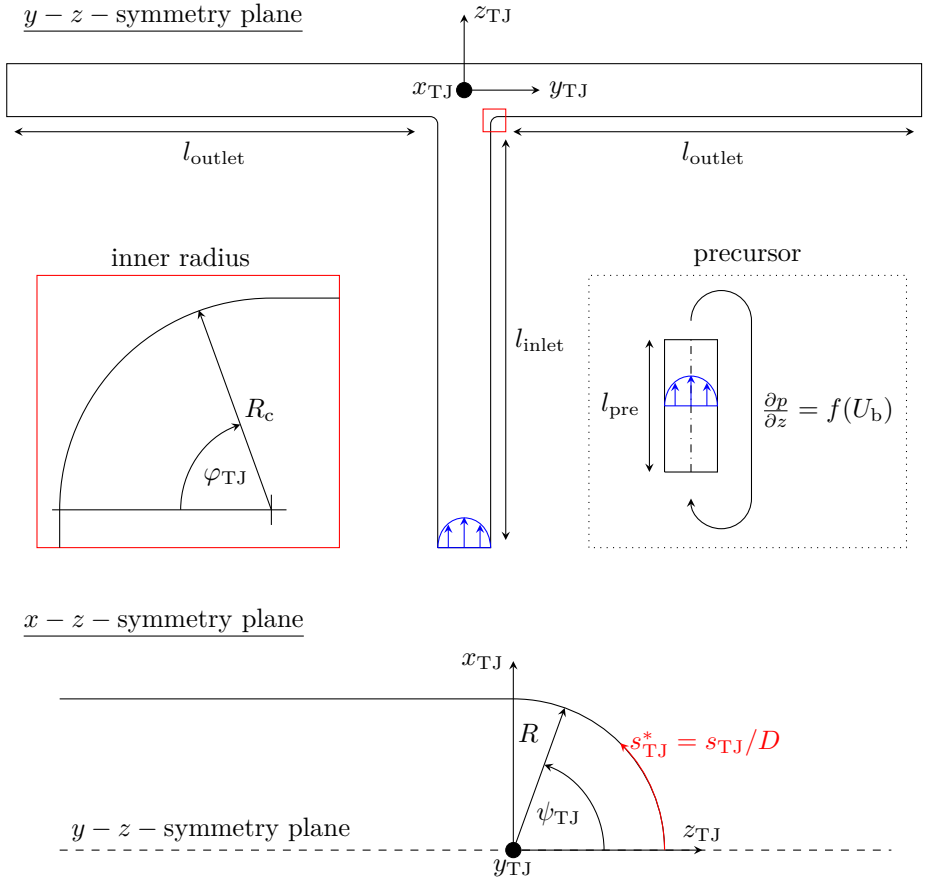


Figure 3.28.: Illustration of the computational domain ($y-z$ - and $z-x$ -symmetry plane) including the T-junction and precursor region. R describes the pipe radius, R_c the radius of the rounded inner radius and φ_{TJ} its angle, $l_{\text{inlet}} = l_{\text{outlet}} = 8 D$ the inlet and outlet length, $l_{\text{pre}} = 2.5 D$ the precursor length, ψ_{TJ} the outlet angle and s_{TJ}^* its coordinate.

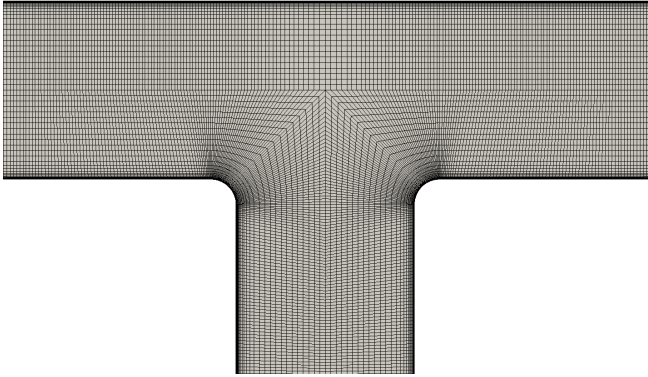


Figure 3.29.: Block-structured hexahedral grid of the T-junction. Only every fourth cell is shown to highlight the grid structure.

The meshed T-junction geometry is presented in Fig. 3.29, whereby only every fourth cell is shown to highlight the grid structure. An octagonal ‘O-grid’ arrangement over the cross-section is applied with a cell arrangement according to Chapter 3.3.

3.6.3. Discussion: First impression

For a first impression of the flow topology within the T-junction, the isocontours of the time-averaged velocity magnitude U/U_b are depicted in Fig. 3.30 for both symmetry planes denoted as $z-x$ - and $y-z$ -symmetry plane as well as several meaningful cross-sections along the outlet with the corresponding inplane velocity streamlines (CS1: $y_{TJ}^* = y_{TJ}/D = 0.64$, CS2: $y_{TJ}^* = 1.14$, CS3: $y_{TJ}^* = 2.14$). The cross-sectional plots display the isocontours of the bulk flow on the left-hand side and the time-averaged turbulent kinetic energy k/U_b^2 on the right-hand side. Symmetries of the T-junction are exploited by displaying just one half and the corresponding symmetry edges are marked with dashed lines. The vortex structures forming in the T-junction are investigated by means of the Γ_1 and Γ_2 criterion according to Graftieaux et al. (2001) (Γ_1 threshold = 0.95 and search window size = 11) and

the corresponding vortex center points are highlighted with magenta colored squares.

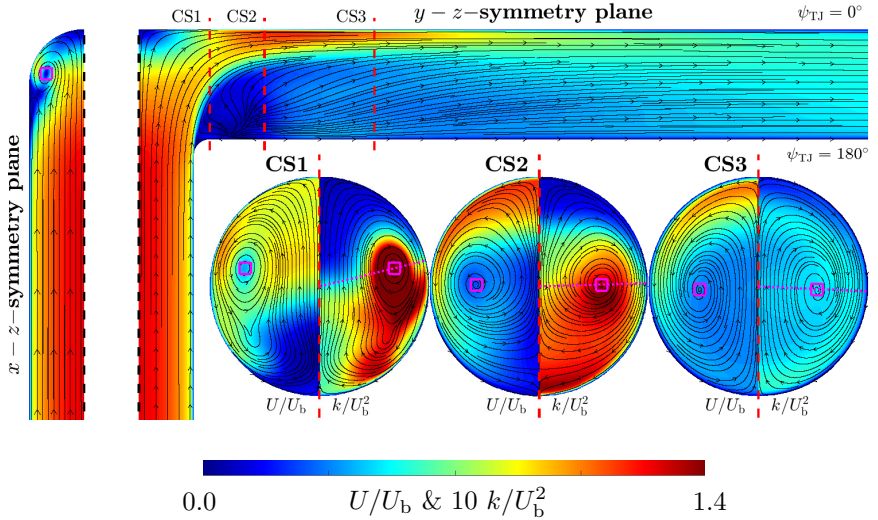


Figure 3.30.: Time-averaged velocity magnitude U/U_b and inplane streamlines within the $x - z$ - and $y - z$ -symmetry planes as well as selected cross-sections (CS1: $y_{TJ}^* = y_{TJ}/D = 0.64$, CS2: $y_{TJ}^* = 1.14$, CS3: $y_{TJ}^* = 2.14$). Latter also depict the turbulent kinetic energy k/U_b^2 . The depiction lines of Fig. 3.36 are marked by dotted magenta lines. and vortex centers by magenta squares. The visualized data are derived from averaging over the symmetry planes.

For clarification, the flow enters the domain via the bottom edge and leaves it via the right edge of Fig. 3.30. The unidirectional streamlines entering the T-junction experience a strong, three-dimensional curvature as a result of the impingement on the pipe-curved counter-wall as can be observed in the $x - z$ - and $y - z$ -symmetry planes. A part of the streamlines is deflected towards the outlet and experiences an acceleration, as can be detected from the red colored regions in the $y - z$ -symmetry plane for $y_{TJ}^* > 0.64$ (CS1)

as well as in the upper part of the cross-sections (around $\psi_{\text{TJ}} = 0^\circ$). The remaining streamlines are deflected along the curvature of the pipe-curved counter-wall, interact with the bulk inflow and roll up to a vortex structure, as evident from the streamline pattern around the magenta colored square in the $x - z$ -symmetry plane. The resulting vortex structure is clearly visible in the cross-sections downstream of the T-junction (see CS1, CS2 and CS3 in Fig. 3.30), suggesting the formation of a counter-rotating vortex tube pair with regard to the symmetric flow configuration. The vortex centers correlate with the regions of increased turbulent kinetic energy, whereby the position of the vortex centers varies along the outlet coordinate y_{TJ}^* .

Before the streamlines are deflected due to the impingement on the pipe-curved counter-wall, they pass the finite inner radius of the T-junction. The continuous shape of the inner radius results in the formation of an adverse pressure gradient (APG). Following the streamlines closest to the wall in the inlet section ($y - z$ -symmetry plane), they cannot follow the shape of the inner radius, which indicates a flow detachment due to the APG. Downstream of the inner radius, a region of low velocity is formed, which extends over a large part of the pipe diameter within the $y - z$ -symmetry plane and reduces the effective cross-section of the bulk flow. The latter seems to supply the described flow acceleration downstream of the impingement. Within the region of low velocity, a complex streamline pattern occurs including a streamline source, which indicates a strong three-dimensional flow character within this region. The region of low velocity is also visible in the bottom region of the cross-sections (around $\psi_{\text{TJ}} = 180^\circ$) in terms of a reduced velocity magnitude and increased turbulent kinetic energy.

Apart from the impingement and the flow detachment, a pronounced tendency towards homogenization of the flow in the cross-sections can be recognized. The clear differences in the cross-sections with respect to the velocity magnitude and turbulent kinetic energy are almost no longer detectable within the cutting plane CS3 (at $y_{\text{TJ}}^* = 2.14$).

Because of the multitude of flow phenomena within the T-junction, a step-by-step consideration of the individual phenomena will be carried out in the following analyzing the formation of the counter-rotating vortex tube pair around the flow impingement and the flow detachment in the T-junction inner radius separately. Finally, considerations will be combined in the context of the entire T-junction geometry. This is supposed to allow for a better

understanding of cause-effect relations of individual phenomena and their interaction.

3.6.4. Discussion: Impingement and vortex tube pair formation

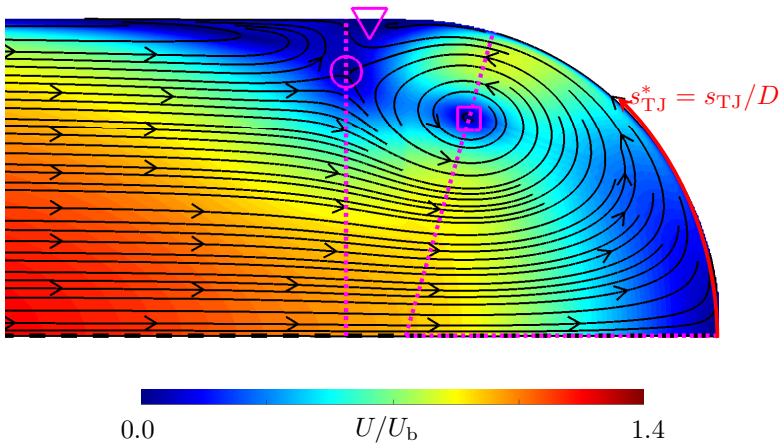


Figure 3.31.: Enlarged sectional view of the $x - z$ -symmetry plane with the isocontours of the velocity magnitude field U/U_b and the corresponding in-plane streamlines depicted. The depiction lines for Fig. 3.33 are marked by dotted magenta lines. Saddle points in the flow are marked by a circle, vortex center according to the Γ_1 -criterion by a square and an saddle-point-related wall impingement by a triangle. The visualized data are derived from averaging over the symmetry planes.

The flow impingement on the pipe-curved counter-wall and the formation of the counter-rotating vortex tube pair are two of the most obvious flow phenomena within the T-junction geometry. Therefore, their origin and effect on the flow will be discussed below being a key parameter to identify

regions prone to erosive or thermal stresses on the wall in terms of wall shear stress or regions of low velocity magnitude. As illustrated in Fig. 3.30, the pipe-curved counter-wall provokes a three-dimensional flow structure resulting in counter-rotating vortex tube pairs. The corresponding region within the $x - z$ -symmetry plane around the impingement is shown enlarged in Fig. 3.31 to allow for a detailed investigation of the flow topology along the pipe-curved counter-wall. Topological key characteristics such as the vortex center, the saddle point and a saddle-point-related wall impingement, are marked by a magenta-colored square, circle and triangle, respectively. For clarity, the outlet coordinate $s_{TJ}^* = s_{TJ}/D$ has its origin in the center of impingement and follows the curvature of the pipe-curved counter-wall and further the straight inlet section within the $x - z$ -symmetry plane. An indicator for regions of increased boiling probability can be identified from the pressure field for which the pressure coefficient relative to the outlet pressure $C_p = (p - p_{\text{outlet}}) / (0.5\rho U_b^2)$ can be used as depicted in Fig. 3.32 top. Note that the coefficient is referenced to a global flow indicator to be comparable with pressure levels at other locations within the T-junction.

A stagnation point exists in the center of impingement at $s_{TJ}^* = 0$, which can be recognized by a peak of the pressure coefficient (see Fig. 3.32 top). Around the stagnation point, a region of low velocity magnitude can be observed, which represents a critical point with regard to the thermal stress in case of heated walls. The deflected flow is continuously accelerated along the curved surface due to an increasing negative pressure gradient along the wall in positive s_{TJ}^* direction ($\partial C_p / \partial s_{TJ}^* < 0$ for $s_{TJ}^* > 0$). At $s_{TJ}^* = \pi/4$ in Fig. 3.31, the flow in the upper vortex region is directed against the main bulk inflow, leading to the formation of a saddle point, which is highlighted by a magenta-colored circle. At this point, the fluid is deflected towards the pipe wall or entrained by the bulk inflow. Fluid, which is entrained by the bulk inflow forms a circulation zone with its rotation center marked by a magenta-colored square in Figure 3.31. This circulation zone represents the origin of the counter-rotating vortex tube pair described above and observed in Fig. 3.30. The fluid which is deflected in direction of the pipe wall impinges and causes a further stagnation point on the wall (see magenta triangle in Fig. 3.31). This impingement can be observed by a local maximum of the pressure coefficient in Fig. 3.32 top at $s_{TJ}^* \approx 0.1 + \pi/4$. Upstream and downstream of the stagnation point, near-wall jets exist and are directed against the outer flow. Due to low

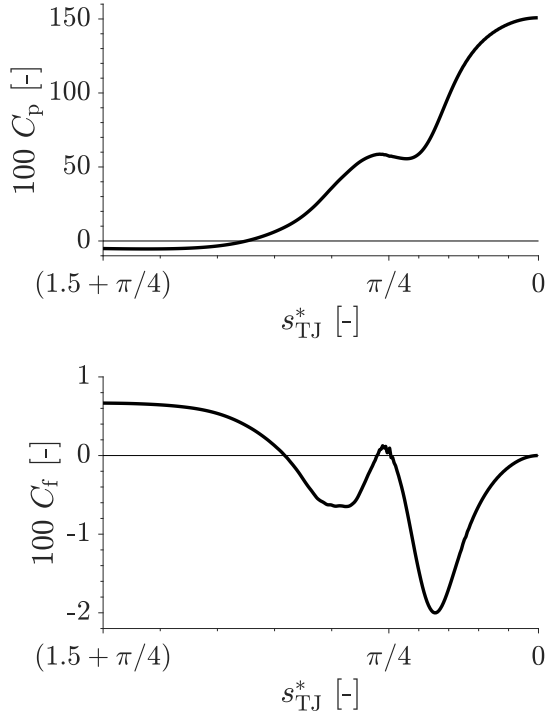


Figure 3.32.: Pressure coefficient related to outlet pressure $C_p = (p - p_{\text{outlet}}) / (0.5\rho U_b^2)$ (top) and friction coefficient $C_f = \tau_w / (0.5\rho U_b^2)$ (bottom) over $s_{TJ}^* = s_{TJ}/D$ within the $x - z$ -symmetry plane.

velocity magnitude in the proximity of the wall, this stagnation point could represent an additional region of high thermal stresses.

To further elaborate effects of flow topology on the pipe wall, the wall shear stress and the corresponding friction coefficient $C_f = \tau_w / (0.5\rho U_b^2)$ is analyzed. It is depicted along s_{TJ}^* within the $x - z$ -symmetry plane in Fig. 3.32 bottom. Along s_{TJ}^* , the friction coefficient has four zero crossings indicating a change of sign of the wall velocity gradient and consequently a change of flow direction.

The zero crossing at $s_{TJ}^* = 0$ is a result of the impingement on the pipe-curved counter wall while the other three crossings can be attributed to the flow topology around the saddle point observed with respect to Fig. 3.31. The friction coefficient decreases for $s_{TJ}^* > 0$ and reaches a minimum at $s_{TJ}^* \approx 0.55$, where the counter rotating vortex tube pair seems to be closest to the pipe wall as evident from Fig. 3.31. Additional characteristics of the friction evolution in terms of a minimum and maximum next to the saddle point and the secondary wall impingement can be observed around the zero-crossing at $s_{TJ}^* \approx 0.1 + \pi/4$, caused by the secondary-wall-impingement-related near-wall flow jets. Further towards the inlet of the T-junction, for $s_{TJ}^* > 0.219 + \pi/4$, the friction coefficient increases again, caused by an increasing wall velocity gradient due to the bulk inflow, which in turn leads to the zero crossings at $s_{TJ}^* \approx 0.55 + \pi/4$. However, the emergence of a counter rotating vortex tube pair and a saddle-point-related wall impingement dominate the wall friction with two pronounced negative friction peaks and presumably also possible erosive processes.

Based on considerations of the flow topology and near-wall characteristics examined above, a quantitative evaluation of flow characteristics within the geometry will be conducted in the following. This will be done with the aid of the velocity and turbulent kinetic energy profiles depicted in Fig. 3.33. Specifically, the impingement, vortex formation and the saddle point region are extracted along the magenta dotted lines in Fig. 3.31. Due to the consideration of the velocity evolution within the $x - z$ -symmetry plane of the T-junction (Fig. 3.33 top), a split of the velocity into two components (wall-tangential velocity u_t and wall-normal velocity u_n) is sufficient. The position of impingement ($s_{TJ}^* = 0$) corresponds to a double symmetry position ($x - z$ - and $y - z$ -symmetry plane), in which only a wall-normal velocity component exists.

The normal velocity component along the impingement position corresponds to the bulk inflow ($u_n/U_b(r/R) = 1$) and decays to zero towards the wall. Due to the one-component velocity field and the continuous decrease of the flow velocity with a moderate velocity gradient, the turbulent kinetic energy around the center of impingement ($k/U_b^2(r/R > 0.6)$) is only slightly increased compared to the center of the quasi undisturbed inflow ($k/U_b^2(r/R = 0)$). However, the impingement region is not a source of increased turbulent production. For $s_{TJ}^* > 0$, the fluid is deflected from the impingement along the pipe-curved counter-wall and a tangential near-wall jet exists according to the negative

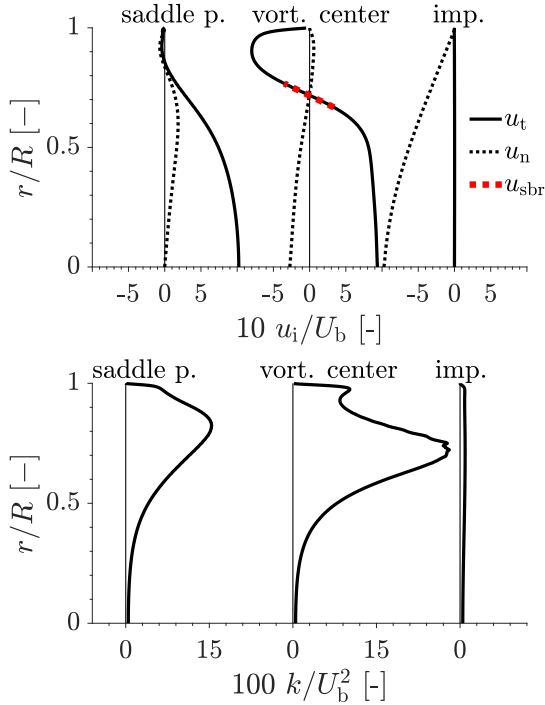


Figure 3.33.: Normalized wall-normal u_n/U_b and tangential velocity u_t/U_b extractions (top) and normalized turbulent kinetic energy k/U_b^2 extractions (bottom) according to dashed lines in Fig. 3.31. **Red dotted line** represents the solid body rotation velocity u_{sbr}/U_b .

tangential velocity for $r/R > 0.7$ along the extraction line through the vortex center in Fig. 3.33 top. Due to the acceleration of the fluid caused by the negative pressure gradient along the curvature (compare Fig. 3.32 top), the velocity magnitude of the tangential near-wall jet reaches a magnitude comparable to the bulk inflow ($|u_t(r/R \approx 0.9)| = 0.8 U_b$). Caused by the tangential near-wall jet, a high wall velocity gradient exists, which leads to the corresponding negative wall shear stress peak discussed with respect to the friction coefficient in Fig. 3.32 bottom. The wall tangential and normal

velocity components have a zero crossing at $r/R \approx 0.7$, which represents the position of the center of the vortex tube ($r_{vc} \approx 0.7 R$). The evolution of the tangential velocity around the vortex center shows a linear slope with respect to the radial distance to the vortex center $r_{sbr} = |r - r_{vc}|$, corresponding to the theory of solid body rotation. Based on the theory of solid body rotation, an estimation of the rotation rate of the vortex tube Ω_{sbr} and its circulation Γ_{sbr} can be done with the assumption that the circumferential velocity follows $u_{sbr} = \Omega_{sbr} r_{sbr}$ for $r_{sbr}/R < 0.1$. The circumferential velocity u_{sbr} is highlighted in Fig. 3.33 top by a red dotted line and is equal to the tangential velocity component, which clearly shows a solid body rotational characteristic of the vortex. According to a linear approximation, the rotation rate of the vortex tube is $|\Omega_{sbr}| \approx 9160$ 1/s and the corresponding circulation approximation of the vortex tube is $\Gamma_{sbr} = 2\pi|\Omega_{sbr}|(0.1R)^2 \approx 0.00176$ m²/s. To validate the analytical circulation approximation, the vortex tube circulation is determined by means of vortex identification according to the methodology introduced by Graftieaux et al. (2001) from the Γ_2 scalar field with a threshold of $2/\pi$. With a measured circulation of $\Gamma_{sbr} \approx 0.0016$ m²/s, the deviation between analytical solid body rotation and measured circulation is less than 10 %, which allows to infer that the vortex tubes represent solid body rotational objects in terms of secondary recirculation zones caused by the impingement. Higher values of the wall normal velocity component for $r/R < 0.7$ along the vortex center extraction line can be attributed to the orientation of the extraction line with respect to the bulk inflow. The corresponding extraction of the turbulent kinetic energy in Fig. 3.33 bottom shows an enhanced turbulence production in the region of the vortex tube as well as the tangential near-wall jet. The position of the higher turbulent kinetic energy peak corresponds to the vortex center with $r = r_{vc} \approx 0.7 R$. The symmetry of the peak is related to the vortex tube and its constant circumferential velocity gradient. Consequently, the vortex tube is one of the key mechanisms for the turbulence production within the T-junction.

Velocity extractions through the saddle point show that the bulk inflow is orthogonal to the extraction line and therefore the tangential velocity at $r/R = 0$ corresponds to the bulk inflow velocity. The saddle point itself can be identified by the zero crossing of both velocity components at $R_{sp} \approx 0.85 R$. Fluid entrainment towards the bulk flow can be identified by the positive wall-normal velocity component for $r < R_{sp}$ and fluid directed towards the pipe

wall by the negative wall-normal velocity for $r > R_{sp}$. Turbulent kinetic energy production is also enhanced in the region of the saddle point as evident from the turbulent kinetic energy peak at $r = R_{sp}$ in Fig. 3.33 bottom. Similar to the vortex tube, the saddle point represents an additional source for turbulent mixing.

3.6.5. Discussion: Flow detachment and formation of a recirculation zone

Before the flow impinges on the pipe-curved counter-wall, it enters the T-junction and passes the rounded inner radius of the T-junction. This radius is strongly curved, which leads to flow detachment of the incoming fluid as evident from the $y - z$ -symmetry plane depiction in Fig. 3.30. As a consequence of flow detachment, a region of low velocity magnitude exists downstream of the inner radius towards the outlet. From illustrated streamlines within the low velocity region, it can be observed that fluid enters the $y - z$ -symmetry plane since streamlines emerge in this region. The emerging fluid stems from the main impingement on the pipe-curved counter-wall after which a part of the fluid is directed along the pipe wall. Towards the outlet, the fluid, which is deflected along the pipe wall, collides with its symmetrical counterpart. This can also be observed in cross-sections displayed at CS2 ($y_{TJ}^* = 1.14$) around $\psi_{TJ} = 180^\circ$ in Fig. 3.30 where streamlines disappear. At the location of collision in the $y - z$ -symmetry plane, a singularity exists, which represents a saddle point. From this saddle point, the emerging fluid is directed radially in the $y - z$ -symmetry plane and the part of fluid directed from the saddle point towards the T-junction inlet is entrained by the main inflow again. The region around the inner radius, where a flow detachment is present and causes the formation of a low velocity region downstream, is a sensitive region with respect to thermal stresses and erosion processes since the inlet and outlets are connected here by welding or other methods in technical realizations. Therefore, flow topology around the inner radius will be discussed in the following to better understand the origin of observed wall-induced flow effects as well as potential boiling and friction phenomena.

An enlarged view of the flow topology around the inner radius in the $y - z$ -symmetry plane is shown in Fig. 3.34. Displayed in-plane streamlines reveal a backflow from the saddle point towards the T-junction inlet from the

3. IC-engine-relevant cooling channel configuration: Water Spider Geometry (WSG)

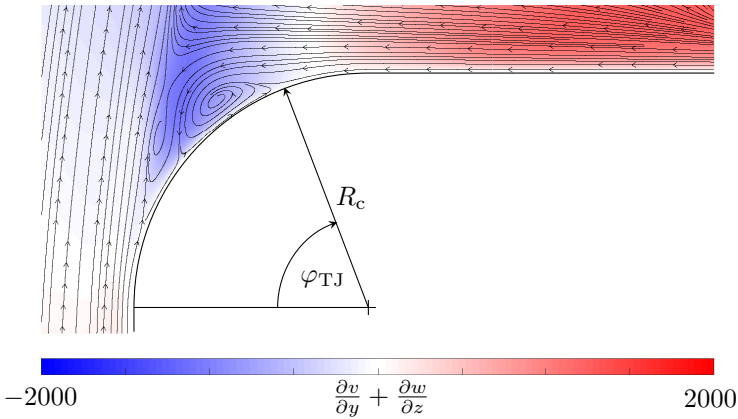


Figure 3.34.: Enlarged view of the inner radius of the T-junction within a slight offset to the $y - z$ -symmetry plane with the two dimensional velocity divergence $\frac{\partial v}{\partial y} + \frac{\partial w}{\partial z}$ displayed in color as well as the inplane streamlines. The visualized data are derived from the averaging over the symmetry planes.

right border ($\varphi_{TJ} = 90^\circ$) to the T-junction inflow from the bottom border ($\varphi_{TJ} = 0^\circ$). The two-dimensional divergence of the v and w velocity component with a slight offset to the $y - z$ -symmetry plane is indicated by the coloring to investigate three-dimensional effects based on continuity. Here, white regions represent a two-dimensional flow topology. Within blue and red colored regions, the continuity is not fulfilled according to the sum of v and w gradients, where the red regions indicate a fluid source and the blue regions a fluid sink. The backflow from the saddle point reaches the T-junction inflow and is deflected in a three-dimensional manner, which is evident from the negative sum of the velocity gradients in Fig. 3.34 coloured in blue. Although the backflow experiences a strong deflection, the inflow remains quasi unaffected, which can be attributed to a significantly larger velocity magnitude of the inflow and consequently its momentum (compare Fig. 3.30). With respect to the streamlines in Figures 3.30 and 3.34, the majority of the backflow is deflected in the direction of the inflow and out of the $y - z$ -symmetry plane. However,

a deflection also occurs in the direction of the T-junction radius, resulting in a vortex topology with two counter-rotating vortices. Here, the vortex towards the outlet is the larger one. The formation of the vortex topology around the T-junction radius is presumably caused by an additional impingement of the deflected streamlines on the wall of the T-junction inner radius. In the following, a focus will be put on the wall-induced flow effects of the prescribed topology in terms of friction and potential regions of boiling around the inner radius.

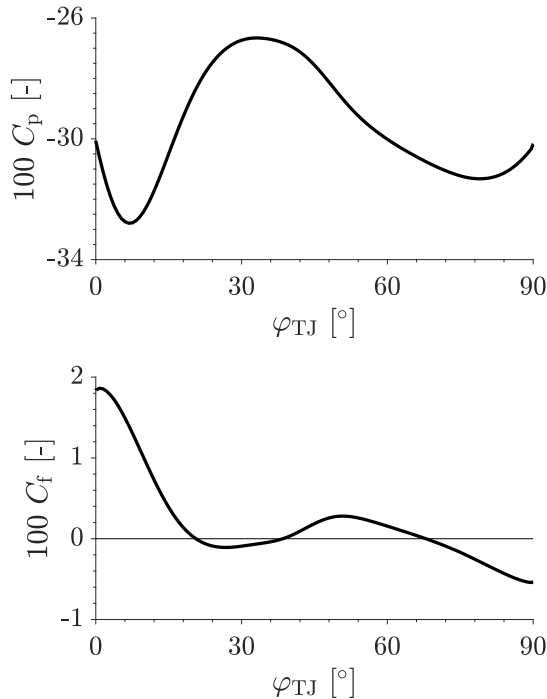


Figure 3.35.: Pressure coefficient related to outlet pressure $C_p = (p - p_{\text{outlet}}) / (0.5\rho U_b^2)$ (top) and friction coefficient $C_f = \tau_w / (0.5\rho U_b^2)$ (bottom) along the T-junction radius over φ_{TJ} within the $y - z$ -symmetry plane.

The flow detachment around the T-junction radius occurs almost immediately after the curvature begins, which can be seen from the first zero crossing of the friction coefficient along the T-junction radius at $\varphi_{TJ} = 20^\circ$, depicted in Fig. 3.35 bottom. Here, the friction coefficient is extracted along the inner radius wall within the $y - z$ -symmetry plane. The flow detachment is accompanied by a strong decrease of the the friction coefficient and experiences two changes of sign in the following, caused by the vortex topology shown in Fig. 3.34. The negative friction coefficient for $\varphi_{TJ} > 70^\circ$ occurs in the region of backflow from the saddle point towards the inflow, discussed with respect to Fig. 3.34. Compared to evaluations of the wall-shear stress in other regions of the T-junction, the shear stress on the wall in the radius of the T-junction is lower. However, due to the vortex topology, alternating shear stresses are induced along the radius in terms of alternating wall-tangential compression and extension. With respect to technical applications and a possible connection variant such as welding, this alternating load has to be considered.

The evolution of the local pressure in terms of the pressure coefficient along the T-junction inner radius in the $y - z$ -symmetry plane in Fig. 3.35 top is in accordance with the zero crossings of the friction coefficient and reflects effects of the observed flow topology. Here, the pressure coefficient is again related to the outlet pressure to allow for a global consideration of the pressure level. A significant maximum pressure drop to $C_p \approx -0.33$ around the T-junction inner radius at about $\varphi_{TJ} = 20^\circ$ can be observed, which is very low compared to other regions of the considered geometry (compare Fig. 3.32 for example). The local pressure drop represents a decrease of pressure towards the vapor pressure, which indicates an increased tendency for phase change around the T-junction inner radius. A cavitation event as well as a boiling phenomenon or mixed forms are potential consequences, which are accompanied by additional friction stresses.

3.6.6. Discussion: Outlet section

Besides the flow detachment around the inner T-junction radius, the main impingement of the inflow on the pipe-curved counter-wall and the associated development of the counter-rotating vortex tube pairs as well as their decay towards the outlet dominate the investigated flow configuration. Characteristics

of vortex tube pairs in the outlet section, corresponding vortex topology and induced effects on pipe walls are subject of the following discussion.

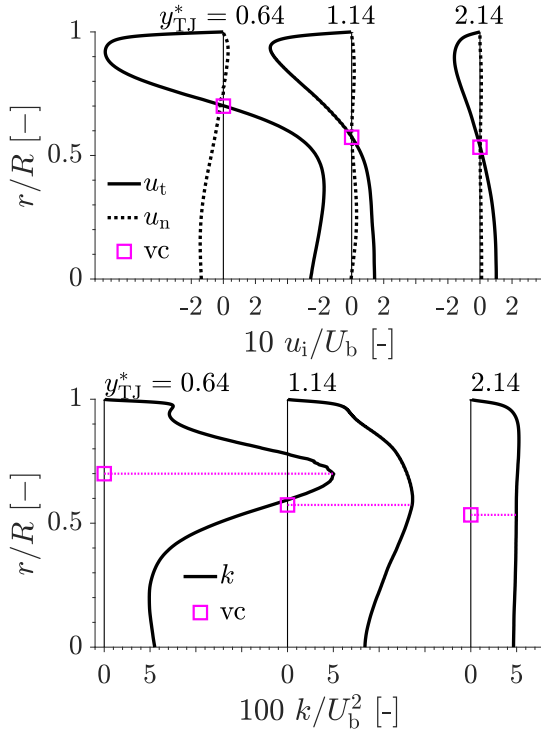


Figure 3.36.: Normalized wall-normal u_n/U_b and tangential velocity u_t/U_b extractions (top) and normalized kinetic turbulent energy k/U_b^2 extractions (bottom) according to magenta dotted lines at the cross-section in Fig. 3.30. The position of the vortex center (vc) are represented by magenta squares.

The illustrated streamlines in Fig. 3.30 show a two-sided character for $y_{TJ}^* > 0.64$ (position of CS1 in Fig. 3.30) in the $y-z$ -symmetry plane in terms of high velocity magnitude on the counter-wall and low magnitude on the wall associated with the inner radius of the T-junction. Corresponding magnitude

differences tend to equalize downstream towards the outlet. The rotational sense of the counter-rotating vortex tubes enhances the convective exchange between the low and high velocity regions (compare velocity magnitude color-coding in cross-sections CS1 ($y_{TJ}^* = 0.64$) to CS3 ($y_{TJ}^* = 2.14$) in Fig. 3.30). Due to the dominating counter-rotating vortex tube pair in the outlet section, their evolution also dominates the corresponding wall-induced effects. The in-plane velocity evolution of the vortex tube pairs in the outlet section is depicted in Fig. 3.36 top to investigate the solid body rotational character of the vortex tube core downstream of its origin ($x - z$ -symmetry plane, compare Fig. 3.33 top). The wall-normal and tangential velocity profiles are depicted from the pipe center at $r/R = 0$ through the corresponding vortex center ($u_t = 0$) to the pipe wall at $r/R = 1.0$. The tangential velocity component at the depicted positions have a qualitatively similar shape compared to the 'vortex center' extraction shown in Fig. 3.33 top. This can be identified by a negative near-wall velocity peak, zero crossing at the vortex center, and a relatively constant tangential velocity up to the pipe center. The tangential velocity, which is approximately equal to the circumferential velocity of the vortex tubes, decreases towards the outlet $y_{TJ}^* > 0.64$ while the vortex center convects to the center of the pipe. The decaying tangential velocity might be related to a viscous decay of vortex tubes from the initially solid body rotational character, discussed with respect to Fig. 3.33 top. The solid-body rotational character of the vortex tubes can also be observed from the tangential velocity at $y_{TJ}^* = 0.64$ around the zero crossing. The linear velocity slope around the zero crossing disappears for $y_{TJ}^* > 0.64$, probably due to a viscous decay. The wall-normal in-plane velocity component is significantly lower than the tangential velocity, similar to the 'vortex center' extraction in Fig. 3.33, and disappears for $y_{TJ}^* > 0.64$, which suggests a purely wall-tangential in-plane velocity component towards the outlet.

To further investigate the vortex tube evolution towards the outlet and a potential viscous decay of them, vortex identification according to Graftieux et al. (2001) is considered to identify the vortex border with a threshold of $\Gamma_2 = 2/\pi$ and search window size of 11, extract its area and derive its radius by $r_{\text{vortex}} = \sqrt{A_{\text{vortex}}/\pi}$. The vortex radius evolution along the outlet section (y_{TJ}^*) is depicted in Fig. 3.37 top normalized by the pipe radius R . Starting from the $x - z$ -symmetry plane $y_{TJ}^* = 0$, a nearly constant vortex radius with $r_{\text{vortex}}/R = 0.25$ can be observed, which is related to the formation

process around the impingement onto the pipe-curved counter-wall and the solid body rotational character of the vortex tube pairs. The radius and thus the cross-sectional area occupied by the vortex tubes in the outlet increases significantly immediately after entering the outlet section for $y_{TJ}^* > 0.8$ with a peak value close to $r_{\text{vortex}} = 0.5$ around $y_{TJ}^* \approx 2$. This evolution corresponds to a spatial expansion of the vortex tubes approximately over the entire outlet cross-section for $y_{TJ}^* > 1.5$. The spatial expansion of the vortex tubes between $y_{TJ}^* = 0.8$ to 5.14 can be probably related to the abstinence of the vortex formation mechanism within the T-junction (impingement onto the pipe-curved counter-wall and saddle-point formation) and the associated spatial focusing of the vortex tubes.

The impact of the counter-rotating vortex tube pair on the flow field is strongly related to its circulation Γ as a characteristic quantity of vortex intensity. The evolution of the circulation of one of the vortex tubes in the outlet section is depicted in Fig. 3.37 bottom, extracted according to the above mentioned methodology. With a circulation of $\Gamma \approx 0.0016 \text{ m}^2/\text{s}$ at the $x - z$ -symmetry plane ($y_{TJ}^* = 0$) the circulation remains nearly constant for $y_{TJ}^* < 0.4$, which corresponds to a constant vortex radius in this range. For $y_{TJ}^* > 0.4$, the circulation of the vortex tubes decreases until circulation dissipates at $y_{TJ}^* = 5.34$. The latter represents the last spatial position where the vortex identification methodology according to Graftieux et al. (2001) detects inplane vortices. This suggests the disappearance of the counter-rotating vortex tube pairs at $y_{TJ}^* = 5.34$. The decrease of circulation from $y_{TJ}^* > 0.4$ occurs concurrent with the decrease of tangential inplane velocity (see Fig. 3.36) and the expansion of the vortex tubes (see Fig. 3.37 top) and supports the observation of viscous vortex decay.

The vortex tube pairs significantly enhance the turbulence production within the flow of the T-junction, as discussed in Fig. 3.33 bottom and their decay has a significant influence on the turbulent characteristics of the flow and correspondingly for mixing characteristics in the outlet section. Similar to Fig. 3.36 top, the turbulent kinetic energy k along the magenta dotted lines at cross-sectional positions of Fig. 3.30 is depicted in Fig. 3.36 bottom. The turbulent kinetic energy at the entrance to the outlet section ($y_{TJ}^* = 0.64$) has a comparable shape to the corresponding 'vortex center' extraction in Fig. 3.33 with a symmetrical peak around the vortex center and a local near-wall peak. Shortly after the entrance into the outlet section ($y_{TJ}^* = 1.14$), the peak of the

3. IC-engine-relevant cooling channel configuration: Water Spider Geometry (WSG)

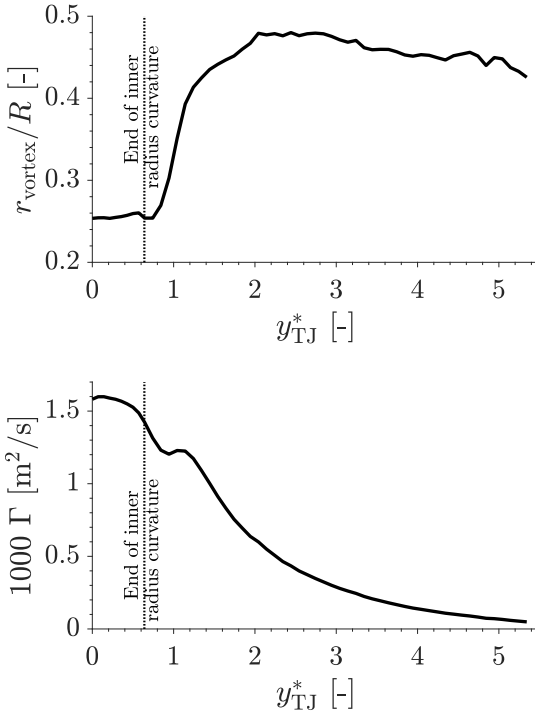


Figure 3.37.: Evolution of the vortex tube pair radius related to the pipe radius r_{vortex}/R (top) and its circulation Γ (bottom) along $y_{TJ}^* = y_{TJ}/D$ in the outlet section. Vortex tube radius is detected by the Γ_2 criterion according to Graftieux et al. (2001) with a threshold of $\pi/2$ and search window size of 11.

turbulent kinetic energy in the vortex center is reduced and a more distributed turbulent kinetic energy can be observed in radial direction. The equalization of the turbulent kinetic energy is even more evident at $y_{TJ}^* = 2.14$, where the peak in the vortex center is no longer detectable and the radial distribution is almost constant implying a termination of turbulence production by the vortex tubes. This evolution can also be attributed to the viscous decay of

the vortex pair.

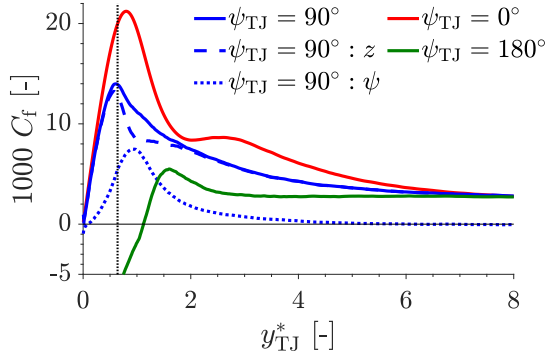


Figure 3.38.: Friction coefficient $C_f = \tau_w / (0.5\rho U_b^2)$ along selected lines in the outlet section over $y_{TJ}^* = y_{TJ}/D$. The solid lines corresponds to the magnitude of the friction coefficient at the intersection between the counter-wall and the $y - z$ -symmetry plane ($\psi_{TJ} = 0^\circ$, red), the extension of the considerations in Figure 3.35 bottom ($\psi_{TJ} = 180^\circ$, green) and the bottom of the outlet section ($\psi_{TJ} = 90^\circ$, blue). For the latter, the components in outlet direction (dashed line) and circumferential direction (dotted line) are depicted. The end of the inner radius curvature is marked by a black dotted line ($y_{TJ}^* = 0.64$).

The corresponding shear stress on the pipe wall in the outlet section will be evaluated in the following with the aid of the friction coefficient C_f , with the knowledge of the flow phenomena already described and the aim of assessing their influence on wall abrasive damage. C_f is shown for selected positions along the outlet coordinate y_{TJ}^* in Fig. 3.38. Here, $\psi_{TJ} = 0^\circ$ (red) describes the intersection of the $y - z$ -symmetry plane with the counter-wall and $\psi_{TJ} = 180^\circ$ (green) the extension of Fig. 3.35 bottom into the outlet section as defined in Fig. 3.28. For both, a component-wise splitting is not considered due to the location of the extraction lines within the $y - z$ -symmetry plane. In order to capture the effects of the vortex tube pairs, the friction coefficient is also shown along the T-junction bottom of the outlet section ($\psi_{TJ} = 90^\circ$, blue) with the corresponding components in outlet direction (dashed line) and circumferential direction (dotted line) as well as its magnitude (solid line).

Frictional forces along the counter-wall ($\psi_{TJ} = 0^\circ$, blue) are very small in the center of the main impingement $y_{TJ}^* = 0$ due to the present stagnation point. A pronounced increase of the friction coefficient for $y_{TJ}^* > 0$ up to a peak values of $C_f = 0.022$ at $y_{TJ}^* \approx 0.8$ can be observed, which can be related to the deflection of the streamlines and acceleration of the flow discussed with respect to Fig. 3.30. From the peak value at $y_{TJ}^* = 0.8$ on, the friction coefficient decreases continuously, which is interrupted by a plateau between $y_{TJ}^* = 2$ and 3.0. The plateau occurs at the location of the largest spatial expansion of the vortex tubes (see Fig. 3.37 top) and is presumably related to the vortex evolution within the outlet section. Within the $y - z$ -symmetry plane, downstream of the T-junction inner radius and in extension of evaluations in Fig. 3.35 bottom ($\psi_{TJ} = 180^\circ$, green), a negative friction coefficient occurs for $y_{TJ}^* < 1.1$. This can be related to the backflow from the saddle point discussed earlier and visible in Fig. 3.34. An additional local wall impingement, associated with the saddle point, causes a zero crossing of the friction coefficient at $y_{TJ}^* = 1.1$. For $y_{TJ}^* > 1.1$, friction effects on the wall increase further and reach a local peak of $C_f = 0.005$ at $y_{TJ}^* = 1.6$, after which the friction coefficient continuously decreases towards the outlet. The overall friction coefficient along the bottom of the T-junction outlet section ($\psi_{TJ} = 90^\circ$, solid blue) increases for $y_{TJ}^* > 0$, which is mainly due to the friction component in the direction of the outlet $C_{f,z}$ (blue dashed line) and can be related to the main impingement. The increase results in a peak at $y_{TJ}^* \approx 0.6$. The circumferential component of friction, indicated by the blue dotted line, allows to investigate vortex tubes effect onto the pipe wall due to the mainly circumferential in-plane characteristics discussed in Fig. 3.36 top for $y_{TJ}^* > 0$. It is important to notice that bottom extractions are influenced by the saddle point near the $x - z$ -symmetry plane, illustrated in Fig. 3.31. This hinders a clear separation of flow topology effects of the circumferential friction component around the $x - z$ -symmetry plane. However, further downstream towards the outlet, the circumferential friction increases and can be attributed mainly to vortex tube induced effects due to the rotational sense of the vortex tubes. This leads to a circumferential friction peak of $C_{f,\psi} \approx 0.0075$ at $y_{TJ}^* = 0.95$, which coincides with the strong spatial expansion of the vortex tubes around this range in conjunction with a comparably high circulation (see Fig. 3.37 top & bottom). Further downstream of the peak, the circumferential friction decreases rather fast, which is an indicator for the influence of the viscous decay of the vortex

tubes. As a preliminary conclusion, it can be said that although wall friction in the outlet section is dominated by the main-impingement-related wall-next flow acceleration, induced effects from the vortex tubes around the T-junction outlet ($y_{TJ}^* = 0.64$, black dotted line in Fig. 3.38) are not negligible and should be taken into account when designing technical applications.

3.6.7. Conclusion and outlook

The investigated isolated T-junction configuration is an industrially highly relevant geometry, especially due to the rounded inner radius with respect to manufacturing techniques such as welding. In view of the limited studies of comparable flow configurations, the flow characterization is carried out using a well-resolved, highly comprehensive Large-Eddy Simulation (LES) with the focus on shear stresses and regions that are potentially sensitive to enhanced thermal stresses as well as possible boiling and cavitation events. In addition to the flow and turbulence fields, the vortex topology within the T-junction configuration is examined with utilizing the vortex identification methodology according to Graftieaux et al. (2001). The latter allows to capture essential vortex-induced flow mechanisms and corresponding relations to wall-induced flow characteristics.

Besides a highly three-dimensional flow impingement onto the pipe-curved counter-wall, a complex vortex topology exists and dominates especially the turbulent production within the T-junction. Relevant vortex structures are a counter-rotating vortex tube pair of initially solid body rotational nature, which can be detected up to $4.7D$ ($y_{TJ} = 5.34 D$) downstream of the T-junction in the outlet sections. The strongest impact of the detected vortex pairs onto the flow topology in terms of flow acceleration and shear stresses can be detected around the T-junction outlet ($y_{TJ}^* \approx 0.64$) due to the spatial expansion of the vortex tube pairs. Both, the increased turbulence production and the additional wall shear stress in circumferential direction decreases to the outlets and indicates the viscous decay of the vortex tubes downstream of the T-junction flow guidance.

The rounded inner T-junction radius and the associated adverse pressure gradient (APG) on its wall cause a flow detachment at the inner radius and the formation of a low velocity region downstream. The detachment is accompanied by a low pressure level and a strong tendency for phase change in this region.

3. IC-engine-relevant cooling channel configuration: Water Spider Geometry (WSG)

The wall shear is rather low, but due to the vortex topology in the inner radius, consisting of two counter-rotating vortices, an alternating load is induced, which can be relevant and critical with respect to the manufacture-related connection variant. The low velocity region downstream of the inner T-junction radius is characterized by a significantly reduced convection rate and thus is critical with respect to thermal load and boiling events. Similar regions with reduced convective transport are the impingement center as well as the additional saddle-point-related wall impingement formed by the deflection along the pipe-curved wall within the $x - z$ -symmetry plane.

Critical locations in the T-junction could be identified with respect to potential erosion and formation of hot spots, and the underlying relationship between flow topology and wall-induced effects could be determined. For further investigations, the modification of the inner radius is recommended, since it represents a critical position especially with regard to the flow separation and the pressure level. A variation of the pipe diameter could also be of interest to selectively influence the formation of the vortex topology with the counter-rotating vortex tube pair. Furthermore, the investigations were conducted only at one volume flux, which suggests a future parameter study to investigate the influence of the inflow bulk Reynolds number on the flow topology.

3.7. Flow in a symmetric pipe T-junction: Confluence of two streams

3.7.1. Introduction

The confluence of flows can be found in numerous technical applications as well as in nature in a multitude of forms. In technical applications, the mixing process of fluids is generally the focus of interest, although the motivation of flow mixing can be fundamentally different. An essential motivation is the mixing of technical fluids to ensure a desired physical property that satisfies the requirements of a technical process. A prominent example is fuel mixing within liquid-fueled rocket engines. Another motivation is the targeted merging of used technical fluids, such as the heated coolant downstream the cooling region, for efficient reprocessing and re-injection into the technical application. A third example can be found in the food industry, where various ingredients have to be mixed in order to obtain a final product. Besides the technical applications, confluence of fluids are ubiquitous and essential to life in nature, the latter especially targeting biological organisms and their hematological system. But also the wide-spread river system on earth with numerous delta formations provides an insight into the ubiquity of flow confluence. Especially the mentioned examples of nature are motivation for numerous scientific investigations. In this context, an in-depth insight into arterial flow characteristics is intended to provide an advantage in diagnosis and prevention of diseases such as the formation of aneurysms. An example is the blood supply of the human brain through the basilar artery, which is formed by a confluence of two vertebral arteries and was investigated in detail by Ravensbergen et al. (1995) within a numerical framework. The Reynolds number present in such arteries is of the order 10^2 , whereby symmetric and asymmetric inflow conditions were examined. The investigation of the basilar artery was extended by consideration of the influence of the inlet angle of the inflow in Ravensbergen et al. (1996). Another field of research represents the confluence of rivers and its flow as well as sedimentation characteristic downstream. Early work in the field can be found from Mosley (1976) and Roy et al. (1988). The former work investigated the flow characteristics of confluent rivers using y-shaped model channels and the latter performed corresponding measurements using a real river confluence. Constantinescu et al. (2011)

explored the three-dimensional flow topology within a river confluence using a scale-resolving numerical framework. To capture the turbulent structures, the Detached-Eddy Simulation (DES) concept with the Spalart Allmaras (SA) one-equation model as SGS model as well as the SA one equation model within a RANS framework were applied. The scale-resolving detection of the flow field enabled an improved agreement with experimental reference data compared to RANS and provided a deeper insight into the turbulent structures, which are difficult to capture experimentally.

The flow confluence discussed in the following represents a symmetrical, pipe-shaped T-junction with finite inner radii in the transition region of the pipe segments, denoted as reverse T-junction. The mentioned configuration has the identical geometrical shape as the T-junction configuration discussed in Chapter 3.6, with the exception of a switched inlet/outlet arrangement. Thus, a similar literature integration would also be appropriate, but is avoided in the present chapter to prevent duplication and reference is made accordingly to the introduction of the T-junction (see Chapter 3.6.1). With respect to the present pipe-shaped reverse T-junction, the work of Ando et al. (2014) and Oka and Ito (2005) should be mentioned, which determined the energy and pressure loss in sharp-edged pipe-shaped T-junction configurations under various symmetrical and asymmetrical flow conditions, as well as different angles of the outlet pipe segment. The confluence of flows is manifold and can adopt a wide variety of forms as briefly illustrated above. The investigation of the flow topology in pipe-shaped confluences is very limited and will therefore be the focus of the following discussion. The present chapter deals with the flow topology of the isothermal single phase flow within a pipe-shaped reverse T-junction configuration relevant to the cooling system of IC engines with respect to the WSG (see Fig. 3.1). The time-averaged flow characteristics including mean velocity and turbulence statistics will be considered as well as vortex characteristics, based on the vortex identification methodology according to Graftieux et al. (2001), to identify and characterize the topological flow mechanism within the reverse T-junction. Special attention is paid to the shearing and abrasive flow phenomena with the wall friction and pressure evolution as appropriate indicators. A unique feature is the finite inner radius around the transition of the inlet to outlet pipe segments, which considers manufacturing-related joining techniques. Due to this realistic geometry, the resulting flow topology around the inner radius can be straightforwardly

incorporated to the design process of such flow guides.

3.7.2. Computational domain

The pipe-shaped reverse T-junction is a double-symmetrical configuration and contains two inlets and one outlet. The geometrical dimensions of the reverse T-junction corresponds to Table 3.1 with a pipe diameter of $D = 3.5$ mm and an inner radius in the transition between the individual pipe segments of $R_c = 0.5$ mm. The inlet and outlet sections are designed to ensure an unaffected flow insight the reverse T-junction by the inlet and outlet patches. These correspond to $l_{\text{inlet}} = l_{\text{outlet}} = 8 D$. Schematic illustrations of the symmetry planes of the computational domain are shown in Figures 3.39 ($x-z$ -symmetry plane) and 3.40 ($y-z$ -symmetry plane). Three coordinates relevant for the following flow discussion are introduced in the schematic illustrations, the inlet angle φ_{rTJ} , the outlet angle ψ_{rTJ} , and the outlet coordinates $s_{\text{rTJ}}^* = s_{\text{rTJ}}/D$. Quantities relevant for the reverse T-junction are indexed with 'rTJ'.

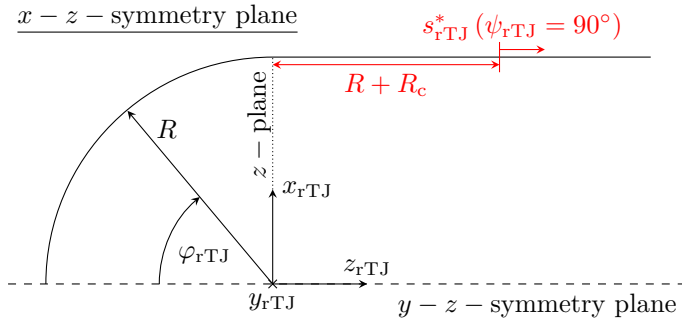


Figure 3.39.: Illustration of the computational domain ($x-z$ -symmetry plane) of the reverse T-junction. φ_{rTJ} describes the inlet angle and $s_{\text{rTJ}}^* = s_{\text{rTJ}}/D$ the outlet coordinate.

Besides the reverse T-junction configuration, the computational domain consists of two further regions, the so-called precursors. The precursors have a length of $l_{\text{pre}} = 2.5 D$ according to Chapter 3.3.3 and guarantee a fully developed pipe flow at both inlets. The fluctuating, fully developed pipe flow

3. IC-engine-relevant cooling channel configuration: Water Spider Geometry (WSG)

$y - z -$ symmetry plane

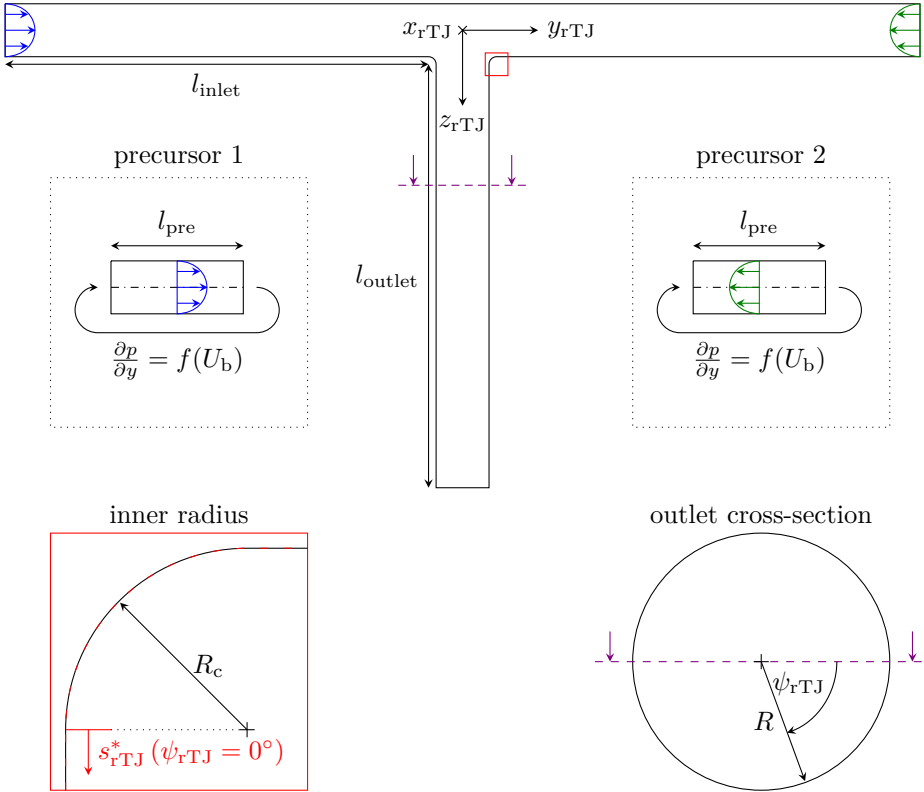


Figure 3.40.: Illustration of the computational domain ($y - z$ -symmetry plane) including the reverse T-junction and both precursor regions. R_c describes the inner radius, $l_{inlet} = l_{outlet} = 8 D$ the inlet and the outlet length, $l_{pre} = 2.5 D$ the precursor length, ψ_{rTJ} the outlet angle and $s_{rTJ}^* = s_{rTJ}/D$ the outlet coordinate.

is generated by a periodic procedure, whereby the volume flux is iteratively adjusted via the pressure gradient and mapped from the center cut of the precursor onto the inlets. To enable independently fluctuating inflows, each inlet is provided with one precursor to avoid any correlation of the inflows.

Due to the location of the reverse T-junction within the entire WSG (see Fig. 3.1), the inlet conditions are consistent with the conditions in the deflections and the bulk Reynolds number at the inlets is $Re_p = Re_{\text{deflection}} (\dot{V} = 2.2 \text{ l/min}) = 7200$. The applied numerical grid with a total number of hexahedral cells $n_{\text{total}} = 107921145$ is identical to that of the T-junction presented in Chapter 3.6.2, except for the double precursors.

3.7.3. Discussion: First impression

For a first insight into the flow topology within the reverse T-junction, the iso-contours of the time-averaged velocity magnitude with the inplane mean streamlines is illustrated in Fig. 3.41. Meaningful slices have been chosen with the two symmetry planes of the geometry ($x - z$ - and $y - z$ -symmetry plane) and the vertical cut through the inlet section ($x - y$ -plane). Symmetries of the reverse T-junction, indicated by dashed black lines, are exploited and only one half is shown. For orientation, the flow enters the geometry via the bottom edge and leaves it via the right edge of the illustration. Besides a general flow visualisation, Fig. 3.41 serves to repeat the origin of two coordinates. The inlet coordinate $y_{\text{rTJ}}^* = y_{\text{rTJ}}/D$ which points from the $x - z$ -symmetry plane towards the inlet patches and the outlet coordinate $s_{\text{rTJ}}^* = s_{\text{rTJ}}/D$ which points from the end of the inner radius curvature to the outlet.

The inflow (bottom edge) experiences an increasing streamline curvature the closer it is to the $x - z$ -symmetry plane, which can be seen especially in the $y - z$ -symmetry plane by means of the streamline curvature. By reaching the $x - z$ -symmetry plane, the flow collides with its symmetrical counterpart and deflects. This impingement can be observed within all three planes by the streamline curvature, with the exception of the $x - z$ -symmetry plane. In the latter, the impingement forms a streamline source from which streamlines spread out in all directions. The streamline characteristics emphasize the three-dimensional character of the impingement with the corresponding formation of a saddle point in the center of the inflow impingement. The streamlines, deflected from the saddle point towards the wall, experience an additional

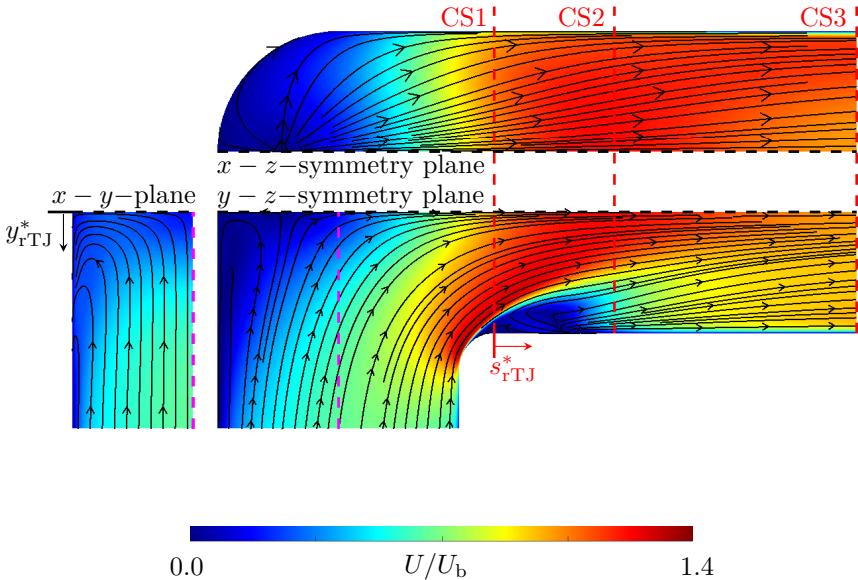


Figure 3.41.: Iso-contours of the velocity magnitude U/U_b within the $x-y$ -plane (bottom left), the $x-z$ - (top) and $y-z$ -symmetry plane (bottom right) of the reverse T-junction with the inplane mean streamlines. The coordinates $y_{rTJ}^* = y_{rTJ}/D$ and $s_{rTJ}^* = s_{rTJ}/D$ are marked for clarity. The locations of cross-sections shown in Fig. 3.42 are marked with CS1 ($s_{rTJ}^* = 0.0$), CS2 ($s_{rTJ}^* = 0.5$) and CS3 ($s_{rTJ}^* = 1.5$). The visualized data is derived from averaging over the symmetry planes.

impingement at the pipe wall. The wall impingement also causes a three-dimensional streamline deflection, which can be observed in the streamlines closest to the wall in all three planes. While the wall deflected streamlines within the $x-z$ -symmetry plane are deflected towards the outlet section, a backward curvature of the streamlines towards the inlet can be observed

in the $y - z$ -symmetry plane and $x - y$ -plane. The backward curvature of the streamlines and associated near-wall backflow towards the inlet is hereinafter referred as streamline roll-up. The streamline roll-up extends over the $y - z$ -symmetry plane and $x - y$ -plane, whereby a qualitative variation in streamline evolution is evident. The roll-up evolution and its influence onto the flow downstream will be addressed in the course of the discussion.

Away from the flow topology and streamline deflection around the inflow impingement and the emerging saddle point, an additional flow characteristic is visible around the rounded inner radius of the reverse T-junction. The rounded inner radius presents a smooth and finite transition between the inlet and outlet pipe segments, which prevents a geometry-induced fixed flow detachment location. However, the inner radius is relatively sharp in comparison to the pipe diameter, which results in a rapid cross-sectional expansion. An acceleration of the inflow as well as strongly curved streamlines can be observed around the inner radius, which can be seen from the red colouring and streamline shape near the inner radius within the $y - z$ -symmetry plane in Fig. 3.41. The wall closest streamline cannot follow the wall curvature of the inner radius and departs from the wall after approximately 60° direction change, which indicates a flow detachment event. Downstream of the observed detachment event, a low velocity region is visible with a complex three-dimensional streamline pattern. Numerous streamlines start within the low velocity region, indicating a $y - z$ -symmetrical flow impingement. Considering the streamlines downstream of the inner radius, the bulk flow has to swerve the region of low velocity, which leads to a reduction of the effective bulk flow cross-section and consequently a bulk flow acceleration, evident from the red colored region between the red dashed lines noted as CS1 and CS2 in Fig. 3.41.

To illustrate the streamline roll-up and its effects downstream of the reverse T-junction in the outlet region ($s_{\text{rTJ}}^* > 0$), selected cross-sections are shown in Fig. 3.42, where CS1 ($s_{\text{rTJ}}^* = 0$) corresponds to the start of the outlet region according to the definition of the outlet coordinate s_{rTJ}^* in Fig. 3.39 and 3.40. In these cross-sections, the iso-contours of the time-averaged velocity magnitude U/U_b (left side) and turbulent kinetic energy k/U_b^2 (right side) as well as the in-plane streamlines are shown to assess the cross flow. Additionally, vortex centers are highlighted by magenta colored squares for the right upper quarter. These are determined with the aid of the Γ_1 criterion (threshold 0.95 and search window size 11) proposed by Graftieaux et al. (2001). The vortex centers are

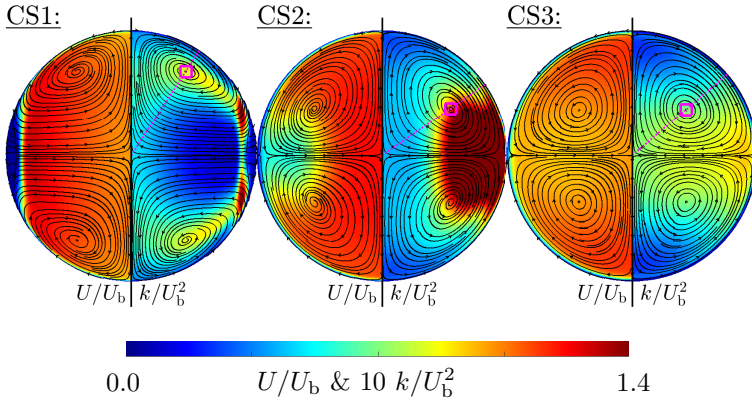


Figure 3.42.: Normalized velocity magnitude U/U_b and turbulent kinetic energy k/U_b^2 on selected cross-sections in the outlet section (CS1 ($s_{rTJ}^* = 0.0$), CS2 ($s_{rTJ}^* = 0.5$) and CS3 ($s_{rTJ}^* = 1.5$)) with the inplane mean streamlines. For clarification of the spatial location of the cross-sections within the reverse T-junction, see Fig. 3.41. The visualized data are derived from averaging over the symmetry planes.

representative for the three remaining quarters and can be reproduced via mirroring on the symmetry axes. For orientation within Fig. 3.42, the left and right outer regions of the cross-sections represent the wake of the inner radius of the reverse T-junction. Due to the double symmetrical character of the reverse T-junction, the flow is discussed within one quarter for simplicity. However, to clarify the flow topology, the entire cross-section is shown.

Considering the depicted inplane streamlines, a roll-up of streamlines can be recognized. Here, the streamlines follow the $y-z$ -symmetry plane towards the pipe center, are deflected along the $x-z$ -symmetry plane and subsequently deviate along the pipe wall. The described streamline pattern corresponds to the roll-up direction of the streamlines in Fig. 3.41, suggesting that the streamline pattern within the cross-sections is a result of the streamline roll-up originating from the symmetrical inflow impingement. The double-symmetrical streamline pattern within the cross-sections, consisting of four

vortices rotating in opposite directions to their neighbors, is preserved in its structure downstream and can be observed in all three cross-sections shown in Fig. 3.42. Although the general vortex topology is preserved downstream, the shape changes. A shift of the vortex center can be observed, which continuously moves to the $x-z$ - and $y-z$ -symmetry plane. Concurrently, the streamlines density especially near the wall for CS1 ($s_{rTJ}^* = 0$) is reduced and becomes more uniform over the radius towards CS3 ($s_{rTJ}^* = 1.5$). A direct interaction of the velocity magnitude and the vortex topology is not evident from Fig. 3.42, but the vortex center within CS1 ($s_{rTJ}^* = 0$) corresponds to a local peak of the turbulent kinetic energy. Further downstream, the match of a local peak of the turbulent kinetic energy and the vortex center can no longer be unambiguously assigned. The vortex center convects along the pipe surface into the suspected wake region of the inner radius and the effects of both are superimposed. In the last cross-section presented (CS3), the vortex center clearly does not correspond to any region of increased turbulence and the observed turbulence-increasing effect of the vortex center in CS1 has disappeared.

The effects of the flow topology around the inner radius can be seen in both, the velocity magnitude as well as the turbulent kinetic energy. Both fields indicate extrema in the outer right and left borders of the cross-sections. According to the characteristic of a flow separation and the discussed flow topology shown in the $y-z$ -symmetry plane (Fig. 3.41), a region of low velocity can be recognized by the deep blue color within CS1 ($s_{rTJ}^* = 0$). This region weakens rapidly and is only faintly visible within CS3 ($s_{rTJ}^* = 1.5$). The turbulent kinetic energy exhibits a significant increase in contrast to the velocity field. Highest values can be observed within CS2 ($s_{rTJ}^* = 0.5$), which extends over almost half the pipe radius. Analogously to the velocity field, the enhancement of the turbulent kinetic energy is hardly identifiable within CS3 ($s_{rTJ}^* = 1.5$). The disappearance of the velocity and turbulent kinetic energy peaks from CS1 ($s_{rTJ}^* = 0$) to CS3 ($s_{rTJ}^* = 1.5$) could be an indication of pronounced cross-sectional secondary motion and a strong flow equalization tendency downstream of the reverse T-junction and thus a result of the double symmetrical vortex topology.

Superficially seen, the flow topology within the reverse T-junction is dominated by two characteristics, the inflow-impingement-related saddle point and the resulting streamline roll-up as well as the flow separation around the inner radius and the formation of a low velocity region downstream. Both charac-

teristics are discussed in detail in the following, with focus on possible flow phenomena such as boiling and cavitation and particularly strong wall stresses caused by the flow itself. In addition, the cross-sectional flow equalization tendency in the outlet section is also discussed with special attention to the influence of vortex topology and flow detachment.

3.7.4. Discussion: Saddle point and roll-up

The double-symmetric vortex topology in the outlet section appears to be a driving force of rapid flow equalization downstream of the reverse T-junction, evident from the streamline pattern and pronounced cross-sectional secondary motion in Fig. 3.42. For a deeper understanding of this mechanism, knowledge of the root-cause for the vortex topology is crucial. As discussed in Figures 3.41 and 3.42, the origin of the vortex topology seems to be the streamline roll-up around the saddle point. The backflow towards the inlets, associated with the streamline roll-up, results in a change of sign of the near-wall velocity gradient. Accordingly, the friction coefficient is considered for an initial assessment of the backflow expansion. With respect to the streamlines illustration in Fig. 3.42, the roll-up expands differently in the $y - z$ -symmetry plane and $x - y$ -plane due to the three-dimensional character of the flow. Considering the latter, the y_{rTJ}^* -friction coefficient $C_{f,y}$ is depicted in Fig. 3.43 top along the inlet coordinate $y_{rTJ}^* = y_{rTJ}/D$ for different circumferential positions in the inlet φ_{rTJ} . Here, $\varphi_{rTJ} = 0^\circ$ represents the intersection of the wall and the $y - z$ -symmetry plane in the inlet section and $\varphi_{rTJ} = 90^\circ$ the corresponding intersection of the wall with the $x - y$ -plane as defined in Fig. 3.39. The inner region of the reverse T-junction, starting with the curvature of the inner radius, is highlighted in gray.

The inflow is directed in the opposite y_{rTJ}^* direction towards the $x - z$ -symmetry plane ($y_{rTJ}^* = 0$), which explains the constant, negative $C_{f,y}$ value at $y_{rTJ}^* = 2$ independent of φ_{rTJ} . Based thereon, a consistent increase in the friction coefficient can be observed with a zero-crossing and a peak close to the $x - z$ -symmetry plane at $y_{rTJ}^* = 0.13$. Due to the $x - z$ -symmetry plane, the friction coefficient vanishes at $y_{rTJ}^* = 0$. The positive excursion of the friction coefficient seems to be related to the streamline roll-up and the backflow towards the inlets. The zero-crossing of the friction coefficient, which implies a change of sign in the wall velocity gradient and thus indicates the

flow direction closest to the wall, is suitable for assessing the spatial expansion of the backflow. The most intensive (and widest spatially spread) backflow can be observed for $\varphi_{rTJ} = 0^\circ$, at which the backflow clearly extends into the inlet with a zero-crossing of the friction coefficient at $y_{rTJ}^* \approx 1$. For increasing φ_{rTJ} , the zero-crossing shifts towards the $x - z$ -symmetry plane, which implies a spatial reduction of the backflow towards the $x - z$ -symmetry plane. Besides the zero-crossing, a positive peak forms near the $x - z$ -symmetry plane. Contrary to the spatial expansion, the positive peak value increases with increasing φ_{rTJ} , with the highest increase between $\varphi_{rTJ} = 45^\circ$ and 90° . The increase of the friction coefficient is accompanied by a stronger near-wall velocity gradient, which indicates an increase in roll-up intensity with increasing φ_{rTJ} .

The detected peak of the friction coefficient at $y_{rTJ}^* = 0.13$ (see Fig. 3.43 top magenta dotted line) suggests a pronounced roll-up-depending flow topology around this position. To investigate the flow condition around the positive friction coefficient peak, the $y_{rTJ}^* = 0.13$ -plane is illustrated in Fig. 3.44 colored by $\lambda = (|S_{ij}| - |\Omega_{ij}|) / (|S_{ij}| + |\Omega_{ij}|)$. This ratio enables an assessment of the present flow condition, where $\lambda = 0$ is equivalent to a simple shear flow, $\lambda < 0$ to a rotational flow and $\lambda > 0$ to a planar extensional flow as proposed within the OpenFOAM code.

In the center of the $y_{rTJ}^* = 0.13$ -plane, a strongly pronounced region with $\lambda > 0$ can be observed. This region is dominated by the symmetrical impingement of the two inflows and the streamline deflection towards the outlet, which is accompanied by a flow acceleration and causes the planar extensional flow character. Towards the outlet, the $\lambda > 0$ region weakens to a simple shear flow. The near-wall region with $\lambda > 0$ has its origin in the wall impingement of the streamlines deflected by the saddle point. The wall impingement in turn causes a partial deflection of the streamlines in the outlet direction and consequently an acceleration of the fluid, which leads to a planar extensional flow character. Towards the outlet, the near-wall region shifts towards the pipe center and weakens. Enclosed by both described regions, a rotational flow region ($\lambda < 0$) can be recognized, which extends from the $y - z$ -symmetry plane within the reverse T-junction into the outlet section. Within the reverse T-junction, the $\lambda < 0$ region exhibits a relatively constant radial position at $r/R = 0.8$ (highlighted by blue dotted line in Fig. 3.44), whereas in the outlet it tends slightly towards the pipe center. Compared to Fig. 3.41, the streamline roll-up around the saddle-point coincides approximately with $r/R \approx 0.8$ and

3. IC-engine-relevant cooling channel configuration: Water Spider Geometry (WSG)

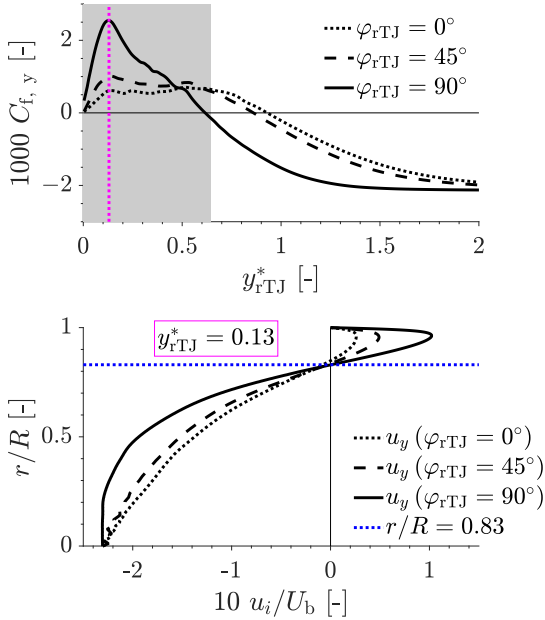


Figure 3.43.: Top: y_{rTJ}^* -friction coefficient $C_{f,y} = \tau_{w,y} / (0.5\rho U_b^2)$ depicted along the inlet coordinate y_{rTJ}^* for selected inlet circumferential angles φ_{rTJ} .
 Bottom: y_{rTJ}^* -velocity component u_y/U_b over pipe radius for selected inlet angles φ_{rTJ} at $y_{rTJ}^* = 0.13$. The blue dotted line indicates the zero crossing of the velocity profiles. The position of the velocity profiles corresponds to the magenta dotted lines in Fig. 3.44.

can be related to the rotational flow region. The tendency of the rotational flow region to shift towards the pipe center in the outlet section is consistent with the vortex center shift illustrated in Fig. 3.42. Hence, the streamline roll-up and the double symmetrical vortex topology in the outlet are related and the streamline roll-up leads to the vortex topology in the outlet section.

For a deeper investigation of the increasing friction coefficient peak with increasing inlet angle φ_{rTJ} at $y_{rTJ}^* = 0.13$ as visible in Fig. 3.43 top, the y_{rTJ}^*

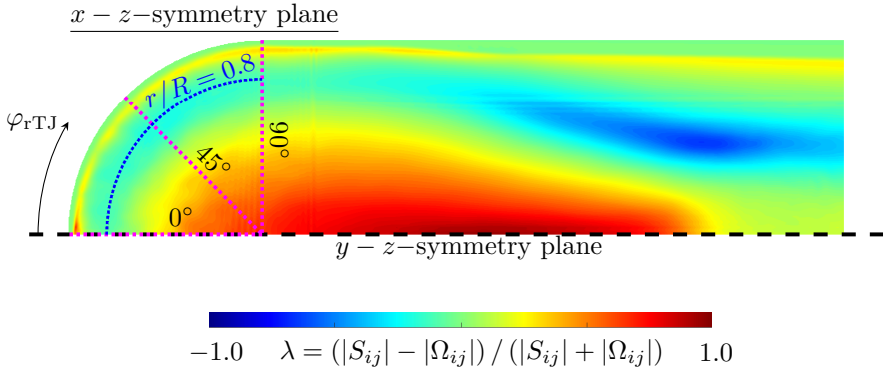


Figure 3.44.: Flow type $\lambda = (|S_{ij}| - |\Omega_{ij}|) / (|S_{ij}| + |\Omega_{ij}|)$ visualized on $y_{rTJ}^* = 0.13$ plane with the symmetrical S_{ij} and asymmetrical part Ω_{ij} of the velocity gradient tensor. The visualized data derived from averaging over the symmetry planes.

velocity component is depicted in Fig. 3.43 bottom from the inlet pipe center ($r/R = 0$) to the wall ($r/R = 1$) at $y_{rTJ}^* = 0.13$ for different inlet angles φ_{rTJ} . For clarity, the paths of the velocity profiles are illustrated in Fig. 3.44 with magenta-colored dotted lines. The velocity profiles exhibit a similar evolution with a negative velocity in the middle of the pipe, a consistent zero-crossing at $r/R \approx 0.83$ (blue dotted line in Fig. 3.43 bottom) and a positive peak close to the wall. Here, a positive y_{rTJ}^* -velocity corresponds to a flow towards the inlets. The positive peak indicates the backflow as a result of the streamline curvature around the saddle point. The velocity of the back-flowing fluid increases with φ_{rTJ} , whereby the maximum value doubles up to $\varphi_{rTJ} = 90^\circ$. Since the position of the peak remains approximately the same, the velocity gradient close to the wall increases accordingly, which is consistent with the discussion of the friction coefficient and the corresponding positive peak depicted in Fig. 3.43 top. The border of the backflow region, evident from the zero-crossing position of the y_{rTJ}^* -velocity component, remains at $r/R = 0.83$ regardless of φ_{rTJ} . This position of the zero-crossing coincides with the rotational flow region within the reverse T-junction discussed in Fig. 3.44. The velocity profile

around the zero-crossing is noticeable, which exhibits an approximately linear and asymmetrical pattern. The associated velocity gradient also exhibits an increase with φ_{rTJ} . Considering the rotational flow character and the linear velocity gradient around the zero-crossing, the fluid around the zero-crossing seems to act according to a solid body rotation with a linear increase in u_y as the distance to the zero-crossing increases. Consequently, the increase of the velocity gradient corresponds to an increasing rotational speed of the developing vortex tube with φ_{rTJ} .

3.7.5. Discussion: Double symmetric vortex topology

The double-symmetric vortex topology consisting of four vortex tubes remains downstream of the reverse T-junction in its structure as discussed in Fig. 3.42. In order to quantify the influence of the vortex topology onto the flow in the outlet section, the Γ_1 (threshold 0.95) and Γ_2 (threshold $\pi/2$) criterion according to Graftieaux et al. (2001) with a search window size of 11 are considered, which provides insights into the circulation evolution of a single vortex tube Γ in the outlet section. The evolution of the circulation of a single vortex tube is depicted in Fig. 3.45 top along the outlet coordinate s_{rTJ}^* .

The maximum circulation within the outlet region is located directly at the beginning at $s_{rTJ}^* = 0$, followed by a continuous decrease of circulation as s_{rTJ}^* increases. The continuous decrease of the circulation in the outlet suggests a purely dissipative vanishing of the vortex tube, which is consistent with the observations in the previous section. The driving force of the vortex topology is the streamline roll-up around the saddle point. Besides this region, no further root cause for the vortex topology seems to exist, which is supported by the continuous decrease of Γ . In addition to the considerations of the vortex tube circulation, the procedure according to Graftieaux et al. (2001) can be used to determine the existence of the vortex tube. A circulation is detected up to $s_{rTJ}^* = 2.8$, after which the detected circulation is in the order of the threshold defined by Graftieaux et al. (2001) and the vortex tubes can no longer be considered to exist.

The assessment of the absolute values depicted in Fig. 3.45 top is not possible without a reference. To quantify the vortex tube intensity in terms of its circulation, the resulting wall shear stress in the outlet section in terms of the friction coefficient C_f is depicted in Fig. 3.45 bottom. To account

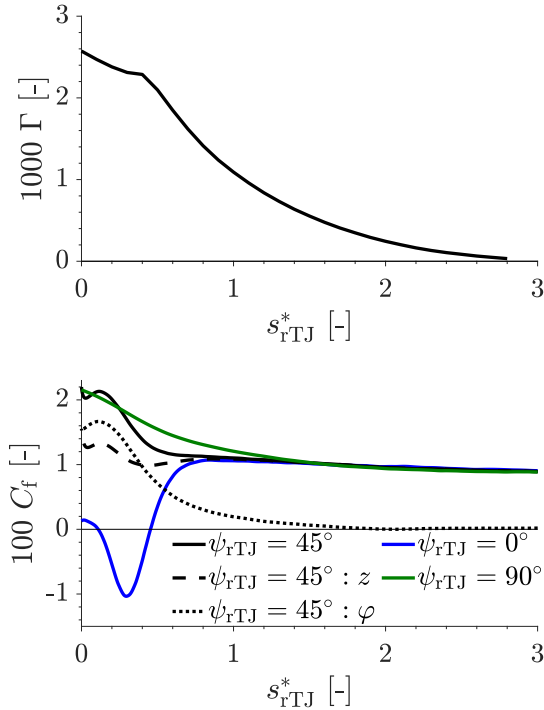


Figure 3.45.: Top: Vorticity Γ of a single vortex tube over the outlet coordinate s_{rTJ}^* .
Bottom: Friction coefficient $C_f = \tau_w / (0.5\rho U_b^2)$ depicted for different outlet angles ψ_{rTJ} over the outlet coordinate s_{rTJ}^* .

for the three-dimensional flow character, the friction coefficient is depicted for different outlet angles ψ_{rTJ} . Here, $\psi_{rTJ} = 0^\circ$ (blue line) corresponds to the intersection of the wall with the $y - z$ -symmetry plane and $\psi_{rTJ} = 90^\circ$ (green line) represents the corresponding intersection with the $x - z$ -symmetry plane as defined in Fig. 3.40. Due to the coincidence with a symmetry plane, no splitting of components is necessary for $\psi_{rTJ} = 0^\circ$ and 90° , since the streamwise component is sufficient to assess the overall friction coefficient. The two symmetry plane curves serve as a reference for $\psi_{rTJ} = 45^\circ$ (black line),

which is split into a streamwise $C_{f,z}$ (dashed black line) and circumferential component $C_{f,\varphi}$ (dotted black line). Especially the circumferential component of the friction coefficient at $\psi_{rTJ} = 45^\circ$ is suitable for assessing the effects of the vortex tube, since the circumferential component is dominated by the inplane velocity and caused by the vortex tubes, as discussed in Fig. 3.42. The friction coefficient for $\psi_{rTJ} = 0^\circ$ is discussed in more detail in Fig. 3.47 in the context of flow detachment around the inner radius of the reverse T-junction. The circumferential component has a peak at $s_{rTJ}^* \approx 0.2$ and decreases downstream until disappearing at $s_{rTJ}^* \approx 2$. Thus, the influence of the vortex tubes on the wall disappears clearly earlier than the circulation evolution suggests (compare Fig. 3.45 top). The peak position of the circumferential component does not coincide with the position of maximum circulation. Note that in Fig. 3.45 bottom a constant circumferential position is considered ($\psi_{rTJ} = 45^\circ$) and the centers of the vortex tubes shift, as discussed in Fig. 3.42, which might explain this deviation. Noteworthy is the dominant expression of the circumferential component for $s_{rTJ}^* < 0.5$, which clearly exceeds the streamwise component. The depicted friction coefficient in Fig. 3.45 bottom emphasizes the significance of the double symmetric vortex topology within the flow topology of the reverse T-junction and its dominant influence especially at the beginning of the outlet section ($s_{rTJ}^* < 0.5$).

For analyzing the in-plane flow characteristics in the outlet section, which is dominated by the vortex tubes, the wall-normal u_n and tangential velocity u_t are depicted in Fig. 3.46 top for selected cross-sections s_{rTJ}^* . The velocity profile depictions are identical to the magenta dotted lines illustrated in Fig. 3.42 and are intersecting the corresponding vortex center positions, which are determined according to the procedure by Graftieaux et al. (2001). Thus, the wall-tangential component corresponds approximately to the circumferential velocity of the vortex tube and the wall-normal component is decoupled from the circumferential velocity of the vortex tubes. Here, the zero-crossing of the wall-tangential and normal velocity corresponds to the present vortex center (vc), highlighted by magenta colored squares according to Graftieaux et al. (2001). The velocity gradient of u_t around the vortex center ($u_t/U_b = 0$) exhibits an approximately linear character. This characteristic was also observed in Fig. 3.43 bottom in the context of streamline roll-up. Thus, the vortex tubes seem to have a solid body rotation character from origin to outlet in core. A strong decrease of the tangential velocity gradient around the vortex centers

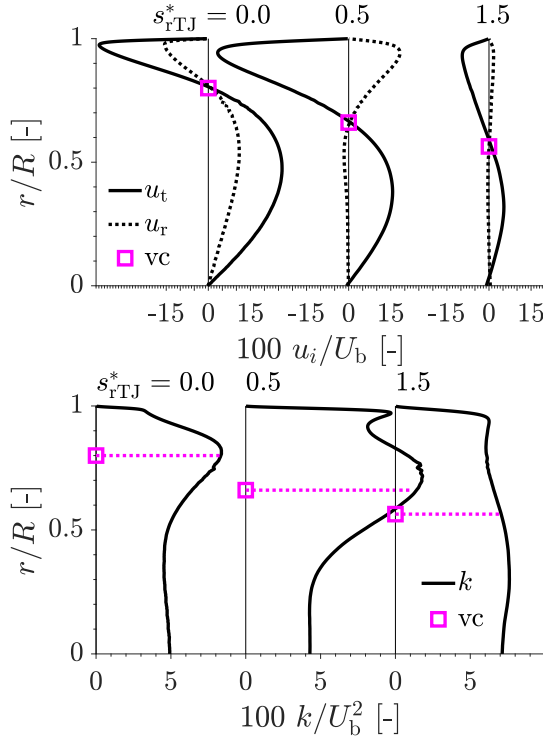


Figure 3.46.: Normalized wall tangential u_t/U_b (solid line) and normal velocity u_n/U_b (dotted line) (top) and normalized turbulent kinetic energy k/U_b^2 (bottom) depicted for selected cross-sections in the outlet section ($s_{rTJ}^* = 0.0, 0.5$ and 1.5) according to magenta dotted lines in Fig. 3.42. The corresponding vc is highlighted by magenta colored squares.

for increasing s_{rTJ}^* can be observed, which is consistent with the Γ evolution discussed with respect to Fig. 3.45 top and demonstrates the dissipative nature of the vortex tubes in the outlet. The near-wall response of the wall tangential velocity is obviously not affected by the decrease of its velocity gradient around the zero crossing in the range of $s_{rTJ}^* = 0$ to 0.5 . Both, the

near-wall velocity gradient and the peak value remain constant, which is not consistent with the circumferential friction coefficient depicted in Fig. 3.45 bottom. The reason for this is probably the vortex-center depending depiction in Fig. 3.46 top compared to the depicted friction coefficient at constant circumferential positions ($\psi_{rTJ} = 45^\circ$) in Fig. 3.45 bottom. The wall-normal velocity component u_n , which is positive in the wall-normal direction, also has a zero-crossing in the vortex center. The zero-crossing is accompanied by a reversal of the wall-normal flow direction in the vortex center, where the wall-normal velocity component is directed away from the vortex center for $s_{rTJ}^* = 0$ and towards it for $s_{rTJ}^* = 0.5$ and 1.5 . Here, the wall-normal flow direction across the vortex center could be an indicator for the expansion of the vortex tube within the cross-section. Consequently, a spatially expanding vortex state is present at the beginning of the outlet and reverses with continuing s_{rTJ}^* .

Similar to Fig. 3.46 top, the turbulent kinetic energy k/U_b^2 is depicted in Fig. 3.46 bottom to investigate the turbulence intensity within the vortex tubes and its evolution. For orientation, the corresponding vortex center is marked by magenta colored squares and dotted lines. As previously discussed for CS1 ($s_{rTJ}^* = 0$) in Fig. 3.42, the peak of turbulent kinetic energy coincides with the associated vortex center. Apart from the peak, the turbulent kinetic energy decreases continuously towards the wall and forms a plateau around the pipe center $r/R = 0$. For $s_{rTJ}^* = 0.5$, the turbulent kinetic energy peak tends to shift towards the pipe center with the vortex center and a second peak near the wall is formed. However, as observed in Fig. 3.42, caution is required, since the effects due to the vortex tube and the wake of the inner radius are superimposed. Noteworthy is the pattern of turbulent kinetic energy at $s_{rTJ}^* = 1.5$, which, despite the strong inhomogeneous distribution at $s_{rTJ}^* = 0.5$, has a quasi-homogeneous distribution of the turbulent kinetic energy over the radius. This emphasizes the pronounced cross-sectional secondary motion and its distinct inplane flow equalization tendency due to the double-symmetric vortex topology and the rapid formation of a homogeneous distribution of the flow over the cross-section downstream of the reverse T-junction.

3.7.6. Discussion: Flow separation

The increased turbulent kinetic energy in the wake of the inner radius, illustrated in Fig. 3.42 within CS2 ($s_{rTJ}^* = 0.5$) and quantified in Fig. 3.46 bottom,

suggests that the flow separation around the inner radius is one of the turbulence driving mechanisms within the reverse T-junction. Before considering the wake of the inner radius in detail, the flow acceleration and separation is investigated around the inner radius. Due to the prominent velocity gradient at the detachment point, the friction coefficient along the inner radius C_f is a suitable basis for discussion of flow separation and depicted in Fig. 3.47 top along s_{rTJ}^* . The path of the depicted friction coefficient corresponds to the intersection of the inner radius with the $y-z$ -symmetry plane, where $s_{rTJ}^* = 0$ describes the beginning of the outlet section according to Figures 3.39 and 3.40. The region of the inner radius is highlighted in gray. Complementary to the friction coefficient, the pressure coefficient $C_p = (p - p_{\text{outlet}}) / (0.5\rho U_b^2)$ along the inner radius is depicted in Fig. 3.47 bottom, whereby the outlet pressure is utilized as the reference pressure for global comparability. To highlight the flow evolution along s_{rTJ}^* , the gradient of the pressure coefficient $\partial C_p / \partial s_{rTJ}^*$ is also depicted. A parallel discussion of the three quantities mentioned, C_f , C_p and $\partial C_p / \partial s_{rTJ}^*$, is appropriate along the inner radius, because the pressure coefficient and its gradient indicate a possible acceleration or deceleration tendency of the flow in addition.

The friction coefficient increases when the flow reaches the curvature of the inner radius, which corresponds to a larger near-wall velocity gradient. A decrease in the pressure coefficient and consequently a negative gradient is accompanied which indicates flow acceleration. Both evolutions become more pronounced towards the inner radius, which can be related to the streamline roll-up and the backflow due to the saddle point, as discussed for example in Fig. 3.41. The backflow causes a reduction of the bulk flow cross-section at a constant inlet volume flux and therefore results in the observed acceleration. According to Fig. 3.43 top, the deepest backflow extension into the inlet section can be seen for $s_{rTJ}^* = -1$, which correlates with the continuous increase and decrease in both, Fig. 3.47 top and bottom. The friction coefficient reaches its maximum at $s_{rTJ}^* \approx -0.2$, which coincides with the zero-crossing of the pressure coefficient and its strongest gradient. In addition to the cross-section reduction, streamline curvature caused by the concave inner radius also has a significant impact here and contributes to the extrema in C_f . The peak value of C_f is followed by a sudden drop in friction coefficient, which leads to a local negative peak at $s_{rTJ}^* \approx -0.1$. The zero-crossing suggests a sign change in near-wall velocity gradient and consequently a flow detachment.

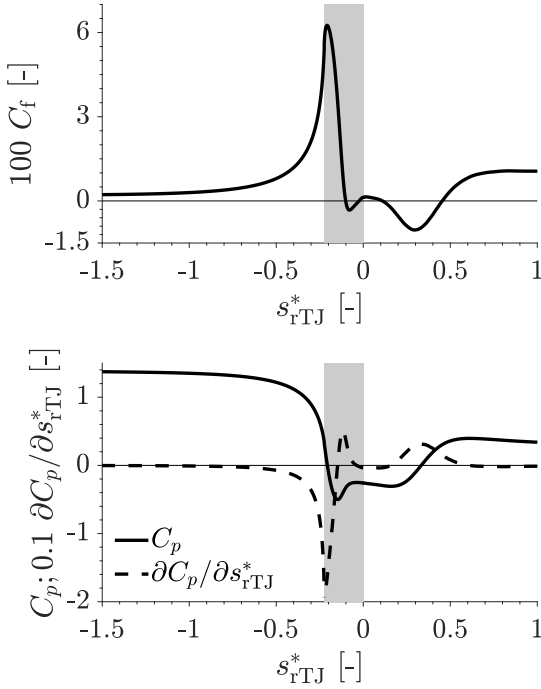


Figure 3.47.: Friction coefficient $C_f = \tau_w / (0.5\rho U_b^2)$ (top) and pressure coefficient $C_p = (p - p_{\text{outlet}}) / (0.5\rho U_b^2)$ and its derivative $\partial C_p / \partial s_{rTJ}^*$ (bottom) over the outlet coordinate s_{rTJ}^* along the intersection of the wall with the $y - z$ -symmetry plane. The outlet pressure p_{outlet} is applied as the reference pressure for global comparability. The region of the inner radius curvature is highlighted in gray.

The drop of C_f is accompanied by a pressure minimum and a disappearing gradient. The collapse of the gradient suggests that the flow could no longer follow the increasingly strong APG along the inner radius and has detached. The C_p minimum indicates a possible critical region with respect to a thermal or pressure-driven phase change phenomenon within the reverse T-junction. Downstream of the detected detachment point, the friction coefficient exhibits

a varying characteristic with three further zero-crossings. In conjunction with multiple sign changes of the pressure coefficient gradient, the flow is changing direction more frequently downstream of the detachment point. The last zero-crossing of C_f at $s_{rTJ}^* \approx 0.45$ seems to limit the low velocity region formed in the wake of the inner radius (see Figures 3.41 or 3.42), as the direction of the flow close to the wall adapts to the bulk flow direction with a positive friction coefficient and consequently a positive wall-nearest velocity gradient.

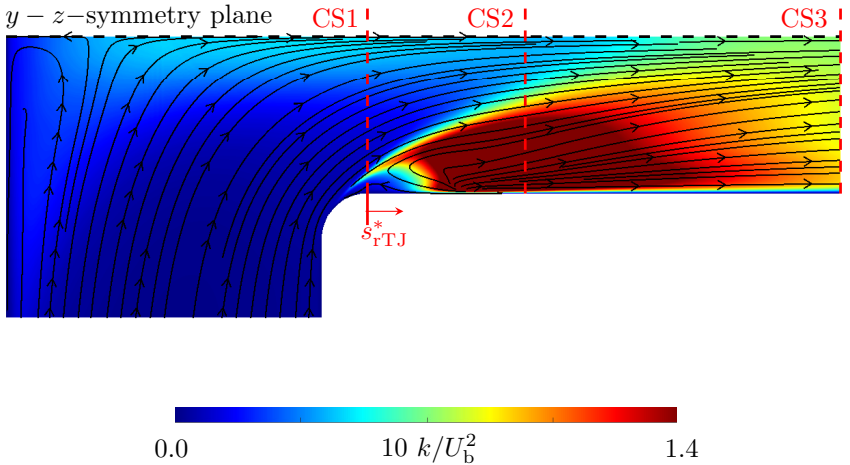


Figure 3.48.: Turbulent kinetic energy k/U_b^2 in the $y - z$ -symmetry plane of the reverse T-junction with the inplane mean streamlines. The locations of cross-sections shown in Fig. 3.42 are marked with CS1 ($s_{rTJ}^* = 0.0$), CS2 ($s_{rTJ}^* = 0.5$) and CS3 ($s_{rTJ}^* = 1.5$). The visualized data are derived from averaging over the symmetry planes.

The remaining two zero-crossings indicate a more complex flow topology in the wake of the inner radius, which will be qualitatively elaborated in the following by means of the streamlines illustrated in Fig. 3.48. In addition, the turbulent kinetic energy is overlaid in color to investigate the turbulence production in the wake of the inner radius. The two remaining zero-crossings

of C_f , which are assigned to the wake flow of the inner radius, originate from an additional vortex structure around $s_{rTJ}^* \approx 0$, as it can be observed from the closed streamline topology in this region in Fig. 3.48. The additional vortex topology causes an alternating stress on the wall within the wake (compare Fig. 3.47 top). The alternating stress is localized in the vicinity of the inner radius, whereas in technical applications the inner radius is constructively predetermined by the connection technology of the pipe structure. Mechanical connection points of two components usually represent weak points in technical structures and, consequently, when designing a comparable structure to the reverse T-junction, an alternating load on the connection has to be considered. The observed increase in turbulent kinetic energy in the wake of the inner radius (see Figures 3.42 and 3.46 bottom) does not originate from the wake itself, as evident from the deep blue region downstream of the inner radius in Fig. 3.48. Instead, a layer of increased turbulent kinetic energy forms around the boundary of the wake region and the bulk flow due to the presence of significant velocity differences and corresponding strong velocity gradients. The turbulence production is highest downstream of the detected wake boundary for $s_{rTJ}^* > 0.45$ and the region of enhanced turbulence extends over a large part of the radius. This causes increased turbulent mixing around the region of low velocity downstream of the inner radius and thus counteracts poor convective exchange by the comparably low velocity magnitude.

3.7.7. Conclusion and outlook

The investigated isolated reverse T-junction configuration, as last geometrical component of the WSG, is a standard flow guidance and can be found in numerous technical applications. The currently considered finite inner radius imitates realistic conditions caused by joining techniques such as welding. The applied well-resolved, highly comprehensive LES with the focus on shear stresses and thermally critical points can be regarded as a reference solution, which offers a gain for future studies in view of the existing reference data in literature. The emerging vortex topology within the reverse T-junction is discussed in detail based on the vortex identification methodology by Graftieaux et al. (2001) in terms of the formation process and the spatial expansion, allowing an insight into the interaction of vortex topology and flow topology as well as identifying vortex-induced wall effects.

The flow-dominating mechanisms within the reverse T-junction are identified in terms of the symmetric inflow impingement, the consecutive roll-up of streamlines and the flow detachment in the finite inner radius. Downstream of the reverse T-junction, a double symmetric vortex structure is formed as a result of the streamline roll-up, consisting of four vortex tubes. The vortex tubes act in the core according to a solid body rotation and exhibit a pure dissipative character in the outlet section. Their spatial extension is determined by means of the Γ_1 – and Γ_2 –criterion according to Graftieaux et al. (2001) with $s_{rTJ} = 2.8 D$. This vortex topology causes a pronounced secondary motion and is the origin of a rapid flow equalization in the outlet section of the reverse T-junction over the cross-section. In addition, the vortex topology has a significant influence on the wall shear, especially at the beginning of the outlet section.

The finite and comparably sharp inner radius of the reverse T-junction provokes a detachment due to a developing adverse pressure gradient (APG). Around the flow detachment, the lowest pressure and the highest wall shear are present, which favors wall degradation effects as well as possible phase changes of the fluid (thermal boiling and/or pressure-induced cavitation). In the wake of the inner radius, a complex vortex topology is created and induces alternating stresses on the wall, which should be taken into account in the technical construction of such connections. The transition region between the wake of the inner radius and the bulk flow is the turbulence determining region within the reverse T-junction. Here, strong velocity gradients cause a layer of increased turbulence production enveloping the wake, which is most pronounced at the end of the wake. The enhanced turbulence production counteracts the low convective exchange in the low velocity region downstream of the inner radius and increases turbulent mixing in it.

The application of a well-resolved, highly comprehensive LES has contributed to a deeper knowledge of a common engineering component within pipe systems, in particular through the consideration of a finite inner radius. Due to the limited consideration of the present chapter to a single Reynolds number, a parameter study with respect to the Reynolds number would help to assess corresponding scaling behaviors of current findings. Additionally, a variation of the finite inner radius might be of interest to specifically attenuate the identified critical points. Furthermore, the influence of the pipe diameter on the resulting vortex topology should be investigated, as this could be a

3. IC-engine-relevant cooling channel configuration: Water Spider Geometry (WSG)

design measure to specifically influence the vortex topology and thus the cross-sectional secondary motion characteristics.

3.8. Water Spider Geometry (WSG)

3.8.1. Introduction

The automotive industry is confronted with a challenging situation in the design of cooling systems of IC engines. The concurrent increase in the performance of IC engines coupled with more stringent emission requirements imposed by the European Union (Heibel, 2009, and Gruden, 2008) lead to increased thermal stresses on the cooling system by methods such as downsizing (van Basshuysen, 2013) and intelligent thermomanagement (Lunanova, 2009). Increased thermal loads on the cooling system and especially on the coolant can provoke undesired phenomena, such as decomposition of the coolant as well as thermal- and/or pressure-driven phase changes. IC cooling systems represent complex flow guidance, which are adapted to the existing space conditions and consequently depend on the engine design. The latter makes a generalization of the cooling systems and the prevailing flow conditions quite difficult. The experimental replication of realistic conditions in IC engines and their cooling systems involves a huge amount of effort, and the development of the glass engine of Baum et al. (2014) and Freudenhammer et al. (2015) is worth mentioning here. Due to the variety of different IC engine designs and the underlying cooling system requirements, a cost-effective option is the application of CFD. Some numerical works concerned with the optimization of cooling systems are Mulemane and Soman (2007), Jafarabadi et al. (2008), Fontanesi et al. (2010) and Fontanesi and Giacomini (2013). Due to the variety of flow phenomena and the multiphase flow nature, the application of commercial CFD software is popular due to the stability and robustness of the underlying codes. In general, CFD is an established element within the automotive industry and enables the comparatively cost-effective assessment of components or entire vehicles at an early stage of development. However, fundamental investigations of new developments are usually difficult and time-consuming due to the multitude of automobiles from various original equipment manufacturers (OEM) and their partly fundamentally different shapes. Here, generic reference bodies offer a possibility, which represent an application-oriented, manufacturer-independent structure and enable cost-effective access for research. For external aerodynamics of automobiles, prominent examples are the Society of Automotive Engineers (SAE) reference model and the

Ahmed body (Ahmed et al., 1984), which represent generic vehicle shapes with modular adaption in case of SAE reference model and serve as a study and benchmark case for a variety of investigations. The design of the WSG follows a comparable idea as the SAE reference model and Ahmed body. A cost-effective gap exists in comparative testing of different coolants under realistic conditions, which may represent the WSG. Complementary numerical and experimental investigations are carried out within the framework of a BMWi project (Klink et al., 2019, and Klink and Wegt, 2021) in terms of a generic pipe structure (WSG) inspired by the coolant guidance around an IC cylinder head. Due to the newly designed flow guidance, the present chapter deals with the isothermal discussion of the flow topology within the WSG on the basis of a well-resolved, highly comprehensive LES reference solution. The discussion includes the flow topology of the WSG as well as the isolated geometrical components from the previous chapters, which allow a comparative insight into the isolated and WSG flow topology as well as an assessment of the superimposed effects within the WSG. More specifically, the experimentally detected locations of pronounced surface degradation (inlet of the second deflection and inner radius of reverse T-junction) are targeted and investigated with respect to a possible unfavorable flow topology.

3.8.2. Computational domain

Complementary to the illustration of the WSG sample in Fig. 1.1 and description of its spatial dimensions in Fig. 3.1, Fig. 3.49 depicts the computational domain of the WSG within the numerical framework. Besides the WSG, the flow guidance up and downstream of the WSG sample are also included within the computational domain due to the fully developed pipe flow character upstream of the pipe necking of the inlet section and the experimental pressure measurement in the outlet section. The mentioned fully developed pipe flow character provides the advantage that the consideration of the entire inlet section of $l_{\text{WSG,inlet}} = 340$ mm according to Fig. 3.1 is not necessary in the numerical framework and is reduced to $l_{\text{inlet}} = 2.5 D_{\text{outer}}$. The reduction of the inlet length is possible due to the precursor connected with the inlet, which guarantees a fully developed pipe flow with a bulk Reynolds number of $\text{Re}_{\text{outer}} = U_{\text{b,outer}} D_{\text{outer}} / \nu = 12600$. This Reynolds number corresponds to $\text{Re}_{\text{b}} = U_{\text{b}} D / \nu = 14400$ related to the pipe diameter D within the WSG

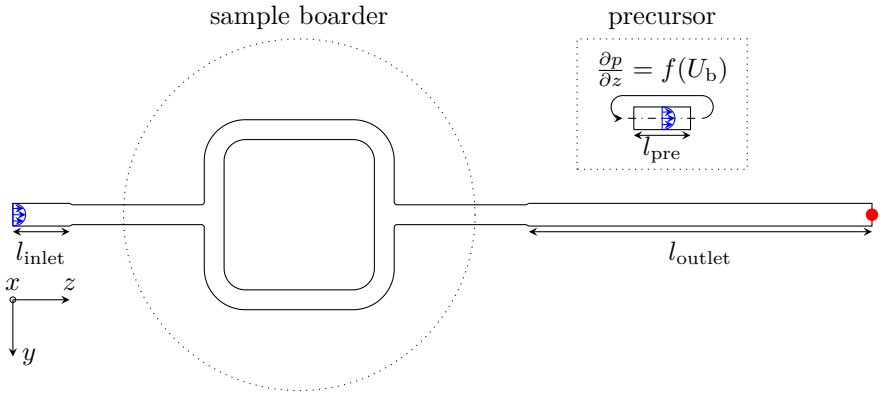


Figure 3.49.: Computational domain of WSG including inlet and outlet section as well as precursor region. The experimental pressure measurement point is highlighted by a red circle.

(compare Table 3.2). The pressure condition within the WSG is of crucial importance for the detection of thermally critical points with respect to possible phase change events. An extended outlet section up to the experimental pressure measurement point is consequently included in the numerical framework according to Fig. 3.1 with a length of $l_{outlet} = l_{WSG,outlet} = 60.5$ mm. A shortening of the outlet section and an analytical estimation of its pressure loss is not advisable due to the deviating character of the flow to a fully developed pipe flow condition downstream the WSG and its outlet necking.

The WSG grid is based on the knowledge of Chapter 3.3 and combines the grids of the 90° -pipe bend, the T-junction and the reverse T-junction described in detail in Sections 3.5.2, 3.6.2 and 3.7.2. The resulting grid contains 290 million hexahedral cells combined in a block-structured grid. For further information related to the grid generation as well as the numerical framework, reference is made to Chapter 3.2.

3.8.3. Discussion: First impression

For a first insight into the flow topology within the WSG, Fig. 3.50 depicts the iso-contours of the time-averaged velocity magnitude U/U_b (top) and turbulent kinetic energy k/U_b^2 (bottom) within the $y-z$ -symmetry plane, which corresponds to the intersection of the half-samples (see Fig. 3.1). The cross-sections of the T-junction outlet (marked with red dotted line) and the reverse T-junction outlet (marked with magenta dotted line) are also shown to provide an insight into the cross-sectional inplane velocity. For clarification, the bulk velocity U_b used for normalization in the following corresponds to the cross-sectional mean velocity within the WSG ($D = 0.0035$ m, $Re_b = 14400$).

The time-averaged inplane streamlines are additionally overlaid on the velocity magnitude field to illustrate three-dimensional flow characteristics. Here, an originating streamline describes the inflow of fluid into the associated plane and a disappearing streamline describes the corresponding outflow of fluid. To provide a clear and enlarged representation of the flow topology within the WSG, the flow guidance upstream and downstream is not visualized in Fig. 3.50. For comparison, the corresponding flow fields of the isolated T-junction (see Chapter 3.6) and isolated reverse T-junction (see Chapter 3.7) are additionally presented in terms of the time-averaged velocity magnitude, kinetic turbulent energy as well as the inplane streamlines.

The flow enters the WSG from the left in Fig. 3.50 and exits it on the right edge. Along the WSG, the flow experiences numerous flow acceleration/deceleration and impingement caused by the geometry-related flow division (T-junction), two deflections (90° -bend), and confluence (reverse T-junction). The already known vortex topologies from the isolated flow discussion also emerge within the WSG with the symmetric counter-rotating vortex tubes downstream of the T-junction, as evident from the inplane velocity streamlines at the T-junction outlet in Fig. 3.50. The situation is different at the outlet of the reverse T-junction, where a double-symmetric vortex topology corresponding to the isolated consideration can be recognized within the inplane streamlines, but deviates significantly in the spatial extent. The two mentioned positions indicate that the flow topology within the WSG exhibits similarities to the isolated considerations of the previous chapters (see Chapters 3.5, 3.6 and 3.7), but also differs partly significantly from each other. A superficial discussion of the flow topology based solely on Fig. 3.50 does not adequately capture the complex, superimposed flow topology within the

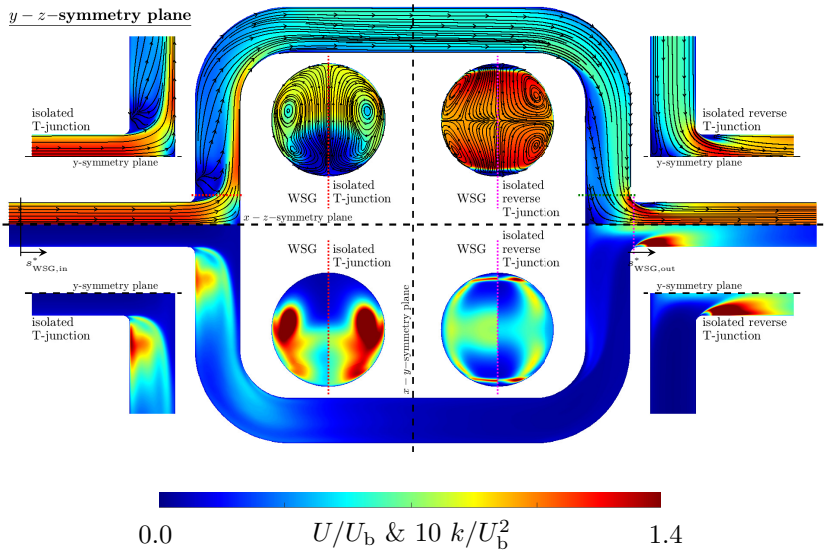


Figure 3.50.: Time-averaged velocity magnitude U/U_b (top) and turbulent kinetic energy k/U_b^2 (bottom) as well as time-averaged inplane streamlines within the WSG $y-z$ -symmetry plane as well as the T-junction outlet (red dotted line) and reverse T-junction outlet (magenta dotted line). For comparison, the isolated T-junction and isolated reverse T-junction results within the corresponding planes are additionally shown. The visualized data are derived from averaging over the symmetry planes.

WSG. Consequently, a detailed discussion of each characteristic geometrical component with the flow division (T-junction), double deflection (first & second deflection) and confluence (reverse T-junction) is conducted in the following. This is preceded by a discussion of the WSG inflow to assess the impact of the upstream located pipe necking onto the flow topology. Therefore, an interactive discussion including the isolated considerations is provided to use the insights from the previous flow discussions and to develop a more in-depth understanding of the flow topology of the WSG.

3.8.4. Discussion: WSG inflow

First, the focus is set on the inflow into the WSG and its evolution. The inflow seems to be unidirectional as evident from the wall parallel streamlines entering the WSG via the left edge of Fig. 3.50. The inflow does not indicate any visible variations in streamwise direction in both, velocity magnitude and turbulent kinetic energy despite the upstream located flow necking and seems to act similar to a fully developed pipe flow. To evaluate the inflow evolution, Fig. 3.51 depicts the time and circumferentially averaged streamwise (wall-parallel) velocity u^+ (top) and turbulent kinetic energy k^+ (bottom) along the WSG inflow pipe radius $(R - r)^+$ within the WSG inlet (black solid line, $s_{\text{WSG,in}}^* = 0$) as well as the profiles at the identical positions within the isolated T-junction (circles).

As a representative and characteristic of a pipe flow, the friction Reynolds number Re_τ is considered first, which gives an indication of the near-wall behavior of the pipe flow. The isolated consideration has a friction Reynolds number of $\text{Re}_\tau = 426$ at the position of the WSG inlet, which is close to a fully-developed pipe flow according to Fig. 3.16. The friction Reynolds number at the WSG inlet is significantly lower than that of the isolated consideration ($\text{Re}_\tau = 398$), which is equivalent to a comparatively lower near-wall velocity gradient and indicates a non-fully-developed pipe flow condition. The normalized velocity profile at the WSG inlet is located above the isolated consideration in Fig. 3.51 top. However, no straightforward shift to the logarithmic law (black dotted line) can be observed as expected with a lower friction Reynolds number, rather a hump-shaped profiles forms around $y^+ = 20$. At the same position, a clear overestimation of the turbulent kinetic energy can be seen (see Fig. 3.51 bottom), whereas the turbulence in the bulk flow is underestimated. The cause for the latter is most likely the upstream positioned pipe necking, which forces an acceleration of the bulk flow due to the cross-sectional constriction and subsequently an appropriate stretching of the turbulent structures. Conversely, the near-wall flow topology along the pipe necking and its sharp edge could provoke a shear layer formation, which could lead to a turbulence increasing effect near the wall.

To assess the requirement for a more in-depth investigation of the pipe necking, the flow evolution within the WSG inlet is investigated and compared with the isolated consideration in the following. For this purpose, Fig. 3.52 depicts the friction coefficient C_f (top) and the pressure coefficient C_p (bot-

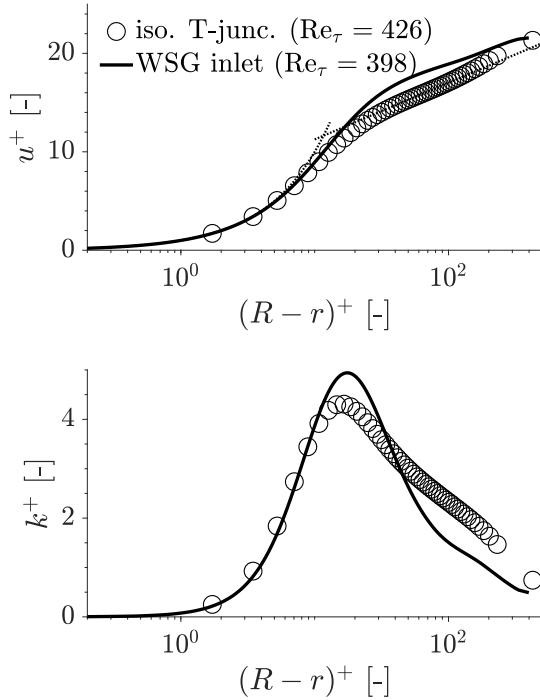


Figure 3.51.: Normalized streamwise velocity u^+ (top) and turbulent kinetic energy k^+ (bottom) along the WSG inflow pipe radius $(R-r)^+$ within the WSG inlet (black line). For comparison, the profiles at the identical positions within the isolated T-junction (circle) are also depicted.

tom) for different WSG inlet angles $\psi_{\text{WSG},\text{in}}$ along the WSG inlet coordinate $s_{\text{WSG},\text{in}}^* = s_{\text{WSG},\text{in}}/D$, which originates at the WSG inlet and is defined in Fig. 3.50. The WSG inlet angle $\psi_{\text{WSG},\text{in}}$ originates at the intersection of the WSG wall with the $y-z$ -symmetry plane and runs in the mathematically positive circumferential direction of the pipe. Exemplary positions are highlighted by dotted lines with the inlet of the isolated T-junction (blue), the end of pipe necking within the WSG (red), the inlet of the WSG sample (green) and the beginning of the T-junction flow guidance (magenta).

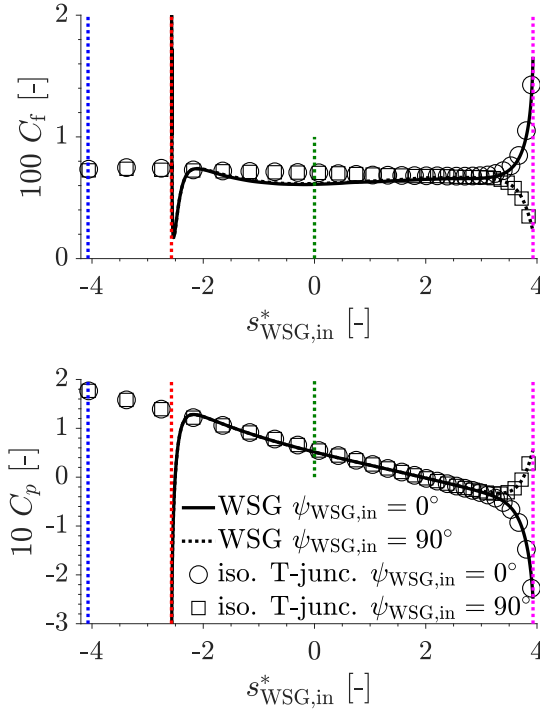


Figure 3.52.: Friction coefficient $C_f = \tau_w / (0.5\rho U_b^2)$ (top) and pressure coefficient $C_p = (p - p(s_{\text{WSG,in}}^* = 2)) / (0.5\rho U_b^2)$ (bottom) over the WSG inlet coordinate $s_{\text{WSG,in}}^*$ for different WSG inlet angles $\psi_{\text{WSG,in}}$ in comparison to the isolated T-junction consideration (symbols). Specific positions are highlighted by dotted colored lines (inlet isolated T-junction, end necking, inlet WSG sample, inlet T-junction).

The friction coefficient within the WSG (Fig. 3.52 top) exhibits a strongly deviating characteristic downstream of the necking compared to the isolated consideration independent of the $\psi_{\text{WSG,in}}$ position with a clear minimum at $s_{\text{WSG,in}}^* = -2.5$ and a decaying oscillating characteristic downstream. The decaying oscillating characteristic results in an underestimation of the friction

coefficient at the WSG inlet ($s_{\text{WSG,in}}^* = 0$), which is consistent with the discussion in Fig. 3.51 and the underestimated friction Reynolds number. The deviations between the WSG and the isolated consideration weaken along the WSG inlet section and disappear for $s_{\text{WSG,in}}^* > 2$. A similar evolution can be observed with respect to the pressure coefficient C_p along the WSG inlet section (Fig. 3.52 bottom). Downstream of the pipe necking, a strong positive pressure gradient is present with a decaying oscillating evolution, which approaches to the isolated consideration and coincides with it for $s_{\text{WSG,in}}^* > 2$.

Both C_p and C_f indicate a strong but limited influence of the pipe necking on the inlet flow topology, which disappears for $s_{\text{WSG,in}}^* > 2$ and approaches to the isolated consideration. Consequently, a deeper investigation of the pipe necking is not necessary, as the flow topology of the WSG and the isolated consideration seem to act similar in the immediate vicinity of the T-junction flow guidance.

3.8.5. Discussion: T-junction

Downstream of the inflow region, the flow reaches the T-junction flow guidance, passes its inlet and impinges onto the pipe-curved counter wall (see Fig. 3.50). A low-velocity region is formed around the point of impingement, which is related to the emergence of a stagnation point and is consistent with Figures 3.30 and 3.33 and the associated discussion. Before the impingement occurs, the flow has to pass the cross-sectional expansion in terms of the inner radius of the T-junction. As evident from the trajectory of the wall-nearest streamline and its deviation from the wall in the region around the inner radius, the flow apparently cannot follow the curvature of the inner radius and detaches. An additional low velocity region is formed downstream the inner radius, which extends over large parts of the T-junction outlet and is the origin of a variety of streamlines. The emerging streamlines, as discussed in detail in Fig. 3.30 and Chapter 3.6.5, originate from the fluid deflected by the impingement along the curvature of the pipe, which enter the $y - z$ -symmetry plane in the region of low velocity. The shear layer between the low velocity region and the bulk flow, and especially the origin of streamlines within the low velocity region, is one of the main sources of turbulence production within the WSG. A characteristic flow phenomenon of the isolated T-junction is the vortex topology created by the impingement on the pipe-curved counter-wall and consists of a pair of

symmetrical counter-rotating vortex tubes (see Chapter 3.6.6). With respect to the depicted inplane streamlines within the T-junction outlet cross-section in Fig. 3.50, a quite similar closed streamline pattern can be seen, which confirms the formation of the symmetric counter-rotating vortex tubes within the WSG. As already discussed in Fig. 3.36, the vortex tubes are also a source of enhanced turbulence production with a clear peak of the turbulent kinetic energy within the vortex tube center. However, the regions of increased turbulence are generally slightly less pronounced in the WSG compared to the isolated T-junction, which can probably be attributed to the presence of the downstream located first deflection and an retroactive effect of its flow topology.

Overall, the flow within the T junction of the WSG acts quite similarly to the isolated consideration discussed in Chapter 3.6. For a quantitative assessment of the flow topology, Fig. 3.53 compares the friction coefficients C_f within the $y - z$ -symmetry plane around the inner radius of the T-junction (top) and along the pipe-curved counter-wall (bottom) of the WSG (solid line) with the isolated T-junction (circles). A detailed discussion of fluid mechanics is not provided here and reference is made to the corresponding Figures 3.35 bottom and 3.38 as well as the associated discussion. Both depictions have a remarkable agreement of the friction coefficient within the WSG and the isolated T-junction. Noteworthy is the identical detachment point location in the inner radius of the T-junction at $\varphi_{TJ} = 20^\circ$ and the position of the peak values. The small deviations in magnitude are probably due to the slightly different inflow evolution, depicted in Fig. 3.51. A clear deviation can only be seen one diameter upstream of the inlet of the first deflection, which is highlighted by a red line. Both evolutions of the friction coefficient confirm the previously observed qualitative agreement between the WSG and the isolated consideration of the T-junction, which makes a more detailed flow discussion obsolete. For further details of the flow and vortex topology within the T-junction, the reader is referred to the isolated consideration in Chapter 3.6.

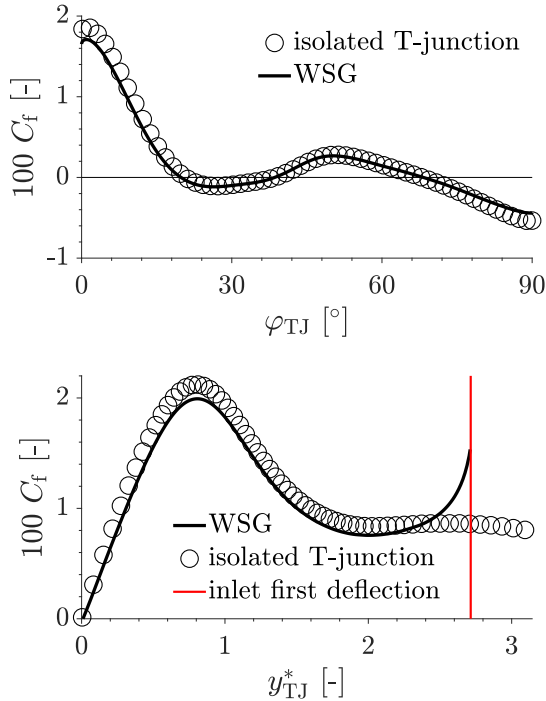


Figure 3.53.: Friction coefficient $C_f = \tau_w / (0.5\rho U_b^2)$ within the WSG $y-z$ -symmetry plane along the T-junction inner radius (top) and the pipe-curved counter wall (bottom). The results of the isolated T-junction (circles) are depicted for comparison. Comparable plots and associated discussion can be found in Figures 3.35 bottom and 3.38.

3.8.6. Discussion: Surface degradation upstream of the second deflection

The experimentally detected pronounced surface degradation around the inlet of the second deflection for the combination of high inlet temperature ($T_{\text{inlet}} = 115 \text{ }^\circ\text{C}$) and low volume flux ($\dot{V} = 2.2 \text{ l/min}$) is presented in Fig. 3.54 in the form of the chemically cleaned, heated sided half-sample after a 96-hour

3. IC-engine-relevant cooling channel configuration: Water Spider Geometry (WSG)

test according to the investigations in Klink and Wegt (2021). Around the inlet of the second deflection, metallic polished regions can be recognized, on which surface degradation has occurred as a result of the flow and thermal conditions within the experiment. The experimental surface degradation is more pronounced on the left hand side, which could have various causes, but is beyond the scope of the present work. The left weighting is advantageous to assume the initial location of origin, which seems to be around the inlet of the second deflection. With increasing tendency to surface degradation, the region expands upstream as can be seen on the left-hand side, but ends at the same position at about half the second deflection ($\varphi_{\text{bend}} = 45^\circ$).

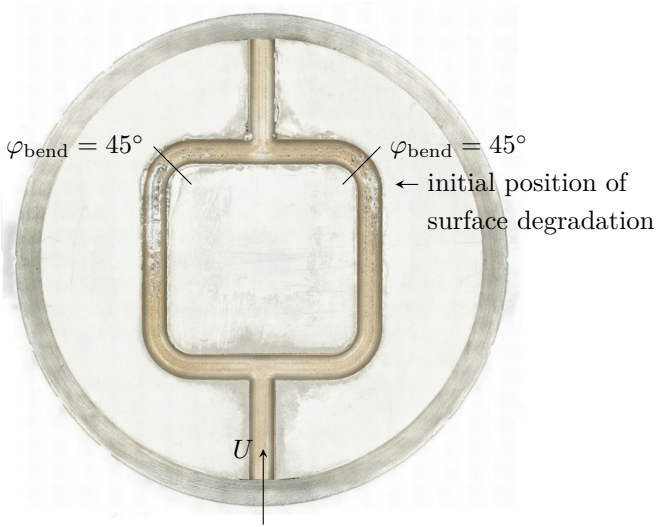


Figure 3.54.: Chemically cleaned, heated sided half-sample after a 96-hour test with $T_{\text{inlet}} = 115^\circ\text{C}$ and $\dot{V} = 2.2\text{ l/min}$ with view on the $y-z$ -symmetry plane. Initial position of surface degradation is marked around the inlet of the second deflection. The picture of the half-sample originates from Klink and Wegt (2021).

Various preliminary investigations indicate that the surface degradation is related to a boiling event, suggesting an insufficient heat transport in the

initial region of surface degradation. Such a surface degradation as illustrated in Fig. 3.54 can cause a dis-function of the technical application or even total failure in the case of realistic components. To adopt appropriate measures to prevent surface degradation, a deeper understanding of the flow topology is essential. Here, the key question lies within the initial cause that initiates surface degradation and, more generally, the susceptibility to such degradation characteristic. The discussions about the positions of surface degradation here and in the following chapter are intended to detect peculiarities of the isothermal flow topology around the mentioned positions and thus indicate a possible initial damage mechanism. A similar discussion has already been conducted in Klink and Wegt (2021) and interested readers are referred to it.

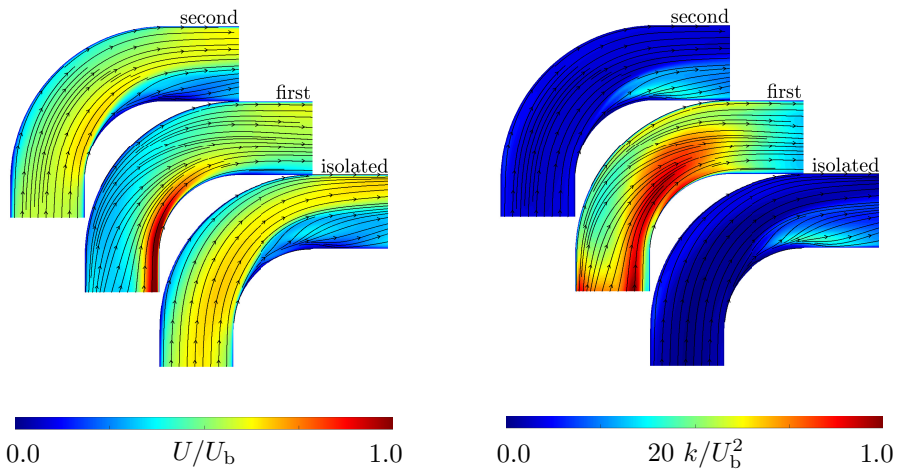


Figure 3.55.: Iso-contours of the time-averaged velocity magnitude U/U_b (left) and turbulent kinetic energy k/U_b^2 (right) with the time-averaged inplane streamlines within $y - z$ -symmetry plane for the isolated deflection (Chapter 3.5) as well as the first and second deflections of the WSG. The visualized data are derived from averaging over the symmetry planes.

To assess the flow conditions around the location of pronounced surface

degradation (inlet of the second deflection), the flow topology within the first and second deflection are evaluated in comparison to the isolated consideration from Chapter 3.5 in the following. For a first insight into the flow topology within the deflections, the iso-contours of the time-averaged velocity magnitude U/U_b (left) and turbulent kinetic energy k/U_b^2 (right) in the $y-z$ -symmetry plane for the three deflections are presented in Fig. 3.55. In addition, the time-averaged streamlines are depicted to pronounce possible deviations in the flow field. The flow enters the deflections from the bottom edge and leaves them at the right edge.

Following first the streamlines of the isolated and second deflection in Fig. 3.55 left, an approximately pipe-parallel flow can be recognized around the inlet which experiences a streamline curvature within the deflections. A flow acceleration is present around the inner radius of the deflections, which is accompanied by a flow separation in the most inner radius of the deflection evident from the wall-nearest streamline. Downstream of the detachment point, a region of low velocity forms, in which various streamlines have their origin. These streamlines arise from a symmetrical impingement of circumferentially oriented streamlines in the $y-z$ -symmetry plane. With the exception of a lower acceleration of the flow and a smaller region of low velocity in the case of the second deflection, the flow topology of the isolated and second deflection is comparable and subsequently the flow topology of the second deflection is in line with the explanations in Chapter 3.5. A similar situation can be observed for the turbulent kinetic energy (Fig. 3.55 right) with an increased turbulent kinetic energy appearing in the region of low velocity downstream of the detachment point and an inconspicuous characteristic apart from it for both, the isolated and second deflection.

The first deflection differs significantly from the isolated and second deflection in both, the velocity and turbulence flow characteristics. The first deflection has a highly inhomogeneous distribution in its inflow, which is focused around the inner radius of the deflection with a clear velocity peak visible by the deep red area in Fig. 3.55 left. The streamlines of the inflow of the first deflection are only partially oriented parallel to the inlet pipe and tend to the inner radius of the first deflection. A flow detachment in the inner radius and the formation of a region of low velocity is not visible. Due to the missing region of low velocity, a more homogeneous distribution of the flow velocity in the outlet can be observed compared to the isolated and second deflection. With respect to the

turbulent kinetic energy, the turbulence level is globally significantly higher than in the other two cases. An increased turbulence occurs predominantly around the inner radius of the deflection and the mentioned velocity peak, which decays comparatively fast downstream the first deflection.

Considering the global observation of the flow topology within the WSG presented in Fig. 3.50, the described characteristics of the first and second deflection are evident, with a highly inhomogeneous inflow into the first deflection and a significantly homogeneous one into the second, as well as the increased turbulence level of the first deflection. The inflow characteristics of the first deflections seem to originate from the upstream located T-junction flow guidance. The flow discussion of the isolated T-junction in Chapter 3.6 revealed a similar inhomogeneous distribution of its outlet flow as found in the inlet region of the first deflection (compare Fig. 3.30). Here, the impingement and streamline curvature in the isolated T-junction leads to a focusing of the volume flux on the impingement side, corresponding downstream to the inner radius side of the first deflection.

For a more detailed investigation of the relation between the T-junction and the first deflection, selected cross-sections of the three deflections are depicted in Fig. 3.56, focusing on the inplane streamline formation. Fig. 3.56 displays the iso-contours of the time-averaged velocity magnitude U/U_b (top) within the cross-sections and the time-averaged kinetic turbulent kinetic energy k/U_b^2 (bottom). The selected cross-sections correspond to the beginning of the deflections ($\varphi_{\text{bend}} = 0^\circ$), a representative cross-section within the deflection ($\varphi_{\text{bend}} = 45^\circ$), the end of the deflection ($\varphi_{\text{bend}} = 90^\circ$) and the flow pattern one diameter downstream of the deflection ($90^\circ + D$). For orientation, the left-hand side of the displayed cross-sections corresponds to the inner and the right-hand side to the outer radius of the deflections.

With an initial view on the isolated and second deflection identified as acting similarly, a comparable streamline characteristic can be observed across all cross-sections. For $\varphi_{\text{bend}} = 0^\circ$, the streamlines point towards the inner radius due to the existing pressure gradient according to the explanations in Chapter 3.5. In the following, a counterclockwise rotating vortex structure forms ($\varphi_{\text{bend}} = 45^\circ$), which is clearly visible downstream of the deflection in the streamline pattern ($90^\circ + D$). The mentioned vortex structure corresponds to the so-called Dean vortices discussed in detail in Chapter 3.5. Although slight deviations between the isolated and second deflection are visible (vortex

center closer to the wall for $\varphi_{\text{bend}} = 45^\circ$ and 90° , no clear formation of a secondary vortex structure for $\varphi_{\text{bend}} = 90^\circ$, the second deflection within the WSG configuration seems to act quite similar to the isolated consideration. This can also be extended to the velocity magnitude (Fig. 3.56 top) and the turbulent kinetic energy (Fig. 3.56 bottom). The region of low velocity is formed in the inner radius, around which a slightly increased turbulence intensity is formed within the isolated and second deflection.

The streamline pattern of the first deflection deviates significantly from the other two. The inflow ($\varphi_{\text{bend}} = 0^\circ$) exhibits a clockwise rotating vortex structure that extends over the entire half of the cross-section. Compared with the flow pattern downstream of the isolated T-junction in Fig. 3.30 and at the T-junction outlet within the WSG depicted in Fig. 3.50, the streamline pattern of $\varphi_{\text{bend}} = 0^\circ$ is comparable in terms of shape and direction of rotation. The mentioned clockwise rotating vortex structure is still visible within the deflection ($\varphi_{\text{bend}} = 45^\circ$), but experiences a shift towards the pipe center due to a counter-rotating second vortex structure forming close to the wall. The second vortex structure corresponds to the rotation direction of the Dean vortex in the isolated and second deflection. This could mean that the second vortex structure has the same mechanism of origin as the Dean vortex, which is found in the acting centrifugal force. At the intersection of both vortex structures along the $y-z$ -symmetry plane, the formation of a saddle point can be observed. The inhomogeneous velocity distribution with a velocity peak at the inner radius presented in Fig. 3.55 is clearly visible for $\varphi_{\text{bend}} = 0^\circ$ and 45° . In this range, there is also an increased turbulence intensity, which exceeds the turbulence level of the isolated and second deflection significantly. The vortex structure discussed for $\varphi_{\text{bend}} = 45^\circ$ is also visible in the outlet of the deflection ($\varphi_{\text{bend}} = 90^\circ$), whereby the clockwise rotating vortex is further convected towards the pipe center and the mentioned saddle point has disappeared. A Dean-vortex driven secondary vortex structure in the region of the inner radius seems not to emerge for the first deflection. Remarkable is the homogeneous distribution of the flow velocity magnitude and the turbulent kinetic energy for $\varphi_{\text{bend}} = 90^\circ$ over the cross-section compared to the upstream located cross-sections as well as the isolated and second deflection. The velocity peak and the increased turbulent kinetic energy in the region of the inner radius for $\varphi_{\text{bend}} = 0^\circ$ and 45° is no longer evident at $\varphi_{\text{bend}} = 90^\circ$ and has equalized over the cross-section. Additionally, a low velocity region is not observable

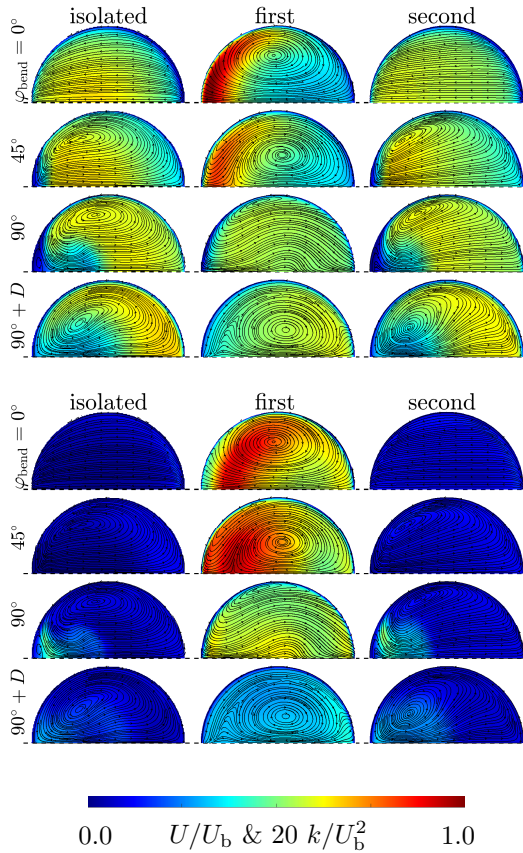


Figure 3.56.: Iso-contours of the time-averaged velocity magnitude U/U_b (top) and turbulent kinetic energy k/U_b^2 (bottom) with the time-averaged inplane streamlines within selected cross-sections for the isolated deflection (Chapter 3.5) as well as the first and second deflections of the WSG. The visualized data are derived from averaging over the symmetry planes.

for the first deflection, as already discussed in Fig. 3.55, which is a dominant flow characteristic within the isolated and second deflection and its absence is probably related to the clearly deviating inflow into the first deflection. Further downstream of the deflection ($90^\circ + D$), a complex vortex pattern is formed, with a central clockwise rotating vortex enclosed by smaller vortices with a surrounding inplane velocity towards the inner radius. The formation of this vortex pattern requires a more in-depth flow analysis and would go beyond the scope of the present discussion. It should be noted that the flow and vortex topology within the first deflection differs significantly from that of the isolated and second deflection. This could have its origin in the flow guidance upstream the first deflection (T-junction) and the associated vortex topology (symmetric vortex tube pair, see Fig. 3.30).

To summarize Figures 3.55 and 3.56, the isolated and second deflection have a similar flow topology, which seems to have its origin in a comparable inflow characteristic. In contrast, the first deflection differs significantly in its flow pattern and seems to be caused by the upstream located T-junction flow guidance within the WSG, whose vortex structure is visible up to $\varphi_{\text{bend}} = 45^\circ$ in the cross-sections of the first deflection. The latter causes an increased turbulence level within the first deflection, which has already completely equalized up to the outlet of the deflection (see Fig. 3.56; 90°). Thus, the first deflection indicates an increased cross-section flow equalization tendency, which presumably causes the homogeneous and unidirectional inflow of the second deflection.

For a deeper insight into the near-wall flow dynamics within the deflections, Fig. 3.57 depicts the pressure $C_p = (p - p(\varphi_{\text{bend}} = 0^\circ)) / (0.5 \rho U_b^2)$ (top) and friction coefficients $C_f = \tau_w / (0.5 \rho U_b^2)$ (bottom) for the isolated, first and second deflection for different cross-sectional circumferential positions ψ_{bend} , where $\psi_{\text{bend}} = 0^\circ$ corresponds to the inner radius of the deflections and $\psi_{\text{bend}} = 180^\circ$ to the outer radius.

With a first look at the isolated (black solid line) and second deflection (red solid line), the pressure as well as the friction coefficient demonstrate a similar response. With slight deviations for C_p along the outer radius ($\psi_{\text{bend}} = 180^\circ$ & $\varphi_{\text{bend}} = 90^\circ$) and the position of the zero-crossing of C_f , it confirms with the conclusion of Figures 3.55 and 3.56 that the isolated and second deflection have a comparable flow topology.

For the first deflection, the situation differs. Although the courses of C_p

and C_f in the outer radius ($\psi_{\text{bend}} = 180^\circ$) are approximately consistent to the remaining two, the deviation increases with decreasing ψ_{bend} . Especially for $\varphi_{\text{bend}} < 30^\circ$, both C_p and C_f exhibit clear peak characteristics, which are probably due to the vortex structure originating from the upstream located T-junction flow guidance. A strong pressure gradient is present in the inlet region of the first deflection (around $\varphi_{\text{bend}} \approx 0^\circ$), which indicates an acceleration of the flow and corresponds to the velocity peak in the inner radius in Fig. 3.55. Complementary to this, the friction coefficient has a peak at the position of the maximum pressure gradient ($\varphi_{\text{bend}} \approx 0^\circ$), which is clearly above the corresponding peaks of the isolated and second deflection. For increasing φ_{bend} , the deviations from the isolated and second deflection appear to decrease, suggesting a decrease of vortex structures driven by the T-junction and is consistent with the observations made with respect to Fig. 3.56.

The near-wall flow topology, discussed by means of C_p and C_f , confirms the comparable flow topology of the isolated and second deflection and the deviating characteristic of the first deflection. The latter exhibits strong deviations, especially at the beginning of the deflection, which decrease with increasing φ_{bend} and increasing ψ_{bend} . In terms of a rapid pressure drop (cavitation event) or an abrasive flow characteristic, the second deflection is inconspicuous and the first deflection would be more appropriate due to the peak characteristic around its inlet. Thus, the origin of the pronounced surface degradation around the inlet of the second deflection does not seem to be found directly within the near-wall pressure and friction characteristics.

The experimentally observed strong boiling activity in the region of the second deflection mentioned at the beginning could indicate an unfavorable flow topology upstream of the second deflection with respect to the heat transport from the wall to the bulk flow. As the pronounced surface degradation occurs primarily in the pipe bottom, Fig. 3.58 middle depicts the cross-sectional wall-normal u_n and tangential velocity profiles u_t from the pipe center $r/R = 0$ to the pipe bottom wall ($r/R = 1$) representing the inplane velocity of the cross-section along $\psi_{\text{bend}} = 90^\circ$ (see blue depiction in Fig. 3.58 top). The profiles correspond to the velocity evolution between the first and second deflection, with their locations illustrated in the top of Fig. 3.58 by means of a sketch. For clarification, the wall-normal component u_n points away from the wall and the wall-tangential component u_t in ψ_{bend} direction.

In the outlet region of the first deflection (CS1), a pronounced cross-sectional

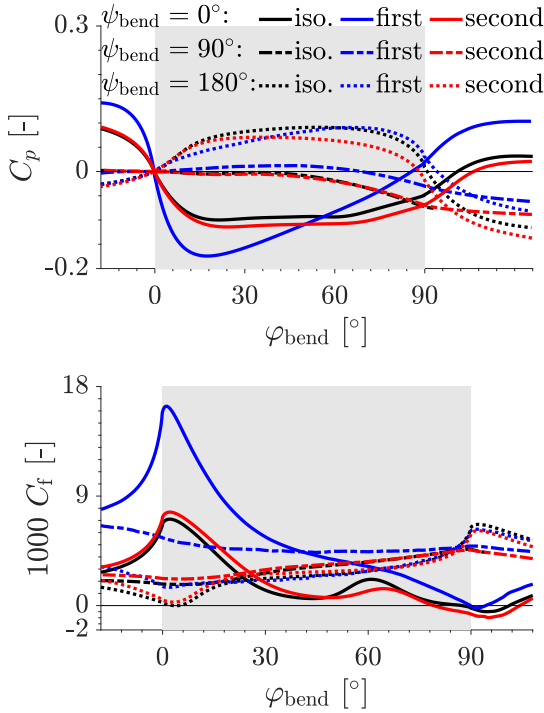


Figure 3.57.: Comparison of the isolated deflection (black lines) discussed in Chapter 3.5 with the first (blue lines) and second deflections (red lines) of the WSG in terms of pressure coefficient $C_p = (p - p(\varphi_{\text{bend}} = 0^\circ)) / (0.5 \rho U_b^2)$ (top) and friction coefficient $C_f = \tau_w / (0.5 \rho U_b^2)$ (bottom) for different circumferential angles ψ_{bend} ($\psi_{\text{bend}} = 0$ corresponds to the inner radius of the deflections) along φ_{bend} .

velocity can be observed, both in the wall-normal and tangential direction. Especially the wall-tangential velocity component can be found in the presented streamline pattern in Fig. 3.56 with the near-wall negative peak corresponding to the second vortex topology. The cross-sectional velocity decreases signifi-

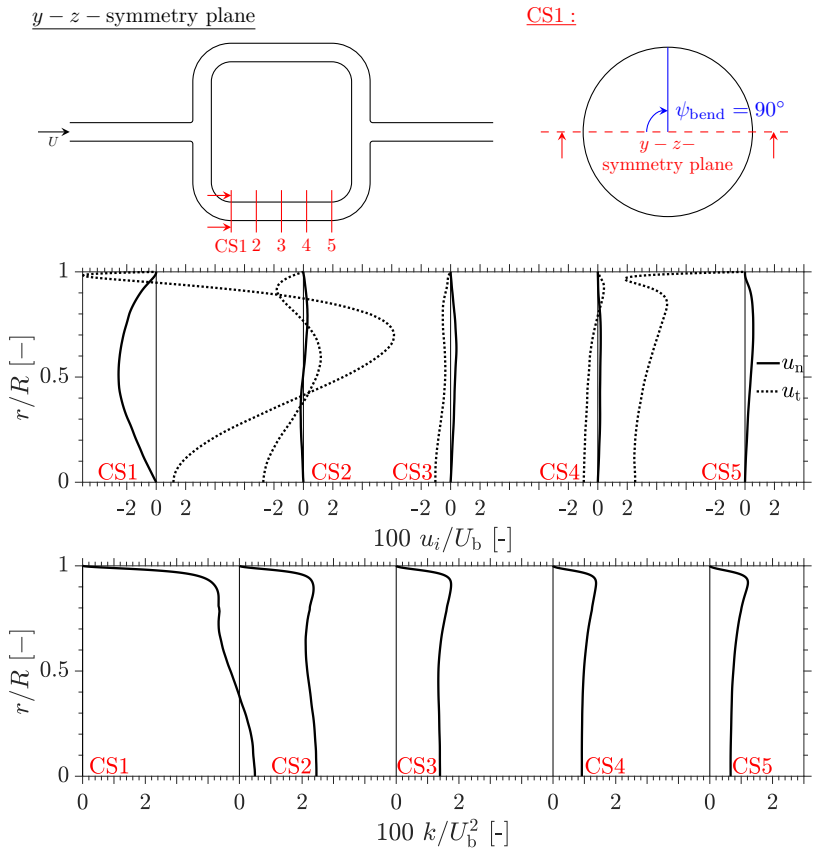


Figure 3.58.: Cross-sectional wall-normal u_n and tangential velocity u_t (middle) and turbulent kinetic energy k/U_b^2 (bottom) from pipe center $r/R = 0$ to pipe wall ($r/R = 1$) along blue extraction line (top, $\psi_{\text{bend}} = 90^\circ$) for selected positions between the first and second deflection as illustrated in the top-sided sketch (cross-section (CS)1 ... 5). The depicted data are derived from averaging over the symmetry planes.

cantly downstream of the outlet of the first deflection, which is consistent with the observed enhanced flow equalization tendency of the first deflection. In the region of the center section of the WSG configuration (CS3), the cross-sectional velocity has nearly disappeared with a maximum cross-sectional velocity of less than 2 % of the bulk velocity. A significant increase in cross-sectional velocity is first seen at the inlet of the second deflection (CS5), which is probably related to the formation of the vortex topology within the second deflection. Thus, the cross-sectional velocity evolution depicted in Fig. 3.58 middle demonstrates that between the first and second deflection, an equalization of the flow and a significant reduction of the cross-sectional velocity occurs. Since the cross-sectional velocity correlates with the convective exchange between the wall and the bulk flow, a comparably low mixing capability exists downstream of the first deflection.

For completion of the analysis, the focus is now on the turbulent kinetic energy and thus the turbulent mixing characteristics of the flow between the first and second deflection. Analogous to the cross-sectional velocity, the turbulent kinetic energy is depicted in Fig. 3.58 bottom with respect to the positions between the first and second deflections (CS1-5). The strongest expression of the turbulent kinetic energy is present at the outlet of the first deflection (CS1). Downstream, a clear and continuous decrease of the turbulent kinetic energy over the entire radius can be seen, which has its minimum expression at the inlet of the second deflection (CS5). The decrease of the turbulent kinetic energy is consistent with the discussion in Fig. 3.56 and the pronounced flow equalization tendency of the first deflection. Subsequently, a strongly decreasing turbulent mixing capability is also present between the first and second deflection, which has its minimum expression in terms of the turbulent kinetic energy at the inlet of the second deflection.

Finally, the experimentally detected pronounced surface degradation around the inlet of the second deflection can be attributed to a strongly reduced flow mixing capability between the first and second deflection. This is caused by an underdeveloped cross-sectional velocity as well as a strongly decreasing turbulent kinetic energy level between both deflections. The origin for this can be found in the upstream located T-junction flow guidance and its characteristic vortex topology. The latter leads to a pronounced cross-sectional secondary motion within the first deflection and to an enhanced equalization tendency of the flow quantities downstream. This suppresses a cross-sectional flow mixing

downstream of the first deflection and favors a heating of the fluid particles near the wall. This distinguishes the region around the second deflection inlet for a susceptibility to a thermally induced phase change. An increased flow mixing capability by means of an enhanced and, in particular, continuously acting cross-sectional velocity could counteract the thermally critical flow condition between the two deflections. An appropriate constructive solution could be to increase the curvature radius of the deflections, which in the most extreme case would lead to a fusion of both to a 180° deflection.

3.8.7. Discussion: Reverse T-junction

Downstream of the second deflection, a non-uniformly distributed velocity and turbulent kinetic energy field is evident from the illustrated $y - z$ -symmetry plane in Fig. 3.50 with weighting towards the outer deflection radius side. The non-uniformly distributed flow fields seem to have their origin in the second deflection and the developing low velocity region downstream of its inner radius. A similar flow topology was illustrated and discussed downstream of the isolated deflection in Fig. 3.20, where the region of low velocity serves as a source of enhanced turbulence production. Besides the non-uniformly distributed flow fields, a pronounced three-dimensional flow pattern is evident from the emerging streamlines within the low velocity region downstream of the inner radius of the second deflection. Emerging streamlines are also observed downstream of the isolated deflection in Fig. 3.20 and can consequently be related to the vortex topology in terms of the Dean vortex evolution within and downstream of the second deflection. The non-uniform, three-dimensional flow pattern remains up to the inlet of the reverse T-junction and increases rather than equalizes. Also within the isolated reverse T-junction, a non-uniform distribution of the velocity and turbulent kinetic energy towards the $x - z$ -symmetry plane is present, but with a considerably weaker and spatially local expression (see Figures 3.41 and 3.50).

How the described flow pattern affects the inflow of the reverse T-junction in comparison to the isolated consideration is presented in Fig. 3.59 by means of the time-averaged velocity magnitude U/U_b (left) and turbulent kinetic energy iso-contours k/U_b^2 in combination with the inplane streamlines of the inlet cross-section (see dotted dark-green line in Fig. 3.50). The upper border represents the beginning of the reverse T-junction inner radius and the dotted

dark-green line the $y - z$ -symmetry plane.

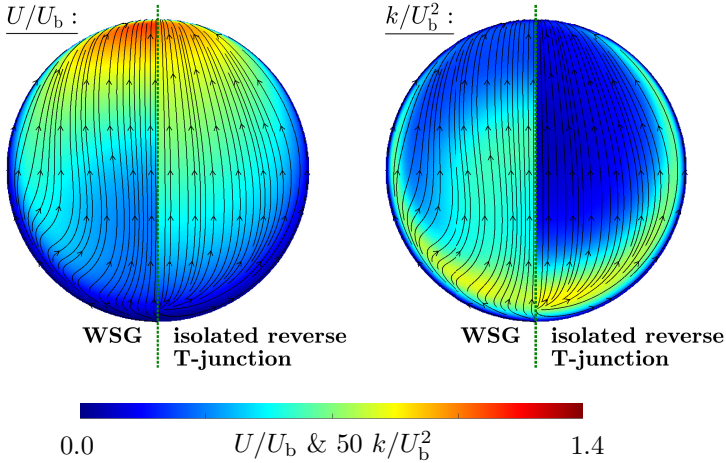


Figure 3.59.: Time-averaged velocity magnitude U/U_b (left) and turbulent kinetic energy k/U_b^2 (right) on the inlet cross-section of the reverse T-junction within the WSG (left, highlighted with a darkgreen dotted line in Fig. 3.50). For comparison, the associated fields of the isolated reverse T-junction (see Chapter 3.7) are also depicted on the inlet cross-section (right). The visualized data are derived from averaging over the symmetry planes.

The flow fields demonstrate similarity with respect to the velocity overshoot around the inner radius (upper boundary) and an increased turbulence level on the opposite side due to the streamline roll-up. The formation of the latter is discussed in detail in Chapter 3.7.4. Within the bulk flow, the flow exhibits a fundamentally contrary characteristic. Compared to the isolated consideration, a reduced velocity magnitude and increased turbulent kinetic energy are present in the cross-section center within the WSG. The region of increased turbulence level extends to the bulk flow in a mushroom shape and demarcates the region of reduced velocity magnitude. A similar cross-sectional flow pattern has been observed downstream of the deflection in

Fig. 3.25 with a mushroom-shaped region of increased turbulence level, which was attributed to the decaying vortex topology of the isolated deflection, and a horseshoe-shaped region of high velocity magnitude. Therefore, the deviating flow pattern depicted in Fig. 3.59 can be attributed to the second deflection, which illustrates the superimposed flow topology within the WSG and the mutual influence of its geometrical components. The described flow topology is presumably also the cause of the higher velocity peak around the inner radius of the reverse T-junction, since the flow has to swerve the region of reduced velocity magnitude around the cross-section center.

The inflow conditions into the reverse T-junction (see Fig. 3.59) seems to provoke a deviation in the flow topology between the isolated consideration and within the WSG. The flow detachment around the inner radius of the reverse T-junction, the emergence of a low velocity region downstream as well as an enhanced turbulent production within the shear layer between the bulk flow and the region of low velocity are similar to the isolated consideration as can be observed in Fig. 3.50. For a detailed discussion the reader is referred to Chapter 3.7.6. In contrast, the symmetrical impingement of the inflows within the $x - z$ -symmetry plane does not appear to imply any streamline roll-up within the WSG evident from the streamline shape in Fig. 3.50. Rather, the streamlines indicate an almost complete deflection in the direction of the WSG outlet. The deflected streamlines adapt comparatively fast to the flow guidance and become wall-parallel shortly after the reverse T-junction, indicating a flow jet around the pipe center. The confluence of these streamlines coincides with an additional region of increased turbulence production around the $x - z$ -symmetry plane. In addition, the region of increased turbulence downstream of the inner radius is significantly reduced in its spatial extension, which could be an indicator for an enhanced cross-sectional secondary motion and thus a comparably stronger flow equalization tendency in contrast to the isolated consideration.

The inplane streamline pattern in the outlet cross-section of the reverse T-junction of the WSG (see magneta dotted line in Fig. 3.50) reveals a double symmetric vortex topology. This has already been elaborated in Chapters 3.7.4 and 3.7.5 and is characteristic for the isolated consideration. However, the double symmetric vortex topology within the WSG is significantly reduced in its spatial extension in the cross-section. The vortex tubes do not extend over the entire cross-sectional quarter and are restricted to the region near the

wall far from the $y - z$ -symmetry plane. Around the $y - z$ -symmetry plane, streamlines extend from the inner radius of the reverse T-junction (upper and lower boundary) to the pipe center, which are presumably connected to the flow jet described within the flow topology in the $y - z$ -symmetry plane. The confluence of the streamlines within the WSG coincides with the region of increased turbulence level, which was previously detected in the $y - z$ -symmetry plane along the $x - z$ -symmetry intersection.

In order to elaborate the deviations between the isolated consideration and the WSG step by step, Fig. 3.60 compares the velocity and turbulent field including the inplane streamlines within the $x - z$ -symmetry plane of the WSG (top) with the isolated consideration (bottom). For orientation, the $y - z$ -symmetry plane is highlighted by a black dashed line and the outlet of the reverse T-junction by a magenta dotted line (see also Fig. 3.50).

In the center of the inflow impingement (see Fig. 3.60 top & left), a saddle point is formed in the isolated consideration, which represents a source of streamlines and these spread radially as discussed in Fig. 3.41. The formation of a saddle point and the radial streamline spreading are not clearly evident within the WSG. Instead, a reduced radial streamline spread from an eventual saddle point can be observed significantly closer to the (left, see Fig. 3.60) wall and displaced by a multitude of emerging streamlines. The emerging streamlines are mainly oriented towards the outlet and seems to cause a distinct wall-parallel streamline formation around the pipe center, which was previously observed and denoted as flow jet in Fig. 3.50. This flow jet is accompanied by an enhanced turbulent production as evident from Fig. 3.60 bottom. Its strongest expression can be observed around the reverse T-junction outlet (see magenta dotted line in Fig. 3.60) with two peaks, one close to the wall and another near the $y - z$ -symmetry plane. This double peak is also evident within the visualized flow field at the outlet of the reverse T-junction in Fig 3.50, which allows an assessment of the origin due to the depicted inplane streamlines. The near-wall peak of the turbulent kinetic energy can be probably assigned to the streamlines deflected by the symmetrical inflow impingement along the wall and the formation of the double-symmetric vortex tubes. The second peak near the $y - z$ -symmetry plane seems to be related to the confluence of the pipe center directed streamlines and the forming flow jet. Although this double peak formation has a dominant influence in the outlet of the reverse T-junction in Fig. 3.60 bottom, the peak downstream

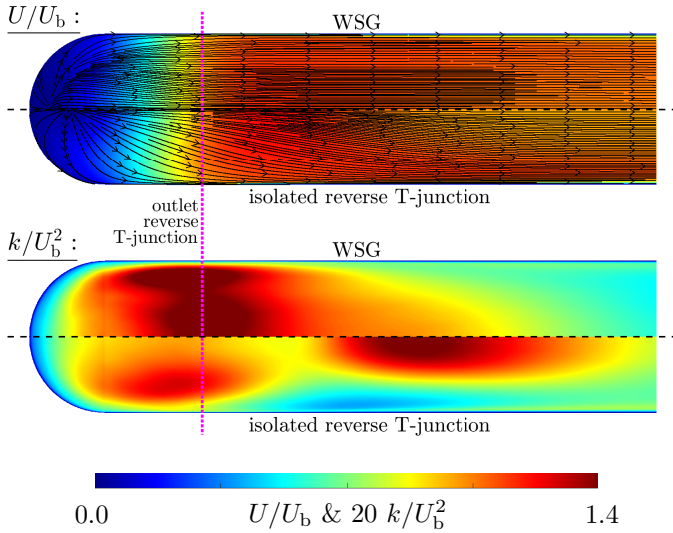


Figure 3.60.: Time-averaged velocity magnitude U/U_b (top) and turbulent kinetic energy k/U_b^2 (bottom) on the $x-z$ -symmetry plane of the reverse T-junction within the WSG and the isolated consideration. The $y-z$ -symmetry plane is highlighted by a black dashed line and the outlet of the reverse T-junction by a magenta dotted line (see also Fig. 3.50). The visualized data derived from averaging over the symmetry planes.

of the inner radius visible in Fig. 3.50 is still the dominant one within the outlet cross-section of the reverse T-junction. However, the depicted peak formation in Fig. 3.60 bottom clearly weakens downstream of the outlet region and equalizes over the pipe cross-section at approximately two diameters downstream. The presented turbulence topology within the WSG deviates from the isolated consideration, which also exhibits two regions of enhanced turbulent production. The first region within the isolated consideration is located upstream of the reverse T-junction outlet and corresponds to the location of rotational flow character observed in Fig. 3.44. This suggests a relationship with the formation process of the double-symmetric vortex

topology, and thus a similar origin as the near-wall peak within the WSG. The second region is located approximately two pipe diameters downstream of the reverse T-junction near the $y - z$ -symmetry plane. This region coincides with the vortex decaying process depicted in Fig. 3.45 and can be related to the viscous dissipation of the double-symmetric vortex topology. Especially the latter region differs from the flow topology within the WSG and indicates a spatially more long-lived vortex topology within the isolated consideration.

Thus, the deviating inflow and the formation of a pipe-center located flow jet within the WSG seems to provoke an enhanced turbulence production around the reverse T-junction outlet compared to the isolated consideration. The increased turbulence level appears to have a positive effect on flow equalization, as indicated by the rapid decrease and equalization of turbulence downstream of the reverse T-junction. Furthermore, the two dominant flow mechanisms within the isolated consideration (streamline roll-up and formation of a double-symmetric vortex topology) seem to be underdeveloped within the WSG. Hence, a different flow evolution downstream of the reverse T-junction within the WSG can be expected, especially due to the indicated more directed flow equalization in Figures 3.50 and 3.60. For a deeper insight into the deviating flow evolution downstream of the reverse T-junction of the WSG, the time-averaged velocity magnitude U/U_b and turbulent kinetic energy k/U_b^2 iso-contours are depicted within selected cross-sections along the WSG outlet coordinate $s_{\text{WSG,out}}^* = s_{\text{WSG,out}}/D$ in Fig. 3.61. The WSG outlet coordinate $s_{\text{WSG,out}}^*$ originates at the outlet of the reverse T-junction and points in the direction of the WSG outlet as defined in Fig. 3.50. Additionally, the time-averaged inplane streamlines are depicted to illustrate the vortex topology evolution downstream of the reverse T-junction. The $s_{\text{WSG,out}}^* = 0$ cross-section is already visualized in Fig. 3.50 and is only depicted again to illustrate the total vortex evolution.

The inplane streamline contour in the outlet cross-section of the reverse T-junction ($s_{\text{WSG,out}}^* = 0$; previously discussed in Fig. 3.50) with the double-symmetric vortex tubes close to the wall and a flow directed from the reverse T-junction inner radius (top and bottom border) to the pipe center experiences a significant variation downstream of the reverse T-junction. For $s_{\text{WSG,out}}^* = 0.5$, the near-wall vortex tubes convect towards the upper and lower borders of the cross-sections near the $y - z$ -symmetry plane. The vortex centers are located in the wake of the inner radius, which represents a region of low velocity and

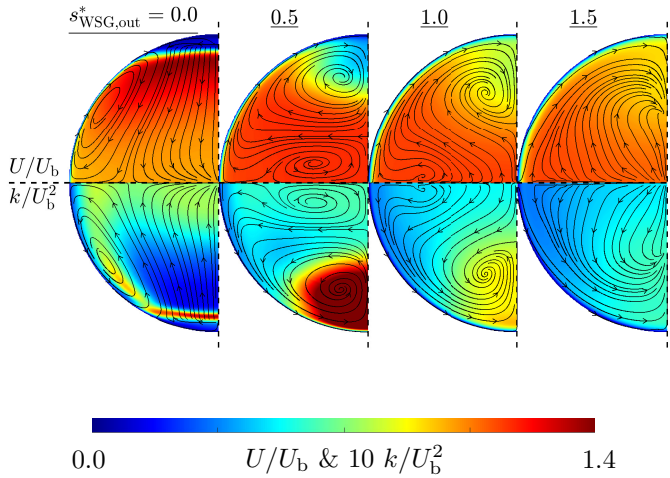


Figure 3.61.: Time-averaged velocity magnitude U/U_b (top) and turbulent kinetic energy k/U_b^2 (bottom) as well as time-averaged inplane streamlines within selected cross-sections downstream of the reverse T-junction within the WSG. The visualized data are derived from averaging over the symmetry planes.

increased turbulence level as discussed in Fig. 3.50. The observed streamlines pointing from the upper/lower cross-sectional borders towards the pipe center ($s_{\text{WSG,out}}^* = 0$) seems to form a second double-symmetric vortex structure near the pipe center, which rotates contrary to the preceding vortex tubes. Despite the deviating inplane velocity, the velocity magnitude and turbulent fields for $s_{\text{WSG,out}}^* = 0.5$ act quite similarly compared to the isolated observation in Fig. 3.42. The second double-symmetrical vortex structure convects along the $x-z$ -symmetry plane to the wall and clearly decreases in its spatial expansion ($s_{\text{WSG,out}}^* = 1.0$). Concurrently, the preceding vortex structure shifts towards the pipe center with a simultaneous relaxation of the streamline curvature and an equalization of the velocity magnitude and turbulent kinetic energy

across the cross-section. Further downstream ($s_{\text{WSG,out}}^* = 1.5$), no vortex structures can be observed within the cross-section. The flow fields exhibit a clear cross-sectional equalization and the effects of the inner radius wake are hardly identifiable. The additional double-symmetrical vortex structure and its interaction with the preceding vortex topology seems to contribute to a rapid cross-sectional flow equalization. This can be inferred by considering the fact that the wake of the inner radius and the vortex tubes are still clearly visible in the cross-section of the isolated consideration depicted in Fig. 3.42 for $s_{\text{rTJ}}^* = 1.5$.

To evaluate the flow equalization and the fluid-wall interaction affected by the flow topology of the reverse T-junction within the WSG, the friction $C_f = \tau_w / (0.5\rho U_b^2)$ (top) and pressure coefficient $C_p = (p - p(s_{\text{WSG,out}}^* = 3.0)) / (0.5\rho U_b^2)$ (bottom) are depicted along the WSG outlet coordinate $s_{\text{WSG,out}}^*$ in Fig. 3.62 in comparison to the isolated consideration (circles). The depictions in Fig. 3.62 represent the intersection between the $y - z$ -symmetry plane and the wall. The region of the inner radius curvature is highlighted in gray and the corresponding friction coefficient is depicted enlarged over the inner radius angle $\varphi_{\text{WSG,out}}$.

The pressure and friction conditions upstream of the inner radius act quite similar to the isolated consideration despite the non-uniform inflow due to the upstream located second deflection discussed in Fig. 3.50. This implies a similar near-wall velocity gradient, which was not obvious, especially considering the deviating flow topology within the $y - z$ -symmetry plane illustrated in Fig. 3.50. Furthermore, a comparable pressure loss over the reverse T-junction is present despite the deviating flow and vortex topology compared to the isolated consideration discussed in Fig. 3.61. In general, the friction and pressure coefficients are quite similar to the isolated consideration, which is why the reader is referred to the discussion along Fig. 3.62 for a detailed evaluation. Noteworthy here is the identical position of the beginning and end of the region of low velocity around the inner radius, marked by the first and last zero-crossing of the friction coefficient. Compared to the isolated consideration, the peak values within the WSG are more pronounced for both, the friction and pressure coefficient. The enhanced positive peak of the friction coefficient at the beginning of the inner radius curvature ($s_{\text{WSG,out}}^* \approx -0.25$) can be attributed to the increased velocity magnitude around the inner radius, illustrated and discussed in Fig. 3.59. Complementary, the pressure coefficient

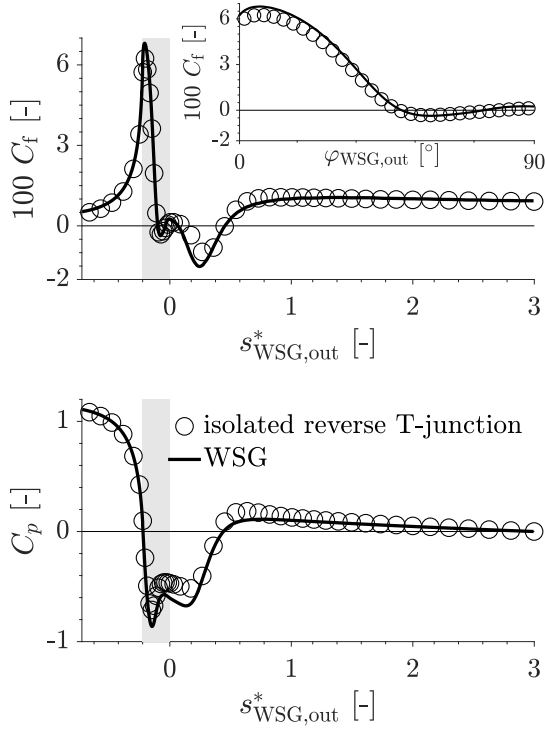


Figure 3.62.: Friction $C_f = \tau_w / (0.5\rho U_b^2)$ (top) and pressure coefficient $C_p = (p - p(s_{WSG,out}^* = 3.0)) / (0.5\rho U_b^2)$ (bottom) along the outlet coordinate $s_{WSG,out}^*$ within the intersection of the wall and the $y - z$ -symmetry plane in comparison to the isolated consideration (circles). The region of the inner radius curvature is highlighted in gray and the corresponding friction coefficient is depicted enlarged over the inner radius angle $\varphi_{WSG,out}$.

also demonstrates a more pronounced drop around the inner radius with a lower pressure level, which indicates a stronger flow acceleration at the beginning of the inner radius and can be consequently related to the higher friction peak. In contrast, the cause of the more pronounced negative friction

peak at $s_{\text{WSG,out}}^* \approx 0.3$ is probably due to the deviating vortex topology within and downstream of the reverse T-junction of the WSG, discussed in Fig. 3.61. Between $s_{\text{WSG,out}}^* = 0$ and 0.5, the vortex structure migrates to the inner radius demonstrating a closer vortex center to the wall as the isolated consideration, which leads to a stronger interaction with the wall and probably to an increased shear effect of the flow. With respect to the indicated rapid equalization of the flow downstream of the reverse T-junction observed in Figures 3.60 and 3.61, the friction and pressure coefficient exhibit a damped response for $s_{\text{WSG,out}}^* > 0.4$ compared to the isolated consideration. The over-swinging in the form of a positive pressure peak at $s_{\text{WSG,out}}^* = 0.6$ is clearly reduced within the WSG, which results in an underdeveloped sign change in the present pressure gradient. The smoother response of the pressure coefficient around $s_{\text{WSG,out}}^* = 0.6$ is accompanied by a reduced friction. A significantly faster equalization of the flow within the WSG downstream of the reverse T-junction is not clearly evident from the C_f and C_p evolutions. However, the entirety of depicted flow fields (see Figures 3.50, 3.60 and 3.61) clearly indicates the increased flow equalization tendency downstream of the reverse T-junction of the WSG compared to the isolated consideration.

Considering the post-experimental WSG sample shown in Fig. 3.54, an pronounced surface degradation can be observed around the inner radius of the reverse T-junction beside the inlet region of the second deflection. As evident from Fig. 3.62, the region around the inner radius is characterized by a high shear stress of the flow as well as a strong pressure drop, which are even more pronounced within the WSG as in the isolated consideration. Additionally, the region of low velocity downstream of the inner radius features a reduced convective transport and is predestined for a local heating of the near-wall fluid. Consequently, the flow topology around the inner radius is predestined for a pressure and/or thermally induced phase change event as well as an increased surface stress as a result of the flow and any contaminants added. Here, a geometric modification of the inner radius would be advantageous to reduce the experimentally detected second surface degradation spot. This can probably be achieved by a smoother transition within the reverse T-junction and could be realized with a larger inner radius.

3.8.8. Conclusion and outlook

The flow topology within the newly designed WSG is investigated by using a well-resolved, highly comprehensive LES including over 290 million cells suitable for serving as a database for future experimental and numerical studies. A detailed flow discussion of the WSG and its geometrical components is done including the isolated flow discussions from the preceding chapters with the 90°-pipe bend in Chapter 3.5 as well as the T-junction and reverse T-junction elaborated in Chapters 3.6 and 3.7. In addition, the inlet region of the WSG upstream of the T-junction is examined to determine pipe necking related effects.

The pipe necking, which is located upstream of the WSG sample and has its origin in the experimentally used sample holder, has an influence on the flow in the inlet region of the WSG and provokes a deviating flow condition to a fully developed pipe flow. However, this effect weakens in intensity towards the T-junction flow guidance. In the immediate vicinity of the T-junction, the influence of the pipe necking vanishes and the flow characteristics coincide with the isolated consideration. Consequently, the pipe necking is located far enough upstream and does not have a serious impact on the flow topology within the WSG. The flow topology within the T-junction is identical to the isolated consideration, most likely due to comparable inflow conditions. The evaluation of the flow topology is based on qualitative assessment of streamline patterns including the vortex topology as well as the evolution of the near-wall velocity gradient in terms of the friction coefficient. Deviations from the isolated consideration only arise in the immediate vicinity of the first deflection. The flow discussion of the first and second deflection is conducted from a problem-oriented perspective with the experimentally detected pronounced surface degradation around the inlet of the second deflection in focus. The flow topology within the first deflection is dominated by the upstream located T-junction and is characterized by an enhanced cross-sectional secondary motion. This leads to a rapid equalization of the flow and thus a reduction of the cross-sectional velocity as well as the turbulent kinetic energy downstream. Both decreases cause a significantly poorer cross-sectional flow mixing capability normal to the wall between both deflections and predestined this region for a significant heating of the near-wall fluid due to a reduced exchange with the bulk flow. As a consequence, the end of the straight pipe section is particularly susceptible to thermally critical effects such as flow boiling and

critical boiling states (e.g. film boiling). This can lead to enhanced thermal stresses within the flow guidance wall and could be the initial mechanism for experimentally detected surface degradation. The extension of the area of pronounced surface degradation under thermally more critical conditions upstream and the limitation around half of the second deflection due to the arising vortex topology support the postulated thermally induced initial damage mechanism. An appropriate constructive solution to counteract surface degradation could be the reduction or avoidance of a straight pipe section between the first and second deflection, leading to a continuous 180° deflection in its strictest form. A continuous vortex structure within the deflection would be provoked, which could cause an increased and especially continuous cross-sectional secondary motion. This would lead to an enhanced cross-sectional flow mixing characteristic along the entire deflection and could prevent local overheating of the near-wall fluid. The last geometrical component within the WSG, the reverse T-junction, deviates from the isolated consideration mainly in the resulting vortex topology, which is characterized by a flow jet around the pipe center and an additional double-symmetric vortex structure. The latter likely causes pronounced cross-sectional secondary motion and thus an enhanced flow equalization downstream of the reverse T-junction. Despite the difference in vortex topology, the friction and pressure coefficients within the $y - z$ -symmetry plane (along $s_{\text{WSG,out}}^*$) are qualitatively similar to the isolated consideration, but with increased peak values due to an enhanced flow acceleration and the wall-closer vortex topology. The increased wall shear of the flow and the rapid pressure drop within the inner radius as well as the low velocity region downstream endanger this region for abrasive flow phenomena, which has also been experimentally determined by eroding the inner radius of the reverse T-junction. In order to reduce wall abrasive effects within the inner radius of the reverse T-junction, a smoother transition is advisable, which can be implemented constructively by a larger inner radius.

Multiple correlations between the WSG and the isolated considerations could be identified with the flow discussions of the isolated geometrical components of the WSG in Chapter 3.5, 3.6 and 3.7. The isolated considerations provided a fundamental basis for the discussion of the WSG flow topology in Chapter 3.8 and enabled an in-depth understanding of the interference of isolated flow characteristics. The two spots of experimentally detected pronounced surface degradation could be linked to the flow topology, the possible initial mechanisms

identified and possible constructive solutions postulated.

In further investigations in the scope of WSG, the constructive solutions postulated in the previous discussion to avoid surface degradation should be validated experimentally and numerically. A continuous increase of the deflection radii as well as of the inner radius of the reverse T-junction is advisable, whereby, for the deflections, the extreme condition of a merged 180° deflection should be considered. In addition, a parameter study of the ratio of pipe diameter to inner radius could be insightful for the vortex generation process and a possible specific adjustment of the vortex topology within the T-junction and reverse T-junction, as especially the circular cross-sectional shape contributes to the emerging vortex topology. And last but not least, the extension of the present flow discussion to the missing volume fluxes listed in Table 3.2 with an adequate turbulence modeling strategy as well as the inclusion of the thermally heated flow configuration are unavoidable for further approximation to the experiments conducted in a complementary manner. A challenging task in the thermally heated case is the reproduction of the flow boiling process with a reasonable effort for the industry representatives within the BMWi project, where the Euler-Euler methodology intensively studied by Krepper and Rzehak (2011) and Krepper et al. (2013) could be a possibility.

3.9. Conclusions and outlook

Chapter 3 'IC-engine-relevant cooling channel configuration: Water Spider Geometry (WSG)' examines the newly designed generic cooling channel flow guidance called Water Spider Geometry (WSG) under isothermal flow conditions with the objective to identify the flow topology, detect critical positions with respect to thermal and erosive degradation and develop constructive countermeasures. Due to the newly designed flow guidance and the lack of meaningful reference data, well-resolved, highly comprehensive Large-Eddy Simulations (LESs) form the basis to provide a reliable assessment of the flow topology and, concurrently, to serve as a reference solution for further investigations. Preliminary investigations were carried out to select a suitable SGS model (WALE, according to Nicoud and Ducros, 1999) and develop an efficient meshing strategy within pipe configurations ('O-grid' arrangement, $R_{\text{block}}/R_{\text{inner}} = 0.8$, $\Delta z^+/\Delta\varphi^+ = 3$, $l_{\text{pre}} = 2.5 D$). The WSG contains three geometrical components, the 90°-pipe bend, T-junction and reverse T-junction, each of them is a standard geometry in a variety of engineering applications. With the exception of the 90°-pipe bend, a lack of meaningful reference data exists in literature for these geometries. Knowledge of the flow topology within the isolated geometrical components is essential for the superimposed consideration within the WSG. The flow discussion of the isolated geometries was preceded to the discussion of the WSG.

The preliminary investigation of the isolated 90° pipe-bend clarified the formation and influence of the vortex structure on the flow topology with the Dean vortex, its associated tertiary vortex as well as a wall-bounded secondary vortex. The circulation evolution of the Dean vortex allowed to determine a possible initial value from which the secondary vortex structures emerge and is identified to $Re_{\Gamma}/De = 0.95$. The latter requires further investigation to identify a possible general validity. The targeted influence on the vortex topology could be suitable to minimize erosive processes in relevant technical applications, and varying the bend curvature could be an appropriate constructive measure with respect to the Dean number. Conversely, such measures may have a negative influence on the turbulence production and consequently the flow mixing capability within and downstream the 90°-pipe bend, which has to be included in the considerations in view of a possible thermal load on the wall.

The isolated consideration of the T-junction allows an insight into the flow dominating mechanisms with the impingement onto the pipe-curved counter-wall and flow detachment around the finite inner radius. Former provokes a counter-rotating vortex tube pair, which dominates the wall-shear stress and turbulence production within the T-junction and could be detected up to $4.7 D$ downstream of the T-junction flow guidance. The flow detachment around the inner radius is accompanied by a low pressure level and a strong tendency for phase change. Downstream, a low velocity region forms with a complex alternating wall load in the vicinity of the inner radius and a reduced convective exchange with the bulk flow. Former could be critical in terms of the joining technique and latter could provoke an overheating of the fluid in the case of heated walls. Critical zones are closely related to the inner radius of the T-junction, which should therefore be the initial focus for structural improvement. A smooth transition with a larger inner radius could reduce the pressure drop and the spatial expansion of the low velocity region. The equalization of the flow is dominated by the vortex topology and appropriate measures for targeted adjustment could be the bulk velocity and the pipe diameter, which determines the curvature of the pipe-curved counter-wall and the angle of deflection.

A characteristic double-symmetric vortex topology downstream of the reverse T-junction is identified within the isolated consideration and determined to be the main cause for a pronounced cross-sectional secondary motion and enhanced flow equalization tendency. The vortex structure can be recognized $2.8 D$ downstream and has its origin in the symmetrical inflow impingement and the associated streamline roll-up. The vortex structure within the reverse T-junction also has a dominant influence on the wall load around the outlet of the reverse T-junction flow guidance. The inner radius provokes a flow detachment and is accompanied with the lowest pressure and highest wall shear. Both is critical due to wall abrasive effects and a possible phase change event. Downstream, a low velocity region forms with an alternating wall stress, which could be critical with respect to the joining technique. The transition region between the wake of the inner radius and the bulk flow is the turbulence determining region within the reverse T-junction and contributes to an enhanced turbulent mixing downstream within a region of low convective exchange. Here, as well as for the isolated T-junction, the considerations are limited to a single Reynolds number, which makes a general validity of the

discussion difficult and a parameter study with respect to the Reynolds number would be appropriate. However, the flow topology around the inner radius seems to provoke critical flow conditions here as well, which could probably be mitigated by increasing the inner radius. Furthermore and in addition to the bulk velocity, the pipe diameter seems to be suitable for specifically influencing the vortex topology and consequently the cross-sectional secondary motion characteristic.

The Water Spider Geometry (WSG) flow discussion provided a fundamental insight into its flow topology and contributed to the clarification of the experimentally observed regions of pronounced surface degradation. In addition, the upstream located pipe necking was demonstrated to have no serious influence on the flow topology within the WSG and the flow within the T-junction act quite similarly to the isolated consideration. The experimentally detected pronounced surface degradation around the inlet of the second deflection has its origin probably in the reduced cross-sectional mixing characteristics between the first and second deflection. The vortical flow pattern within the T-junction causes a fundamentally different flow topology within the first deflection in comparison to the isolated consideration and results in a rapid flow equalization within and downstream of the first deflection. The latter causes a poorer convective exchange of the near-wall and bulk flow, which favors an overheating of the near-wall fluid and increases the surface-damaging boiling tendency of the flow. The spatial expansion of surface degradation in the experiments occurs upstream as the thermal critical conditions increases. Downstream, the developing vortex topology within the second deflection counteracts and favors an increased convective exchange. An appropriate constructive solution could be the reduction or avoidance of a straight pipe section between the first and second deflection, leading to a continuous 180° deflection in its strictest form. A permanently existing continuous vortex structure within the deflection would be provoked, which would cause an increased and continuous cross-sectional mixing characteristic of the flow over the entire deflection and prevent local overheating of the near-wall fluid. A second experimentally observed location of pronounced surface degradation around the inner radius of the reverse T-junction coincides with the critical flow condition recognized in the isolated consideration in the context of flow detachment. A similar but more pronounced flow topology is present around the inner radius of the reverse T-junction within the WSG, with a stronger

expression caused by the deviating flow and vortex topology. In order to defuse this region, a smoother transition is advisable, which can be implemented constructively by a larger inner radius.

The flow topology and the dominant mechanisms within the WSG and its isolated geometrical components are captured with well-resolved, highly comprehensive LESs and related, contributing to a deeper insight into mechanism of actions within the WSG. The LESs claim to be reference solutions and serve as a basis for further research in the field of WSG. Critical positions with regard to possible surface degradation are identified and solutions are proposed. However, attention has to be paid to the validation of the solution proposals in the further investigations, whether experimental or numerical or complementary. Furthermore, the considerations should be extended to the remaining volume fluxes/Reynolds numbers listed in Table 3.2, which are available for the isolated consideration of the T-junction and reverse T-junction, but would have gone beyond the scope of the present work. For the WSG, the use of hybrid RANS/LES methods could be considered, as the present WSG simulation with the lowest volume flux has explored the limits of the available computational capacity. But also RANS-based RSM could be a possibility, as they represent a cost-efficient compromise between computational resources and physically correct consideration of the flow with, e.g., the anisotropy effects of the Reynolds stress tensor. Finally, the extension to non-isothermal flow conditions and the numerical modeling of the boiling process with an industrially justifiable effort has to be focused. A multitude of investigations have already been done within the scope of the WSG, which are not subject of the present work, and have highlighted the research requirements in the field of flow boiling. A suitable starting point could be the Euler-Euler methodology, in which for example Krepper and Rzehak (2011) and Krepper et al. (2013) have already done intensive groundwork. In addition to further research efforts in the field of WSG, the general validity of the initial value for the emergence of secondary structures of $Re_{\Gamma}/De = 0.95$ within the 90° -pipe bend configuration should also be focused. This could be a powerful instrument for a variety of engineering applications to selectively modify the vortex topology and consequently the fluid mechanical properties of deflections.

4. Development of an ω_h -based elliptic-blending-related Reynolds-stress model

The extensive study of the Water Spider Geometry (WSG) and its isolated geometrical components in Chapter 3 has highlighted the multiple flow phenomena characterizing the flow topology within the geometries with various flow detachments and reattachments as well as impingements accompanied by a frequent alternation of flow acceleration and deceleration. Besides the multiple flow phenomena, the frequent flow deflections and the circular cross-section cause a distinctive vortex topology, which has a dominant influence on the cross-sectional, wall-normal flow pattern as well as on the turbulence production within the WSG. The Large-Eddy Simulation (LES) study of the WSG and its isolated geometrical components are accompanied by an enormous computational effort, which has its justification in the gap of meaningful reference data in the literature and is intended to serve as a reference basis for further investigations. These investigations, which are mainly focused on parameter studies, consideration of additional flow phenomena (non-isothermal) as well as the verification of the constructive proposals postulated in Chapter 3.8.8, require a significantly more cost-efficient numerical framework. Applying the same LES framework would be disproportionate and would compromise the intent of Chapter 3. More cost-efficient numerical frameworks could be based on scale-resolving simulations, where hybrid RANS/LES methods would be appropriate to model the turbulence with less effort than LES. Various new developments and improvements in the field have been made in recent years, but have in common a transient problem approach and a necessary time-averaging of the flow quantities. Although scale-resolving simulations are advantageous in particular for capturing the turbulent mixing capability of the

flow, the time-averaging procedure of the flow variables entails an enormous additional time effort, which can be critical especially in industrial applications. Thus, despite the continuous developments of hybrid RANS/LES methods, the industrial standard continues to be RANS-based methods due to the possibility of a steady-state approach and the associated omission of time-averaging.

The complex flow topology within the WSG and its distinct vortex topology motivated the development of a near-wall Reynolds Stress Model (RSM), which focuses on the correct reproduction of flow conditions in the region of adverse pressure gradient (APG) and the avoidance of the well-known problem of streamline backbending around the reattachment point. The modeling strategy as well as the validation of the model using various well-known benchmark configurations is presented in the following.

4.1. Introduction

Differential Reynolds Stress models (RSM), known also as Second-Moment Closure (SMC) models, implying the solving of the equations governing the dynamics of all six Reynolds stress components, represent certainly the highest modeling level in the RANS computational framework. They are inherently capable of treating a number of features departing substantially from those encountered in simple fully developed wall-parallel flows obeying the state of equilibrium: Effects of variable pressure gradients, flows affected by streamline curvature originating from the configuration guidance, but also characterizing separating and reattaching flows as well as swirling and rotating flows. It can be generally said that all three-dimensional flows exhibit strong departure from the conditions underlying the logarithmic law for the velocity field and two associated features related to local equilibrium between the production and dissipation of the turbulent kinetic energy $k = \overline{u_i u_i} / 2$ ($P_k = \varepsilon$) and the uniformity of the Reynolds stress structure parameters $\overline{u_i u_j} / k$. Unlike eddy-viscosity based RANS models carrying no information about the Reynolds stress anisotropy into the momentum equation, the RSM can inherently differentiate between both the strength of wall-related viscous effects and the kinematic wall blockage, with the latter representing the rationale of the Reynolds stress anisotropy.

The most near-wall RSM versions being in use nowadays are heavily based on the model formulations proposed in the seventies of the last century by

Hanjalic and Launder (1972), Launder et al. (1975) and Gibson and Launder (1978), representing their high Reynolds number asymptotes. Here, a first near-wall RSM derived by Hanjalic and Launder (1976) to account for the viscous sublayer should also be mentioned. A common procedure of adapting these models to the near-wall region is to account for the near-wall-related terms, such as the gradient production term $P_{\varepsilon,3}$ (i.e., $P_{\omega,3}$) in the dissipation rate equation, and, more importantly, to adequately express the model coefficients as functional dependencies on the wall-proximity processes. The latter are governed by the viscosity-related effects (represented, e.g., through the Reynolds number of turbulence $Re_t = k^2/(\nu\varepsilon)$) and turbulence anisotropy effects (represented through the invariants of the Reynolds-stress anisotropy tensor $a_{ij} = \overline{u_i u_j}/k - 2\delta_{ij}/3$) and is related in particular to the pressure-strain model term Φ_{ij} and the stress-dissipation correlation ε_{ij} . Accordingly, the prime goal is to return the correct asymptotic behavior of both the Reynolds stress and the stress-dissipation components when approaching the solid wall. The near-wall RSM by Hanjalic and Jakirlic (1998) (see also Hanjalic et al., 1995), its homogeneous-dissipation-based variants by Jakirlic and Hanjalic (2002) and Jakirlić and Maduta (2015), with the pressure-strain model term representing a linear formulation in terms of a_{ij} (in line with the Gibson and Launder (1978) proposal), are such examples. In addition to a_{ij} the model coefficients are modeled also in terms of the stress-dissipation anisotropy $e_{ij} = \varepsilon_{ij}/\varepsilon - 2\delta_{ij}/3$ with $\varepsilon = \varepsilon_{ii}/2$ representing the dissipation rate of the kinetic energy of turbulence. The inclusion of the model coefficients dependency on viscous and non-viscous anisotropy effects has also been utilized by Craft (1998), but in the framework of a much more complex pressure-strain term model, formulated in terms of a_{ij} up to third order. A relevant overview of different proposals for the Φ_{ij} -model coefficients can be found in Jakirlic and Hanjalic (2013).

One of the most interesting RSM proposal has been formulated by Durbin (1993). He introduced the so-called Elliptic Relaxation Method (ERM) applied to a quasi-homogeneous model of the redistribution term accounting herewith for the wall-related mean flow and turbulence inhomogeneities. The relevant so-called elliptic relaxation operator also comprises a non-weighted form of the stress-dissipation correlation model. Accordingly, this tensorially consistent formulation waived the necessity to express the model coefficients in the form of adequately designed, mostly in an ad-hoc manner, functional relationships.

The quasi-homogeneous Φ_{ij} model variant utilized by Durbin (1993) as the source term in the corresponding elliptic relaxation equation consisted of the return-to-isotropy and the isotropization-of-production proposals for the slow and rapid redistributive terms, respectively. Both model terms are amongst others specified in Launder et al. (1975). However, this procedure can be universally applied to any other model scheme, as convincingly illustrated by Wizman et al. (1996). Here, both the Speziale et al. (1991) quadratic formulation has been adopted as well as the cubic formulation by Craft and Launder (1996) (specified also in Craft, 1998).

Manceau and Hanjalić (2002) adopted Durbin's elliptic relaxation approach, but instead of solving the equation for the entire elliptic relaxation tensor f_{ij} , they replaced it by its scalar counterpart, the elliptic relaxation function f , as also applied in a similar form in the eddy-viscosity version ($\overline{v^2} - f$) of the elliptic relaxation model of turbulence, Durbin (1991). Herewith, the number of elliptic relaxation equations to be simultaneously solved is significantly reduced, but the important structural features of the baseline Durbin's RSM, especially with respect to the non-local wall blockage, are preserved. In addition, this new model formulation, termed as 'elliptic blending' (EB) RSM, short Elliptic Blending Model (EBM), provides wall-boundary conditions for the elliptic blending function (denoted by α) being less sensitive to the wall distance y . For comparison, f_{ij} behaves proportional to y^{-4} as it approaches the solid wall. Finally, the function α , representing the solution of an adequately simplified elliptic equation, is utilized as a blending function between the quasi-homogeneous, off-wall redistributive pressure-strain model term (the model from Speziale et al. (1991) has been adopted) and its near-wall related expression, the formulation of which satisfies the corresponding wall-approaching asymptotic behavior. The same function α is used for modeling the stress dissipation correlation to appropriately link its wall-vicinity related anisotropic formulation and Rotta's off-wall isotropic counterpart. Manceau (2015) gave a recapitulation of the EBM progress by means of its physical rationale and application. A number of other publications adopted the elliptic blending idea within the Reynolds stress modeling concept, as, e.g., Thielen et al. (2005), Billard et al. (2012) and Sporschill et al. (2021).

The present modeling activity represents an upgrade of the linear pressure-strain correlation model by Jakirlić and Maduta (2015) towards a non-linear quadratic formulation (utilizing the Speziale et al. (1991) formulation) by

applying an appropriately adjusted elliptic blending approach by Manceau and Hanjalić (2002). By doing so, the complex functional dependencies in the model coefficients could be replaced by their constant values. Furthermore, the employment of the wall-reflection term in line with the Gibson and Launder (1978) proposal could be omitted. Some further adjustments are made in addition, dealing mostly with the functional form of the turbulent viscosity in the turbulent diffusion models in both Reynolds stress and dissipation rate equations. This form, employing a specific switch between the Kolmogorov and turbulent scales, contributed to the avoidance of a dissipation rate source term, the so-called length-correction term, introduced by Hanjalic and Jakirlic (1998) to remedy the well-known RSM-specific anomaly related to the beakbending of the mean dividing streamline at the point of reattachment. Numerical robustness is considerably enhanced by an algorithmic treatment of the Reynolds stress tensor within the momentum equation, representing a blend between the solutions originating directly from the corresponding governing equations and a variably-treated small amount (not more than 25%) of those Reynolds stress components obtained by utilizing the Boussinesq correlation. The model feasibility is intensively tested in a large number of attached flows as well as in two- and three-dimensional wall-bounded flows subjected to separation from sharp-edged, flat and continuously curved surfaces.

The intention in this chapter is not to attempt a review of Reynolds stress modeling activities. Accordingly, not all relevant model formulations can be mentioned here. Nevertheless, let us mention in summary a few important developments and applications, e.g.: Cécora et al. (2015) computed several two- and three-dimensional wing configurations by two adopted near-wall RSMs. Klein et al. (2015) reviewed amongst others five selected RSM versions by means of computing a series of flows subjected to complex straining due to cross-sectional area variation, different pressure gradients and separating flows. Gerolymos and Vallet (2016) applied a fairly complex RSM to flows in three-dimensional ducts with varying cross-sectional area. Kuwata and Suga (2015) dealt with a RSM extension concerning the flow over porous surfaces in relation to environmental vegetation flows. A further RSM extension in relation to flows over macro rough walls is formulated by Kuwata et al. (2019). Eisfeld and Rumsey (2020) focused on the lengthscale correction applied to some separating flows by using their RSM formulation, which combines the Speziale et al. (1991) formulation of the pressure-strain correlation in the

4. Development of an ω_h -based elliptic-blending-related Reynolds-stress model

off-wall region and an appropriately adjusted Φ_{ij} model from Launder et al. (1975) for the near-wall region. Recently, a text book devoted primarily to the 'second-moment routes to closure' has been published by Hanjalic and Launder (2011).

4.2. Model formulation

The Reynolds Stress Model (RSM) representing the background model formulation of the present development, denoted as ω_h -based elliptic-blending-related Reynolds-stress model (EBM), has been proposed by Jakirlić and Maduta (2015). The model formulation encompasses the equations describing the dynamics of the six components of the Reynolds stress tensor $\overline{u_i u_j}$ coupled with the scale-supplying equation governing the homogeneous portion of the specific dissipation rate defining the inverse time scale $\omega^h = \varepsilon^h/k$.

The concept of the so-called homogeneous dissipation of turbulence with

$$\varepsilon_{ij}^h = \varepsilon_{ij} - \frac{1}{2}\nu \frac{\partial^2 \overline{u_i u_j}}{\partial x_l \partial x_l} \quad (4.1)$$

representing the homogeneous fraction of the total stress-dissipation correlation and

$$\varepsilon^h = \varepsilon - \frac{1}{2}\nu \frac{\partial^2 k}{\partial x_l \partial x_l} \quad (4.2)$$

denoting the corresponding homogeneous dissipation rate of the kinetic energy of turbulence k . The homogeneous dissipation rate concept was initially proposed by Jovanovic et al. (1995) and was adopted as a turbulence modeling rationale by Jakirlić (1997) and Jakirlic and Hanjalic (2002). This concept offers the possibility to capture the correct asymptotic behaviour of the dissipation correlation tensor ε_{ij} when approaching the solid wall without the necessity to include any wall-topography-related parameter as well as to return the correct near-wall shape of the dissipation rate profile. This concept was further followed by Jakirlić and Maduta (2015) by transforming the ε^h equation into the equation governing the specific homogeneous dissipation rate $\omega^h = \varepsilon^h/k$ by applying the relationship $D\omega^h/Dt = D(\varepsilon^h/k)/Dt = 1/k D\varepsilon^h/Dt - \varepsilon^h/k Dk/Dt$. In the course of this transformation, the so-called General Gradient Diffusion Hypothesis (GGDH), representing the basis of the turbulent diffusion modeling within both the $\overline{u_i u_j}$ and ε^h equations, has been replaced by its Simple Gradient Diffusion Hypothesis (SGDH) variant with the turbulent viscosity ν^* as the diffusion determining parameter. The resulting model equation as well as the companion Reynolds stress model equation, including the meaning of individual terms, read as follows:

$$\begin{aligned}
 \frac{D\overline{u_i u_j}}{Dt} = & \frac{\partial}{\partial x_m} \left[\underbrace{\left(\frac{1}{2} \nu \delta_{mn} + \sigma \nu^* \delta_{mn} \right) \frac{\partial \overline{u_i u_j}}{\partial x_n}}_{\text{viscous \& turbulent diffusion}} \right] \\
 & - \underbrace{\left(\overline{u_i u_k} \frac{\partial U_j}{\partial x_k} + \overline{u_j u_k} \frac{\partial U_i}{\partial x_k} \right)}_{\text{production}} \\
 & + \underbrace{\Phi_{ij}}_{\text{pressure-redistribution}} - \underbrace{\varepsilon_{ij}^h}_{\text{destruction}}
 \end{aligned} \tag{4.3}$$

$$\begin{aligned}
 \frac{D\omega^h}{Dt} = & \frac{\partial}{\partial x_k} \left[\underbrace{\left(\frac{1}{2} \nu + \sigma \nu^* \right) \frac{\partial \omega^h}{\partial x_k}}_{\text{viscous \& turbulent diffusion}} \right] + \underbrace{C_{\omega,1} \frac{\omega^h}{k} P_k}_{\text{production}} \\
 - & \underbrace{C_{\omega,2} \omega^h \omega^h}_{\text{destruction}} + \frac{2}{k} \underbrace{\left(\frac{C_{CD,1}}{2} \nu + C_{CD,2} \nu^* \right) \frac{\partial \omega^h}{\partial x_k} \frac{\partial k}{\partial x_k}}_{\text{cross-diffusion (CD)}} \\
 & + \underbrace{C_{\omega,3} \frac{\nu}{\omega^h} \frac{\partial^2 U_i}{\partial x_j \partial x_k} \frac{\partial^2 U_i}{\partial x_j \partial x_k}}_{\text{gradient production } P_{\omega,3}}
 \end{aligned} \tag{4.4}$$

with $P_k = -\overline{u_i u_j} \partial U_i / \partial x_j$ denoting the production of the kinetic energy of turbulence. In order to close the transport equation of the Reynolds stress tensor, model formulations for the pressure redistribution term Φ_{ij} and the stress-dissipation correlation ε_{ij}^h are required. The present activity focuses primarily on modeling the pressure redistribution process Φ_{ij} by utilizing the elliptic blending procedure proposed by Manceau and Hanjalić (2002) and the turbulent diffusion in both equations (D_{ij}^t and $D_{\omega^h}^t$) in terms of a suitably defined turbulent viscosity ν^* within the SGDH. Furthermore, a hybrid coupling procedure of the mean velocity and Reynolds stress fields in the RANS equation of motion is illustrated, contributing substantially to the numerical robustness enhancement.

4.2.1. Pressure redistribution model term Φ_{ij}

A commonly applied strategy to provide the correct asymptotic behavior of the Reynolds stress components by approaching the wall within a near-wall modeling concept is to use an off-wall, high Reynolds number model version and to express adequately the model coefficients as functions of dimensionless invariant variables accounting for viscous (mostly in terms of the Reynolds number of turbulence $Re_t = k^2/(\nu\varepsilon)$) and non-viscous, kinematic wall-blocking effects (represented by the invariants of the Reynolds-stress and, possibly, stress-dissipation anisotropy tensors $a_{ij} = \overline{u_i u_j}/k - 2\delta_{ij}/3$ and $e_{ij} = \varepsilon_{ij}^h/\varepsilon - 2\delta_{ij}/3$ respectively), as utilized, e.g., in Jakirlić and Maduta (2015). The objective is to ensure the relevant vanishing behavior of the entire pressure-strain tensor by integrating the model equations down to the wall. However, the model coefficient functions are fairly sensitive to variably imposed flow straining, which could be particularly evident in e.g. the case of two-phase flows with phase change. Accordingly, the employment of coefficient constants instead of functions would contribute strongly to the stability of the numerical procedure in conjunction with a RSM. This, as well as the goal to more adequately model the non-linear nature of the pressure-scrambling process motivated the present development.

The pressure redistribution term Φ_{ij} is presently modeled following the blending procedure conceptualized by Manceau and Hanjalić (2002). Accordingly, a high Reynolds number formulation Φ_{ij}^h valid in the 'homogeneous' off-wall core flow is appropriately blended with a wall-related formulation Φ_{ij}^w satisfying the correct asymptotic wall behavior:

$$\Phi_{ij} = (1 - f_\Phi) \Phi_{ij}^w + f_\Phi \Phi_{ij}^h \quad \text{with} \quad f_\Phi = \alpha^3 \quad (4.5)$$

The blending function f_Φ is defined as a cubic power of the elliptic function α ($f_\Phi = \alpha^3$) representing the solution of the so-called elliptic equation (see Eq. (4.8) and associated discussion).

Any well-known formulation for modeling the homogeneous, high Reynolds number pressure redistribution term Φ_{ij}^h can be applied, as reviewed in the introduction. Presently, the non-linear, second-order (in terms of Reynolds stress anisotropy tensor $b_{ij} = a_{ij}/2$) formulation derived by Speziale et al. (1991), according to suggestion by Manceau (2015), is adopted:

$$\begin{aligned}
 \Phi_{ij}^h &= - \left(C_1 + C_{1s} \frac{P_k}{k\omega^h} \right) \omega^h b_{ij} \\
 &+ C_2 \omega^h k \left(b_{ik} b_{kj} - \frac{1}{3} b_{kl} b_{kl} \delta_{ij} \right) \\
 &+ \left(C_3 - C_{3s} \sqrt{b_{kl} b_{kl}} \right) k S_{ij} \\
 &+ C_4 k \left(b_{ik} S_{jk} + b_{jk} S_{ik} - \frac{2}{3} b_{lm} S_{lm} \delta_{ij} \right) \\
 &+ C_5 k (b_{ik} \Omega_{jk} + b_{jk} \Omega_{ik})
 \end{aligned} \tag{4.6}$$

with $S_{ij} = 0.5 (\partial U_i / \partial x_j + \partial U_j / \partial x_i)$ representing the mean rate-of-strain tensor and $\Omega_{ij} = 0.5 (\partial U_i / \partial x_j - \partial U_j / \partial x_i)$ the mean rate-of-rotation tensor. The values of the model constants, specified in Table 4.1, correspond exactly to those values proposed originally by Speziale et al. (1991).

C_1	C_{1s}	C_2	C_3	C_{3s}	C_4	C_5
3.4	1.8	4.2	0.8	1.3	1.25	0.4

Table 4.1.: Coefficient constant values in Φ_{ij}^h model term, Eq. (4.6).

The companion wall-related pressure redistribution term Φ_{ij}^w has been postulated by Manceau and Hanjalić (2002) as an algebraic expression in terms of the Reynolds stress tensor $\overline{u_i u_j}$. The model formulation complies with the exact asymptotic behavior of the pressure-strain tensor by approaching the solid wall. In order to provide the corresponding behavior of individual Φ_{ij}^w components, the unit wall-normal vectors n_i , denoting the direction of the flow non-homogeneity, are adequately utilized. They are determined by the gradient of the elliptic function α normalized by its modulus in accordance with $n_i = \nabla \alpha / |\nabla \alpha|$. Interested readers are referred to Manceau and Hanjalić (2002) and Manceau (2015) for a detailed derivation of the near-wall formulation of the pressure redistribution model term Φ_{ij}^w . The relevant expression reads in the present $\overline{u_i u_j} - \omega^h$ modeling framework as follows:

$$\begin{aligned} \Phi_{ij}^w &= -5\omega^h [\overline{u_i u_k} n_j n_k + \overline{u_j u_k} n_i n_k - 0.5 \overline{u_k u_l} n_k n_l (n_i n_j + \delta_{ij})] \quad (4.7) \\ &\text{with } n_i = \frac{\nabla \alpha}{|\nabla \alpha|} \end{aligned}$$

The functional form of the blending function f_Φ , which constitutes the resultant pressure redistribution term Φ_{ij} (Eq. (4.5)), represents one of the key details in this blending procedure. Its cubic-power dependency on the elliptic function α (Eq. (4.8)) is presently adopted, in line with the Manceau (2015) suggestion.

$$\alpha - L_\alpha^2 \nabla^2 \alpha = 1 \quad \text{with} \quad L_\alpha = 12 \frac{\nu^{3/4}}{(k\omega^h)^{1/4}} \quad (4.8)$$

The functional dependency of the blending function f_Φ , which corresponds to the cubic potency of the elliptic function α provides a continuous but sharp transition between the wall-proximity ($f_\Phi = 0$) and off-wall ($f_\Phi = 1$) limits. The elliptic equation (Eq. (4.8)) is derived as a function of the lengthscale L_α , which decisively defines the behavior of the elliptic function α and thus the correct blending of the pressure redistribution term. Assuming a sharp switch between the two sub-domains (near-wall and far-wall regions) and limiting the influence of the near-wall formulation (Φ_{ij}^w) just to the immediate wall vicinity, the lengthscale L_α is modeled in terms of the Kolmogorov length scale only: $L_\alpha = 12\nu^{3/4}/(k\omega^h)^{1/4}$. Here, a fractional inclusion of the turbulent length scale would lead to a more diffuse transition of the elliptic function between the wall-nearest and far-field zones, resulting in a greater influence of the wall-related pressure redistribution formulation propagating further away from the wall. A well-known and advantageous characteristic of the elliptic blending function f_Φ is a fairly unified behavior over different flow configurations, as illustrated in Fig. 4.1 by means of the fully developed channel flow computations for two investigated Reynolds numbers: $\text{Re}_\tau = 395$ and 5200.

Herewith, the use of the classical wall-reflection term modeling the influence of the wall occurrence on both the slow and mean-flow-dependent rapid pressure-scrambling processes, as originally proposed by Gibson and Launder, 1978, is omitted.

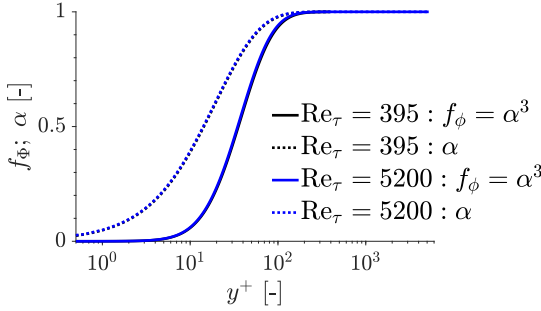


Figure 4.1.: Elliptic blending function $f_\Phi = \alpha^3$ (solid) and elliptic function α (dotted line) for channel flow with $Re_\tau = 395$ (black lines) and $Re_\tau = 5200$ (blue lines) along channel height y^+ predicted by EBM.

4.2.2. Stress-dissipation correlation model term ε_{ij}^h

The destruction process of the Reynolds stress components represented by the stress-dissipation tensor ε_{ij}^h is presently modeled as proposed by Jakirlic and Hanjalic (2002) and Jakirlić and Maduta (2015). The corresponding formulation blends between its off-wall isotropic limit proportional to $2k\omega^h\delta_{ij}/3$ (corresponding to $f_s = 0$) and its anisotropic wall-related expression $\overline{u_i u_j} \omega^h$ (with $f_s = 1$ at the wall itself). The choice of the blending factor f_s has been discussed in detail by Jakirlic and Hanjalic (2002), whereby a combination of the two-componentality parameters A ($A = 1 - 9(A_2 - A_3)/8$; $A_2 = a_{ij}a_{ji}$; $A_3 = a_{ij}a_{jk}a_{ki}$) and E ($E = 1 - 9(E_2 - E_3)/8$; $E_2 = e_{ij}e_{ji}$; $E_3 = e_{ij}e_{jk}e_{ki}$) of both large-scale and small-scale motions has proven to be advantageous. The relevant formulation is adopted also for the present model as follows:

$$\varepsilon_{ij}^h = f_s \omega^h \overline{u_i u_j} + (1 - f_s) \frac{2}{3} k \omega^h \delta_{ij} \quad (4.9)$$

with $f_s = 1 - \sqrt{AE^2}$

The origin of this formulation represents an attempt to take into account the corresponding layering of the flow structure transitioning from the energy-containing turbulent scales, represented by A , and dissipative scales, represented by E . The two-componentality parameter of the small-scale dissipative

motion E requires the dissipation tensor itself for the calculation within the numerical procedure, which results in a nesting of the model and can cause numerical instabilities. Therefore, an alternative formulation can be defined in terms of A only as $f_s = 1 - A^{3/2}$. This formulation has been checked in channel flow without noticeable differences in the results, but was not followed later.

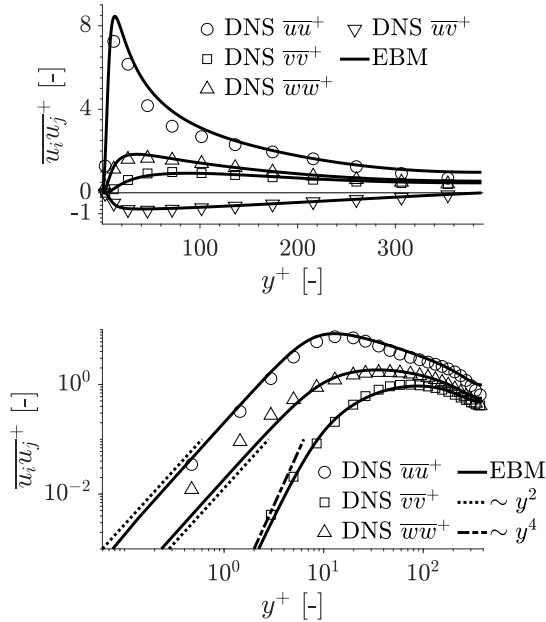


Figure 4.2.: Reynolds-stress components in linear (top) and double logarithmic scaling (bottom) for channel flow with $\text{Re}_\tau = 395$ along channel height y^+ predicted by EBM (solid line). The DNS data by Moser et al. (1999) are depicted for comparison (symbols).

Fig. 4.2 depicts exemplarily the distribution of the individual Reynolds stress components across the fully developed channel flow at $\text{Re}_\tau = 395$ ($\text{Re}_b \approx 13750$) illustrating their correctly returned intensity and exact asymptotic behavior in terms of the profile slopes by approaching the solid wall. Further channel-

flow-related results up to Reynolds numbers of $Re_\tau = 5200$ ($Re_b \approx 250000$) are presented in Chapter 4.3.

4.2.3. Specific dissipation rate equation $D\omega^h/Dt$

The relevant scale-supplying equation solved simultaneously with the Reynolds stress equation (Eq. (4.3)), formulated in terms of the homogeneous part of the specific dissipation rate ω^h ($= \varepsilon^h/k$) is given by Eq. (4.4). Its exact wall value, corresponding to $\omega_{wall}^h = \nu/y_{wall}^2$, does not require any turbulent quantity and depends only on the wall distance of the wall-adjacent computational node y_{wall} .

The so-called cross-diffusion (CD) term arises from the procedure transforming the molecular and turbulent diffusion terms within the ε^h equation into the ω^h equation. The value of the constant $C_{CD,1}$ could be determined analytically with respect to satisfying the wall limits of ω^h , implying that only its molecular diffusion and viscosity-affected sink term have to be in balance with the CD in the near-wall region. Adopting the standard value for the model constant $C_{\omega,2} = 0.8$ results in the value of $C_{CD,1} = 0.55$. The constant $C_{CD,2}$ is calibrated by means of computing the mixing layer, which is dominated by the CD. The correctly predicted spreading rate is finally achieved with the value of $C_{CD,2} = 0.5$.

Otherwise, the formulation corresponds exactly to that proposed by Jakirlić and Maduta (2015). Most of the model constants take the same standard values, as summarized in Table 4.2.

$C_{\omega,1}$	$C_{\omega,2}$	$C_{\omega,3}$	σ	$C_{CD,1}$	$C_{CD,2}$
0.44	0.8	0.003	1.0	0.55	0.5

Table 4.2.: Model constants of the ω^h transport equation

The value of the model constant $C_{\omega,3} = 0.003$ multiplying the gradient-production term $P_{\omega,3}$, taking the very standard form with reference to Launder and Sharma (1974), is calibrated by comparing its profile with the exact DNS reference (Mansour et al., 1988), Fig. 4.3. Note that here the $P_{\varepsilon,3}$ term, not its $P_{\omega,3}$ equivalent, is depicted. The profile form exhibits only positive values, not following the DNS-relevant sign-changing tendency. Jakirlic and Hanjalic (2002) derived a formulation resulting in a profile progressing in close

agreement with the DNS data. For this formulation it was proven in some subsequent computational studies that it does not substantially contribute to the final outcome with respect to the velocity and turbulent quantity fields. Therefore, its simpler formulation as depicted in Eq. (4.4) is presently retained.

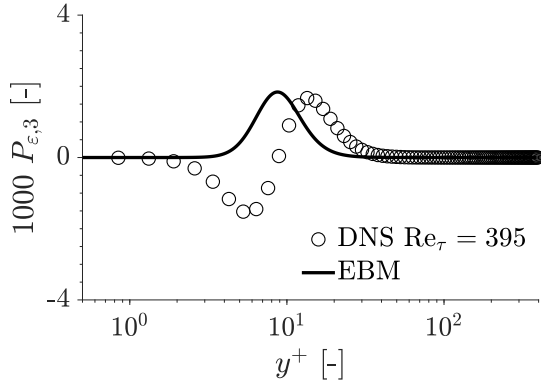


Figure 4.3.: Gradient-production term $P_{\epsilon,3}$ for channel flow with $Re_{\tau} = 395$ along channel height y^+ predicted by EBM (solid line). The DNS data by Mansour et al. (1988) are depicted for comparison (circle).

Fig. 4.4 top depicts exemplarily the profile of the homogeneous specific dissipation rate ω^h within a fully developed channel flow with $Re_{\tau} = 395$, representing the direct solution of Eq. (4.4) as the independent scale-supplying variable of the present EBM. Its total counterpart ω is also depicted. A close agreement with the reference DNS database is obvious. Fig. 4.4 bottom depicts both the homogenous (ϵ^h) and non-homogeneous ($0.5 \nu \partial^2 k / (\partial x_l \partial x_l)$) fractions of the total viscous dissipation rate ϵ , converted from the ω -related quantities in accordance to Eq. (4.2).

4.2.4. Turbulent diffusion model terms D_{ij}^t and $D_{\omega^h}^t$

The most-widely used formulation for modeling the turbulent diffusion in wall-bounded flows resembles the so-called gradient-approach expressed in terms of the second-derivative of the dependent variable multiplied by an appropriately defined coefficient ('diffusion coefficient'), which represents a

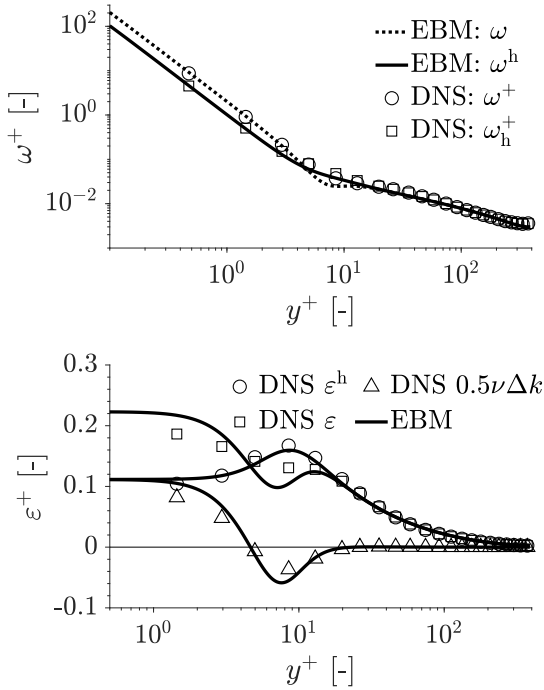


Figure 4.4.: Top: Homogeneous ω^h (solid line) and entire specific dissipation rate ω (dotted line) for channel flow with $Re_\tau = 395$ along channel height y^+ predicted by EBM (solid line). The DNS data by Moser et al. (1999) are depicted for comparison (symbols).

Bottom: Total viscous dissipation rate ε and its homogeneous (ε^h) and non-homogeneous ($0.5\nu\partial^2k/(\partial x_l\partial x_l)$) parts (in accordance to Eq. (4.2)) for channel flow with $Re_\tau = 395$ along channel height y^+ predicted by EBM (solid line). The DNS data by Moser et al. (1999) are depicted for comparison (symbols).

product between a characteristic time scale and the square of a characteristic velocity scale: $\tau \times \vartheta^2$. In the model formulation denoted as General Gradient Diffusion Hypothesis (GGDH) (Daly and Harlow, 1970), the time scale is

represented by $\tau \propto k/\varepsilon$ and the squared velocity scale by $\vartheta^2 \propto \overline{u_i u_j}$. The transformation of the ε^h -equation into the ω^h -equation suggested a simplified model relationship in which $\vartheta^2 \propto k$ resulting finally in the SGDH formulation, with the turbulent viscosity included: $k^2/\varepsilon^h = k/\omega^h \propto \nu_t$ (the option of using further the GGDH is of course possible). The model coefficient $\sigma = 1$ is adopted to be equal in both governing equations (see Equations (4.3) and (4.4)). Its unity value has been illustrated in Fig. 4.5 to result in a close agreement of the individual turbulent diffusion D_{ij}^t components with the DNS reference within a fully developed channel flow at $\text{Re}_\tau = 395$.

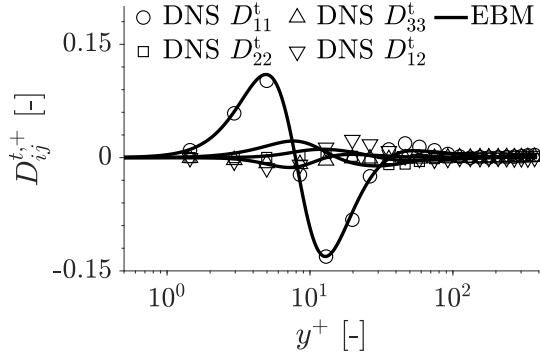


Figure 4.5.: Turbulent diffusion D_{ij}^t components for channel flow with $\text{Re}_\tau = 395$ along channel height y^+ predicted by EBM (solid lines). The DNS data by Moser et al. (1999) are depicted for comparison (symbols).

Furthermore, an adequately modified turbulent viscosity (denoted by ν^* in Equations (4.3) and (4.4)) is introduced presently. Similar to the model of Basara and Jakirlić (2003), ν^* is formulated in terms of a turbulent velocity scale as $k^{0.5}$, the two-componentality parameter A accounting for the turbulence anisotropy effects and a length scale L^* , see Eq. (4.10). The characteristic length scale L^* relates presently to the length scale of the Kolmogorov dissipative eddies, multiplied by a functional dependency modelled in terms of the turbulent Reynolds numbers, the conventional one $\text{Re}_t = k/(\nu\omega^h)$ and the wall-distance-based one $\text{Re}_y = k^{1/2}y/\nu$, as presented in Eq. (4.11). This functional dependency provides an adequate enhancement of turbulent diffusion in the off-wall region being especially suitable for flows at higher Reynolds

numbers. The advantageous effect has been furthermore detected in separated flows at the region of reattachment, utilized also for calibrating the final L^* formulation. The anomalous 'backbending' of the mean dividing streamline underneath the reattachment point, representing an inherent weakness of all RSM formulations and is not present in eddy-viscosity model computations, could be reliably avoided for the considered benchmark cases by applying the reformulated SGDH. In contrast, Hanjalic and Jakirlic (1998) avoided backbending by introducing an additional source term into the dissipation rate equation, the so-called 'lengthscale correction' term, which has been later followed by Einfeld and Rumsey (2020). The positive influence of the turbulent diffusion in relation to adjusting the angle under which the mean dividing streamline reattaches, mention in Hanjalic and Jakirlic (1998), is recalled here. Accordingly, an appropriately formulated turbulent diffusion term, while waiving the necessity of including such source terms as proposed by Hanjalic and Jakirlic (1998), contributed in addition to a reasonable model's numerical robustness of the numerical model. The final outcome is illustrated exemplary in the periodic flow over a series of two-dimensional hills with $Re_h = 10600$ and 37000 in Fig. 4.6 with the focus on the mean diving streamline and its behavior in the reattachment area.

$$\nu^* = k^{0.5} AL^* \quad (4.10)$$

$$L^* = \left(10 + \frac{Re_y^2}{25 Re_t} \right) \frac{\nu^{3/4}}{(\omega^h k)^{1/4}} \quad (4.11)$$

4.2.5. Reynolds stress tensor blending in momentum equation

Implementation of a seven-equation RSM, governing the dynamics of six highly-interacting Reynolds stress components and the dissipation rate of kinetic energy of turbulence as well as their coupling with the velocity field in the momentum equation, into a numerical code has been always a very demanding task. Numerical algorithms aiming at overcoming the relevant difficulties, especially in conjunction with higher-order discretization methods, were the topics of a number of studies in the past. In this regard the works of Obi et al.

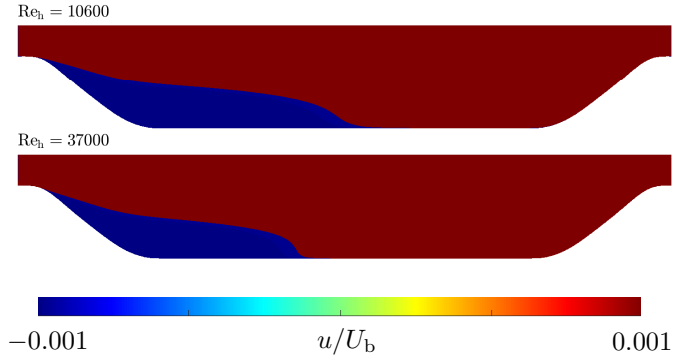


Figure 4.6.: Regions with positive (red) and negative (blue) axial velocities in the periodic hill configuration at $Re_h = 10600$ (top) and 37000 (bottom) illustrating the effect of the adopted diffusion model on the flow behavior at the separation and reattachment points.

(1991) and more recently of Basara (2004) and Moor-Yossef (2014) should be consulted.

To enhance the robustness and smoothness of numerical convergence of the present EBM formulation, a slightly modified blending procedure suggested by Maduta et al. (2015) is applied to the Reynolds stress tensor $\overline{u_i u_j}$ entering the equation of motion. This procedure has its origin in the proposal of Basara and Jakirlić (2003) with the so-called hybrid Eddy-Viscosity/Reynolds-stress model of turbulence, in which the entire Reynolds stress tensor in the RANS equation of motion is approximated via the Boussinesq correlation. In the framework of the EBM and the $\overline{u_i u_j}$ -blending procedure not the entire Reynolds stress tensor is transferred to the momentum equation, but a fraction of it, and a smaller remaining part is replaced by its Boussinesq approximation (see Eq. (4.13)). A constant fraction of $\overline{u_i u_j}$ valid within the entire computational domain, as suggested by Maduta et al. (2015), is not adopted here in order to avoid potentially negative influences in the region close to the wall. Therefore,

a variable blending function β is introduced, which depends on the turbulent Reynolds number Re_t and is calibrated interactively in an intensive computational campaign for a number of flow configurations. Its profile is exemplary depicted in Fig. 4.7 across the channel flow for $\text{Re}_\tau = 395$ and 5200. It is obvious that its asymptotic maximum (for $\text{Re}_t \rightarrow \infty$), characteristic for the region close to symmetry plane, amounts to $\beta_{\max} = 0.25$.

$$\overline{u_i u_j} = (1 - \beta) \overline{u_i u_j} + \beta (-2\nu_t S_{ij} + 2/3k\delta_{ij}) \quad (4.12)$$

with $\beta = 0.25 \frac{\text{Re}_t}{300 + \text{Re}_t}$

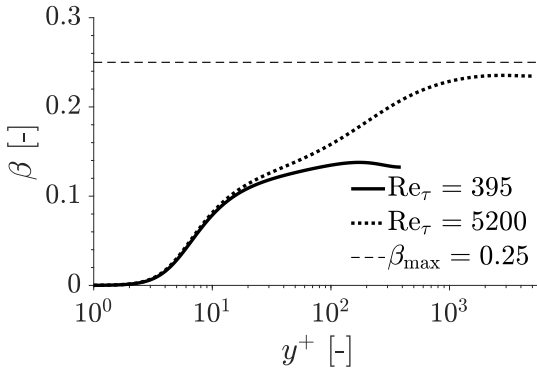


Figure 4.7.: β -blending function for channel flow with $\text{Re}_\tau = 395$ (solid line) and 5200 (dotted line) along channel height y^+ predicted by EBM. Its maximum possible value of $\beta_{\max} = 0.25$ is denoted by a dashed line.

The model formulation for the turbulent viscosity ν_t in Eq. (4.13) resembles the one proposed by Basara and Jakirlić (2003), Eq. (4.13). It is, amongst others, expressed in terms of the two-componentality parameter A , mimicking the influence of the Reynolds stress anisotropy. The characteristic length scale L_{ν_t} is defined as a maximum function, whereby in addition to the Kolmogorov and turbulent length scale, the Taylor microscale is also taken into consideration. The application of the Taylor microscale contributed to a smooth transition between the individual length scales and provides a

more continuously progressing trend. The model parameters of the individual lengthscales ($C_\eta = 4$, $C_\lambda = 0.9$ and $C_L = 0.17$) are calibrated on the basis of the model coefficient $C_\mu = [\overline{uv}/(\partial U/\partial y)](k/\varepsilon^2)$, representing actually a structure parameter, in comparison with the DNS reference data for the channel flow at $\text{Re}_\tau = 395$ (see Fig. 4.8 top). The resulting variation of the relevant lengthscale L_{ν_t} is depicted in Fig. 4.8 bottom, with special attention paid to the position of the intersections between the individual lengthscales.

$$\nu_t = C_\mu A k^{0.5} L_{\nu_t} \quad (4.13)$$

$$L_{\nu_t} = \max[\max(L_\eta, L_\lambda), L_L] \quad (4.14)$$

$$\text{with } L_\eta = C_\eta \frac{\nu^{0.75}}{(k\omega^h)^{0.25}} \quad L_\lambda = C_\lambda \sqrt{\frac{10\nu}{\omega^h}} \quad L_L = C_L \frac{\sqrt{k}}{\omega^h}$$

A summarized model specification of the EBM with the governing equations and associated model formulations can be found in Appendix A. To assess the general validity of the presented EBM formulation, a variety of benchmark cases are considered in the following. The benchmark cases include some canonical two-dimensional flow configurations (fully-developed channel (Chapter 4.3) and pipe flows (Chapter 4.4)), developing flows (a zero-pressure gradient boundary layer (Chapter 4.5) and a high Reynolds number APG boundary layer (Chapter 4.6)), flow separation from sharp-edged (backward-facing step (BFS), Chapter 4.7) and continuous curved walls (periodic hill, Chapter 4.8) as well as three-dimensional, geometry-sensitive flow separation in differently configured 3D diffuser configurations (Chapter 4.9). Finally, the EBM is applied to the WSG and its suitability for near-industry flow configurations is discussed. As these are well-known flow configurations, a detailed physical description of the flow is omitted and reference is given to the respective reference papers. All subsequent simulations have been performed within the finite-volume based open-source toolbox OpenFOAM[®] version 19.12, in which the EBM formulation is implemented.

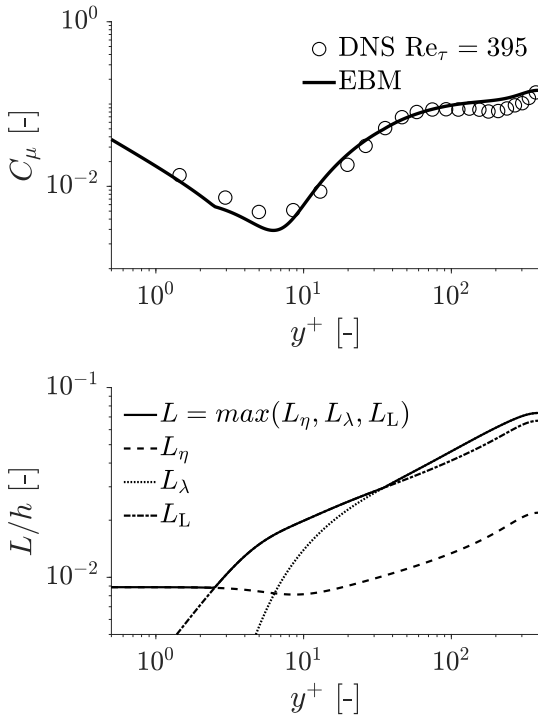


Figure 4.8.: **Top:** Profile of the model structure parameter $C_\mu = \overline{uv} / (\partial U / \partial y) (k / \varepsilon^2)$ for channel flow with $Re_\tau = 395$ along channel height y^+ predicted by EBM (solid lines). The DNS data by Moser et al. (1999) are depicted for comparison (circles). **Bottom:** Lengthscale (Eq. 4.14) normalized by the channel height (L_{ν_τ} / h) for channel flow with $Re_\tau = 395$ along channel height y^+ predicted by EBM (solid lines). The corresponding Kolmogorov lengthscale L_η (dashed line), Taylor lengthscale L_λ (dotted line) and turbulent lengthscale L_L (dashed-dotted line) are illustrated for completeness.

4.3. Channel flow

The channel flow representing a baseline wall-bounded flow configurations is considered as a most suitable benchmark for near-wall turbulence modeling and is therefore used in conjunction with the present model formulation to validate the individual model terms. The validation process benefits especially from an extraordinary intensive reference database available, originating mostly from high-fidelity DNS studies. In order to ensure a consistent behavior of the EBM as far as possible, a global consideration is carried out within the framework of the fully developed flow in a plane channel and over a friction Reynolds number range from $Re_\tau = 180$ up to 5200. The results obtained are discussed along with the relevant DNS database. Therefore, numerical grids consisting of only one cell in the streamwise direction, enabled through the inlet-outlet periodicity, and an appropriate cell number across the channel, from lower to the upper wall, are applied, with the first cell clearly positioned in the viscous sublayer to guarantee $y^+ < 1$. The grid size for the individual friction-based Reynolds numbers are summarized in Table 4.3. The grid resolutions listed, representing the final outcome of a grid study, provide grid-independent solutions. The discretization of the convective terms is done completely with CDS. The EBM results are evaluated in the following by comparing directly to the DNS data provided by Moser et al. (1999) and Lee and Moser (2015).

Re_b	5700	13750	20000	40000	87000	250000
$Re_{\tau,DNS}$	180	395	550	1000	2000	5200
$Re_{\tau,EBM}$	182	390	541	1000	2010	5217
n_{total}	200	400	600	1000	1400	2000

Table 4.3.: Total number of cells n_{total} for the considered channel flow configurations with bulk Reynolds number Re_b . The predicted friction Reynolds number by DNS $Re_{\tau,DNS}$ and EBM $Re_{\tau,EBM}$ are also listed.

A key integral parameter of all flow configurations is the friction coefficient $C_f = \tau_w / (0.5\rho U_b^2)$, which describes the flow straining onto the wall and is accompanied by the correct prediction of the velocity wall gradient. The friction coefficient is essential for the assessment of a channel flow as it is directly related to its friction Reynolds number. The friction coefficients

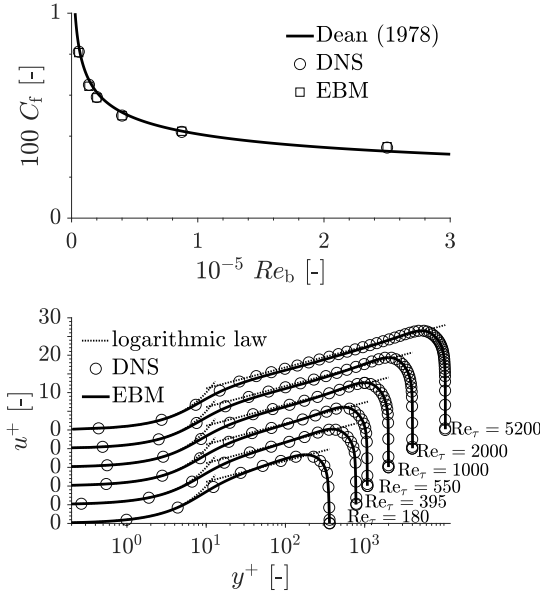


Figure 4.9.: top: Predicted channel friction coefficient $C_f = \tau_w / (0.5\rho U_b^2)$ depicted over the bulk Reynolds number range $Re_b = U_b h / \nu$ by EBM (squares) in comparison with the DNS data by Moser et al. (1999) and Lee and Moser (2015) (circles) as well as an empirical correlation by R. B. Dean (1978) (solid line).

bottom: Normalized velocity profiles u^+ in channel flows with $Re_\tau = 180$ up to 5200 depicted over dimensionless wall distance y^+ predicted by EBM (solid line). The DNS data by Moser et al. (1999) and Lee and Moser (2015) (circles) and the logarithmic law (dotted line) with $\kappa = 0.41$ and $B = 5.5$ are depicted for comparison.

predicted by the present EBM for the considered channel configurations are depicted in Fig. 4.9 top. In addition to the reference DNS data, the C_f -development following the empirical formulation by R. B. Dean (1978) with $C_f = 0.073 Re_b^{-0.25}$ is also added to Fig. 4.9 top for a more intensive evaluation. The friction coefficient values resulting from the EBM application agree very

well with the DNS data over the entire Reynolds number range, as it is also confirmed by the direct comparison of the friction-based Reynolds numbers in Table 4.3. Herewith, the capability of the EBM of correctly capturing the wall-shear stress over the entire Reynolds number range characterized by different turbulence levels is demonstrated. The EBM-related results are very much consistent with the tendency of the Dean's empirical approach, despite a slight overestimation pertinent to the highest friction Reynolds number. The highest friction Reynolds number exceeds possibly the validity of the empirical solution, which can be explained to some extent by the identical deviation of both the DNS and the EBM results from the empirical curve at $\text{Re}_\tau = 5200$.

The velocity profiles normalized by the friction velocity $u^+ = u/u_\tau$ are depicted in Fig. 4.9 bottom over the entire friction Reynolds number range. The logarithmic law for the wall-parallel velocity $u^+ = \ln y^+/\kappa + B$ (depicted by dotted line, $\kappa = 0.41$ and $B = 5.5$) is also illustrated in addition to the DNS data (circles). The EBM results exhibit consistent behavior following directly the logarithmic law independent of the Reynolds number, showing excellent agreement with the DNS reference data within all characteristic regions of the channels' cross-sectional area. Besides the near-wall velocity gradient, discussed in the following in relation to Fig. 4.9 top, the curvature of the velocity profile in the buffer layer ($5 < y^+ < 30$) as well as the velocity peak around the channel symmetry, characterized by a very small wake, are challenging for turbulence models. This is especially the case when considering a larger Reynolds number range. The EBM results capture nicely the Reynolds number dependency illustrated by a corresponding widening of the logarithmic layer in terms of the Reynolds number increase.

The logarithmic law (or 'law of the wall') can also be expressed by the velocity gradient being proportional to the von Kàrmàn constant κ . It is a well-known universal constant, which takes the value of $\kappa = 0.41$ in the logarithmic layer featured by the local equilibrium assumption implying the equality of the production rate of the kinetic energy of turbulence and its dissipation rate. Accordingly, the von Kàrmàn constant should be correctly returned by a turbulence model. In order to verify the capability of the EBM in capturing correctly the von Kàrmàn constant, it is evaluated for the entire Reynolds number range considered. Fig. 4.10 top displays the κ -profiles across the channel flow calculated from the expression $\kappa = (y^+ \partial u^+ / \partial y^+)^{-1}$, which is applied to both the EBM and DNS results. For the range of validity of

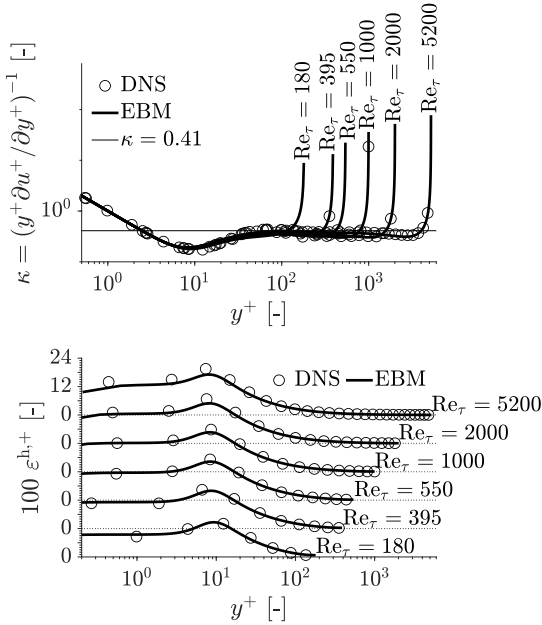


Figure 4.10.: Top: The von Kàrmàn constant $\kappa = (y^+ \partial u^+ / \partial y^+)^{-1}$ depicted over dimensionless wall distance y^+ within channel flows from $Re_\tau = 180$ up to 5200 predicted by EBM (solid line). The DNS data by Moser et al. (1999) and Lee and Moser (2015) (circles) and the equilibrium law with $\kappa = 0.41$ and $B = 5.5$ are depicted for comparison. Bottom: Homogeneous dissipation rate $\varepsilon^{h,+}$ over dimensionless wall distance y^+ within channel flows from $Re_\tau = 180$ up to 5200 predicted by EBM (solid line). The DNS data by Moser et al. (1999) and Lee and Moser (2015) (circles) are depicted for comparison.

the logarithmic law ($y^+ > 30$), the κ profiles related to the EBM coincide nicely with the DNS data over the entire Reynolds number range. The results obtained match exactly the standard value of the von Kàrmàn constant corresponding to $\kappa = 0.41$ within the logarithmic region. Outside the validity range of the equilibrium law, no match with $\kappa = 0.41$ is expected.

The scale-supplying variable serving for the definition of characteristic scales within the EBM formulation is represented by the specific homogeneous dissipation rate ω^h ($= \varepsilon^h/k$). To evaluate its profiles within the channel configuration characterized by the strong negative near-wall gradient (see, e.g., its profiles in Fig. 4.4), the homogeneous dissipation rate ε^h is depicted in Fig. 4.10 bottom for the considered Reynolds number range as a representative of ω^h . The reproduction of the near-wall characteristics of the homogeneous dissipation rate represents a great challenge for turbulence models, where special attention should be paid to its asymptotic near-wall behavior as well as its peak detected at $y^+ \approx 8$. The homogeneous dissipation rate predicted by the EBM follows closely the DNS data, especially in relation to its correct wall and maximum values as well as the position of the latter. A slight underestimation of the peak value by the EBM is noticeable only for the highest Reynolds number considered.

The EBM-predicted Reynolds stress intensities within the channel are depicted in terms of the streamwise component \overline{u}^+ in Fig. 4.11 top, the wall-normal component \overline{v}^+ in Fig. 4.11 bottom, the spanwise component \overline{w}^+ in Fig. 4.12 top and the shear stress component \overline{uv}^+ in Fig. 4.12 bottom. As in the previous figures, the results obtained over the entire Reynolds number range are shown as well as the corresponding DNS data (circles). Within the framework of a fully developed channel flow, the shear stress component \overline{uv}^+ is particularly crucial, since it is the only contribution of the turbulence field to the momentum equation. Consequently, the reproduction of the shear component is closely linked to the correct prediction of the velocity field. Accordingly, the high quality of the velocity profiles prediction (discussed in relation to Fig. 4.9 bottom) is 'mirrored' in the \overline{uv}^+ profiles in Fig. 4.12 bottom, in which a very good agreement with the DNS data can be seen over the entire Reynolds number range. Only a very slight underestimation of \overline{uv}^+ in the range from $y^+ = 20$ to 60 for the highest Reynolds number can be observed, which is associated with the applied $\overline{u_i u_j}$ -blending within the equation of motion (see Eq. (4.13)). This deviation is regarded as acceptable keeping in mind the advantages of the $\overline{u_i u_j}$ -blending in terms of the convergence stability and subsequent numerical robustness of the EBM formulation.

The predicted normal Reynolds stress intensity components of the Reynolds stress tensor (\overline{u}^+ , \overline{v}^+ , \overline{w}^+) are largely consistent with the DNS data over the entire Reynolds number range, with the performance of \overline{u}^+ (Fig. 4.11 top)

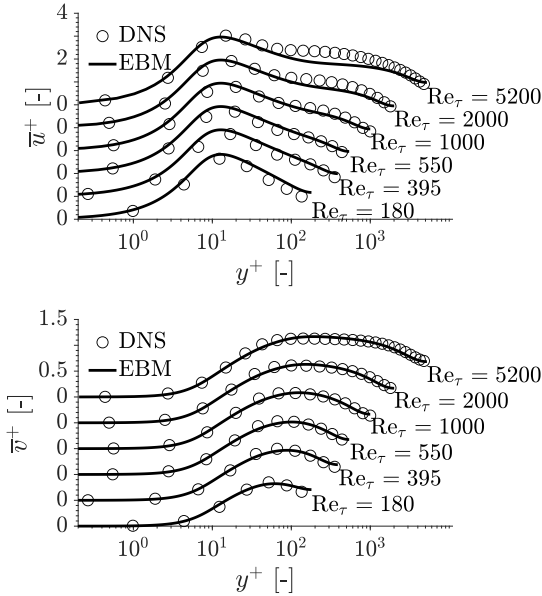


Figure 4.11.: Reynolds stress intensity components $\bar{u}^+ = \sqrt{\overline{uu}}/u_\tau$ (top) and $\bar{v}^+ = \sqrt{\overline{vv}}/u_\tau$ (bottom) for channel flows with $Re_\tau = 180$ up to 5200 predicted by EBM (solid line). The DNS data by Moser et al. (1999) and Lee and Moser (2015) (circles) are depicted for comparison.

being highlighted. Since the streamwise Reynolds stress component \bar{u}^+ is quantitatively the largest Reynolds stress component, it decisively determines the turbulent level of the flow making it even more important to capture correctly the \bar{u}^+ peak with respect to more complex flows in which the channel flow represents the inflow. As can be seen in Fig. 4.11 top and in regard to the DNS data, the peak value and position are reproduced accurately over the entire Reynolds number range, illustrating also a high predictive capability in capturing correctly the Reynolds number dependence. Only towards higher Reynolds numbers a slight shift in the peak position towards the channel wall can be observed. Overall good prediction of the normal-to-wall \bar{v}^+ and spanwise

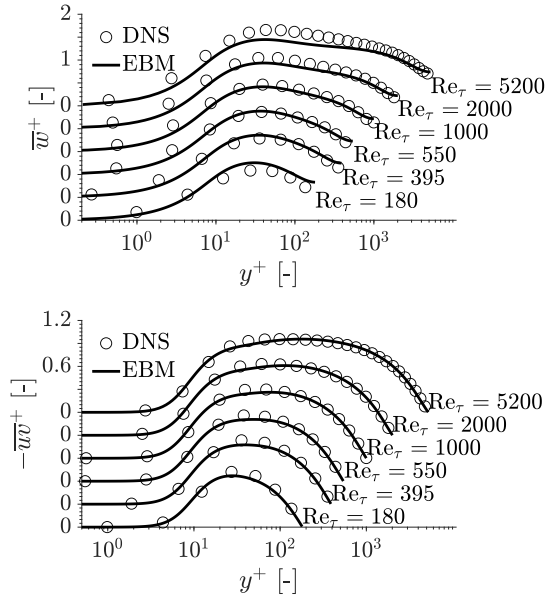


Figure 4.12.: Reynolds stress intensity $\overline{w}^+ = \sqrt{\overline{wv}}/u_\tau$ (top) and component $\overline{wv}^+ = \overline{wv}/u_\tau$ (bottom) for channel flows with $Re_\tau = 180$ up to 5200 predicted by EBM (solid line). The DNS data by Moser et al. (1999) and Lee and Moser (2015) (circles) are depicted for comparison.

(\overline{w}^+) components is directly associated with the advantageous modelling of the pressure redistribution process via the elliptic-blending approach (Eq. (4.5)).

4.4. Pipe flow

Similar to the fully developed flow in a plane channel, the fully developed pipe flow with its axis-symmetric characteristics represents also an important benchmark for the validation of near-wall turbulence models and will therefore be considered in the following. Compared to a plane channel flow, the correct prediction of the pipe flow is regarded as somewhat more challenging, since, despite an obviously uni-directional flow, there is a slight, but still important influence of the transverse curvature. A certain Reynolds number range up to $Re_\tau = 1000$, covered also by several DNS studies, is considered presently to enable a consistent investigation of the EBM predictability. The two-dimensional grid slice with the cell distribution resembling an 'O-grid' arrangement (corresponding to that illustrated, e.g., in Fig. 3.3) is configured accordingly to ensure the wall distance of the wall-closest computational node smaller than $y^+ < 1$ (relevant to grid-cell height of $\Delta r_{\min}^+ < 2$) and subsequently a grid-independent solution. The corresponding grid characteristics are listed in Table 4.4. Similar to the channel flow, the fully developed flow state has been achieved by applying the periodic inlet/outlet boundary conditions. The discretization of the convective terms is done completely with CDS. The EBM results, which are obtained by utilizing a respective circumferential spatial averaging according to the axis-symmetric character of the pipe flow, are assessed by means of the DNS data by El Houry et al. (2013).

Re_b	5300	11700	19000	37700
$Re_{\tau,DNS}$	180	360	550	1000
$Re_{\tau,EBM}$	184	363	552	1002
n_{total}	3072	4800	6336	25600
$\Delta r_{\min\dots\max}^+$	1...9	1...14.2	1...20	1...19.9
$\Delta\varphi^+$	8.8	14	19.4	19.5

Table 4.4.: Characteristics of the applied grids for the considered pipe flow bulk Reynolds numbers Re_b in terms of the total cell number n_{total} as well as the dimensionless minimal and maximal radial $\Delta r_{\min, \dots, \max}^+$ and circumferential spatial extents $\Delta\varphi^+$ of the cells. The predicted friction Reynolds number by DNS $Re_{\tau,DNS}$ and EBM $Re_{\tau,EBM}$ are also listed.

The semi-log plots of the velocity profiles u^+ for the considered Reynolds number range predicted by the EBM formulation (solid line) are depicted in Fig. 4.13 in comparison to the reference DNS data by El Khoury et al. (2013) (circles) and the logarithmic law with $\kappa = 0.41$ and $B = 5.5$ (dotted line). The EBM-related velocity profiles exhibit a behavior complying consistently with the Reynolds number increase and respective widening of the logarithmic layer in close agreement with the DNS data. The characteristics of the velocity profiles in terms of capturing correctly the linear behavior in the viscous sublayer, the curvature in the buffer layer, the logarithmic law region along with its specific gradient as well as the wake and the associated velocity peak in the pipe center are captured according to the reference DNS. Concerning the velocity behavior in the immediate wall vicinity with respect to the wall-related velocity gradient, the friction Reynolds number Re_τ is captured with a deviation of less than 2% relative to the DNS data as summarized in Table 4.4, representing the issue of great importance towards correct assessment of the wall shear stress.

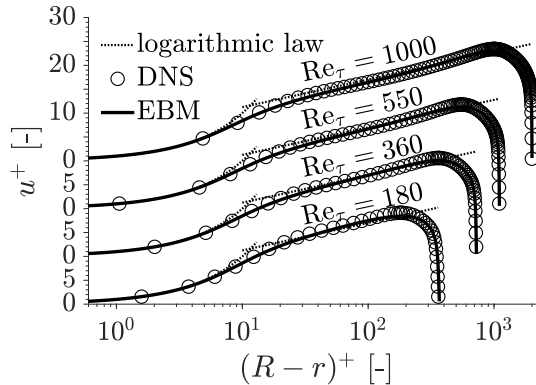


Figure 4.13.: Normalized semi-log plots of the velocity profiles u^+ for pipe flows with $Re_\tau = 180$ up to 1000 predicted by EBM (solid line). The DNS data by El Khoury et al. (2013) (circles) and the logarithmic law (dotted line) with $\kappa = 0.41$ and $B = 5.5$ are depicted for comparison.

Complementary to the velocity profiles, the normal Reynolds stress intensities and the shear stress component are depicted in Figures 4.14 and 4.15 along

with the reference DNS data by El Khoury et al. (2013). Similar to the unidirectional channel flow ($\partial/\partial x_z = 0$), the turbulent influence in the momentum equation within the pipe framework is dominated exclusively by the shear stress component $\overline{u_r u_z}^+$ and consequently, the quality of its reproduction is decisive for the successful prediction of the velocity fields. The predicted shear stress component shows a behavior consistent with the considered Reynolds number range following closely the DNS data over the entire pipe radius. A slight underprediction of $\overline{u_r u_z}^+$ between $y^+ = 20$ and 60 can be observed. It can be, analogous to the discussion associated with the channel, related to the $\overline{u_i u_j}$ -blending methodology (see Eq. (4.13)). However, this slight underestimation of the $\overline{u_r u_z}^+$ maximum has no noticeable influence on the velocity field, also in terms of the friction Reynolds number. The correct prediction of the streamwise Reynolds stress intensity component $\overline{u_z}^+$ (Fig. 4.14 (top)), representing the Reynolds stress tensor component contributing mostly to the kinetic energy of turbulence, is very important, especially with regard to more complex pipe systems, in which the fully developed pipe flow is used as inlet condition. Its peak value as well as the relevant wall distance are correctly reproduced by the EBM in accordance with the DNS data. Additionally, a slight overestimation of $\overline{u_z}^+$ near the pipe center can be observed, which could be a consequence of a somewhat higher peak value, but is limited to the lowest considered Reynolds number. The reproduction of two remaining normal Reynolds stress intensity components $\overline{u_r}^+$ and $\overline{u_\varphi}^+$ is of similarly high quality.

The briefly presented results of the EBM application to the fully developed pipe flow configuration confirm the impression gained within the channel flow computational campaign (see Chapter 4.3) and demonstrate the capability of the EBM to correctly reproduce the flow conditions of axis-symmetric pipe structures.

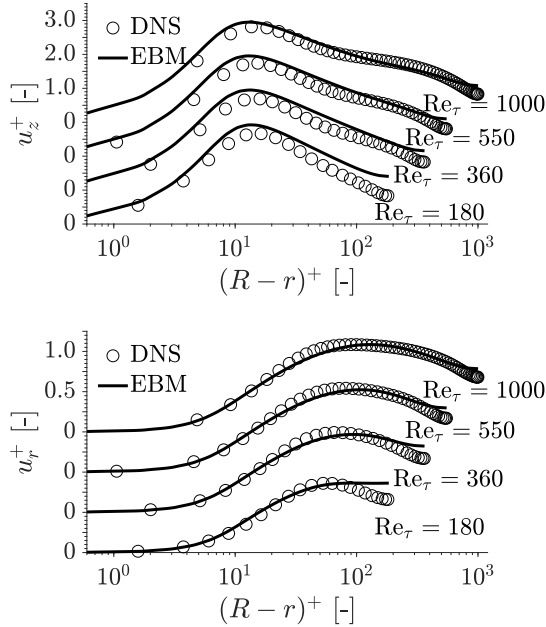


Figure 4.14.: Reynolds stress intensity components $\bar{u}_z^+ = \sqrt{\overline{u_z u_z}}/u_\tau$ (top) and $\bar{u}_r^+ = \sqrt{\overline{u_r u_r}}/u_\tau$ (bottom) for pipe flows with $Re_\tau = 180$ up to 1000 predicted by EBM (solid line). The DNS data by El Khoury et al. (2013) (circles) are depicted for comparison.

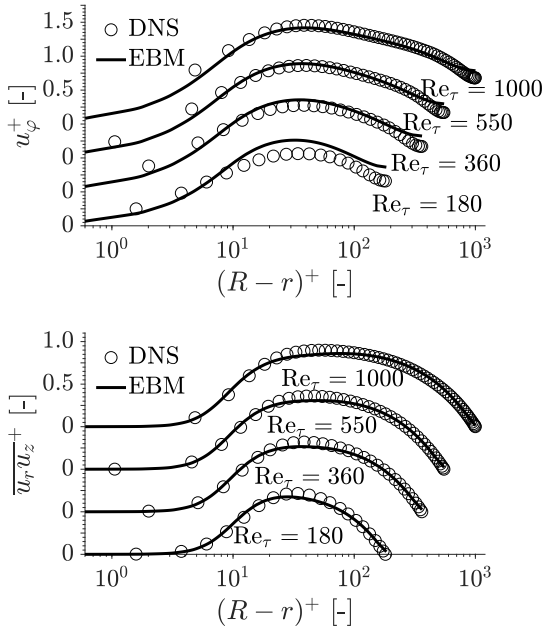


Figure 4.15.: Reynolds stress intensity component $\overline{u_\varphi^+} = \sqrt{\overline{u_\varphi u_\varphi}}/u_\tau$ (top) and shear component $\overline{u_r u_z}^+ = \overline{u_r u_z}/u_\tau$ (bottom) for pipe flows with $Re_\tau = 180$ up to 1000 predicted by EBM (solid line). The DNS data by El Khoury et al. (2013) (circles) are depicted for comparison.

4.5. Zero pressure gradient boundary layer

The previous two sections have demonstrated the capability of the EBM formulation by predicting fully developed flow conditions within channels and pipes. For evaluating the prediction of a developing flow by the EBM formulation, the spatial flow evolution over a flat plate is considered in the following, the so-called zero pressure gradient boundary layer. The boundary layer flow exhibits a farfield Reynolds number of $Re_\infty = U_\infty h / \nu = 207000$ related to the computational domain height h and farfield velocity U_∞ . To avoid a transition zone in the immediate vicinity downstream of the inlet, the DNS data from Schlatter and Örlü (2010) at $Re_\Theta = 670$ are set as inlet condition of the boundary layer with the non-existing fields generated by a frozen simulation procedure. The applied hexahedral, block-structured grid is characterized by a maximal wall distance of the wall closest cell of $y^+ < 0.6$ and a maximal streamwise cell size of $x^+ = 2.0$, which results in a grid-independent solution. The discretization of the convective terms is done completely with CDS.

The predicted friction coefficient $C_f = \tau_w / (0.5\rho U_\infty^2)$ by the EBM formulation is depicted in Fig. 4.16 top over the momentum thickness related Reynolds number Re_Θ . From the described inlet conditions, the friction coefficient could be reproduced according to the reference data by Schlatter and Örlü (2010) and Eitel-Amor et al. (2014) for $Re_\Theta < 2000$. For larger momentum thickness related Reynolds numbers ($Re_\Theta > 2000$), a slight deviation from the reference data can be seen, which corresponds to an overestimation of the friction coefficient related to the present momentum thickness related Reynolds number. Considering that both quantities, the friction coefficient C_f and the momentum thickness related Reynolds number Re_Θ , are results of the simulation, the depicted evolution in Fig. 4.16 top is reasonable up to very large momentum thickness related Reynolds numbers.

The corresponding velocity evolution of the boundary layer is depicted in Fig. 4.16 bottom in terms of the normalized streamwise velocity u^+ at $Re_\Theta = 2000, 4000$ and 8200 . The reference data of Schlatter and Örlü (2010) and Eitel-Amor et al. (2014) are again added to evaluate the results, as well as the equilibrium law with $\kappa = 0.41$ and $B = 5.5$. The resulting velocity profiles of the EBM follow the reference data, regardless of the momentum-thickness related Reynolds number, starting from the viscous sublayer, via the buffer

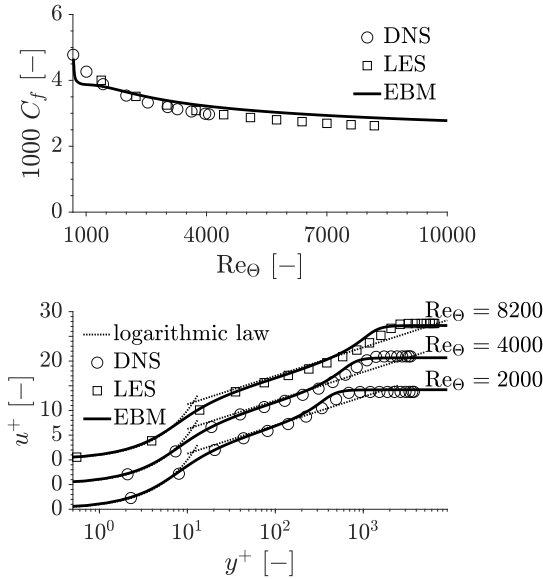


Figure 4.16.: Top: Friction coefficient of a zero-pressure-gradient boundary layer $C_f = \tau_w / (0.5\rho U_\infty^2)$ predicted by EBM (solid line). Reference data in terms of DNS simulation (circles) by Schlatter and Örlü (2010) and LES simulation (squares) by Eitel-Amor et al. (2014) are depicted for comparison.

Bottom: Streamwise velocity evolution $u^+ = u/u_\tau$ within a zero-pressure-gradient boundary layer depicted over normalized wall distance $y^+ = yu_\tau/\nu$ at $Re_\Theta = 2000, 4000$ and 8200 predicted by EBM (solid line). Reference data in terms of DNS (circles) by Schlatter and Örlü (2010) and LES (squares) by Eitel-Amor et al. (2014) as well as the equilibrium law with $\kappa = 0.41$ and $B = 5.5$ are depicted for comparison.

layer to the logarithmic range. Here, the detection of the curvature within the buffer layer and the reproduction of the logarithmic law for $y^+ > 30$ are to be emphasized. The deviations in the outer layer are due to the overestimation

of the friction coefficient at a given momentum thickness Reynolds number, which has been discussed in Fig. 4.16 top.

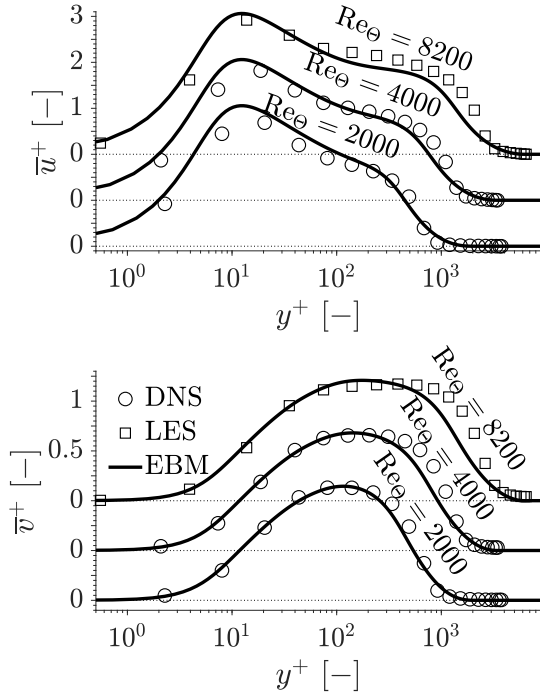


Figure 4.17.: Streamwise $\bar{u}^+ = \sqrt{\overline{uu}}/u_\tau$ (top) and wall-normal Reynolds stress evolution $\bar{v}^+ = \sqrt{\overline{vv}}/u_\tau$ (bottom) within a zero-pressure-gradient boundary layer depicted over normalized wall distance $y^+ = yu_\tau/\nu$ at $Re_\Theta = 2000, 4000$ and 8200 predicted by EBM (solid line). Reference data in terms of DNS (circles) by Schlatter and Örlü (2010) and LES (squares) by Eitel-Amor et al. (2014) are depicted for comparison.

In order to conclude the considerations of the boundary layer, Figures 4.17 and 4.18 present the evolution of the Reynolds stresses at $Re_\Theta = 2000, 4000$ and 8200 . The reference data by Schlatter and Örlü (2010) and Eitel-

Amor et al. (2014) are added similar to Fig. 4.16 bottom. Regardless of the momentum thickness related Reynolds number, a globally correct evolution of the Reynolds stress components can be recognized, which are consistent in shape and magnitude to the DNS data. Starting from the region closest to the wall, the stresses predicted with the EBM follow the reference DNS data despite a slight underestimation of the spanwise component \overline{w}^+ accompanied by a likewise slight overestimation of the streamwise component \overline{u}^+ . The latter can also be seen in a slight overestimation of the \overline{u}^+ peak value. With regard to the RANS-based EBM formulation, the described deviations are justifiably small and should not obscure the close agreement and reproduction of the turbulence evolution in comparison with the DNS data. A clearer underestimation of the turbulent level independent of the momentum thickness related Reynolds stress components can be observed in the transition region of the boundary layer with the farfield. The gradient of the Reynolds stresses seems to be too pronounced for $y^+ > 300$, whereas the cause is difficult to determine. However, the results presented here have verified the ability of the EBM to detect developing flows up to large momentum thickness related Reynolds numbers, which is not self-evident for RANS-based turbulence models.

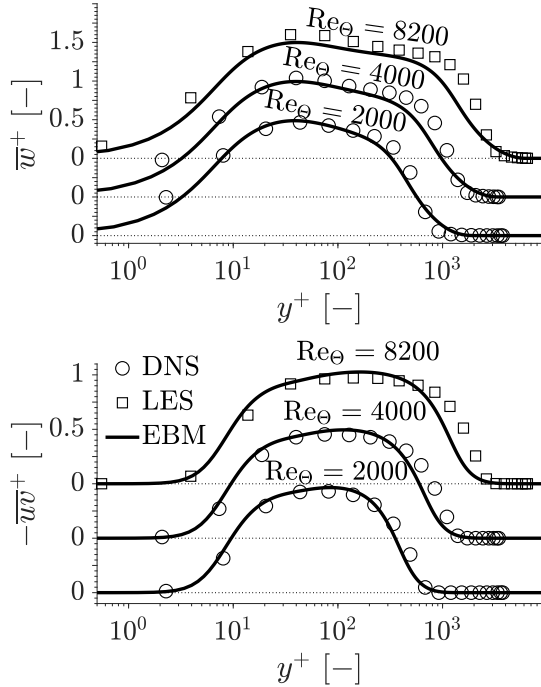


Figure 4.18.: Spanwise $\overline{w}^+ = \sqrt{\overline{w\overline{w}}}/u_\tau$ (top) and shear Reynolds stress evolution $\overline{wv}^+ = \overline{wv}/u_\tau^2$ (bottom) within a zero-pressure-gradient boundary layer depicted over normalized wall distance $y^+ = yu_\tau/\nu$ at $Re_\theta = 2000, 4000$ and 8200 predicted by EBM (solid line). Reference data in terms of DNS (circles) by Schlatter and Örlü (2010) and LES (squares) by Eitel-Amor et al. (2014) are depicted for comparison.

4.6. Flow past a rounded step - APG flow

As already mentioned within the discussion of channel flows (see Chapter 4.3), the reproduction of highly turbulent flows is a challenging task for RANS-based turbulence models especially in the detection of the correct turbulence level. The EBM formulation has already indicated its ability to reproduce the flow topology of highly turbulent flows within the generic channel flow $Re_\tau = 5200$. However, the general capability of a turbulence model is not directly provided by the observation of a generic case, such as the channel flow. Therefore, the considerations are extended by an additional highly turbulent flow case, denoted by TC01 (“incipient” case) within the European Project ‘HiFi-TURB’ (see Alaya et al., 2020). The TC01 flow configuration represents a rounded backward facing step geometry and is closely related to the axis-symmetric afterbody test case investigated by Disotell and Rumsey (2017), but is suitably modified for a more convenient computational access. The flow experiences an APG due to the continuous expanding shape of the rounded backstep but remains attached over the entire computational domain. To avoid the laminar-turbulent transition of the boundary layer, the inflow corresponds to a fully turbulent boundary layer with a momentum thickness related Reynolds number of $Re_\Theta = 1455$. The highly turbulent character of the TC01 arises from the Reynolds number related to the step height $h = 0.62 R_{\max}$ and the farfield velocity U_∞ with $Re_h = U_\infty h / \nu = 78500$. Here, R_{\max} is a further characteristic parameter, the maximum forebody radius, which describes the radius of the first part section in the original axis-symmetric geometry within the work of Disotell and Rumsey (2017) and is translated to the two-dimensional consideration. The computational domain extends in its entirety over $12.1 R_{\max}$ in flow direction, with the inlet positioned $4.5 R_{\max}$ upstream of the rounded backstep and the outlet $5.5 R_{\max}$ downstream of the rounded backstep. The normal-to-wall height of the computational domain is set to $34 R_{\max}$, whereby this height is chosen to ensure that the zero gradient boundary condition assumed on the top of the computational domain does not influence the pressure conditions on the wall. For a detailed description of the flow domain, reference is made to Alaya et al. (2021). The mesh of the TC01 case corresponds to a block-structured, hexahedral grid with $n_{\text{total}} = 130000$ cells in total. The discretization of the convective terms within the numerical procedure is done with CDS.

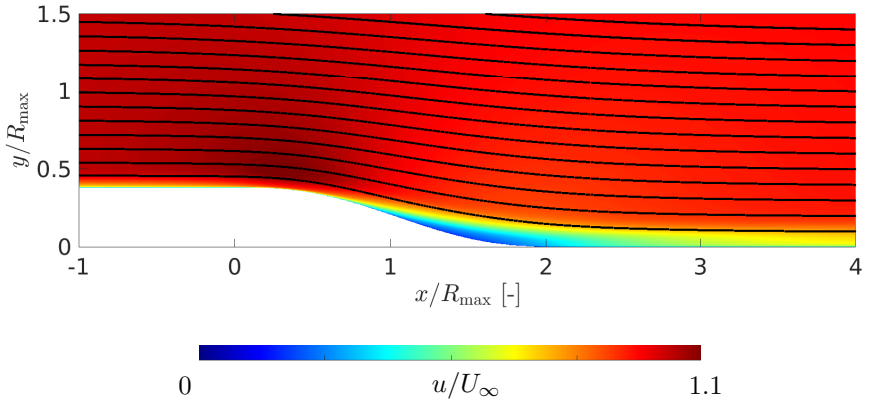


Figure 4.19.: Enlarged visualisation of the iso-contours of the streamwise velocity u/U_∞ and the streamlines around the rounded backstep predicted by EBM.

For a first insight into the flow topology predicted by the EBM, the iso-contours of the streamwise velocity and the streamlines are illustrated in Fig. 4.19. The developing boundary layer flow enters the domain via the left edge, experiences a cross-sectional expansion at $x/R_{\max} = 0$ up to 2.1 and leaves the domain via the right edge. As a result of the cross-sectional expansion, the flow in the nearest vicinity of the rounded backstep is decelerated, however, no flow detachment is present, as can be seen from the scale and the coloring in Fig. 4.19.

For evaluating the flow predicted by the EBM, the friction coefficient $C_f = \tau_w / (0.5\rho U_\infty^2)$ along the wall is suitable for a first global reference, representing the detection of the correct wall velocity gradient. The friction coefficient is depicted in Fig. 4.20 along the streamwise coordinate x/R_{\max} , which has its origin at the beginning of the rounded backstep curvature. To enable a comparison, the DNS data by Massa and Colombo (2021) are depicted as reference data (circle).

As mentioned, the inflow ($x/R_{\max} = -4.5$) corresponds to a developing boundary layer with a momentum thickness related Reynolds number of

$Re_\Theta = 1455$. The inlet friction coefficient of the EBM is slightly overestimated in comparison to the DNS data, which is consistent with the discussion of Fig. 4.16 top. Downstream the inlet, the DNS data deviate from the general evolution of the friction coefficient of a boundary layer flow and exhibit a peak immediately after the inlet. This behavior can probably be attributed to the numerical procedure used to generate synthetic turbulent structures within the DNS framework. As the DNS data are not subject of discussion, an evaluation of the EBM results far upstream of the rounded step ($x/R_{\max} < -2$) is omitted. In the vicinity of the rounded backstep ($x/R_{\max} > -2$), the predicted friction coefficient by EBM and DNS are converging and coincide for $x/R_{\max} > -0.5$. The friction peak at the beginning of the rounded backstep curvature at $x/R_{\max} = 0.15$ is reproduced in position and magnitude by the EBM. Along the curvature of the rounded backstep, the friction coefficient drops abruptly, resulting in a minimum at $x/R_{\max} = 1.5$. The EBM can qualitatively reproduce the drop. However, the drop is slightly too sharp predicted by the EBM, which results in a slight underestimation of the friction coefficient around $x/R_{\max} \approx 1$. Downstream the minimum in the so-called recovery zone the friction coefficient increases and adapts to the boundary layer flow again. Both, DNS and EBM are in line in this region and no significant deviations can be observed.

To evaluate the capability of the EBM reproducing the flow evolution over the rounded backstep of the TC01, the evolution of the streamwise velocity u , turbulent kinetic energy k and shear Reynolds stress component \overline{uv} is depicted in Figures 4.21, 4.22 and 4.23 at selected streamwise positions ($x/R_{\max} = 0, 1, 2, 3, 4$) along the dimensionless wall-normal distance (y/R_{\max} and y^+). For each flow quantity, two different forms of depiction are provided, a linear depiction normalized by the farfield velocity U_∞ (top) and a semi-logarithmic depiction normalized by the friction velocity u_τ (bottom). Again, the reference DNS data by Massa and Colombo (2021) are depicted for comparison (circles).

As the friction coefficient (see Fig. 4.20) has already indicated, the linear depictions of the flow quantities demonstrate excellent agreement with the DNS data. The EBM could reproduce the flow deceleration as a result of the cross-sectional expansion and the arising APG as well as the enhanced turbulent production within the shear layer between the region of low velocity magnitude near the rounded backstep and the farfield flow. Only a slight overestimation of k and \overline{uv} is present at $x/R_{\max} = 2$.

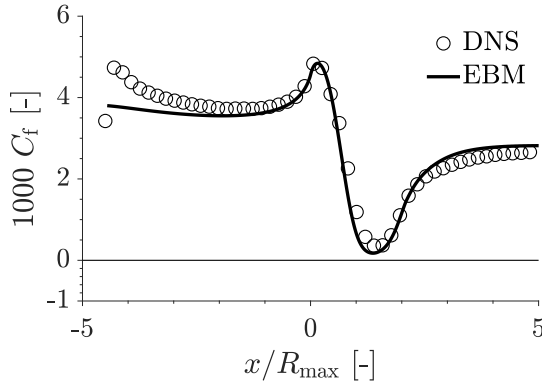


Figure 4.20.: Friction coefficient $C_f = \tau_w / (0.5\rho U_\infty^2)$ depicted along the streamwise coordinate x/R_{\max} predicted by EBM (solid line) in comparison to the DNS data by Massa and Colombo (2021) (circles).

A similar impression can be seen for the semi-logarithmic depictions normalized with u_τ , which is significantly more challenging to reproduce for the EBM due to the inclusion of the near-wall velocity gradient via u_τ . With respect to the streamwise evolution of the friction coefficient already discussed in Fig. 4.20, a basic agreement with the DNS data is not surprising, whereby the reproduction of the velocity in the outer layer has to be emphasized. However, the u_τ -normalization clearly emphasizes potential deviations in the near-wall behavior of the flow, which leads to additional deviations in the depicted evolutions. Besides the overestimation of the turbulence at $x/R_{\max} = 2$, a deviation for $x/R_{\max} = 1$ from the DNS data can be seen independent of the flow quantity. Considering the agreement of the EBM and DNS linear depictions at $x/R_{\max} = 1$, the cause of the deviations at $x/R_{\max} = 1$ can be found in the evolution of the friction coefficient (compare Fig. 4.20). As already mentioned, the minimum friction coefficient is slightly underestimated by the EBM. Although the deviation of the friction coefficient is comparatively small, the low level of the friction coefficient around its minimum causes it to be more significant and leads to the mentioned deviation in the u_τ -normalized flow quantities at $x/R_{\max} = 1$.

Finally, the results presented within the TC01 case proved the capability of

4. Development of an ω_h -based elliptic-blending-related Reynolds-stress model

the EBM to correctly reproduce highly turbulent, APG-driven flow configurations in terms of both flow topology and turbulence level. Slight deviations have been identified and discussed, but do not weaken the generally close agreement with the DNS data.

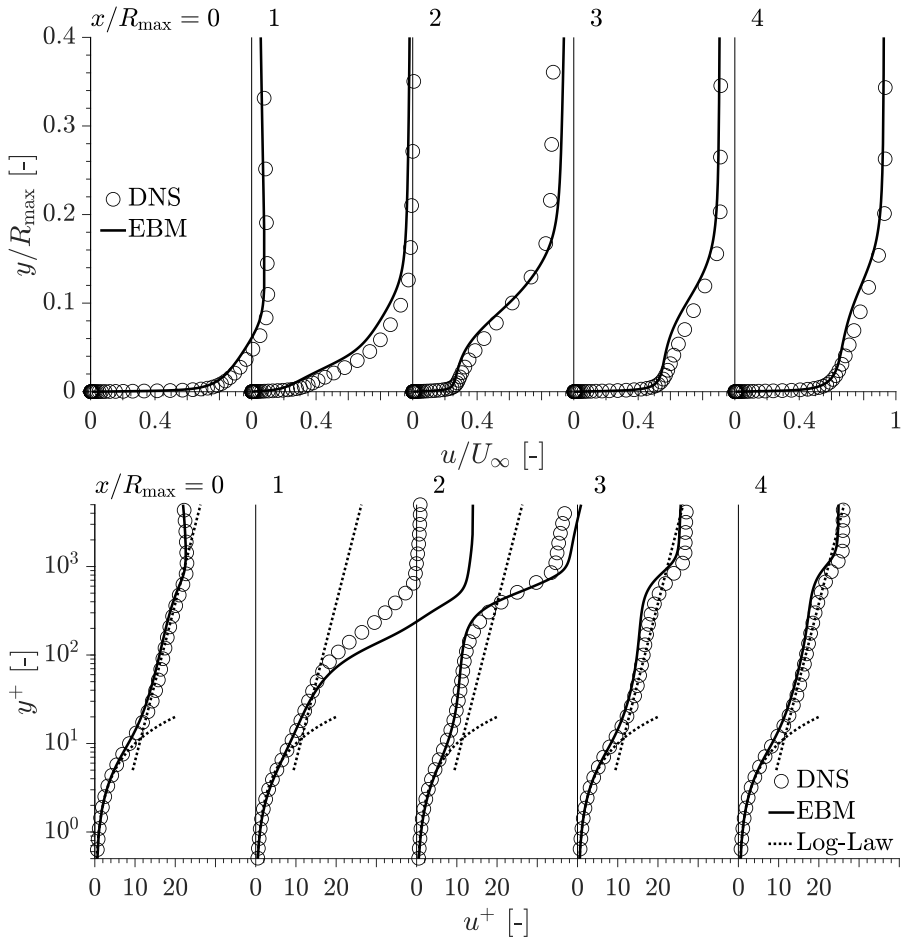


Figure 4.21.: Streamwise velocity component normalized by the farfield velocity u/U_∞ (top) and friction velocity $u^+ = u/u_\tau$ at selected positions within the TC01 case ($x/R_{\max} = 0, 1, 2, 3, 4$) along the domain height y/R_{\max} (top) and y^+ (bottom) predicted by the EBM (solid line) in comparison to the DNS data by Massa and Colombo (2021) (circles) as well as the log law (dotted line).

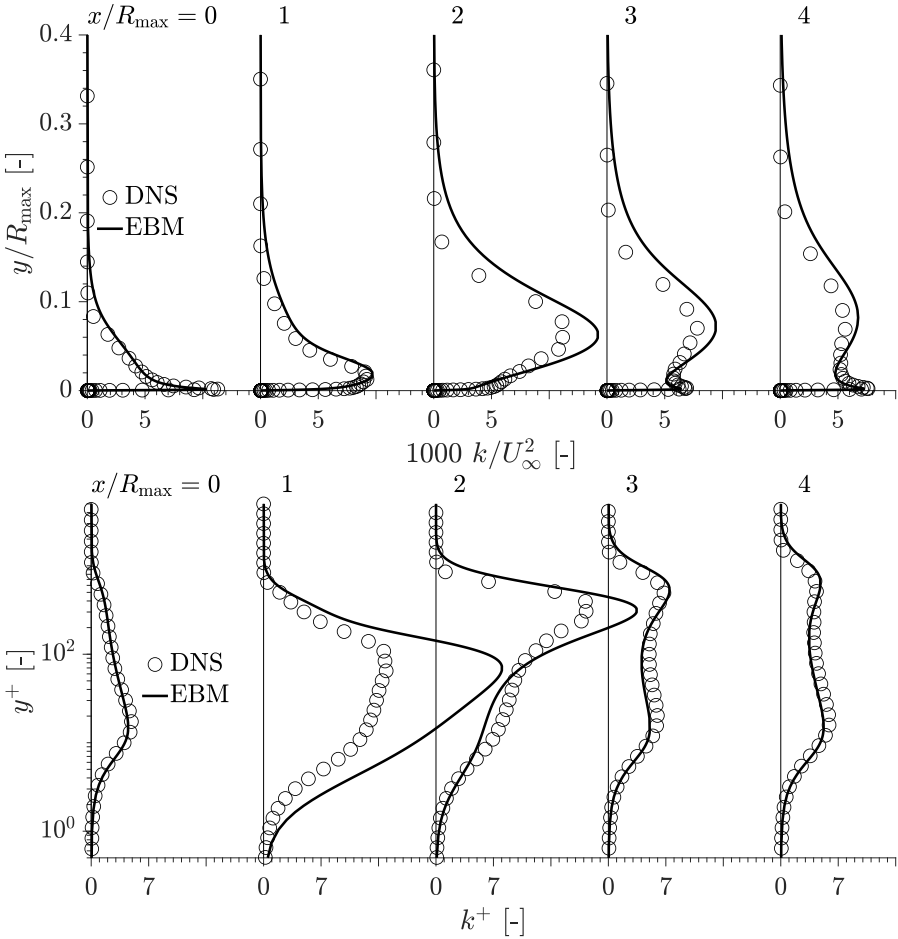


Figure 4.22.: Turbulent kinetic energy normalized by the farfield velocity k/U_{∞}^2 (top) and friction velocity $k^+ = k/u_{\tau}^2$ at selected positions within the TC01 case ($x/R_{\max} = 0, 1, 2, 3, 4$) along the domain height y/R_{\max} (top) and y^+ (bottom) predicted by the EBM (solid line) in comparison to the DNS data by Massa and Colombo (2021) (circles).

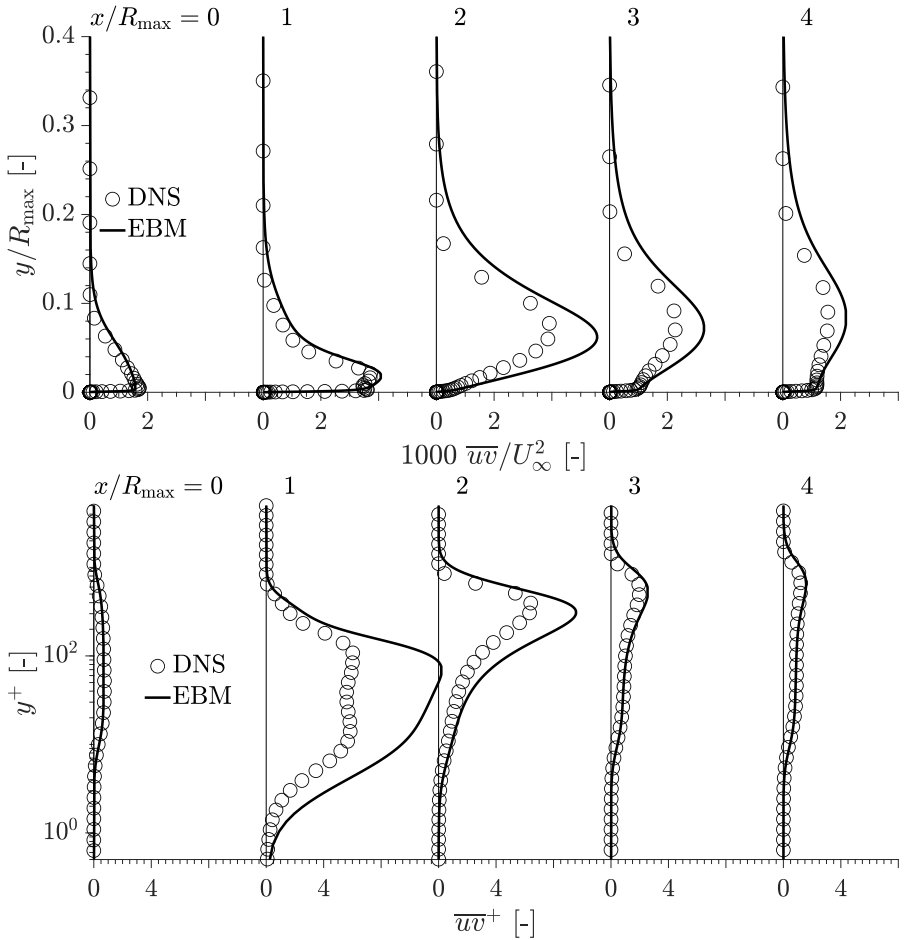


Figure 4.23.: Reynolds shear stress component normalized by the farfield velocity $\overline{uv}/U_{\infty}^2$ (top) and friction velocity $\overline{uv}^+ = \overline{uv}/u_{\tau}^2$ at selected positions within the TC01 case ($x/R_{\max} = 0, 1, 2, 3, 4$) along the domain height y/R_{\max} (top) and y^+ (bottom) predicted by the EBM (solid line) in comparison to the DNS data by Massa and Colombo (2021) (circles).

4.7. Flow past Backward-facing step (BFS)

Fully developed and developing flow conditions, which are strictly following the wall topology, have been considered in the previous chapters. Under certain conditions, a flow is not able to follow the wall topology and detaches, for example by passing a sharp edge. The reason for flow detachment is always an emerging adverse pressure gradient (APG), however, the flow situation that exists at an expanding sharp edge is characterized by a fixed detachment point compared to other detachment situations. Such a geometry-induced flow detachment is often applied in technical applications, e.g., automotive industry, to provide a defined flow topology and to guarantee the functionality independent of the upstream flow conditions. A well-known benchmark case in fluid mechanics is the flow over a right-angled step, the so-called backward-facing step (BFS), which is studied extensively by Driver and Seegmiller (1985), Jovic and Driver (1995) and Le et al. (1997). Within the BFS, a developing flow passes a right-angled step with height h and experiences a sudden expansion of its cross-section. The sharp edge of the step causes a geometry-induced flow separation with a reattachment of the flow far downstream of the step. The flow topology is usually characterized by the step-height Reynolds number $Re_h = U_\infty h / \nu$ with the free-stream velocity of the developing flow U_∞ as well as by the ratio of the inlet to the outlet height. For the present work, the experimental conditions according to Driver and Seegmiller (1985) are applied due to the challenging step-height Reynolds number of $Re_h = 36000$ and an inlet to outlet height ratio of $8/9$. The challenging flow conditions can be illustrated by the corresponding channel-based inlet Reynolds number, which is $Re_b = 8hU_b / \nu = 288000$ with $U_b = U_\infty$ and approximately equivalent to a channel friction Reynolds number of $Re_\tau = 5200$, discussed in Chapter 4.3.

The computational domain of the BFS configuration extends $4h$ upstream and $50h$ downstream of the step, with an inlet height equal to $8h$. The inlet length of $4h$ is chosen based on the first available data set from Driver and Seegmiller (1985), which serves as inlet data. The block-structured, two-dimensional, hexahedral grid applied consists of $n_{\text{total}} = 260000$ cells, which guarantees a grid-independent solution of the simulation. According to the low Reynolds character of the EBM, a dimensionless wall distance of the cell closest to the wall of $y^+ < 1$ is considered. The discretization of the convective term is done with CDS.

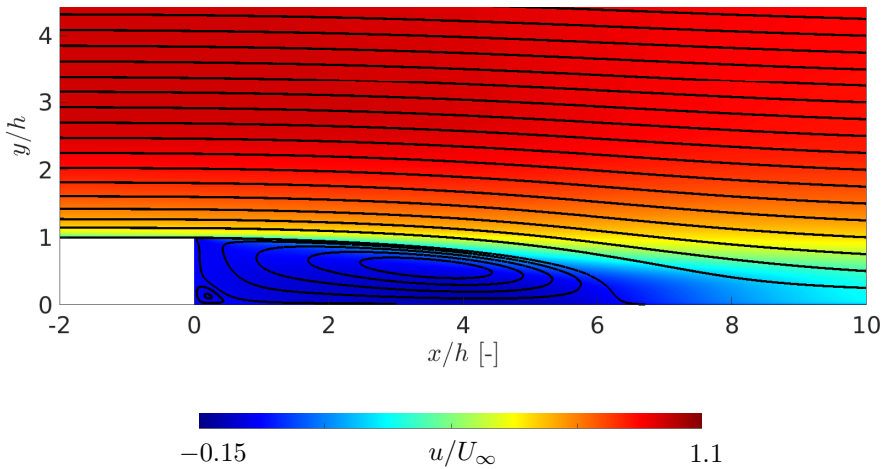


Figure 4.24.: Enlarged visualisation of the iso-contours of the streamwise velocity u/U_∞ and the streamlines around the right-angled step predicted by EBM.

For a first insight into the flow topology, the streamwise velocity u/U_∞ as well as the streamlines are illustrated in Fig. 4.24 with focus on the step region, where the developing channel flow enters the domain via the left side, passes the step and leaves the domain via the right side. The streamwise coordinate x is introduced, which has its origin at the right-angled step. The corresponding pressure $C_p = (p - p(x/h = 37.5)) / (0.5\rho U_\infty^2)$ and friction coefficient $C_f = \tau_w / (0.5\rho U_\infty^2)$ along the bottom wall are depicted in Fig. 4.25 as well as the streamwise velocity u/U_∞ and Reynolds stress $\overline{u_i u_j} / U_\infty^2$ evolutions in Figures 4.26 and 4.27. A result-oriented brief interactive flow discussion follows to assess the quality of the EBM results.

As the developing inflow passes the step ($x/h = 0$), it experiences a sudden cross-sectional expansion and detaches at the sharp edge of the step, which is accompanied by a sudden drop in friction coefficient (see Fig. 4.25). A recirculation zone forms in the step corner and is enclosed by the bulk streamlines. According to the zero-crossing of the streamwise velocity depicted in Fig. 4.26

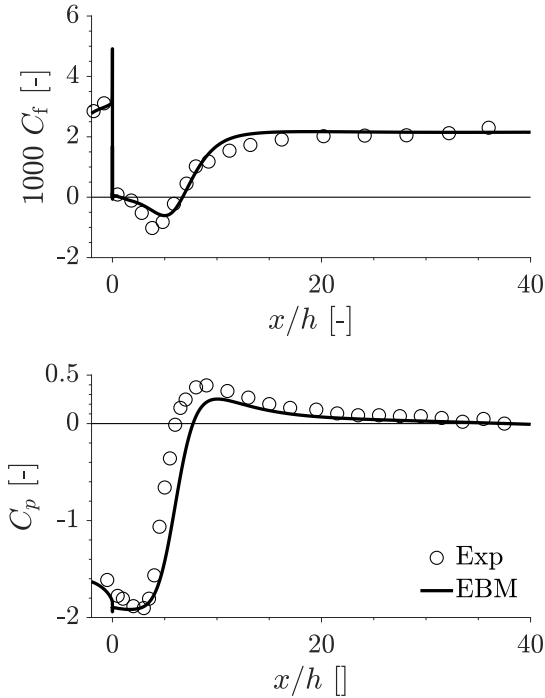


Figure 4.25.: Bottom friction coefficient $C_f = \tau_w / (0.5\rho U_\infty^2)$ (top) and pressure coefficient $C_p = (p - p(x/h = 37.5)) / (0.5\rho U_\infty^2)$ (bottom) of the backward facing step with $Re_h = 36000$ calculated by EBM (solid line) in comparison to the reference data by Driver and Seegmiller (1985) (circles).

top, a main clockwise rotating vortex exists in the recirculation zone with a clearly smaller one in the immediate vicinity of the corner as can be observed in the streamline pattern in Fig. 4.24.

The free shear layer between the recirculation zone and the bulk flow is the origin of enhanced turbulence production and causes peak values in all Reynolds stresses. The evolution of the Reynolds stresses and their peak characteristics within the free shear layer could be reproduced by the EBM with deviations

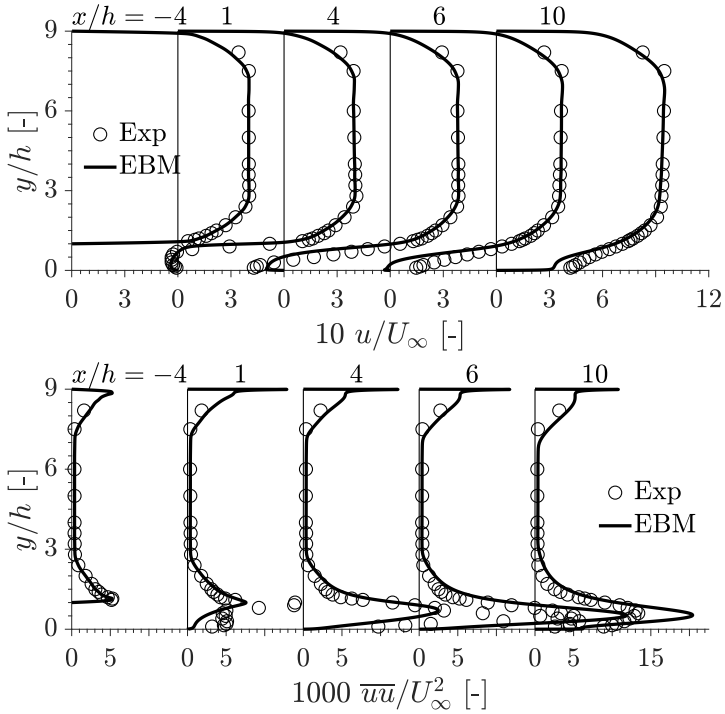


Figure 4.26.: Streamwise velocity u/U_∞ (top) and Reynolds stress component \overline{uu}/U_∞^2 (bottom) depicted over the channel height y/h of the backward facing step with $Re_h = 36000$ calculated by EBM (solid line) in comparison to the reference data by Driver and Seegmiller (1985) (circles).

in the wall-normal component \overline{vv} . The bulk flow streamlines continuously move closer to the wall downstream of the edge and reattach smoothly, which indicates an avoidance of backbending within the BFS configuration. The length of the recirculation zone was determined by Driver and Seegmiller (1985) with $x/h \approx 6.28$ and is captured by the EBM formulation with a deviation of less than 7% ($x/h = 6.71$). Attention should be paid to some inconsistency

of the experimental reference data, indicating a reattached velocity profile at $x/h = 6$, which is not in agreement with the corresponding experimental friction coefficient. Downstream of the reattachment point, the flow equalizes over the cross-section with an increasing streamwise velocity near the bottom wall and a weakening of the shear layer induced peak of the Reynolds stresses. In this region, an overestimation of the \overline{uu} and \overline{vv} peak can be observed at $x/h = 10$ within the turbulence evolution predicted by the EBM.

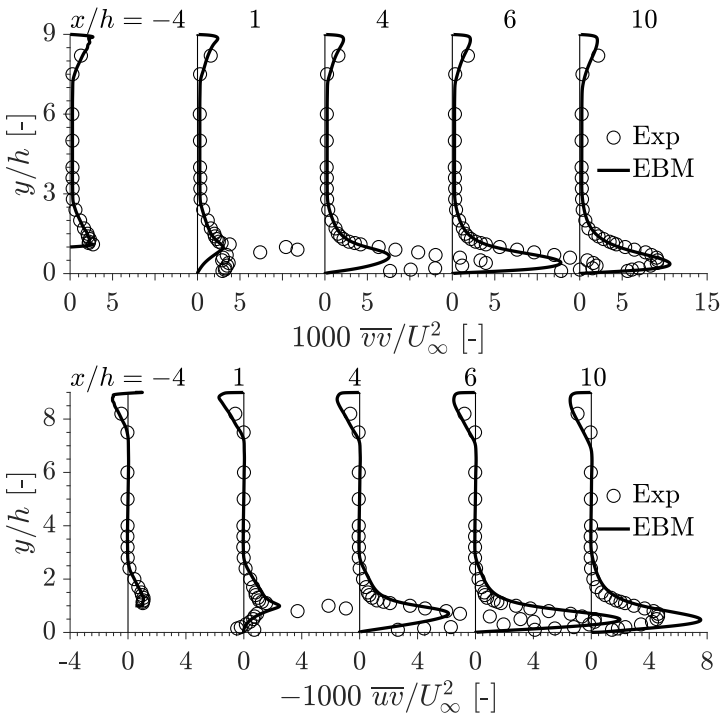


Figure 4.27.: Reynolds stress component \overline{vv}/U_∞^2 (top) and \overline{uv}/U_∞^2 (bottom) depicted over the channel height y/h of the backward facing step with $Re_h = 36000$ calculated by EBM (solid line) in comparison to the reference data by Driver and Seegmiller (1985) (circles).

The presented data prove the capability of the EBM to reproduce a geometry-induced flow separation while avoiding streamline backbending. Both the length of the recirculation zone and the flow evolution could be reproduced according to the reference data by Driver and Seigmiller (1985). The deviations predicted by the EBM are acceptable in view of the highly turbulent flow configuration with $Re_h = 36000$ ($Re_b = 8hU_b/\nu = 288000$).

4.8. Flow past a periodically arranged 2D hill

Contrary to the previously handled backward-facing step flow, characterized by a fixed point separation at a sharp edge (see Chapter 4.7), the boundary layer separation at a continuous curved wall represents a much greater challenge for Reynolds-Averaged Navier-Stokes (RANS) models. Here, the detachment point is not fixed, but oscillates over a larger wall area, which subsequently leads to a strong unsteadiness of the separated shear layer. Its interaction with the bulk flow results in more intense momentum exchange due to enhanced turbulence activity. This represents a highly fluctuating flow event which is beyond the reach of the time-averaged rationale of the RANS models. Typical outcome of actually all RANS models is a lower turbulence level in the detached shear layer, correlated with a weaker momentum transport across it, and a correspondingly longer flow reversal region.

A suitable benchmark for RANS model validation is the periodic hill configuration. The periodic hill forms a flow over periodically arranged hills, where only one valley is considered and the geometry is imitated via periodic boundary conditions. The design of the lower wall, on which the hills are mounted, is in accordance with Fröhlich et al. (2005) and the upper wall remains flat. The characteristic flow Reynolds number $Re_h = U_{\text{inflow}}h/\nu$ is based on the mean inflow velocity U_{inflow} and hill height h as characteristic velocity and length. According to the experimental and LES-predicted investigations by Rapp (2008) and by Breuer et al. (2009), Reynolds numbers of $Re_h = 10600$ and 37000 are considered in the following. Comparable 'channel' Reynolds numbers with the clearance height as characteristic length ($2.035 h$) are $Re_b = U_{\text{inflow}}(2.035h)/\nu = 21571$ and $Re_b = 75295$, emphasizing more aptly the respective turbulent activity level of the configurations considered. The computations are carried out on a block-structured hexahedral grid with 285×240 ($Re_h = 10600$) and 570×480 ($Re_h = 37000$) cells. The discretization of the convective terms is done completely with CDS.

The predicted flow field of the EBM for both Reynolds numbers is visualized in Fig. 4.28 with the iso-contours of the streamwise velocity u/U_{inflow} and the associated streamlines. The flow enters the periodic hill domain via the left plane and leaves it via the right one. As mentioned above, the inflow and outflow planes are connected to each other via periodic boundaries. The streamline interpretation reveals clearly the separation bubble shortening cor-

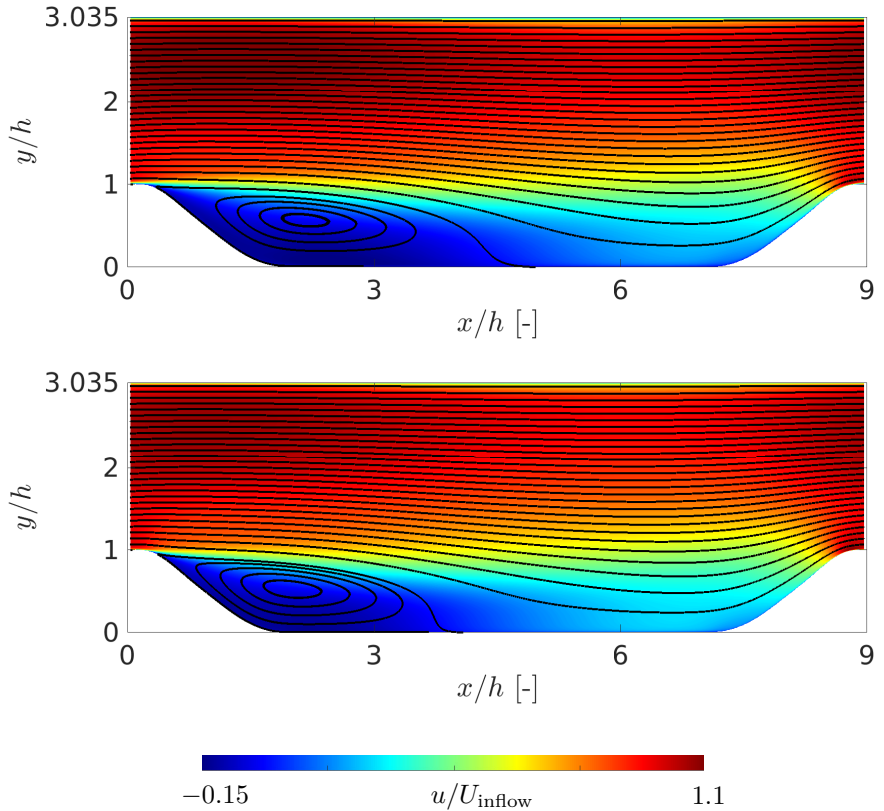


Figure 4.28.: Iso-contours of the mean streamwise velocity u/U_{inflow} and corresponding streamlines in the periodic hill flow at $Re_h = 10600$ (top) and $Re_h = 37000$ (bottom).

related with the turbulence activity intensification within the separated shear layer in terms of the flow Reynolds number increase (see discussion associated with the Reynolds stress field development, Figures 4.30 and 4.31). To evaluate the quality of the EBM results, Fig. 4.29 gives an insight into the near-wall flow characteristic in terms of the skin friction coefficient $C_f = \tau_w / (0.5\rho U_{\text{inflow}}^2)$ at

the bottom wall along the streamwise coordinate x/h . Furthermore, the evolution of the streamwise velocity u/U_{inflow} and the Reynolds stress components $\overline{u_i u_j}/U_{\text{inflow}}^2$ is displayed in Figures 4.30 and 4.31 at selected streamwise positions ($x/h = 0.05, 0.5, 1.0, 2.0, 3.0, 4.0, 5.0, 6.0, 7.0$ and 8.0). The reference data by Rapp (2008) (triangle) and Breuer et al. (2009) (circles and squares) are added for comparison, with the data for the higher Reynolds number ($Re_h = 37000$) highlighted in blue for clarity. An interactive assessment of the EBM results follows mutually for both Reynolds numbers.

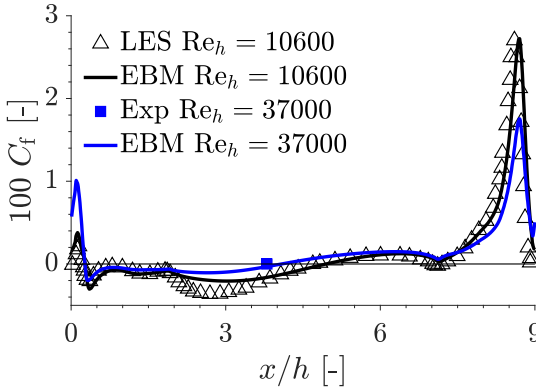


Figure 4.29.: Skin friction coefficient $C_f = \tau_w / (0.5\rho U_{\text{inflow}}^2)$ development at the lower hill-shaped wall for $Re_h = 10600$ (black solid line) and $Re_h = 37000$ (blue solid line) predicted by EBM. Reference data by Breuer et al. (2009) (LES, $Re_h = 10600$, triangles) and Rapp (2008) (Experiment, $Re_h = 37000$, fulfilled black square) are depicted for comparison.

The inflow into the periodic hill domain exhibits a distinct near-wall velocity peak and a consequent anisotropic Reynolds stress contribution, which is clearly pronounced towards the bottom wall independent of the Reynolds number (see for example first depiction in Fig. 4.30 bottom). With regard to the narrowing of the cross-section by approaching the upstream-located second hill a continuous flow acceleration causes an increased velocity gradient at the wall (as visible for instance at $x/h \approx 0.8$, Fig. 4.30-upper), resulting in a local

peak of the friction coefficient ($C_f \approx 0.0028$) at $x/h \approx 8.6$, Fig. 4.29. While the flow is subjected globally to an adverse pressure gradient, the accelerated flow over the windward side of the hill is associated with the favorable pressure gradient (see e.g., Fig. 11 in Breuer et al. (2009)). The latter is directly correlated with the C_f increase that ends with the previously mentioned peak. The corresponding pressure is, according to Breuer et al. (2009), even negative at this location. Toward the hill crest at $x/h \approx 9$, i.e. at $x/h \approx 0$, the skin friction coefficient decreases to a zero value. Immediately afterward a next local increase occurs at $x/h \approx 0.15$. Subsequently, the friction coefficient development indicates negative values within the flow reversal region.

As already discussed, an adverse pressure gradient (APG) occurs downstream of the first hill, arising from the cross-sectional expansion and causes a flow detachment immediately downstream of the inlet plane at the bottom wall. The position of the detachment predicted by the EBM is independent of the considered Reynolds number (see first zero-crossing in Fig. 4.29). At least for the lower Reynolds number, this outcome is consistent with the reference data by Breuer et al. (2009) (we recall that the corresponding database for the higher Reynolds number does not exist). The flow detachment causes the formation of a recirculation zone downstream of the first hill with a clockwise rotating sense as can be observed by the sign change of the streamwise velocity in Fig. 4.30 top. The shear layer between the recirculation zone and the bulk flow causes a region of enhanced turbulence production with global peaks characterizing all Reynolds stress components as can be seen in Fig. 4.31 for example. The enhanced turbulence production is reproduced reasonably well by the EBM, but with a slight delay resulting in an underestimation of the Reynolds stress components in the middle section of the periodic hill domain in streamwise direction. The position of flow reattachment and consequently the length of the recirculation zone depends on the considered Reynolds number and is shorter for the higher Reynolds number. As mentioned previously, this is in accordance with the level of turbulence activity in the separated layer, which directly controls the momentum transport between the backflow region and the mainstream (Figures 4.30 and 4.31, note the almost four times higher normalization factor, representing the inflow velocity, for the higher Reynolds number). The reattachment point can be identified by the second zero-crossing of the friction coefficient C_f in Fig. 4.29 and corresponds to reference values of $x/h = 4.69$ for $Re_h = 10600$ by Breuer et al. (2009) and $x/h = 3.8$ for

$Re_h = 37000$ by Rapp (2008). The EBM formulation can reproduce the length of the recirculation zone with an error less than 8 %, which correspond to a reattachment point of $x/h = 4.953$ ($Re_h = 10600$) and $x/h = 4.078$ ($Re_h = 37000$), respectively. This slight enlargement of the separation zone is consistent with the previously discussed underprediction of the turbulence intensity within the separated shear layer. Downstream of the reattachment point, the flow relaxes over the entire height of the computational domain and the turbulence production due to the mean shear decreases correspondingly. The magnitude of the Reynolds stress components returned by the EBM recovers appropriately agreeing well with the reference data. The flow reaches the slope of the second hill and experiences a narrowing of the cross-section as mentioned in the beginning, which causes an acceleration of the flow near the bottom wall accompanied by a decrease in turbulence. The rapid change in flow acceleration and subsequent deceleration, as well as a weakening and intensification of turbulence production, cannot be followed closely by the EBM and the predicted velocity and turbulence development exhibits certain quantitative deviations. However, noteworthy is the detection of the sign change of the shear Reynolds stress component on the slope of the second hill (see Fig. 4.31 bottom).

The result-oriented flow discussion of the periodic hill configuration has demonstrated the capability of the EBM to reproduce correctly the associated flow topology for both hill height related Reynolds numbers in reasonable agreement with the reference data. In this context, the calculated friction coefficient following closely the LES reference data can be particularly emphasized.

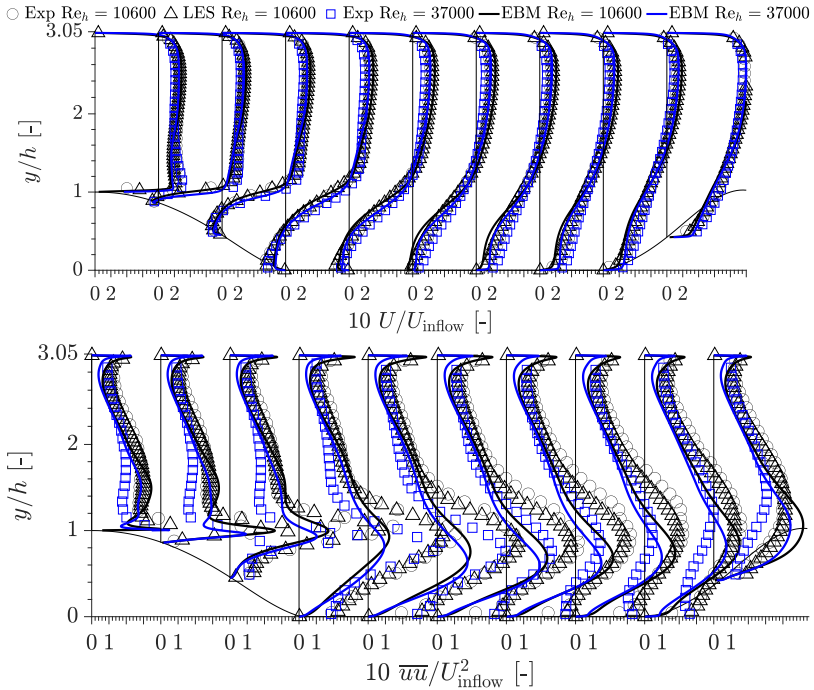


Figure 4.30.: Streamwise velocity u/U_{inflow} (top) and streamwise Reynolds stress component $\overline{uu}/U_{inflow}^2$ (bottom) profiles at selected streamwise positions ($x/h = 0.05, 0.5, 1.0, 2.0, 3.0, 4.0, 5.0, 6.0, 7.0$ and 8.0) depicted over the flow domain height y/h predicted by EBM for $Re_h = 10600$ (black line) and $Re_h = 37000$ (blue line). The reference data by Rapp (2008) (black circles and blue squares) and Breuer et al. (2009) (black triangles) are shown for comparison.

4. Development of an ω_h -based elliptic-blending-related Reynolds-stress model

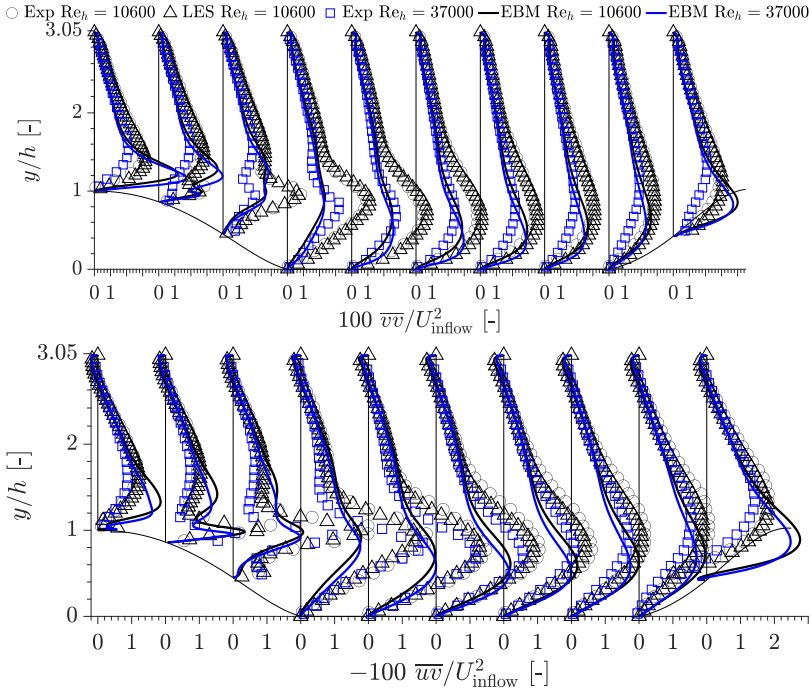


Figure 4.31.: Spanwise $\overline{v\overline{v}}/U_{\text{inflow}}^2$ (top) and shear Reynolds stress component $\overline{w\overline{v}}/U_{\text{inflow}}^2$ (bottom) profiles at selected streamwise positions ($x/h = 0.05, 0.5, 1.0, 2.0, 3.0, 4.0, 5.0, 6.0, 7.0$ and 8.0) depicted over the flow domain height y/h predicted by EBM for $Re_h = 10600$ (black line) and $Re_h = 37000$ (blue line). The reference data by Rapp (2008) (black circles and blue squares) and Breuer et al. (2009) (black triangles) are shown for comparison.

4.9. Flow in a 3D-diffuser

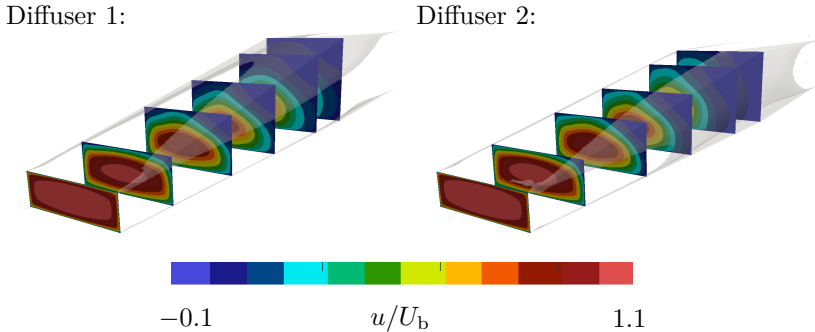


Figure 4.32.: Iso-contours of streamwise velocity u/U_b at selected cross-sections ($x/h = 0; 2; 5; 8; 12; 15$) for diffuser 1 (left) and diffuser 2 (right) predicted by EBM. The $u/U_b = 0$ surface is illustrated in gray to highlight the separation zone.

The cases considered up to now are characterized by a two-dimensional mean flow topology with a more or less isolated flow phenomenon such as flow separation at a continuously expanding cross-section (periodic hill). The validation study of the EBM is extended in the following to a three-dimensional flow topology with a more complex separation structure, since the fluid mechanics problems in technical applications are rarely of two-dimensional nature. The 3D-diffuser configurations have been often computed in the framework of different computational workshops for the collaborative testing of turbulence models as reported by Steiner et al. (2009) and Jakirlić et al. (2010). It represents a suitable case featured by a complex three-dimensional flow separation, as it has a highly geometry-sensitive detachment characteristics. The reference experimental data for both diffuser configurations are provided by Cherry et al. (2006), Cherry et al. (2008) and Cherry et al. (2009). Additionally, this database is enriched by the high-fidelity DNS of the diffuser 1 by Ohlsson et al. (2010). Within the 3D-diffuser configuration, a fully developed duct flow with a width to height ratio of $b/h = 3.33$ and a bulk Reynolds number of

$Re_b = U_b h / \nu = 10000$ experiences a two-sided, cross-sectional expansion over the right and top walls. The other two sidewalls of the 3D-diffuser (bottom & left) do not experience any expansion and remain flat, see Fig. 4.32. Two 3D-diffuser configurations have been defined, differing in the opening angles of the cross-sectional expansion. The so-called diffuser 1 has a right-sided opening angle of $\alpha_{\text{right}} = 2.56^\circ$ and a top-sided opening angle of $\alpha_{\text{top}} = 11.3^\circ$, which provokes a flow separation over the top wall. In contrast, the second configuration, diffuser 2 ($\alpha_{\text{right}} = 4.0^\circ$ and $\alpha_{\text{top}} = 9.0^\circ$), exhibits a flow separation over the right wall. Both configurations are considered in the following in order to investigate the capability of the EBM to reproduce such geometry-sensitive flow detachment characteristics. To assess the EBM results, the numerical investigation by Ohlsson et al. (2010) with a DNS of diffuser 1 and the experimental study of Cherry et al. (2006), Cherry et al. (2008) and Cherry et al. (2009) within the Magnetic Resonance Velocimetry (MRV) framework for both configurations are applied. A detailed description of the diffuser geometries as well as a summary of the numerical and experimental works in connection with the 3D-diffuser can be found on 'www.kbwiki.ercoftac.org', to which interested readers are referred. The spatial discretization of both diffusers is provided by block-structured grids with hexahedral cell topology, where the grid for diffuser 1 contains 3.1 million cells and for diffuser 2 4.3 million cells. The discretization of the convective term within the numerical procedure is done with CDS.

For a first insight into the flow topology of both diffuser configurations calculated with the EBM, the iso-contours of the streamwise velocity component u/U_b are depicted within selected cross-sections ($x/h = 0; 2; 5; 8; 12; 15$) in Fig. 4.32 for diffuser 1 (left) and diffuser 2 (right). The streamwise coordinate x originates from the start of the duct cross-sectional expansion within the diffusers. For highlighting the three-dimensional separation region, the $u/U_b = 0$ volume contour is illustrated as a gray surface in addition. The fully developed duct flow entering the diffuser experiences an APG at the bottom wall (see Fig. 4.33 bottom) due to the two-sided cross-sectional expansions and subsequently a reduced wall shear (see Fig. 4.33 top). Both the skin friction and pressure coefficients predicted by the EBM are in a very good agreement with the experimental and numerical reference data for the diffuser 1. The friction and pressure coefficients for the diffuser 2 exhibit developments following closely those of the diffuser 1. This is in agreement with the LES

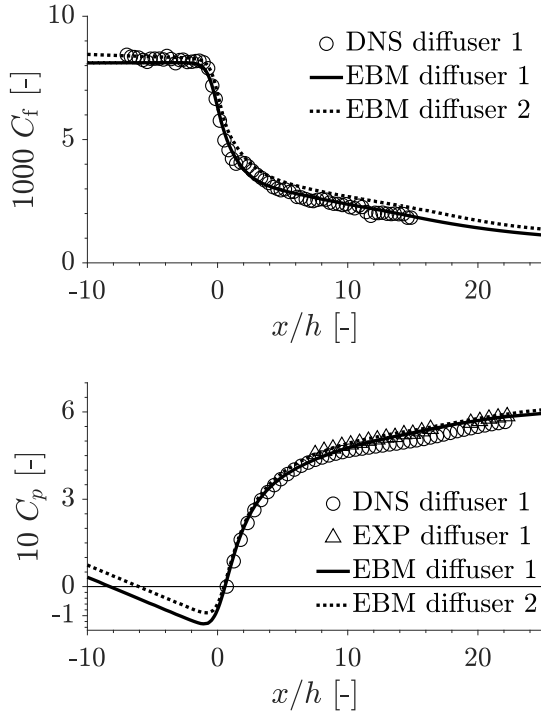


Figure 4.33.: Friction coefficient $C_f = \tau_w / (0.5\rho U_b^2)$ (top) and pressure coefficient $C_p = (p - p(x/h = 0.05)) / (0.5\rho U_b^2)$ (bottom) development over the streamwise coordinate x/h for both diffuser configurations with $Re_b = 10000$. The EBM results (solid line) are depicted in comparison to the reference data by Ohlsson et al. (2010) (circles) and Cherry et al. (2009) (triangles) .

computational study by Hajaali and Stoesser (2021). The expanding right- and top-sided walls also cause an APG, which provokes the characteristic flow separation within the diffuser. The flow detachment originates for both configurations in the right- and top-sided duct corners and expands either over the top-sided wall (diffuser 1) or the right-sided wall (diffuser 2), as

characterized at the beginning as a geometry-sensitive flow detachment. Thus, Fig. 4.32 demonstrates that the EBM is capable to qualitatively reproduce the geometry-sensitive flow separation within the diffuser.

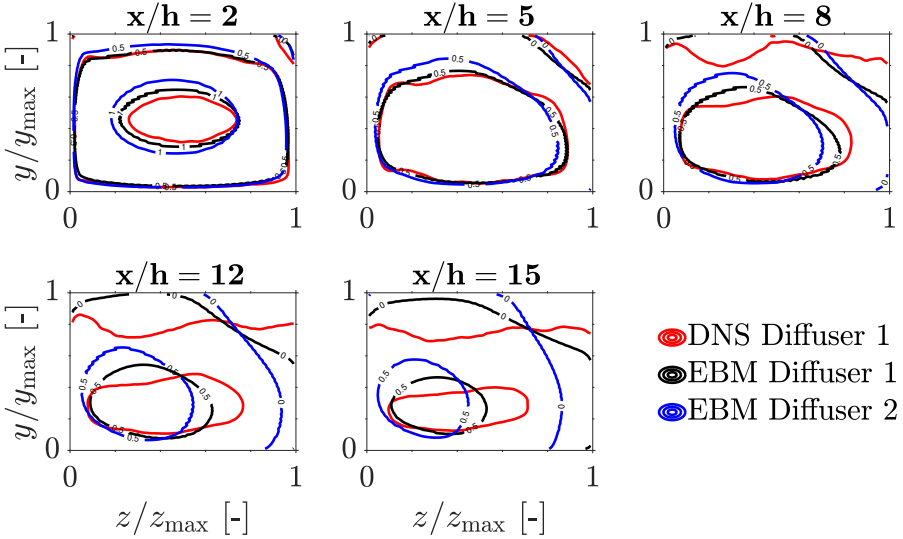


Figure 4.34.: Streamwise velocity iso-contour plots for selected cross-sections for diffuser 1 (back solid line) and diffuser 2 (blue solid line) with $Re_b = 10000$ predicted by EBM. The reference DNS data for diffuser 1 by Ohlsson et al. (2010) are depicted for comparison (red solid line). The numbers at the individual velocity iso-contours denote the value of u/U_b .

Complementary to the flow visualization in Fig. 4.32, some selected streamwise velocity iso-contours of diffuser 1 calculated by EBM (black solid line) are compared with the reference DNS data by Ohlsson et al. (2010) (red solid line) in Fig. 4.34 to evaluate the flow separation evolution. In addition, the contour lines of diffuser 2 predicted by EBM (blue solid line) are depicted for completeness (with no reference counterpart for the diffuser 2). The contour denoted with '0' is equal to $u/U_b = 0$. For better comparability of the differently sized

cross-sections, the relevant side lengths of the individual sections are suitably normalized by their corresponding height y_{\max} and width z_{\max} respectively. The fully developed duct flow entering the diffuser experiences a global flow deceleration due to the cross-sectional expansion. The deceleration of the flow with increasing x/h is evident from the iso-contour shape by a disappearing iso-contour denoted by '1' and a reduction of the enclosed area interpreted by the isocontour '0.5' for $x/h = 5$ for example. The flow separation has its origin in the upper right corner and extends over the entire top-sided wall with increasing x/h . The flow topology predicted by the EBM is in close agreement with the DNS data for $x/h < 8$. The initial separation point and its spatial expansion as well as the shifting of the bulk flow towards the bottom wall is correctly reproduced. Between $x/h = 5$ and 8, the DNS predicts a rapid expansion of the flow separation over the entire top wall, with the separation region locally protruding significantly into the diffuser section and provoking a deformation of the iso-contour '0.5'. The EBM reproduces an extension of the flow separation over the top wall, but the flow is still partially attached for $x/h = 8$. Furthermore, the squeezing of the iso-contour '0.5' is also not represented, which is probably related to the partially attached flow at the top wall. With increase in the streamwise coordinate x/h , the flow separation predicted by the EBM along the upper wall continuously enlarges, while still indicating a partial attached flow condition at $x/h = 12$, while the DNS predicts a quite strong separation topology at the top wall. Consequently, the squeezing of the bulk flow is not longer reproduced. A completely detached flow pattern on the upper wall within the flow topology predicted by the EBM can first be recognized in the last depiction of Fig. 4.34 for $x/h = 15$. However, the flow topology predicted by the EBM does not exhibit a continuous detachment along the top wall with the zero velocity contour showing an inclined tendency toward the left and right corners of the top wall.

Although Fig. 4.34 depicts a delayed flow detachment characteristics with a non-uniform distribution along the top wall, the EBM has responded correctly to the geometry-sensitive flow separation within diffuser 1 and detects the flow separation at the top wall. The detection of the correct detachment location is a great challenge for a RANS-based turbulence model like the EBM, since most RANS-based turbulence models incorrectly predict the flow detachment along the right wall.

To complete the evaluation of the EBM results within the 3D-diffusers,

a concluding overview of the flow evolution exemplary within the vertical central plane at $z/b = 0.5$ is provided. Therefore, the predicted profiles of the streamwise velocity u/U_b and Reynolds stress component \bar{u}_{RMS}/U_b at selected streamwise positions x/h are depicted across the duct height y/h in Fig. 4.35 for both diffuser configurations. The available experimental and numerical reference data are plotted for comparison.

Independent of the diffuser configuration, the flow passes into the diffuser and experiences a deceleration of the velocity field as a result of the cross-sectional expansion. An accompanied shift of the velocity peak in the direction of the continuously elevating duct center as well as a reduction of the turbulence peak close to the wall are the consequence. Both have been captured and reproduced by the EBM in accordance with the reference data, where especially the correct turbulence level as well as the peak of the velocity are to be emphasized. The shift of the velocity peak causes a flattening of the near-wall velocity profile toward the bottom wall ($y/h = 0$), which is reflected in the friction coefficient development in Fig. 4.33 top. The evolution of the friction coefficient could be reproduced by the EBM, which can also be seen in the near-wall velocity formation of diffuser 1 depicted in Fig. 4.35 top for $y/h < 0.5$. Here, a slight deviation can be observed in the bottom near-wall velocity profile of diffuser 2, where the experimental reference data indicate a more pronounced deceleration than the flow field predicted by the EBM. Approaching the top wall, the detachment characteristics of diffuser 1 becomes more present in the flow topology indicated by a velocity sign change and region of backflow ($u/U_b < 0$). Considering the spatially delayed detachment characteristics of the EBM discussed with respect to Fig. 4.34, a deviation of the predicted velocity field in top wall proximity is expected. The EBM clearly underestimates the spatial extension of the separation region and predicts a negative velocity only in the immediate vicinity of the top wall. In contrast, the streamwise Reynolds stress component profile close to the top wall could be reproduced correctly by the EBM.

The EBM results of the two diffuser configurations have demonstrated the capability of the EBM to qualitatively reproduce a geometry-sensitive detachment characteristics. Although there is a spatial delay in the detachment characteristics in diffuser 1, the detachment topology coincides with the reference data, which is especially noteworthy in the context of RANS-based turbulence models. Apart from the detachment issue, the flow topology in

terms of the streamwise velocity and Reynolds stress components as well as their near-wall behavior have been reproduced by the EBM in reasonably good agreement with the reference data.

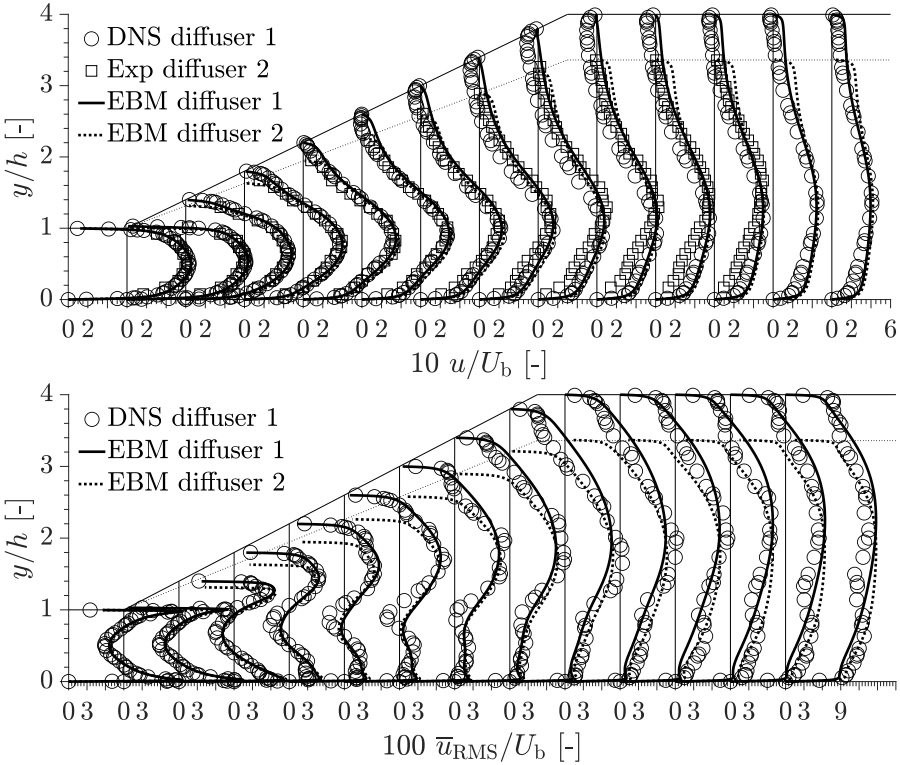


Figure 4.35.: Streamwise velocity u/U_b (top) and Reynolds stress component \bar{u}_{RMS}/U_b (bottom) profiles at selected streamwise positions depicted across the duct height y/h for diffuser 1 (solid line) and diffuser 2 (dotted line) with $Re_b = 10000$. The experimental (square, Cherry et al., 2008) and numerical reference data (circles, Ohlsson et al., 2010) are depicted for comparison.

4.10. Flow in the WSG

As a final evaluation case of the EBM formulation, the Water Spider Geometry (WSG) discussed in Chapter 3.8 will be considered in the following as an industry-related flow guidance with a highly complex flow topology. As already discussed, the WSG is characterized by a variety of flow phenomena and combines many of the individual flow phenomena discussed previously, such as flow separation due to an APG. The WSG differs from the benchmark cases considered so far with the circular cross-section, which introduces an additional complexity with flow separation along a non-flat surface, here concave curved.

Within the framework of RANS-based turbulence models and the prediction of steady flow states, the possibility exists to exploit the symmetry planes of the computational domain to significantly reduce the grid size and save computational resources. According to the symmetrical character of the WSG, namely the $x - z$ - and $y - z$ -symmetry plane illustrated in Fig. 3.49, the computational domain can be reduced to a quarter within the RANS-based investigations. The $x - y$ -symmetry plane cannot be utilized due to the definition of the flow guidance. A further simplification to the computational domain of LES (Fig. 3.49) can be done within the RANS framework with the neglect of an additional precursor region. Due to the steady flow condition, the fully developed pipe flow at the WSG inlet can be enabled by mapping from the flow domain immediately downstream of the inlet. Apart from the exploitation of symmetries and the neglect of the precursor region, the computational domain is identical to the LES domain and accordingly reference is made to Figures 3.1 and 3.49 for the geometrical dimensions. The spatial discretization of the RANS-based computational domain originates from a preliminary grid study in order to guarantee a grid-independent solution. A block-structured fully-hexahedral grid with 1 million cells has been identified as sufficient for the present study. This corresponds to a 4 million cell grid without exploiting the symmetries and represents a significant reduction compared to the LES grid with 290 million cells developed in Chapter 3.

For the discretization of the convective terms, a blending procedure between CDS and UDS is applied as described in Chapter 2.3.3 with a CDS fraction of 70 %. The complex flow guidance and the spatial discretization complicate the convergence of the RANS procedure. Therefore, a pseudo transient approach is

applied to generate a convergent steady flow field. The corresponding temporal terms are discretized with the implicit Euler method (see Chapter 2.3.2).

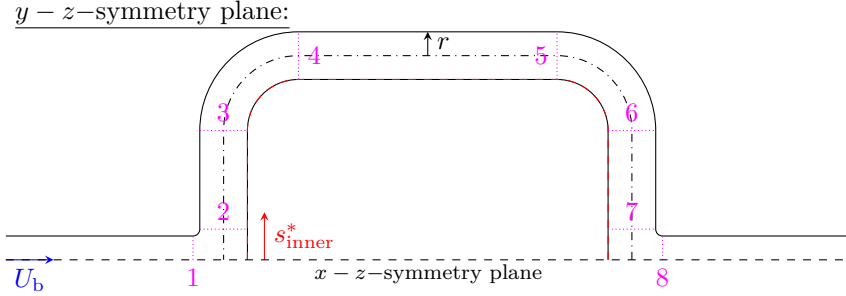


Figure 4.36.: Schematic illustration of the WSG with characteristic positions highlighted by magenta dotted lines (1: T-junction inlet; 2: T-junction outlet; 3: 1. deflection inlet; 4: 1. deflection outlet; 5: 2. deflection inlet; 6: 2. deflection outlet; 7: reverse T-junction inlet; 8: reverse T-junction outlet). The inner coordinate $s_{\text{inner}}^* = s_{\text{inner}}/D$ and its path are introduced by a red marked arrow and a dashed line.

As a first insight into the flow topology predicted by the EBM, the friction coefficient $C_f = \tau_w / (0.5\rho U_b^2)$ (top) and the pressure coefficient $C_p = (p - p(s_{\text{inner}}^* = 0)) / (0.5\rho U_b^2)$ (bottom) along the inner coordinate $s_{\text{inner}}^* = s_{\text{inner}}/D$ are depicted in Fig. 4.37. The inner coordinate s_{inner}^* runs according to the red dashed line in Fig. 4.36 along the intersection of the $y-z$ -symmetry plane and the flow guidance wall starting from the center of impingement within the T-junction ($s_{\text{inner}}^* = 0$). The LES of the WSG discussed in detail in Chapter 3 is plotted as reference (circles).

The detailed flow discussion of the WSG in Chapter 3.8 demonstrates a complex flow and vortex topology in which multiple flow phenomena are superimposed and mutually affect each other. A characteristic of the WSG has been found to be the rapid transition between unsteady highly turbulent and strongly equalized flow conditions, which is accompanied by distinct spatial gradients of the flow quantities. The friction coefficient C_f as a representative of the near-wall flow characteristics in terms of the near-wall velocity gradient as

well as the pressure coefficient C_p indicate the flow complexity by a pronounced variation along the inner coordinate s_{inner}^* , which imply a strong near-wall flow acceleration and deceleration. Starting from the sharp increase ($s_{\text{inner}}^* > 0$) and the peak of the friction coefficient downstream of the T-junction outlet ($s_{\text{inner}}^* \approx 0.75$) supported by a favorable pressure gradient (FPG), the friction coefficient experiences several changes of sign along s_{inner}^* indicating a pronounced flow separation structure closely linked to the geometrical components of the WSG. The intensity of the single flow separation events varies significantly, as evident from the spatial extension of the negative expression of the friction coefficient. Each flow separation event is accompanied by an APG provoking the flow detachment. An underdeveloped flow separation event is noticeable around the outlet of the first deflection followed by much more pronounced ones around the outlet of the second deflection as well as within the reverse T-junction. The latter indicates the streamline roll-up due to the three-dimensional flow deflection within the reverse T-junction described in Chapter 3.7.4. Apart from the flow separation, the pressure coefficient demonstrates pronounced FPG around the T-junction outlet as well as the deflection inlets. Subsequently, the friction coefficient experiences sharp alterations over shortest distances with its double peak downstream of the T-junction and its underdeveloped flow separation around the first deflection outlet as well as a similar situation within the second deflection. The pronounced spatial alteration indicates a pronounced interplay between flow acceleration and deceleration and confirms the rapid transition between fundamentally different flow conditions described earlier.

The determination of both, the correct position and spatial extension of flow separation as well as the pronounced spatial alteration of the near-wall flow characteristics, is a highly challenging task for turbulence models, especially for RANS-based models. The EBM demonstrates a remarkable agreement with the reference LES data and is able to reproduce the described WSG characteristics in terms of flow separation as well as rapid transition between different flow states. The agreement in position and magnitude of the peak values and sign changes of the friction coefficient as well as the coinciding evolution of the pressure coefficient have to be emphasized. Only the decrease of the friction coefficient upstream of the first deflection as well as the pressure drop within the first deflection deviates slightly from the reference LES data.

An all-encompassing discussion of the flow and turbulence evolution of

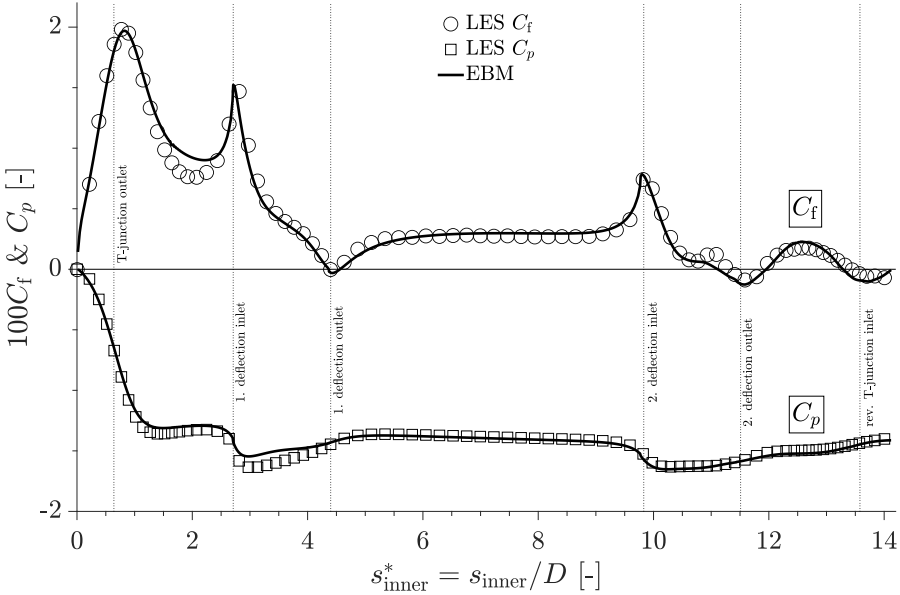


Figure 4.37.: Friction coefficient $C_f = \tau_w / (0.5\rho U_b^2)$ and pressure coefficient $C_p = (p - p(s_{inner}^* = 0)) / (0.5\rho U_b^2)$ along the inner coordinate of the WSG $s_{inner}^* = s_{inner}/D$ predicted by EBM (solid lines) and LES (symbols). Characteristic positions are highlighted according to Fig. 4.36.

the WSG predicted by the EBM would go beyond the scope of the present chapter. Instead, a brief extraction of the flow and turbulence evolution within the $y - z$ -symmetry plane at characteristic positions is depicted in Figures 4.38 and 4.39 in terms of the velocity magnitude U and the Reynolds stress components. For the latter, the root mean squares ($\sqrt{uu}, \sqrt{vv}, \sqrt{ww}$) are presented to account for the significantly different turbulence levels within the WSG and to ensure a meaningful comparison. The depictions correspond to the magenta dotted lines in Fig. 4.36 and are intended to provide a general insight into the capabilities of the EBM as far as possible. Similar to Fig. 4.37,

the LES data from Chapter 3.8 are depicted as reference, where the data of the Reynolds stress components correspond to the resolved part. For orientation and with the exception of the T-junction inlet and reverse T-junction outlet depictions, the radial position $r/R = 1$ corresponds to the evolution of the friction coefficient depicted in Fig. 4.37.

The flow topology within the WSG is characterized by numerous geometry-driven flow redirections, flow divisions and confluences, which are closely related to the formation of a dominant vortex topology and cause a distinct separation structure. The vortex topology as well as the separation structure are the turbulence driving flow mechanisms especially downstream of the T-junction and reverse T-junction and determine the turbulence level within the WSG. These insights are the result of the detailed flow discussion in Chapter 3 and interested readers are referred accordingly. However, the listed insights of the WSG can also be found in the brief depiction of the flow and turbulence evolution in Figures 4.38 and 4.39. The symmetric flow topology entering the WSG (see T-junction inlet in Fig. 4.38 top) experiences a strong radial variation due to the mentioned geometry-driven mechanisms and forms an asymmetrical peak characteristic. The asymmetrical peak is not fixed in its radial position and alters along the flow guidance of the WSG from $r/R > 0.5$ downstream of the T-junction and within the first deflection to the opposite side ($r/R < -0.5$) at the outlet of the second deflection as well as downstream. Complementary to the asymmetric peak formation, numerous low velocity regions are present especially downstream of convex surfaces. The most pronounced low velocity region can be observed downstream of the inner radius of the T-junction but also downstream of the second deflection as well as the reverse T-junction. The shear layers enveloping the low velocity regions and bounding them from the bulk flow exhibit strong spatial velocity gradients and cause enhanced turbulence production, which can be observed at the outlets of the T-junction and reverse T-junction. Especially the shear layer in the inner radius of the reverse T-junction (see rev. T-junction outlet) is the origin of an extremely sharp near-wall turbulence peak evident in the depicted Reynolds stress components. Apart from the shear layers, the intensity of the forming vortex tubes within the T-junction and reverse T-junction and its spatial velocity gradients are also a driving force of turbulence within the WSG. Both, the symmetric vortex tube pair due to the impingement within the T-junction (see 1. deflection inlet $r/R > 0.3$) and the flow confluence

within the reverse T-junction and its forming double-symmetric vortex tubes (see rev. T-junction outlet $-0.3 < r/R < 0.3$) contribute to the turbulence production and causes local peak formations within the depicted Reynolds stress components.

With focus on the reproduction capabilities of the flow topology within the WSG of the EBM formulation, the excellent reproduction of the velocity evolution is noticeable. The alternation of the velocity magnitude peak as well as the corresponding shear layers are consistent with the reference data, which has already been indicated by the discussed friction coefficient in Fig. 4.37 top. Merely a slight overestimation of the flow magnitude can be seen in the region of low velocity downstream of the inner radius of the T-junction. Besides the velocity evolution, the demonstrated highly anisotropic turbulence topology is a challenging task for RANS-based models, especially with respect to the correct redistribution. The EBM can capture the anisotropic character, but tends to slightly underestimate the turbulence level. The redistribution of the Reynolds stress components seems to follow the reference data with one exception, the wall-normal component $\sqrt{\overline{v'v'}}$ at the T-junction outlet. A slight overestimation for $r/R > 0.5$ is present with a wrongly predicted symmetric profile over the radius.

The deviation at the T-junction outlet does not deceive the whole impression that the depictions in Figures 4.37, 4.38 and 4.39 have demonstrated the capability of the EBM to reproduce an industry-related benchmark case with partly consistency with the reference LES. Consequently, the quality of the depicted results and the required computing resources in comparison to the reference LES distinguished the EBM formulation for further investigations within the scope of the WSG.

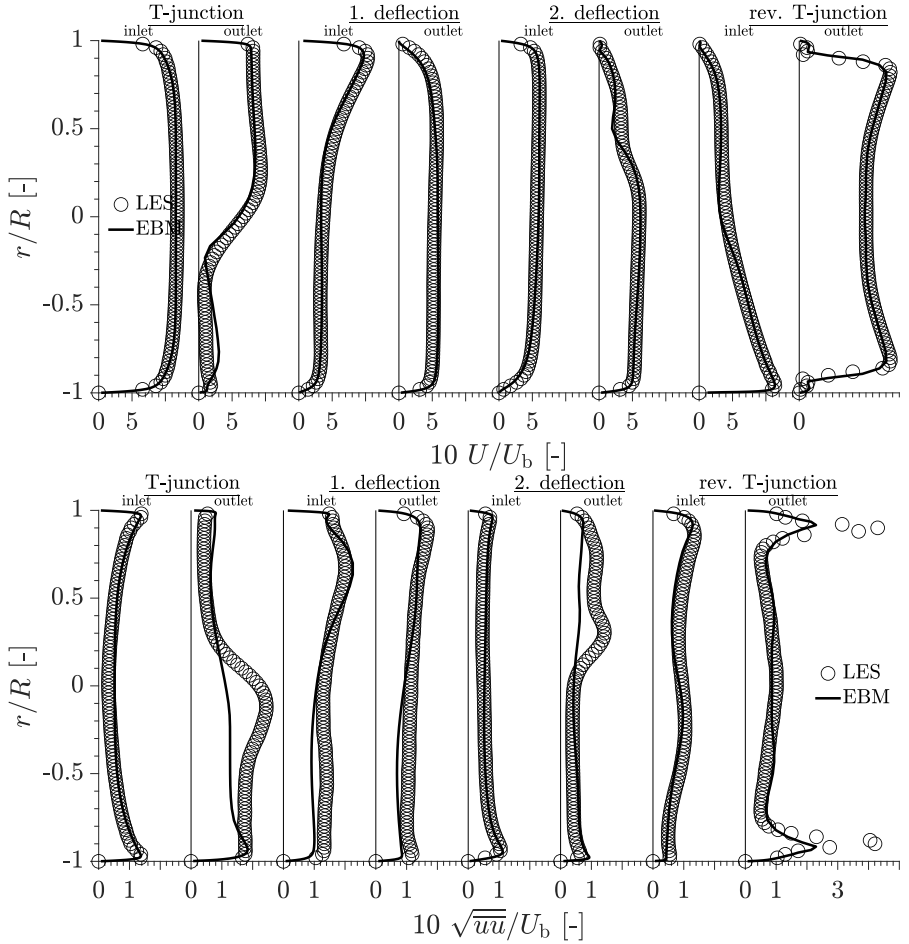


Figure 4.38.: Velocity magnitude U/U_b (top) and streamwise Reynolds stress component \sqrt{uu}/U_b (bottom) over the pipe radius r/R at characteristic positions within the WSG according to Fig. 4.36 predicted by EBM (solid line) and LES (circles).

4. Development of an ω_h -based elliptic-blending-related Reynolds-stress model

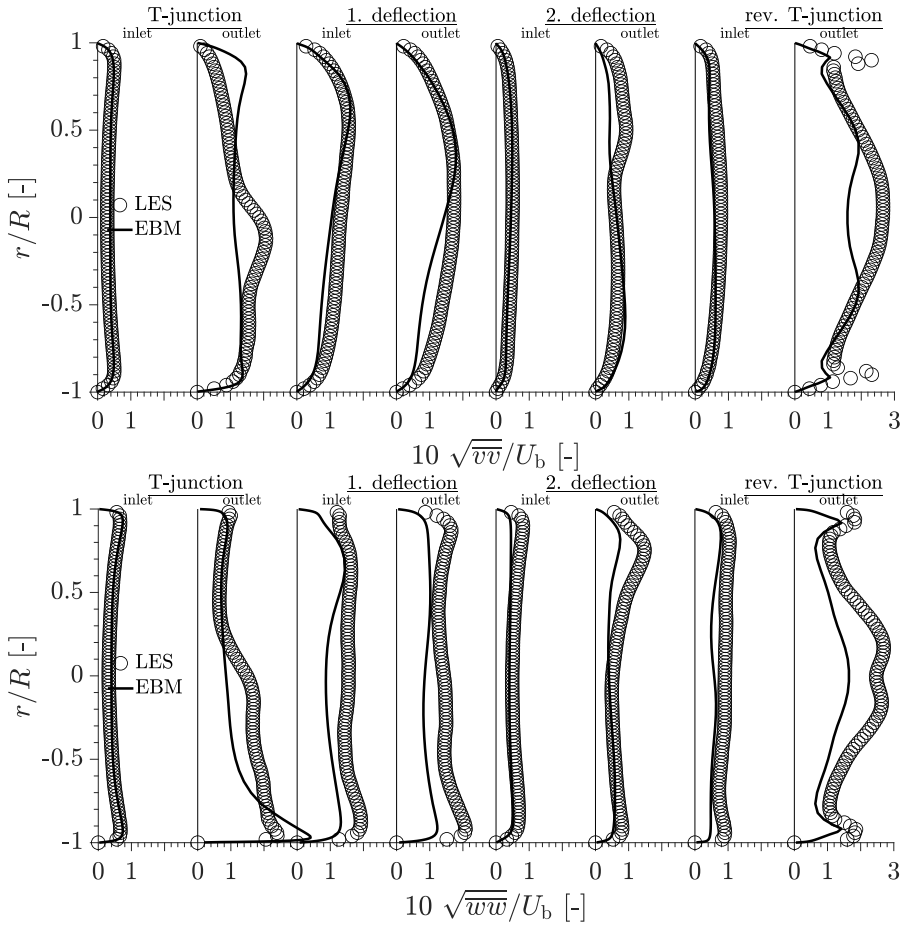


Figure 4.39.: Wall-normal Reynolds stress component $\sqrt{v'v'}/U_b$ (top) and wall-tangential Reynolds stress component $\sqrt{w'w'}/U_b$ (bottom) over the pipe radius r/R at characteristic positions within the WSG according to Fig. 4.36 predicted by EBM (solid line) and LES (circles).

4.11. Conclusion and outlook

An ω_h -based elliptic-blending-related Reynolds-stress model (EBM) is elaborated within the present chapter with a detailed insight into the modeling strategy, the calibration of the functional dependencies in model coefficients and corresponding constants as well as the validation considering several suitable benchmark cases. The model formulation is based on the homogeneous specific dissipation rate concept of Jakirlić and Maduta (2015) and the elliptic-blending approach proposed by Manceau and Hanjalić (2002) aiming at combining the advantages of both strategies with the special focus on the asymptotically correct wall behavior of the ω^h variable as well as the robust treatment of the pressure redistribution term within the elliptic procedure. The model validation study focuses on the adverse pressure gradient (APG)-driven separating flow conditions and the associated critical events with respect to the flow detachment and reattachment as well as the formation of the recirculation zone. Concerning the reattachment point, the well-known non-physical streamline backbending issue could be avoided by employing the proposed EBM. The computational remedy of this anomaly can be attributed to a skillful reformulation of the Simple Gradient Diffusion Hypothesis (SGDH) model accounting for a characteristic length modification expressed in terms of the Kolmogorov lengthscale L_η , the turbulent Reynolds number Re_t , and the wall-distance-related turbulent Reynolds number Re_y . Furthermore, a strict limitation of the near-wall-related pressure redistribution term proposed by Manceau and Hanjalić (2002) could be achieved by reducing the corresponding lengthscale applied in the elliptic equation to the Kolmogorov part only in conjunction with the high-Reynolds second-order (in term of a_{ij}) pressure redistribution formulation by Speziale et al. (1991) valid in the off-wall region. The calibration of the model constants has been performed by computing a large number of flow cases featured by a high structural complexity in order to ensure a greatest possible general validity of the EBM formulation. The consideration of the WSG as an industry-related flow-guiding configuration concludes the validation study and demonstrates the capability of the EBM formulation in predicting highly complex flow topologies characterized by a multitude of interacting flow phenomena.

The quality of the EBM results within the WSG demonstrate the suitability of the EBM formulation to enable insights and to answer the remaining

questions elaborated in Chapter 3.8. Especially, the geometry adaptation of the WSG aiming at the avoidance of critical flow conditions could be supported by applying the EBM formulation with a reasonable computational effort. However, the full elaboration of the WSG-related study includes a pronounced heat input causing a complex conjugated heat transfer problem, which represents a further step in the validation of the EBM formulation. The suitability of the EBM for non-isothermal flow conditions has not been proven so far and has to be verified for the thermally loaded WSG in future studies. The non-isothermal flow condition associated with a possible boiling event and the resulting two-phase flow topology poses an additional challenge. An industry-relevant approach to account computationally for the possible boiling events could be the Euler-Euler methodology, which has been, for instance, investigated in detail by Krepper and Rzehak (2011) and Krepper et al. (2013). The relevant challenge will be the near-wall region, where usually wall functions for the wall modeling are applied. Herewith, the flow boiling cannot be captured down to the viscose sublayer as inherently provided within the EBM formulation.

Instability-Sensitive Elliptic-Blending-related Reynolds Stress Model (ISEBM)

An extension of the EBM towards an eddy-resolving hybrid RANS/LES formulation represents also a challenging task, whereby the robust treatment of the pressure redistribution term could be beneficial compared to other RSM-based SGS models. There are several possibilities for a hybrid RANS/LES formulation published in literature. The Scale Adaptive Simulation (SAS) methodology proposed by Egorov and Menter (2008) and extended by Maduta et al. (2015) has been explored in the context of the present EBM formulation.

The extension of the EBM to a RANS/LES formulation is possible, as illustrated in Appendix B, but some difficulties related to the elliptic procedure have been identified. The EBM functions as SGS model in the context of the RANS/LES formulation and the predicted turbulent quantities represent only a fraction of the total turbulence intensity, the modeled fraction. This scale-resolving operating mode in relation to a RANS-based model is appropriate in general as the two studies cited above have proven. However, the Kolmogorov lengthscale representing a key quantity in the EBM formulation, especially

within the elliptic equation, takes significantly increased values within the scale-resolving mode. Within the elliptic-blending approach this causes a shift of the blending position of the pressure redistribution term to a wall-distant positions depending on the ratio of modeled to total turbulent kinetic energy. An extension of the operating range of the near-wall formulation away from the wall is the consequence, which is in contrast to its physically compliant operating range. As a possible solution, the Kolmogorov lengthscale formulation accounting for both the modeled and resolved fractions is applied within the elliptic function. For this purpose, a segment-wise time averaging of the velocity field is implemented to capture the resolved fractions of the flow quantities during runtime.

The near-wall pressure redistribution term postulated by Manceau and Hanjalić (2002) has quite a lot of benefits within the RANS framework as presented in the context of the EBM formulation. However, in the scale-resolving mode, the near-wall formulation has a dissipative effect, which causes a significant reduction of the modeled turbulent kinetic energy in the operating range of the near-wall formulation. An all-encompassing solution could unfortunately not be elaborated, but a significant improvement of the results could be achieved by suppressing adequately the Reynolds stress tensor used in the near-wall formulation with the ratio of the modeled to the total turbulent kinetic energy. Another possibility offers a blending of the near-wall pressure redistribution formulation between the proposals of Manceau and Hanjalić (2002) and Jakirlić (1997). The latter has proven to be advantageous in the scale-resolving mode by Maduta et al. (2015). Here, the ratio of modeled to total turbulent kinetic energy is also proposed as the blending parameter. The latter solution procedure would result in a similar formulation as the Improved Instability Sensitive Reynolds Stress Model (IISRSM) proposed by Maduta et al. (2015), but with a different model formulation for steady, RANS-like inflow conditions as well as for a second-order off-wall pressure redistribution term.

The proposed solutions guarantee no influence on the SGS model, here the EBM formulation, if the hybrid RANS/LES formulation has to work in RANS mode. The model formulation of the briefly presented suggestion of a hybrid RANS/LES formulation with the EBM as SGS model is summarized in Appendix B.

5. Conclusions and outlook

The present work provides a comprehensive insight into the flow topology and relevant structural properties within common pipe structures constituting the newly designed configuration termed as Water Spider Geometry (WSG). It represents a reference test sample of a generic cooling channel relevant to Internal Combustion (IC) engines. The complementary experimental investigations conducted within a relevant test bench - the so-called Modulare Heißtestanlage (MHTA) (Klink et al., 2019, Klink and Wegt, 2021) - represent a baseline reference motivating the numerical investigations. These are intended to provide detailed insight into the flow structure being not accessible for measurement techniques and subsequently to identify critical thermal and abrasive flow conditions. In addition to the WSG configuration simulated in its entirety, differently configured pipe sections combined within the WSG including flow deflection (90°-pipe bend), division (T-junction), and confluence (reverse T-junction) have been individually simulated. Herewith, a more in-depth comprehension of the flow field within the WSG have been achieved. This is primarily motivated by the lack of meaningful reference data especially for the T-junction and reverse T-junction due to the enhanced complexity in relation to the cross-sectional shape and the smooth transition between the pipe segments in terms of a finite radius. For capturing of isothermal flow topology within the WSG as well as within its aforementioned individual elements, the computational framework utilizing a well-resolved, highly comprehensive Large-Eddy Simulation (LES) for the considered configurations was elaborated and applied. Along with the computational study, the mandatory analysis of quality assessment measures following closely the corresponding theoretical constraints established in the relevant literature has been performed. It resulted in a cost-effective grid-cell distribution, resembling an 'O-grid' arrangement across the circular pipe geometry with the following characteristic parameters $R_{\text{block}}/R = 0.8$, $\Delta z^+/\Delta\varphi^+ = 3$ and $l_{\text{pre}} = 2.5 D$.

In conjunction with the Wall-Adapting Local Eddy-viscosity (WALE) subgrid-scale (SGS) model (according to Nicoud and Ducros, 1999), describing the dynamics of the unresolved turbulence motion, this grid design has proven to be advantageous with regard to the quality of the results and optimum utilization of computational resources.

The discussion of the flow in the considered pipe structures includes an application-oriented assessment of the flow topology with special attention to possible thermal and abrasive critical flow conditions serving as a guideline for a failure-proof engineering design of similar flow guiding configurations. The inner radii of the T-junction and reverse T-junction were found to be primarily prone to abrasive and thermal-critical flow conditions with a combination of enhanced wall shear, flow separation and the formation of low velocity regions downstream. A more gradual expansion of the cross-section through an increased inner radius could contribute to mitigate a possible critical flow condition and to avoid an abrasive flow mechanism. Beside the detection of critical flow conditions, a deeper understanding of the flow physics within the pipe structures could be elaborated and the well-known dominant influence of vortex structures within pipe flow deflections (Dean vortex) could also be identified within the T-junction and reverse T-junction. Symmetric and double-symmetric vortex tube formations are emerging, which have a significant influence on the cross-sectional secondary motion. This contributes to the equalization tendency of the flow topology downstream of the flow guides as well as to the flow/wall interaction. Due to the distinctive vortex topology identified within the pipe structures, the flow analysis has been effectively extended by introducing the vortex identification methodology proposed by Graftieux et al. (2001). The vortex identification methodology allows a deeper insight into the distinctive vertical flow topology within the pipe configurations and enables an assessment of the vortex formation process, vortex/wall interaction and its spatial extent in terms of vortex center tracking, area expansion and circulation evolution. Thereby, the vortex evolution emphasizes the relevance of the cross-sectional (inplane) velocity within the considered pipe structures and its influence on the wall loading in regions of enhanced circulation. Especially in the case of the 90° -pipe bend, a similarity in the circulation evolution is elaborated by a proposed normalization in terms of the circulation Reynolds number Re_Γ and the Dean number De . A critical non-dimensional circulation ($Re_\Gamma/De = 0.95 - 0$) could be identified from which on the secondary structures

are formed. Due to the limited parameter variation with only the volume flux, further investigations have to follow for a general validity of the postulated critical circulation.

The isolated considerations of the pipe structures, which are combined in the WSG, and the findings drawn from the in-depth analysis have contributed significantly to an enhanced understanding of the WSG-relevant flow topology. The flow mechanisms identified in the isolated consideration of the WSG-constituting geometric elements could be recognized in superimposed form and the knowledge gained could be transferred to the significantly more complex WSG flow topology. One of the main intentions behind the detailed flow discussion are the experimentally identified regions of pronounced surface degradation between the two deflection localities and at the inner radius of the reverse T-junction, which could be assigned to the associated flow topology. For the former, a substantial decrease in the cross-sectional velocity is responsible for a lower convective heat transport from the wall into the bulk flow indicating the triggering of a critical boiling state. An appropriate countermeasure could be the shortening of the straight pipe segment and a concurrent increase of the deflection radii, which in the most extreme form would result in a continuous 180°-pipe deflection. This would force a regular vortex topology along the deflection and significantly increase the cross-sectional velocity. The inner radius of the reverse T-junction combines the lowest system pressure with a high wall shear peak and a low velocity region downstream. This causes an increased risk for thermal and/or cavitation phase change events with the possibility for a critical boiling state as well as enhanced abrasive effects of the flow and possible contaminations. To mitigate the inner radius of the reverse T-junction and reduce the aforementioned surface abrasive mechanisms, an increase of the inner radius and thus a weakening of the abrupt cross-sectional expansion could be appropriate.

Furthermore, the well-resolved, highly comprehensive LES of the WSG with more than 290 million cells represents a reference solution of the newly designed flow-guiding configuration and a basis for future investigations within the scope of cooling systems of IC engines. This is also true for the development of an ω_h -based elliptic-blending-related Reynolds-stress model (EBM), which is a cost-effective proposal to continue the investigations within the scope of the WSG and the proposed constructive countermeasures. The cost-efficient

character arises from being a Reynolds-Averaged Navier-Stokes (RANS)-based turbulence model, which does not require time-consuming averaging of flow fields as well as allowing the exploitation of symmetries of the configuration while being able to reproduce the anisotropic characteristics of turbulence. The EBM provides a synthesis of the proposals of Jakirlić and Maduta (2015) and Manceau and Hanjalić (2002), combining the advantages of the homogeneous specific dissipation rate concept with the robust elliptic blending procedure of the pressure redistribution term. With the smooth flow guidance of the WSG and the localities imposed to adverse pressure gradient (APG)-driven flow conditions as a reference feature, the focus concerning the formulation and calibration of the EBM formulation is set to APG-driven and flow separating flow conditions. This was ensured by the inclusion of a diversity of fundamental benchmark cases in the calibration and validation process sensitizing the model formulation to the appropriate flow behavior. Special attention was paid to the non-physical phenomenon denoted 'backbending', which means the backbending of the mean dividing streamline at the point of reattachment. This is a well-known anomaly, specifically related to Reynolds Stress Model (RSM) concept and is mostly remedied in the past by some ad-hoc formulations or is argued to be a numerical artifact within the flow topology. Due to an elaborate investigation of the phenomenon 'backbending' and the assumption of its origin in an imbalance within the Reynolds stress transport equation around the reattachment, it could be purposefully avoided within the considered benchmark cases. It succeeded by a reformulation of the turbulent diffusion model formulated in terms of Simple Gradient Diffusion Hypothesis (SGDH) involving the Kolmogorov lengthscale η , the turbulent Reynolds number Re_t and the wall-distance-related turbulent Reynolds number Re_y . Within the validation procedure, some canonical two-dimensional flow configurations (fully-developed channel and pipe flows), developing flows (a zero-pressure gradient boundary layer and a high Reynolds number APG boundary layer (denoted by TC01)), flow separation from sharp-edged (backward-facing step (BFS)) and continuous curved walls (periodic hill) as well as three-dimensional, geometry-sensitive flow separation in differently configured 3D diffuser configurations were included. Herewith, a broader applicability of the developed EBM formulation has been ensured by delivering consistently reasonable results with partially high-level agreement with the reference data. Finally, the EBM has been applied to the WSG, as a representative of an industry-oriented flow

configuration, enabling the valuable conclusions of the validation procedure, as it was the initial intention towards developing a new RSM. The EBM-related results demonstrated a remarkable consistency with the reference LES results supporting so its ability to be a suitable model formulation for further investigations within the scope of the WSG.

However, the thermal load of the WSG along with the experimental investigations has not yet been considered, as the validation of the EBM was presently limited to isothermal flow conditions. The one-sided heating of the WSG causes a complex conjugated heat transfer problem with strongly non-isothermal flow conditions of the coolant and the possibility of local phase change events. The suitability of the EBM for non-isothermal flow conditions cannot be ultimately derived from the present validation procedure. It requires further validation work including relevant convective heat transfer problems, complex conjugated heat transfer configurations as well as flow boiling cases. For the latter, the Euler-Euler procedure for multiphase flow computations is considered as a suitable option, as exemplary demonstrated in intensive studies by Krepper and Rzehak (2011) and Krepper et al. (2013).

Finally, the possibility of extending the EBM to a hybrid RANS/LES formulation has been explored on the basis of the proposal by Egorov and Menter (2008) and the extension by Maduta et al. (2015), the so-called Instability-Sensitive Elliptic-Blending-related Reynolds Stress Model (ISEBM). The instantaneous velocity field as well as the time-averaged velocity and the corresponding Reynolds stress component profiles resulting from the simulation of a fully developed channel flow ($Re_\tau = 180$) are exemplary displayed in Appendix B. Further work on this eddy-resolving EBM formulation towards its broader application is necessary.

Specific novel contributions of the present work: Summary

1. Water Spider Geometry (WSG) represents by itself a completely new design of a reference test sample reflecting much more properly the flow complexity occurring in cooling channels of realistic IC engines
2. A comprehensive Large-Eddy Simulation (LES)-related flow database is created for this ‘unknown’ geometry and the comparative assessment of the results with those obtained by simulating its constitutive elements (90°-pipe bend, T-junction, reverse T-junction) enabled a deep insight

into the structural flow properties. The flow database can serve as a reference for relevant future studies (the second phase of the Arbeitsgemeinschaft industrieller Forschungsvereinigungen (AiF)/Forschungsvereinigung Verbrennungskraftmaschinen (FVV) project ‘Flow erosion’ (Klink and Wegt, 2021)). The present thesis will be the basis for these investigations.

3. This detailed three-dimensional flow field (velocity and pressure fields) mapping enables the detection of the localities with enhanced potential for the surface degradation.
4. The methodology for characterizing the vortical flow topology by Graftieaux et al. (2001) was introduced: Herewith a qualitative and quantitative in-depth insight could be gained into the behavior of the Dean vortices, typical for the flows in curved pipes, in terms of their onset, development, spatial tracking, structural properties and subsequent decay
5. The Reynolds Stress Model (RSM) development including a thorough interactive validation by introducing the elliptic-blending methodology resulted in a numerically robust formulation for a broader use.

A. EBM - Model Specification

1. Transport equation of homogeneous dissipation rate ω^h :

$$\boxed{\frac{D\omega^h}{Dt} = \frac{\partial\omega^h}{\partial t} + U_i \frac{\partial\omega^h}{\partial x_i} =}$$

$$\begin{aligned} & \frac{\partial}{\partial x_k} \left[\left(\frac{1}{2}\nu + \sigma\nu^* \right) \frac{\partial\omega^h}{\partial x_k} \right] + C_{\omega,1} \frac{\omega^h}{k} P_k - C_{\omega,2} \omega^h \omega^h \\ & + \frac{2}{k} \left(\frac{C_{CD,1}}{2} \nu + C_{CD,2} \nu^* \right) \frac{\partial\omega^h}{\partial x_k} \frac{\partial k}{\partial x_k} + C_{\omega,3} \frac{\nu}{\omega^h} \frac{\partial^2 U_i}{\partial x_j \partial x_k} \frac{\partial^2 U_i}{\partial x_j \partial x_k} \end{aligned}$$

$$\text{with } P_k = -\overline{u_i u_j} \partial U_i / \partial x_j$$

$C_{\omega,1}$	$C_{\omega,2}$	$C_{\omega,3}$	σ	$C_{CD,1}$	$C_{CD,2}$
0.44	0.8	0.003	1.0	0.55	0.5

2. Transport equations of Reynolds stress tensor $\overline{u_i u_j}$:

$$\boxed{\frac{D\overline{u_i u_j}}{Dt} = \frac{\partial\overline{u_i u_j}}{\partial t} + U_k \frac{\partial\overline{u_i u_j}}{\partial x_k} =}$$

$$\begin{aligned} & \frac{\partial}{\partial x_m} \left[\left(\frac{1}{2}\nu\delta_{mn} + \sigma\nu^*\delta_{mn} \right) \frac{\partial\overline{u_i u_j}}{\partial x_n} \right] - \left(\overline{u_i u_k} \frac{\partial U_j}{\partial x_k} + \overline{u_j u_k} \frac{\partial U_i}{\partial x_k} \right) \\ & \quad + \Phi_{ij} - \varepsilon_{ij}^h \end{aligned}$$

$$\text{with } \sigma = 1.$$

3. Turbulent diffusion model terms D_{ij}^t and $D_{\omega^h}^t$:

$$\boxed{\nu^* = k^{0.5} AL^*} \quad \text{with} \quad L^* = \left(10 + \frac{Re_y^2}{25 Re_t} \right) \frac{\nu^{3/4}}{(\omega^h k)}$$

$$\text{and} \quad Re_t = k/(\nu\omega^h) \quad \text{and} \quad Re_y = k^{1/2}y/\nu.$$

4. Pressure redistribution model term Φ_{ij} :

$$\boxed{\Phi_{ij} = (1 - f_\Phi) \Phi_{ij}^w + f_\Phi \Phi_{ij}^h} \quad \text{with} \quad f_\Phi = \alpha^3$$

$$\boxed{\alpha - L_\alpha^2 \nabla^2 \alpha = 1} \quad \text{with} \quad L_\alpha = 12 \frac{\nu^{3/4}}{(k\omega^h)^{1/4}}$$

$$\boxed{\Phi_{ij}^w} = 5\omega^h [\overline{u_i u_k} n_j n_k + \overline{u_j u_k} n_i n_k - 0.5 \overline{u_k u_l} n_k n_l (n_i n_j + \delta_{ij})]$$

$$\text{with} \quad n_i = \frac{\nabla \alpha}{|\nabla \alpha|}$$

$$\begin{aligned} \boxed{\Phi_{ij}^h} = & - \left(C_1 + C_{1s} \frac{P_k}{k\omega^h} \right) \omega^h b_{ij} + C_2 \omega^h k \left(b_{ik} b_{kj} - \frac{1}{3} b_{kl} b_{kl} \delta_{ij} \right) \\ & + \left(C_3 - C_{3s} \sqrt{b_{kl} b_{kl}} \right) k S_{ij} + C_4 k \left(b_{ik} S_{jk} + b_{jk} S_{ik} - \frac{2}{3} b_{lm} S_{lm} \delta_{ij} \right) \\ & + C_5 k (b_{ik} \Omega_{jk} + b_{jk} \Omega_{ik}) \end{aligned}$$

C_1	C_{1s}	C_2	C_3	C_{3s}	C_4	C_5
3.4	1.8	4.2	0.8	1.3	1.25	0.4

5. Stress-dissipation correlation model term ε_{ij}^h :

$$\boxed{\varepsilon_{ij}^h = f_s \omega^h \overline{u_i u_j} + (1 - f_s) \frac{2}{3} k \omega^h \delta_{ij}} \quad \text{with} \quad f_s = 1 - \sqrt{A} E^2$$

and $A = 1 - 9(A_2 - A_3)/8$ and $A_2 = a_{ij} a_{ji}$ and $A_3 = a_{ij} a_{jk} a_{ki}$

and $E = 1 - 9(E_2 - E_3)/8$ and $E_2 = e_{ij} e_{ji}$ and $E_3 = e_{ij} e_{jk} e_{ki}$

and $a_{ij} = \overline{u_i u_j} / k - 2\delta_{ij}/3$ and $e_{ij} = \varepsilon_{ij}^h / \varepsilon - 2\delta_{ij}/3$

6. Reynolds stress tensor blending in momentum equation:

$$\boxed{\overline{u_i u_j} = (1 - \beta) \overline{u_i u_j} + \beta \nu_t S_{ij}} \quad \text{with} \quad \beta = 0.25 \frac{Re_t}{300 + Re_t}$$

and $\nu_t = C_\mu A k^{0.5} L_{\nu_t}$ and $L_{\nu_t} = \max[\max(L_\eta, L_\lambda), L_L]$

and $L_\eta = C_\eta \frac{\nu^{0.75}}{(k\omega^h)^{0.25}}$ and $L_\lambda = C_\lambda \sqrt{\frac{10\nu}{\omega^h}}$ and $L_L = C_L \frac{\sqrt{k}}{\omega^h}$

C_μ	C_η	C_λ	C_L
1.0	4	0.9	0.17

B. Instability-Sensitive Elliptic-Blending-related Reynolds Stress Model

Formulation

The model formulation of the Instability-Sensitive Elliptic-Blending-related Reynolds Stress Model (ISEBM) is identical to the EBM formulation described in Chapter 4.2 and summarized in Appendix A except for the following modifications. It should be noted that the total turbulent quantities do not enter the model formulation as in the RANS mode. In the hybrid RANS/LES mode, the model formulation only receives the modeled fractions.

1. ω^h -transport equation:

The ω^h -transport equation and its model approaches are similar to the EBM formulation (see Eq. (4.4)) with an additional source term P_{SAS} on the right-hand side:

$$\left(\frac{D\omega^h}{Dt}\right)_{\text{ISEBM}} = \left(\frac{D\omega^h}{Dt}\right)_{\text{EBM}} + P_{\text{SAS}} \quad (\text{B.1})$$

The additional source term is formulated in terms of the second derivative of the velocity field and has the form:

$$P_{\text{SAS}} = C_{\text{SAS},1} (T_1 - C_{\text{SAS},2} T_2)$$
$$T_1 = 40.0 \cdot 1.775 \cdot 0.41 \cdot \frac{\partial^2 U_i}{\partial x_i^2} \sqrt{k} \quad (\text{B.2})$$

$$T_2 = 3 k \max \left(\frac{1}{\omega^h} \frac{\partial \omega^h}{\partial x_i} \frac{\partial \omega^h}{\partial x_i}, \frac{1}{k^2} \frac{\partial k}{\partial x_i} \frac{\partial k}{\partial x_i} \right) \quad (\text{B.3})$$

The model constants $C_{\text{SAS},1} = 0.003$ and $C_{\text{SAS},2} = 40$ are chosen according to Maduta et al. (2015).

2. Elliptic blending-related lengthscale L_α :

To ensure a behavior of the elliptic function α that is independent of the local value of $k_{\text{mod}}/k_{\text{total}}$, the total turbulent quantities are applied to the elliptic blending-related lengthscale L_α :

$$L_\alpha = 12 \frac{\nu^{3/4}}{(k_{\text{total}} \omega_{\text{total}}^h)^{1/4}} \quad (\text{B.4})$$

3. Wall-near pressure redistribution approach:

To reduce the dissipative character of Manceau's near-wall formulation in the scale-resolving mode, the pressure redistribution formulation postulated by Jakirlić (1997) $\Phi_{ij}^{\text{Jakirlic}}$ is included in the ISEBM. This formulation has proven to be advantageous in the scale-resolving mode according to Maduta et al. (2015). A blending between Manceau's $\Phi_{ij}^{\text{Manceau}}$ (Eqn. (4.8)) and Jakirlić's formulation $\Phi_{ij}^{\text{Jakirlic}}$ in the near-wall region with the cubic ratio of the modeled to turbulent kinetic energy as blending function has been found to be beneficial.

$$\phi_{ij}^w = \left(\frac{k_{\text{mod}}}{k_{\text{total}}} \right)^3 \phi_{ij}^{\text{Manceau}} + \left[1 - \left(\frac{k_{\text{mod}}}{k_{\text{total}}} \right)^3 \right] \phi_{ij}^{\text{Jakirlic}} \quad (\text{B.5})$$

Illustration

The channel flow with a friction Reynolds number of $Re_\tau = 180$ is selected to briefly illustrate the capabilities of the ISEBM. The numerical procedure is conducted on a comparatively coarse grid with a total cell number of $n_{\text{total}} = 43750$, whose closest cell to the wall is entirely in the viscous sublayer $y^+ < 1$. The discretization is done with CDS for the convective term and the second-order backward-differencing scheme (see Eqn. (2.47)) for the temporal terms.

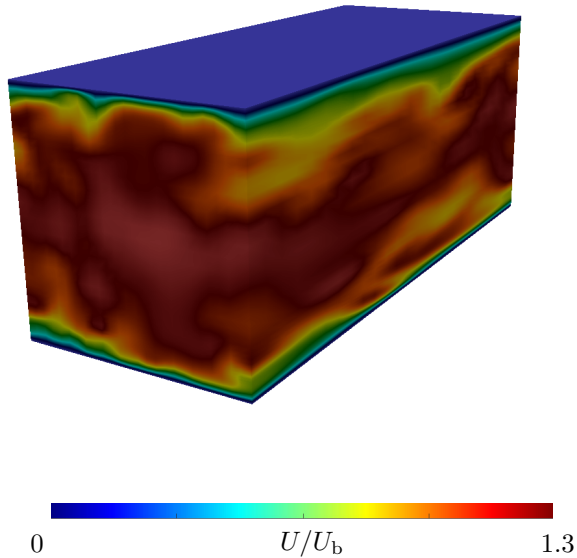


Figure B.1.: Iso-contours of the instantaneous velocity magnitude of a channel flow with $Re_\tau = 180$ predicted by the ISEBM.

The resulting instantaneous velocity magnitude field is illustrated in terms of its iso-contours in Fig. B.1 to demonstrate the fluctuating character of the

flow topology. The corresponding time-averaged flow quantities predicted by the ISEBM are depicted in Fig. B.2 with the streamwise velocity u^+ (top left) and the Reynolds stress components $\overline{u_i u_j}^+$ (bottom) along the channel height y^+ . For evaluation of the ISEBM results, the DNS data from Lee and Moser (2015) (symbols), the results of the EBM (blue solid line) and of a WALE Large-Eddy Simulation (LES) on the ISEBM-grid are depicted. In addition, the ratio $k_{\text{mod}}/k_{\text{total}}$ is depicted in Fig. B.2 top right.

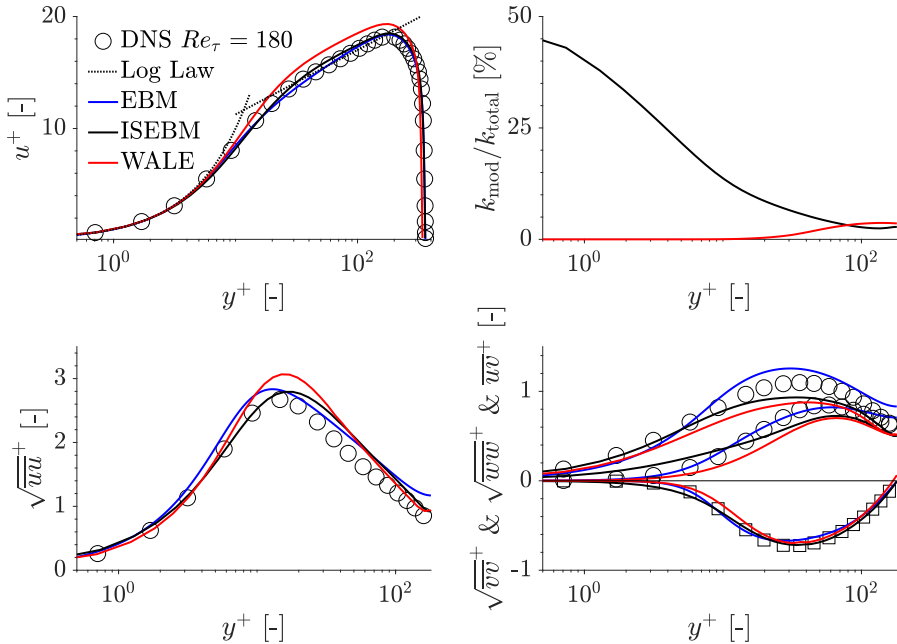


Figure B.2.: Streamwise velocity u^+ (top left), Reynolds stress components $\overline{u_i u_j}^+$ (bottom) and modeled to total turbulent kinetic energy ratio $\frac{k_{\text{mod}}}{k_{\text{total}}}$ (top right) depicted over the channel height predicted by EBM (blue solid line), ISEBM (black solid line) and WALE (red solid line). The DNS data by Lee and Moser (2015) are depicted for comparison (symbols).

Bibliography

- Adechy, D., & Issa, R. (2004). Modelling of annular flow through pipes and T-junctions. *Computers & Fluids*, 33(2), 289–313 (cit. on p. 90).
- Ahmed, S. R., Ramm, G., & Faltin, G. (1984). Some salient features of the time-averaged ground vehicle wake. *SAE Transactions*, 473–503 (cit. on p. 140).
- Alaya, E., Knopp, T., & Grabe, C. (2020). *Provision of validation-test-case descriptions*. (tech. rep.). (Cit. on p. 218).
- Alaya, E., Knopp, T., & Grabe, C. (2021). Design of a parametrized numerical experiment for a 2d turbulent boundary layer flow with varying adverse pressure gradient and separation behaviour (cit. on p. 218).
- Ando, T., Shakouchi, T., Takamura, S., & Tsujimoto, K. (2014). Effects of flow rate ratio on loss reduction of T-junction pipe. *Journal of Fluid Science and Technology*, 9(3), JFST0045–JFST0045 (cit. on p. 116).
- Ayhan, H., & Sökmen, C. N. (2012). CFD modeling of thermal mixing in a T-junction geometry using LES model. *Nuclear Engineering and Design*, 253, 183–191 (cit. on p. 90).
- Azzopardi, B. t., & Whalley, P. (1982). The effect of flow patterns on two-phase flow in a T-junction. *International Journal of Multiphase Flow*, 8(5), 491–507 (cit. on p. 90).
- Baehr, H., & Stephan, K. (2006). Heat and mass transfer. ; Wärme- und Stoffübertragung (cit. on pp. 30, 31).
- Baliga, B., & Patankar, S. (1980). A new finite-element formulation for convection-diffusion problems. *Numerical Heat Transfer*, 3(4), 393–409 (cit. on p. 27).
- Basara, B. (2004). Employment of the second-moment turbulence closure on arbitrary unstructured grids. *International Journal of Numerical Methods in Fluids*, 44, 377–407. <https://doi.org/10.1002/fld.646> (cit. on p. 197)

- Basara, B., & Jakirlić, S. (2003). A new, hybrid turbulence modelling strategy for industrial CFD. *International Journal of Numerical Methods in Fluids*, 42(1), 89–116. <https://doi.org/10.1002/flid.492> (cit. on pp. 195, 197, 198)
- Bassett, M., Winterbone, D., & Pearson, R. (2001). Calculation of steady flow pressure loss coefficients for pipe junctions. *Proceedings of the Institution of Mechanical Engineers, part C: Journal of Mechanical Engineering Science*, 215(8), 861–881 (cit. on p. 91).
- Basshuysen, R., & Schäfer, F. (2015). *Handbuch Verbrennungsmotor: Grundlagen, Komponenten, Systeme, Perspektiven*. Springer Fachmedien Wiesbaden. (Cit. on p. 33).
- Baum, E., Peterson, B., Böhm, B., & Dreizler, A. (2014). On the validation of LES applied to internal combustion engine flows: Part 1: Comprehensive experimental database. *Flow, Turbulence and Combustion*, 92(1-2), 269–297 (cit. on p. 139).
- Behnke, L. (2009). Vorhersage kritischer Siedezustände in Brennelementstrukturen von Leichtwasserreaktoren bei variablem Druck (cit. on p. 2).
- Berger, A., Talbot, L., & Yao, L. (1983). Flow in curved pipes. *Annual Review of Fluid Mechanics*, 15, 461–512. <https://doi.org/10.1146/annurev.fl.15.010183.002333> (cit. on p. 61)
- Billard, F., & Laurence, D. (2012). A robust k - ϵ - v^2/k elliptic blending turbulence model applied to near-wall, separated and buoyant flows. *International Journal of Heat and Fluid Flow*, 33(1), 45–58 (cit. on p. 13).
- Billard, F., Revell, A., & Craft, T. (2012). Application of recently developed elliptic blending based models to separated flows. *International Journal of Heat and Fluid Flow*, 35, 141–151. <https://doi.org/10.1016/j.ijheatfluidflow.2012.04.012> (cit. on p. 182)
- Boussinesq, J. (1877). *Essai sur la théorie des eaux courantes*. Impr. nationale. (Cit. on p. 15).
- Braess, H.-H., & Seiffert, U. (2011). *Vieweg Handbuch Kraftfahrzeugtechnik*. Springer-Verlag. (Cit. on p. 35).
- Breuer, M., Peller, N., Rapp, C., & Manhart, M. (2009). Flow over periodic hills - numerical and experimental study in a wide range of Reynolds numbers. *Computers and Fluids*, 38(2), 433–457 (cit. on pp. 232, 234, 235, 237, 238).

-
- Cécora, R.-D., Radespiel, R., Eisfeld, B., & Probst, A. (2015). Differential Reynolds-stress modeling for aeronautics. *AIAA Journal*, *53*(3), 739–755. <https://doi.org/10.2514/1.J053250> (cit. on p. 183)
- Chen, K. K., Rowley, C. W., & Stone, H. A. (2015). Vortex dynamics in a pipe T-junction: Recirculation and sensitivity. *Physics of Fluids*, *27*(3), 034107 (cit. on p. 90).
- Chen, X., McLaury, B. S., & Shirazi, S. A. (2004). Application and experimental validation of a computational fluid dynamics (CFD)-based erosion prediction model in elbows and plugged tees. *Computers and Fluids*, *33*(10), 1251–1272. <https://doi.org/10.1016/j.compfluid.2004.02.003> (cit. on p. 63)
- Cherry, E., Elkins, C., & Eaton, J. (2008). Geometric sensitivity of three-dimensional separated flows. *International Journal of Heat and Fluid Flow*, *29*(3), 803–811 (cit. on pp. 239, 240, 246).
- Cherry, E., Elkins, C., & Eaton, J. (2009). Pressure measurements in a three-dimensional separated diffuser. *International Journal of Heat and Fluid Flow*, *1*(30), 1–2 (cit. on pp. 239–241).
- Cherry, E., Iaccarino, G., Elkins, C., & Eaton, J. (2006). Separated flow in a three-dimensional diffuser: Preliminary validation. *Annual Research Briefs*, *2006*(85), 57–83 (cit. on pp. 239, 240).
- Claeys, S., & Lievens, S. (2006). Coolants at elevated temperatures. *Journal of ASTM International*, *3*(10), 1–10 (cit. on p. 34).
- Constantinescu, G., Miyawaki, S., Rhoads, B., Sukhodolov, A., & Kirkil, G. (2011). Structure of turbulent flow at a river confluence with momentum and velocity ratios close to 1: Insight provided by an eddy-resolving numerical simulation. *Water Resources Research*, *47*(5) (cit. on p. 115).
- Craft, T. J. (1998). Developments in a low-Reynolds-number second-moment closure and its application to separating and reattachment flows. *International Journal of Heat and Fluid Flow*, *19*, 541–548. [https://doi.org/10.1016/S0142-727X\(98\)10020-6](https://doi.org/10.1016/S0142-727X(98)10020-6) (cit. on pp. 181, 182)
- Craft, T. J., & Launder, B. E. (1996). A Reynolds stress closure designed for complex geometries. *International Journal of Heat and Fluid Flow*, *17*(3), 245–254. [https://doi.org/10.1016/0142-727X\(96\)00038-0](https://doi.org/10.1016/0142-727X(96)00038-0) (cit. on p. 182)

- Daly, B. J., & Harlow, F. H. (1970). Transport equations in turbulence. *Physics of Fluids*, 13(11), 2634–2649. <https://doi.org/10.1063/1.1692845> (cit. on p. 194)
- Dean, R. B. (1978). Reynolds number dependence of skin friction and other bulk flow variables in two-dimensional rectangular duct flow (cit. on p. 202).
- Dean, W. R. (1928). Fluid motion in a curved channel. *Proceedings of the Royal Society of London. Series A, Containing Papers of a Mathematical and Physical Character*, 121(787), 402–420. <https://doi.org/10.1098/rspa.1928.0205> (cit. on pp. 61, 72)
- Di Liberto, M., Di Piazza, I., & Ciofalo, M. (2013). Turbulence structure and budgets in curved pipes. *Computers and Fluids*, 88(-), 452–472. <https://doi.org/10.1016/j.compfluid.2013.09.028> (cit. on p. 62)
- Diehl, A. (2006). *Zum Verhalten metallischer Werkstoffe in Kühlkreisläufen von Verbrennungskraftmaschinen unter Komplexbeanspruchung* (Doctoral dissertation). Technical University of Darmstadt, Germany. Shaker Verlag, Aachen. <https://hds.hebis.de/ulbda/Record/HEB178837598>. (Cit. on p. 3)
- Disotell, K. J., & Rumsey, C. L. (2017). *Development of an axisymmetric afterbody test case for turbulent flow separation validation*. National Aeronautics; Space Administration, Langley Research Center. (Cit. on p. 218).
- Dörnenburg, F., Lades, K., & Kenningley, S. (2010). Neue Technik für höhere Warmfestigkeit von Aluminiumkolben. *MTZ-Motortechnische Zeitschrift*, 71(4), 246–249 (cit. on p. 33).
- Downs, S., & James, E. (1987). Jet impingement heat transfer—a literature survey. *ASME, AIChE, and ANS, 24th National Heat Transfer Conference and Exhibition* (cit. on p. 90).
- Driver, D. M., & Seegmiller, H. L. (1985). Features of a reattaching turbulent shear layer in divergent channel flow. *AIAA Journal*, 23(2), 163–171 (cit. on pp. 226, 228–231).
- Duchardt, T., Andersohn, G., & Oechsner, M. (2015). Corrosion behavior of en ac-alsi10mg in boiling coolant with various average flow temperatures. *Materials and Corrosion*, 66(9), 931–939 (cit. on p. 33).

-
- Durbin, P. (1991). Near-wall turbulence closure modeling without “damping functions”. *Theoretical and Computational Fluid Dynamics*, 3(1), 1–13 (cit. on pp. 13, 182).
- Durbin, P. (1993). A Reynolds stress model for near-wall turbulence. *Journal of Fluid Mechanics*, 249, 465–498. <https://doi.org/10.1017/S0022112093001259> (cit. on pp. 181, 182)
- Durbin, P. (1996). On the k - ε stagnation point anomaly. *Int. J. Heat and Fluid Flow*, 17, 9–90 (cit. on p. 13).
- Egorov, Y., & Menter, F. (2008). Development and application of SST-SAS turbulence model in the DESIDER project. In *Advances in Hybrid RANS-LES Modelling* (pp. 261–270). Springer. (Cit. on pp. 256, 263).
- Eisfeld, B., & Rumsey, L. C. (2020). Length-scale correction for Reynolds-stress modeling. *AIAA Journal*, 58(4), 1518–1528. <https://doi.org/10.2514/1.J058858> (cit. on pp. 183, 196)
- Eitel-Amor, G., Örlü, R., & Schlatter, P. (2014). Simulation and validation of a spatially evolving turbulent boundary layer up to $Re_\theta = 8300$. *International Journal of Heat and Fluid Flow*, 47, 57–69 (cit. on pp. 213–215, 217).
- El Khoury, G. K., Schlatter, P., Noorani, A., Fischer, P. F., Brethouwer, G., & Johansson, A. V. (2013). Direct numerical simulation of turbulent pipe flow at moderately high Reynolds numbers. *Flow, Turbulence and Combustion*, 91(3), 475–495. <https://doi.org/10.1007/s10494-013-9482-8> (cit. on pp. 38, 42, 45, 47–50, 52, 208–212)
- Ferziger, J. H., Perić, M., & Street, R. L. (2002). *Computational methods for fluid dynamics* (Vol. 3). Springer. (Cit. on p. 25).
- Fontanesi, S., Cicalese, G., & Giacomini, M. (2010). *Multiphase CFD-CHT analysis and optimization of the cooling jacket in a v6 diesel engine* (tech. rep.). SAE Technical Paper. (Cit. on p. 139).
- Fontanesi, S., & Giacomini, M. (2013). Multiphase CFD-CHT optimization of the cooling jacket and fem analysis of the engine head of a v6 diesel engine. *Applied Thermal Engineering*, 52(2), 293–303 (cit. on p. 139).
- Freudenhammer, D., Peterson, B., Ding, C.-P., Boehm, B., & Grundmann, S. (2015). The influence of cylinder head geometry variations on the volumetric intake flow captured by magnetic resonance velocimetry. *SAE International Journal of Engines*, 8(4), 1826–1836 (cit. on p. 139).

- Fröhlich, J., Mellen, C. P., Rodi, W., Temmerman, L., & Leschziner, M. A. (2005). Highly resolved large-eddy simulation of separated flow in a channel with streamwise periodic constrictions. *Journal of Fluid Mechanics*, *526*, 19–66 (cit. on p. 232).
- Fukagata, K., & Kasagi, N. (2002). Highly energy-conservative finite difference method for the cylindrical coordinate system. *Journal of Computational Physics*, *181*, 478–498. <https://doi.org/10.1006/jcph.2002.7138> (cit. on p. 38)
- Gau, C., & Chung, C. M. (1991). Surface Curvature Effect on Slot-Air-Jet Impingement Cooling Flow and Heat Transfer Process. *Journal of Heat Transfer*, *113*(4), 858–864. <https://doi.org/10.1115/1.2911214> (cit. on p. 90)
- Germano, M., Piomelli, U., Moin, P., & Cabot, W. H. (1991). A dynamic subgrid-scale eddy viscosity model. *Physics of Fluids A: Fluid Dynamics*, *3*(7), 1760–1765. <https://doi.org/10.1063/1.857955> (cit. on pp. 18, 19)
- Gerolymos, G. A., & Vallet, I. (2016). Reynolds-stress model prediction of 3-d duct flows. *Flow, Turbulence and Combustion*, *96*(4), 45–93. <https://doi.org/10.1007/s10494-015-9648-7> (cit. on p. 183)
- Gibson, M. M., & Launder, B. E. (1978). Ground effects on pressure fluctuations in the atmospheric boundary layer. *Journal of Fluid Mechanics*, *86*(3), 491–511. <https://doi.org/10.1017/S0022112078001251> (cit. on pp. 181, 183, 189)
- Graftieaux, L., Michard, M., & Grosjean, N. (2001). Combining PIV, POD and vortex identification algorithms for the study of unsteady turbulent swirling flows. *Measurement Science and Technology*, *12*(9), 1422–1429. <https://doi.org/10.1088/0957-0233/12/9/307> (cit. on pp. v, vii, 63, 68, 74, 83, 84, 87, 91, 94, 102, 108–110, 113, 116, 121, 128, 130, 136, 137, 260, 264, 305)
- Gruden, D. (2008). *Umweltschutz in der Automobilindustrie*. Vieweg+ Teubner. (Cit. on pp. 2, 139).
- Hajaali, A., & Stoesser, T. (2021). Flow separation dynamics in three-dimensional asymmetric diffusers. *Flow, Turbulence and Combustion*, 1–27 (cit. on p. 241).
- Hanjalic, K., & Jakirlic, S. (1998). Contribution towards the second-moment closure modelling of separating turbulent flows. *Computers and Fluids*,

-
- 27(2), 137–156. [https://doi.org/10.1016/S0045-7930\(97\)00036-4](https://doi.org/10.1016/S0045-7930(97)00036-4) (cit. on pp. 181, 183, 196)
- Hanjalic, K., Jakirlic, S., & Hadzic, I. (1995). Computation of oscillating turbulent flows at transitional Re-numbers. In F. Durst, N. Kasagi, B. Launder, F. Schmidt, K. Suzuki, & J. Whitelaw (Eds.), *Turbulent Shear Flows 9* (pp. 323–342). Springer-Verlag, Berlin-Heidelberg (ISBN 3-540-577041). (Cit. on p. 181).
- Hanjalic, K., & Launder, B. E. (2011). *Modelling Turbulence in Engineering and the Environment: Second-Moment Routes to Closure* (First). Cambridge University Press. (Cit. on p. 184).
- Hanjalic, K., & Launder, B. E. (1972). A Reynolds stress model of turbulence and its application to thin shear flows. *Journal of Fluid Mechanics*, 52(4), 609–638. <https://doi.org/10.1017/S002211207200268X> (cit. on p. 181)
- Hanjalic, K., & Launder, B. E. (1976). Contribution towards a Reynolds-stress closure for low-Reynolds-number turbulence. *Journal of Fluid Mechanics*, 74(4), 593–610. <https://doi.org/10.1017/S0022112076001961> (cit. on p. 181)
- Hanjalić, K., Popovac, M., & Hadžiabdić, M. (2004). A robust near-wall elliptic-relaxation eddy-viscosity turbulence model for cfd. *International Journal of Heat and Fluid Flow*, 25(6), 1047–1051 (cit. on p. 15).
- Hattori, H., Iwase, M., Houra, T., & Tagawa, M. (2014). DNS and LES for turbulent heat transfer and mixing in T-junction channel flow. *10th Engineering Turbulence Modelling and Measurement Conference (ETMM10)* (cit. on p. 90).
- Heibel, M. (2009). *Das wahrgenommene Umweltbewusstsein einer Automarke und dessen Effekt auf die Beziehung zum Verbraucher*. GRIN Verlag. (Cit. on pp. 2, 139).
- Hirsch, C. (1988). *Numerical computation of internal & external flows: Fundamentals of numerical discretization*. John Wiley & Sons, Inc. (Cit. on p. 25).
- Huang, Y., & Green, M. A. (2015). Detection and tracking of vortex phenomena using Lagrangian coherent structures. *Experiments in Fluids*, 56(7), 1–12 (cit. on p. 74).

- Jafarabadi, M., Chamani, H., Malakizadi, A., & Jazayeri, S. A. (2008). A fast coupled CFD-thermal analysis of a heavy duty diesel engine water cooling system. *ASME International Mechanical Engineering Congress and Exposition*, 48715, 663–670 (cit. on p. 139).
- Jakirlic, S., & Hanjalic, K. (2002). A new approach to modelling near-wall turbulence energy and stress dissipation. *Journal of Fluid Mechanics*, 459, 139–166. <https://doi.org/10.1017/S0022112002007905> (cit. on pp. 181, 185, 190, 192)
- Jakirlic, S., & Hanjalic, K. (2013). A DNS-based re-examination of coefficients in the pressure-strain models in Second-moment Closures. *Fluid Dynamics Research*, 45(5), 055509. <https://doi.org/10.1088/0169-5983/45/5/055509> (cit. on p. 181)
- Jakirlić, S., Kavelilil, G., Sirbubalo, E., Breuer, M., von Terzi, D., & Borello, D. (2010). B in 14th ERCOFTAC SIG15 Workshop on Refined Turbulence Modelling: Turbulent Flow Separation in a 3-D Diffuser. *ERCOFTAC Bulletin*, December, (85) (cit. on p. 239).
- Jakirlić, S., & Maduta, R. (2015). Extending the bounds of 'steady' RANS closures: Toward an instability-sensitive Reynolds stress model. *Int. J. Heat and Fluid Flow*, 51, 175–194. <https://doi.org/j.ijheatfluidflow.2014.09.003> (cit. on pp. v, vii, 5, 62, 181, 182, 185, 187, 190, 192, 255, 262)
- Jakirlić, S. (1997). *Reynolds-Spannungs-Modellierung komplexer turbulenter Strömungen*. Herbert Utz Verlag, München. <https://www.utzverlag.de/catalog/book/48103>. (Cit. on pp. 185, 257, 270, 308)
- Jambunathan, K., Lai, E., Moss, M., & Button, B. (1992). A review of heat transfer data for single circular jet impingement. *International Journal of Heat and Fluid Flow*, 13(2), 106–115 (cit. on p. 90).
- Jovanovic, J., Ye, Q.-Y., & Durst, F. (1995). Statistical interpretation of the turbulent dissipation rate in wall-bounded flows. *Journal of Fluid Mechanics*, 293, 321–347. <https://doi.org/10.1017/S002211209500173X> (cit. on p. 185)
- Jovic, S., & Driver, D. (1995). Reynolds number effect on the skin friction in separated flows behind a backward-facing step. *Experiments in Fluids*, 18(6), 464–467 (cit. on p. 226).
- Kaiser, M. (2009). *Korrosion metallischer werkstoffe unter beaufschlagung von kühlmittelzusätzen für verbrennungskraftmaschinen* (Doctoral disser-

-
- tation). Technical University of Darmstadt, Germany. Shaker Verlag, Aachen. <https://hds.hebis.de/ulbda/Record/HEB215633318>. (Cit. on p. 3)
- Kalpakli, A., Örlü, R., & Alfredsson, H. (2012). Dean vortices in turbulent flows: Rocking or rolling? *Journal of Visualization*, *15*, 37–38. <https://doi.org/10.1007/s12650-011-0108-8> (cit. on p. 61)
- Kalpakli, A., & Örlü, R. (2013). Turbulent pipe flow downstream a 90° pipe bend with and without superimposed swirl. *International Journal of Heat and Fluid Flow*, *41*, 103–111. <https://doi.org/10.1016/j.ijheatfluidflow.2013.01.003> (cit. on p. 61)
- Kalpakli Vester, A., Örlü, R., & Alfredsson, P. H. (2016). Turbulent flows in curved pipes: Recent advances in experiments and simulations. *Applied Mechanics Reviews*, *68*(5)(5), 050802-1–050802-25. <https://doi.org/10.1115/1.4034135> (cit. on pp. 61, 66)
- Khosla, P., & Rubin, S. (1974). A diagonally dominant second-order accurate implicit scheme. *Computers & Fluids*, *2*(2), 207–209 (cit. on p. 24).
- Kissing, J., Wegt, S., Jakirlic, S., Kriegseis, J., Hussong, J., & Tropea, C. (2020). Leading edge vortex formation and detachment on a flat plate undergoing simultaneous pitching and plunging motion: Experimental and computational study. *International Journal of Heat and Fluid Flow*, *86*, 108726 (cit. on p. 74).
- Klein, T. S., Craft, T. J., & Iacovides, H. (2015). Assessment of the performance of different classes of turbulence models in a wide range of non-equilibrium flows. *International Journal of Heat and Fluid Flow*, *51*, 229–256. <https://doi.org/10.1016/j.ijheatfluidflow.2014.10.017> (cit. on p. 183)
- Klink, A., Reitz, R., Engler, T., & Oechsner, M. (2019). Assessment of the flow induced corrosion behaviour in generic pipe conduits used in modern engine cooling systems. *European Federation of Corrosion Event No. 445, Sevilla, Spain*. <http://eurocorr.efcweb.org/2019/abstracts/17/203336.pdf> (cit. on pp. v, vii, 3, 31, 140, 259)
- Klink, A., & Wegt, S. (2021). Strömungsinduzierte Korrosion und Erosion in Kühlkanälen von Verbrennungskraftmaschinen, IGF-Vorhaben Nr. 20224 N/1 „Strömungserosion“ (cit. on pp. v, vii, 3, 29, 140, 150, 151, 259, 264).

- Kolmogorov, A. N. (1941). The local structure of turbulence in incompressible viscous fluid for very large Reynolds numbers. *Cr Acad. Sci. URSS*, *30*, 301–305 (cit. on pp. 11, 13).
- Krepper, E., & Rzehak, R. (2011). CFD for subcooled flow boiling: Simulation of debora experiments. *Nuclear Engineering and Design*, *241*(9), 3851–3866 (cit. on pp. 173, 177, 256, 263).
- Krepper, E., Rzehak, R., Lifante, C., & Frank, T. (2013). CFD for subcooled flow boiling: Coupling wall boiling and population balance models. *Nuclear engineering and design*, *255*, 330–346 (cit. on pp. 173, 177, 256, 263).
- Krumbein, B. (2019). A modeling framework for scale-resolving computations of turbulent flow over porous and rough walls (cit. on p. 52).
- Krumbein, B., Termini, V., Jakirlić, S., & Tropea, C. (2018). Flow and heat transfer in cross-stream type t-junctions: A computational study. *International Journal of Heat and Fluid Flow*, *71*, 179–188 (cit. on p. 90).
- Kuwata, Y., & Suga, K. (2015). Progress in the extension of a second-moment closure for turbulent environmental flows. *International Journal of Heat and Fluid Flow*, *51*, 268–284. <https://doi.org/10.1016/j.ijheatfluidflow.2014.10.011> (cit. on p. 183)
- Kuwata, Y., Suga, K., & Kawaguchi, Y. (2019). An extension of the second moment closure model for turbulent flows over macro rough walls. *International Journal of Heat and Fluid Flow*, *77*, 186–201. <https://doi.org/10.1016/j.ijheatfluidflow.2019.04.003> (cit. on p. 183)
- Launder, B. E., & Sharma, B. I. (1974). Application of the energy-dissipation model of turbulence to the calculation of flow near a spinning disk. *Letters in Heat and Mass Transfer*, *1*, 131–138. [https://doi.org/10.1016/0094-4548\(74\)90150-7](https://doi.org/10.1016/0094-4548(74)90150-7) (cit. on pp. 62, 192)
- Launder, B. E., Reece, G. J., & Rodi, W. (1975). Progress in the development of a Reynolds-stress turbulence closure. *Journal of Fluid Mechanics*, *68*(3), 537–566. <https://doi.org/10.1017/S0022112075001814> (cit. on pp. 181, 182, 184)
- Le, H., Moin, P., & Kim, J. (1997). Direct numerical simulation of turbulent flow over a backward-facing step. *Journal of Fluid Mechanics*, *330*, 349–374 (cit. on p. 226).

-
- Lee, M., & Moser, R. D. (2015). Direct numerical simulation of turbulent channel flow up to. *Journal of Fluid Mechanics*, *774*, 395–415 (cit. on pp. 201, 202, 204, 206, 207, 272).
- Lilly, D. K. (1992). A proposed modification of the Germano subgrid-scale closure method. *Physics of Fluids A: Fluid Dynamics*, *4*(3), 633–635. <https://doi.org/10.1063/1.858280> (cit. on pp. 18, 19)
- Lunanova, M. (2009). In *Optimierung von Nebenaggregaten* (pp. 93–266). Springer. (Cit. on pp. 2, 139).
- Lupi, V., Canton, J., & Schlatter, P. (2020). Global stability analysis of a 90°-bend pipe flow. *International Journal of Heat and Fluid Flow*, *86*, 108742-1–108742-9. <https://doi.org/10.1016/j.ijheatfluidflow.2020.108742> (cit. on p. 62)
- Maduta, R., Jakirlić, S., & Ullrich, M. (2015). A numerically upgraded instability-sensitized Reynolds stress model for complex turbulent flow applications. *Turbulence, Heat and Mass Transfer 8, Hanjalić et al. (Eds.), Begell House Inc., ISBN 978-1-56700-427-4*, 299–302. <https://doi.org/10.1615/ICHMT.2015.THMT-15.550> (cit. on pp. 197, 256, 257, 263, 270)
- Manceau, R. (2015). Recent progress in the development of the Elliptic Blending Reynolds-stress model. *International Journal of Heat and Fluid Flow*, *51*, 195–220. <https://doi.org/10.1016/j.ijheatfluidflow.2014.09.002> (cit. on pp. 182, 187–189)
- Manceau, R., & Hanjalić, K. (2002). Elliptic blending model: A new near-wall Reynolds-stress turbulence closure. *Physics of Fluids*, *14*(2), 744–754. <https://doi.org/10.1063/1.1432693> (cit. on pp. v, vii, 5, 182, 183, 186–188, 255, 257, 262, 308)
- Mansour, N. N., Kim, J., & Moin, P. (1988). Reynolds-stress and dissipation-rate budgets in a turbulent channel flow. *Journal of Fluid Mechanics*, *194*, 15–44. <https://doi.org/10.1017/S0022112088002885> (cit. on pp. 192, 193)
- Massa, C., & Colombo, A. (2021). DNS of an APG flow over a rounded step. *EU Project HiFi-TURB, Grant Agreement No. 814837* (cit. on pp. 219–221, 223–225).
- Menter, F. R. (1992). Improved two-equation k-omega turbulence models for aerodynamic flows. *NASA Sti/recon Technical Report N, 93*, 22809 (cit. on p. 15).

- Moor-Yossef, Y. (2014). Unconditionally stable time marching scheme for Reynolds stress models. *Journal of Computational Physics*, 276, 635–664. <https://doi.org/10.1016/j.jcp.2014.07.047> (cit. on p. 197)
- Moser, R. D., Kim, J., & Mansour, N. N. (1999). Direct numerical simulation of turbulent channel flow up to $Re_\tau = 590$. *Physics of fluids*, 11(4), 943–945 (cit. on pp. 191, 194, 195, 200–202, 204, 206, 207).
- Mosley, M. P. (1976). An experimental study of channel confluences. *The Journal of Geology*, 84(5), 535–562 (cit. on p. 115).
- Mulemane, A., & Soman, R. (2007). *CFD based complete engine cooling jacket development and analysis* (tech. rep.). SAE Technical Paper. (Cit. on p. 139).
- Nicoud, F., & Ducros, F. (1999). Subgrid-scale stress modelling based on the square of the velocity gradient tensor. *Flow, Turbulence and Combustion*, 62(3), 183–200. <https://doi.org/10.1023/A:1009995426001> (cit. on pp. 18, 20, 21, 48, 56, 174, 260)
- Obi, S., Peric, M., & Scheuerer, G. (1991). Second-moment calculation procedure for turbulent flows with collocated variable arrangement. *AIAA Journal*, 29(4), 585–590. <https://doi.org/10.2514/3.10624> (cit. on p. 196)
- Ohlsson, J., Schlatter, P., Fischer, P. F., & Henningson, D. S. (2010). Direct numerical simulation of separated flow in a three-dimensional diffuser. *Journal of Fluid Mechanics*, 650, 307 (cit. on pp. 239–242, 246).
- Oka, K., & Ito, H. (2005). Energy losses at tees with large area ratios. *J. Fluids Eng.*, 127(1), 110–116 (cit. on p. 116).
- Phares, D. J., Smedley, G. T., & Flagan, R. C. (2000). The wall shear stress produced by the normal impingement of a jet on a flat surface. *Journal of Fluid Mechanics*, 418, 351–375 (cit. on p. 90).
- Pope, S. B. (2000). *Turbulent Flows*. Cambridge University Press. <https://doi.org/10.1017/CBO9780511840531>. (Cit. on pp. 11, 14, 15, 17, 51, 53, 56)
- Prandtl, L. (1925). Bericht über die Entstehung der Turbulenz. *Z. Angew. Math. Mech*, 5, 136–139 (cit. on p. 15).
- Rapp, C. (2008). *Experimentelle Studie der turbulenten Strömung über periodische Hügel* (Doctoral dissertation). Ph. D. Thesis, Technische Universität München. (Cit. on pp. 232, 234, 236–238).

-
- Ravensbergen, J., Krijger, J., Hillen, B., & Hoogstraten, H. (1995). Merging flows in an arterial confluence: The vertebro-basilar junction. *Journal of Fluid Mechanics*, *304*, 119–141 (cit. on p. 115).
- Ravensbergen, J., Krijger, J., Hillen, B., & Hoogstraten, H. (1996). The influence of the angle of confluence on the flow in a vertebro-basilar junction model. *Journal of Biomechanics*, *29*(3), 281–299 (cit. on p. 115).
- Reustle, A. (2012, April 10). *Cooling channels in the cylinder head of an internal combustion engine* (U.S. pat. 8,151,743 B2). (Cit. on p. 4).
- Reynolds, O. (1895). IV. on the dynamical theory of incompressible viscous fluids and the determination of the criterion. *Philosophical Transactions of the Royal Society of London.(a.)*, (186), 123–164 (cit. on p. 14).
- Richardson, L. F. (1922). *Weather prediction by numerical process*. Cambridge University Press. (Cit. on p. 11).
- Röhrig, R., Jakirlić, S., & Tropea, C. (2015). Comparative computational study of turbulent flow in a 90° pipe elbow. *International Journal of Heat and Fluid Flow*, *55*, 120–131. <https://doi.org/10.1016/j.ijheatfluidflow.2015.07.011> (cit. on pp. 31, 61)
- Roy, A. G., Roy, R., & Bergeron, N. (1988). Hydraulic geometry and changes in flow velocity at a river confluence with coarse bed material. *Earth Surface Processes and Landforms*, *13*(7), 583–598 (cit. on p. 115).
- Rütten, F., Meinke, M., & Schröder, W. (2001). Large-eddy simulations of 90° pipe bend flows. *Journal of Turbulence*, *003*. <https://doi.org/10.1088/1468-5248/2/1/003> (cit. on p. 62)
- Rütten, F., Meinke, M., & Schröder, W. (2005). Large-eddy simulation of low frequency oscillations of the dean vortices in turbulent pipe bend flows. *Physics of Fluids*, *17*(3), 035107-1–035107-11. <https://doi.org/10.1063/1.1852573> (cit. on p. 62)
- Sattarzadeh Shirvan, S. (2011). Experimental study of complex pipe flow [Technical Reports from Royal Institute of Technology, KTH Mechanics, SE-100 44 Stockholm, Sweden]. (Cit. on p. 66).
- Schäfer, M. (2006). *Computational Engineering: Introduction to Numerical Methods* (Vol. 321). Springer. (Cit. on pp. 21, 22, 25).
- Schlatter, P., & Örlü, R. (2010). Assessment of direct numerical simulation data of turbulent boundary layers. *Journal of Fluid Mechanics*, *659*, 116 (cit. on pp. 213–215, 217).

- Schmitt, G., & Fässler, K. (1990). Korrosion in Kühlkreisläufen. *Abschlussbericht Tagungshandbuch zum 5. Korrosionum* (cit. on p. 33).
- Sharif, M., & Mothe, K. (2010). Parametric study of turbulent slot-jet impingement heat transfer from concave cylindrical surfaces. *International Journal of Thermal Sciences*, 49(2), 428–442 (cit. on p. 90).
- Smagorinsky, J. (1963). General circulation experiments with the primitive equations: I. The basic experiment. *Monthly weather review*, 91(3), 99–164. [https://doi.org/10.1175/1520-0493\(1963\)091<0099:GCEWTP>2.3.CO;2](https://doi.org/10.1175/1520-0493(1963)091<0099:GCEWTP>2.3.CO;2) (cit. on p. 18)
- Solnordal, C. B., Wong, C. Y., & Boulanger, J. (2015). An experimental and numerical analysis of erosion caused by sand pneumatically conveyed through a standard pipe elbow. *Wear*, 336, 43–57. <https://doi.org/10.1016/j.wear.2015.04.017> (cit. on p. 63)
- Sommerfeld, M., & Huber, N. (1999). Experimental analysis and modelling of particle-wall collisions. *International Journal of Multiphase Flow*, 25(6-7), 1457–1489. [https://doi.org/10.1016/S0301-9322\(99\)00047-6](https://doi.org/10.1016/S0301-9322(99)00047-6) (cit. on p. 63)
- Speziale, C. G., Sarkar, S., & Gatski, T. B. (1991). Modelling the pressure-strain correlation of turbulence: An invariant dynamical systems approach. *Journal of Fluid Mechanics*, 227, 245–272. <https://doi.org/10.1017/S0022112091000101> (cit. on pp. 182, 183, 187, 188, 255, 294, 295)
- Sporschill, G., Billard, F., Mallet, M. 1., & Manceau, R. (2021). Reynolds stress RANS models for industrial aeronautical applications. In F. Chinesta, R. Abgrall, O. Allix, D. Néron, & M. Kaliske (Eds.), *14th World Congress in Computational Mechanics (WCCM) and ECCOMAS Congress 2020*. (Cit. on p. 182).
- Spurk, J. H., & Aksel, N. (1989). *Strömungslehre* (Vol. 4). Springer. (Cit. on p. 10).
- Steiner, H., Jakirlic, S., Kadavelil, G., Manceau, R., Saric, S., & Brenn, G. (2009). 13th ERCOFTAC workshop on refined turbulence modelling. *ERCOFTAC Bulletin*, 79, Graz–University (cit. on p. 239).
- Stoffregen, J. (2009). *Motorradtechnik: Grundlagen und Konzepte von Motor, Antrieb und Fahrwerk*. Springer-Verlag. (Cit. on p. 33).
- Sun, T., & Teja, A. S. (2003). Density, viscosity, and thermal conductivity of aqueous ethylene, diethylene, and triethylene glycol mixtures between

-
- 290 K and 450 K. *Journal of Chemical & Engineering Data*, 48(1), 198–202 (cit. on pp. 34, 35).
- Thielen, L., Hanjalic, K., Jonker, H. J., & Manceau, R. (2005). Predictions of flow and heat transfer in multiple-impinging jets with an Elliptic-Blending second-moment closure. *International Journal of Heat and Mass Transfer*, 48(8), 1583–1598. <https://doi.org/10.1016/j.ijheatmasstransfer.2004.10.025> (cit. on p. 182)
- Tunstall, R., Laurence, D., Prosser, R., & Skillen, A. (2016). Large eddy simulation of a T-junction with upstream elbow: The role of Dean vortices in thermal fatigue. *Applied Thermal Engineering*, 107, 672–680. <https://doi.org/10.1016/j.applthermaleng.2016.07.011> (cit. on pp. 62, 90)
- Van Driest, E. R. (1956). On turbulent flow near a wall. *Journal of the Aeronautical Sciences*, 23(11), 1007–1011. <https://doi.org/10.2514/8.3713> (cit. on pp. 18, 20)
- van Basshuysen, R. (2013). *Ottomotor mit Direkteinspritzung: Verfahren, Systeme, Entwicklung, Potenzial*. Springer-Verlag. (Cit. on pp. 2, 139).
- Versteeg, H. K., & Malalasekera, W. (2007). *An introduction to computational fluid dynamics: The finite volume method*. Pearson education. (Cit. on p. 25).
- Vester, A. K., Sattarzadeh, S. S., & Örlü, R. (2016). Combined hot-wire and PIV measurements of a swirling turbulent flow at the exit of a 90-deg pipe bend. *Journal of Visualization*, 19(2)(2), 261–273. <https://doi.org/10.1007/s12650-015-0310-1> (cit. on p. 66)
- Vieira, E. R., Mansouri, A., McLaury, S. B., & Shirazi, A. S. (2016). Experimental and computational study of erosion in elbows due to sand particles in air flow. *Powder Technology*, 288, 339–353. <https://doi.org/10.1016/j.powtec.2015.11.028> (cit. on p. 63)
- Walker, C., Simiano, M., Zboray, R., & Prasser, H.-M. (2009). Investigations on mixing phenomena in single-phase flow in a T-junction geometry. *Nuclear Engineering and Design*, 239(1), 116–126 (cit. on p. 90).
- Wang, Z., Örlü, R., Schlatter, P., & Chung, Y. M. (2018). Direct numerical simulation of a turbulent 90° bend pipe flow. *International Journal of Heat and Fluid Flow*, 73, 199–208. <https://doi.org/10.1016/j.ijheatfluidflow.2018.08.003> (cit. on p. 62)

- Webb, B., & Ma, C.-F. (1995). Single-phase liquid jet impingement heat transfer. In *Advances in Heat Transfer* (pp. 105–217). Elsevier. (Cit. on p. 90).
- Wegt, S., Hartmann, J., Jakirlic, S., Tropea, C., Klink, A., Reitz, R., Engler, T., & Oechsner, M. (2020). Computational study on the erosive surface degradation in a pipe elbow by relevance to internal combustion engine cooling systems. *CORROSION 2020 Conference and Expo, Houston, TX, USA, March 15-19, NACE-2020-14801*. <https://www.onepetro.org/conference-paper/NACE-2020-14801> (cit. on p. 63)
- Wegt, S., Maduta, R., Kissing, J., & Jakirlic, S. (2002). LES-based vortical flow characterization in a 90°-turned pipe bend. *Computer and Fluids (under consideration for publication)* (cit. on pp. 3, 17, 30).
- Wizman, V., Laurence, D., Kanniche, M., Durbin, P., & Demuren, A. (1996). Modeling near-wall effects in second-moment closures by elliptic relaxation. *International Journal of Heat and Fluid Flow*, 17(3), 255–266. [https://doi.org/10.1016/0142-727X\(96\)00031-8](https://doi.org/10.1016/0142-727X(96)00031-8) (cit. on p. 182)
- Wu, X., & Moin, P. (2008). A direct numerical simulation study on the mean velocity characteristics in turbulent pipe flow. *Journal of Fluid Mechanics*, 608, 81. <https://doi.org/10.1017/S0022112008002085> (cit. on p. 38)
- Yang, G., Choi, M., & Lee, J. S. (1999). An experimental study of slot jet impingement cooling on concave surface: Effects of nozzle configuration and curvature. *International Journal of Heat and Mass Transfer*, 42(12), 2199–2209 (cit. on p. 90).
- Yang, Z., Peng, X., & Ye, P. (2008). Numerical and experimental investigation of two phase flow during boiling in a coiled tube. *International Journal of Heat and Mass Transfer*, 51(5-6), 1003–1016. <https://doi.org/10.1016/j.ijheatmasstransfer.2007.05.025> (cit. on p. 63)

Acronyms

AiF Arbeitsgemeinschaft industrieller Forschungsvereinigungen

APG adverse pressure gradient

BFS backward-facing step

BMWi Bundesministerium für Wirtschaft und Energie

CD cross-diffusion

CDS Central Difference Scheme

CFD Computational Fluid Dynamics

CS cross-section

CV control volume

DES Detached-Eddy Simulation

DNS Direct Numerical Simulation

EBM Elliptic Blending Model

EBM ω_h -based elliptic-blending-related Reynolds-stress model

ERM Elliptic Relaxation Method

FPG favorable pressure gradient

FVM Finite-Volume Method

FVV Forschungsvereinigung Verbrennungskraftmaschinen

GGDH General Gradient Diffusion Hypothesis

IC Internal Combustion

IISRSM Improved Instability Sensitive Reynolds Stress Model

ISEBM Instability-Sensitive Elliptic-Blending-related Reynolds Stress Model

LES Large-Eddy Simulation

MHTA Modulare Heißtestanlage

MEG monoethylene glycol

MPA-IfW Center for Structural Materials

MRV Magnetic Resonance Velocimetry

OEM original equipment manufacturers

pH potentia hydrogenii

RANS Reynolds-Averaged Navier-Stokes

RSM Reynolds Stress Model

SA Spalart Allmaras

SAE Society of Automotive Engineers

SAS Scale Adaptive Simulation

SGDH Simple Gradient Diffusion Hypothesis

SMC Second-Moment Closure

SST Shear Stress Transport

SLA Strömungslehre- und Aerodynamik

SGS subgrid-scale

UDS Upwind Difference Scheme

vc vortex center

WALE Wall-Adapting Local Eddy-viscosity

WSG Water Spider Geometry

List of Symbols - Latin letters

Symbol	Description	Unit
a	Distance between vortex centers	m
a_E	Linear equation system prefactor of node 'E'	—
a_{ij}	Invariants of the Reynolds-stress anisotropy tensor	—
a_N	Linear equation system prefactor of node 'N'	—
a_P	Linear equation system prefactor of node 'P'	—
a_S	Linear equation system prefactor of node 'S'	—
a_W	Linear equation system prefactor of node 'W'	—
A	Two-componentality parameter of the energy-containing turbulent scale motion	—
A^+	Van Driest model constant	—
A_{vortex}	Cross-sectional area of vortex tube	m ²
A_2	Second invariant of the energy-containing turbulent scale motion	—
A_3	Third invariant of the energy-containing turbulent scale motion	—
b	Channel width	m
b_{ij}	Reynolds stress anisotropy tensor	—
b_P	Linear equation system prefactor (explicit) of node 'P'	—
B	Constant of logarithmic law	—
c	Midpoint of faces	—
C	Nodes	—
$C_{CD,1}$	Viscous cross diffusion constant	—

Symbol	Description	Unit
$C_{CD,2}$	Turbulent cross diffusion constant	—
C_f	Friction coefficient	—
$C_{f,\varphi}$	Friction coefficient in circumferential direction (reverse T-junction).	—
$C_{f,\psi}$	Friction coefficient in circumferential direction (T-junction)	—
$C_{f,y}$	Friction coefficient in inlet direction (reverse T-junction)	—
$C_{f,z}$	Friction coefficient in outlet direction (T-junction)	—
C_k	Smagorinsky model constant	—
C_L	Model constant of turbulent lengthscale	—
C_p	Pressure coefficient	—
C_s	Smagorinsky constant	—
$C_{SAS,1}$	SAS constant 1	—
$C_{SAS,2}$	SAS constant 2	—
C_T	Model constant of turbulent timescale	—
C_w	WALE model constant	—
C_ε	Smagorinsky model constant	—
C_λ	Model constant of Taylor micro scale	—
C_η	Model constant of Kolmogorov lengthscale	—
C_μ	Model constant of turbulent viscosity	—
$C_{\omega,1}$	Production constant of specific homogeneous dissipation rate	—
$C_{\omega,2}$	Dissipation constant of specific homogeneous dissipation rate	—
$C_{\omega,3}$	Gradient production constant of specific homogeneous dissipation rate	—
C_1	Model constant within the high-Reynolds number pressure-redistribution proposed by Speziale et al. (1991)	—
C_{1s}	Model constant within the high-Reynolds number pressure-redistribution proposed by Speziale et al. (1991)	—

Symbol	Description	Unit
C_2	Model constant within the high-Reynolds number pressure-redistribution proposed by Speziale et al. (1991)	—
C_3	Model constant within the high-Reynolds number pressure-redistribution proposed by Speziale et al. (1991)	—
C_{3s}	Model constant within the high-Reynolds number pressure-redistribution proposed by Speziale et al. (1991)	—
C_4	Model constant within the high-Reynolds number pressure-redistribution proposed by Speziale et al. (1991)	—
C_5	Model constant within the high-Reynolds number pressure-redistribution proposed by Speziale et al. (1991)	—
Co	Courant number	—
D	Pipe diameter	m
D_{ij}	Diffusion of Reynolds stress tensor	m^2/s^3
D_{ij}^p	Pressure diffusion of Reynolds stress tensor	m^2/s^3
D_{ij}^t	Turbulent diffusion of Reynolds stress tensor	m^2/s^3
D_{ij}^ν	Molecular diffusion of Reynolds stress tensor	m^2/s^3
D_{outer}	Outer pipe diameter of Water Spider Geometry (WSG)	m
$D_{\omega^h}^t$	Turbulent diffusion of homogeneous specific dissipation rate	$1/\text{s}^2$
De	Dean number	—
De_{crit}	Critical Dean number	—
e	East-sided face midpoint	—
e_{ij}	Stress-dissipation anisotropy	—
E	Two-componentality parameter of the small-scale dissipative motion	—
E	East-sided node	—

List of Symbols - Latin letters

Symbol	Description	Unit
$E(\kappa_{\text{eddy}})$	Energy of turbulent eddies with wavenumber κ_{eddy}	m^2/s^2
E_2	Second invariant of the small-scale dissipative motion	—
E_3	Third invariant of the small-scale dissipative motion	—
f	Sum of volume forces of scalar field ϕ	—
f	Elliptic relaxation function	—
f_{ij}	Elliptic relaxation tensor	—
f_s	Blending function of dissipation tensor	—
f_Φ	Elliptic relaxation function	—
h	Characteristic domain height	m
I_i	Momentum balance of the Navier-Stokes equation	m/s^2
\bar{I}_i	Momentum balance of the Reynolds-Averaged Navier-Stokes (RANS) equations	m/s^2
I'_i	Momentum balance of the fluctuations	m/s^2
k	Turbulent kinetic energy	m^2/s^2
k^+	Dimensionless turbulent kinetic energy	—
k_{mod}	Modelled part of turbulent kinetic energy	m^2/s^2
k_{SGS}	Subgrid-Scale (SGS) part of turbulent kinetic energy	m^2/s^2
k_{total}	Total turbulent kinetic energy	m^2/s^2
l	Turbulent eddy length	m
l_{inlet}	Inlet pipe length	m
l_{outlet}	Outlet pipe length	m
l_{pre}	Precursor length	m
l_{WSG}	Sample disc diameter	m
$l_{\text{WSG,inlet}}$	Inlet pipe length upstream of the Water Spider Geometry (WSG)	m

Symbol	Description	Unit
$l_{\text{WSG,necking}}$	Necking length within Water Spider Geometry (WSG) sample holder	m
$l_{\text{WSG,outlet}}$	Outlet pipe length downstream of the Water Spider Geometry (WSG)	m
l_0	Characteristic length of the largest eddies	m
L	Lengthscale of turbulent eddies	m
L^*	Lengthscale of turbulent diffusion model approach	m
\vec{L}	Summarized right-hand side of transport equations of arbitrary scalar function	m
\mathcal{L}	Characteristic lengthscale	m
L_{ij}	Difference of subtest-scale stress tensor and subgrid-scale stress tensor	m^2/s^3
L_L	Turbulent lengthscale	m
L_α	Lengthscale of turbulent eddies within the elliptic function	m
L_η	Lengthscale of the smallest eddies	m
L_λ	Taylor lengthscale	m
L_{ν_t}	Lengthscale of turbulent viscosity model approach	m
\dot{m}_c	Mass flux through face 'c'	kg/s
\vec{M}	Point	m
n	North-sided face midpoint	—
n_c	Normal vectors on the faces of a control volume	—
n_{cores}	Total number of computer cores	—
n_{cs}	Number of grid cells within the pipe cross-section	—
n_i	Wall normal vector	—
n_{total}	Total number of grid cells	—
N	Number of control volumes	—
N	North-sided node	—
p	pressure	$\text{kg}/\text{m}/\text{s}^2$

List of Symbols - Latin letters

Symbol	Description	Unit
\bar{p}	Time-averaged pressure	kg/m/s ²
\tilde{p}	Spatial-filtered pressure	kg/m/s ²
p_{mean}	Cross-sectional mean pressure	kg/m/s ²
p_{outlet}	Outlet pressure	kg/m/s ²
P	Node	—
P_{ij}	Production of Reynolds stress components	m ² /s ³
P_k	Production of turbulent kinetic energy	m ² /s ³
P_{SAS}	SAS production term	1/s ²
$P_{\varepsilon,3}$	Gradient production term of dissipation rate	m ² /s ⁴
$P_{\omega,3}$	Gradient production term of specific dissipation rate	1/s ²
\dot{Q}	Heat flux	W
r	Radial position	m
r_{sbr}	Radial distance from vortex center	m
r_{vc}	Radial position of vortex center	m
r_{vortex}	Radius of vortex tube	m
R	Pipe radius	m
R_{block}	Inner block radius	m
R_c	Curvature of deflection/90°-pipe bend	m
R_{inner}	Inner radius of (reverse) T-junction	m
R_{max}	Maximum forebody radius	m
R_{sp}	Radial position of saddle point	m
Re	Reynolds number	—
Re _b	Bulk Reynolds number	—
Re _{deflection}	Bulk Reynolds number within the Water Spider Geometry (WSG) deflections	—
Re _h	Height-related Reynolds number	—
Re _{outer}	Bulk Reynolds number of the outer Water Spider Geometry (WSG) section	—
Re _t	Turbulent Reynolds number	—
Re _y	Wall-distance-based turbulent Reynolds number	—
Re _Γ	Circulation-related Reynolds number	—

Symbol	Description	Unit
Re_{Θ}	Momentum-thickness-related Reynolds number	—
Re_{τ}	Friction Reynolds number	—
$Re_{\tau,DNS}$	Friction Reynolds number of reference Direct Numerical Simulation (DNS)	—
$Re_{\tau,EBM}$	Friction Reynolds number predicted by ω_h -based elliptic-blending-related Reynolds-stress model (EBM)	—
Re_0	Characteristic Reynolds number of the largest eddies	—
Re_{∞}	Farfield Reynolds number	—
$(R - r)^+$	Dimensionless wall distance within a pipe configuration	—
s	South-sided face midpoint	—
s_{inner}	Inner coordinate of the Water Spider Geometry (WSG)	m
s_{inner}^*	Normalized inner coordinate of the Water Spider Geometry (WSG)	—
s_{rTJ}	Outlet coordinate of reverse T-junction	m
s_{rTJ}^*	Normalized outlet coordinate of reverse T-junction	—
s_{TJ}	Outlet coordinate of T-junction	m
s_{TJ}^*	Normalized outlet coordinate of T-junction	—
$s_{WSG,in}$	Coordinate within the Water Spider Geometry (WSG) inlet section	m
$s_{WSG,in}^*$	Dimensionless coordinate within the Water Spider Geometry (WSG) inlet section	—
$s_{WSG,out}$	Coordinate within the Water Spider Geometry (WSG) outlet section	m
$s_{WSG,out}^*$	Dimensionless coordinate within the Water Spider Geometry (WSG) outlet section	—
S	Surface area	m ²
S	South-sided node	—

List of Symbols - Latin letters

Symbol	Description	Unit
S_c	Surface of face 'c'	m^2
S_{ij}	Rate of strain tensor	1/s
\bar{S}_{ij}	Mean rate of strain tensor	1/s
\tilde{S}_{ij}	Spatial-filtered rate of strain tensor	1/s
\hat{S}_{ij}	Test-filtered spatial-filtered rate of strain tensor	1/s
S_{ij}^d	Traceless symmetric part of the square of the velocity gradient tensor	1/s
t	Time	s
t^n	Discrete moments	s
T	Timescale of turbulent eddies	s
T_{ij}	Subtest-scale stress tensor	m^2/s^3
T_{inlet}	Inlet temperature	K
u	Streamwise velocity	m/s
u^+	Dimensionless streamwise velocity	—
\bar{u}^+	Root mean square of dimensionless streamwise Reynolds stress component	—
u_{cr}	Curvature-radial velocity	m/s
u_n	Wall-normal velocity	m/s
\bar{u}_r^+	Root mean square of dimensionless radial Reynolds stress component	—
\bar{u}_{RMS}	Root mean square of streamwise Reynolds stress component	—
u_{sbr}	Circumferential velocity around vortex center	m/s
u_t	Wall-tangential velocity	m/s
\vec{u}_{vortex}	Self-induced velocity	m/s
u_y	Velocity in inlet direction (reverse T-junction)	m/s
u_z	Streamwise velocity	m/s
$u_{z,RMS}$	Root mean square of streamwise Reynolds stress component	m/s
\bar{u}_z^+	Root mean square of dimensionless streamwise Reynolds stress component	—
u_η	Kolmogorov velocity scale	m/s
u_0	Characteristic velocity of the largest eddies	m/s

Symbol	Description	Unit
u_τ	Friction velocity	m/s
$\overline{u_\varphi^+}$	Root mean square of dimensionless circumferential Reynolds stress component	—
$u(l)$	Turbulent eddy velocity	m/s
$\overline{u\bar{u}}$	Streamwise Reynolds stress component	m^2/s^2
$\overline{u_i u_j}$	Reynolds stress tensor	m^2/s^2
$\overline{u_i u_j^+}$	Dimensionless Reynolds stress tensor	—
$\overline{u_r u_r^+}$	Dimensionless radial Reynolds stress component	—
$\overline{u_r u_z^+}$	Dimensionless shear Reynolds stress component within a pipe configuration	—
$\overline{u_z u_z^+}$	Dimensionless streamwise Reynolds stress component	—
$\overline{u_\varphi u_\varphi^+}$	Dimensionless circumferential Reynolds stress component	—
$\overline{w\bar{v}}$	Shear Reynolds stress component	m^2/s^2
$\overline{w\bar{v}^+}$	Dimensionless shear Reynolds stress component	—
U	Velocity magnitude	m/s
\mathcal{U}	Characteristic velocity scale	m/s
U_b	Bulk velocity	m/s
$U_{b,\text{outer}}$	Bulk velocity of the outer Water Spider Geometry (WSG) section	m/s
U_i	Velocity vector	m/s
$\overline{U_i}$	Time-averaged velocity vector	m/s
$\widetilde{U_i}$	Spatially-filtered velocity vector	m/s
U_{inflow}	Mean inflow velocity	m/s
U_∞	Farfield velocity	m/s
v	Velocity component in y -direction	m/s
$\overline{v^+}$	Root mean square of dimensionless wall-normal Reynolds stress component	—
$\overline{v^2}$	Wall-normal Reynolds stress component	m^2/s^2
$\overline{v\bar{v}}$	Wall-normal Reynolds stress component	m^2/s^2
V	Volume	m^3
\dot{V}	Volume flux	m^3/s

List of Symbols - Latin letters

Symbol	Description	Unit
V_{cell}	Cell volume	m^3
w	Velocity component in z -direction.	m/s
w	West-sided face midpoint	—
\bar{w}^+	Root mean square of dimensionless spanwise Reynolds stress component	—
\overline{ww}	Wall-tangential Reynolds stress tensor	m^2/s^2
W	West-sided node	—
x	Streamwise coordinate	m
x^+	Dimensionless streamwise cell size	—
x_e	East-sided face-midpoint position	m
x_E	East-sided node position	m
x_i	Location vector	m
x_n	Normal-to-the-wall coordinate	m
x_P	Node position 'P'	m
y	Normal wall distance	m
y^+	Dimensionless wall distance	—
y_{bend}	Coordinate within the 90° -pipe bend	m
y_{bend}^*	Dimensionless coordinate within the 90° -pipe bend	—
y_{max}	Maximal edge length in height direction	—
y_{wall}	Wall distance of the wall-adjacent computational node	m
y_{rTJ}	Coordinate within the reverse T-junction	m
y_{rTJ}^*	Dimensionless coordinate within the reverse T-junction	—
y_{TJ}	Coordinate within the T-junction	m
y_{TJ}^*	Dimensionless coordinate within the T-junction	—
z	Spanwise position	m
z_{bend}	Coordinate within the 90° -pipe bend	m
z_{bend}^*	Dimensionless coordinate within the 90° -pipe bend	—

Symbol	Description	Unit
z_{\max}	Maximal edge length in width direction	m

List of Symbols - Greek letters

Symbol	Description	Unit
α	Elliptic blending function	—
α_{Diff}	Diffusion coefficient	m^2/s
α_{right}	Right-sided opening angle	$^\circ$
α_{top}	Top-sided opening angle	$^\circ$
α_ϕ	Under relaxation factor of ϕ	—
β	Blending factor of Reynolds-stress tensor blend	—
β_{flux}	Flux blending factor	—
β_{max}	Maximum blending factor of Reynolds-stress tensor	—
γ_e	East-sided interpolation factor	—
Γ	Vorticity	m^2/s
Γ_{Dean}	Vorticity of the Dean vortex	m^2/s
Γ_{sbr}	Vorticity of vortex tube	$1/\text{s}$
Γ_1	Scalar field according to Graftieaux et al. (2001)	—
Γ_2	Scalar field according to Graftieaux et al. (2001)	—
δ_{ij}	Kronecker delta	—
δS_c	c-sided face length of control volume (CV)	m
δV	Volume of control volume (CV)	m^3
Δ	Filter width	m
$\hat{\Delta}$	Subtest-scale filter width	m
Δ_{filter}	Filter width	m
Δ_{max}	Maximal cell width	m
Δ_{SGS}	Filter width	m

Symbol	Description	Unit
Δr^+	Dimensionless radial cell size	—
Δr_{\min}^+	Minimal dimensionless radial cell size	—
$\Delta r_{\min}^+, \dots, \max$	Min/max dimensionless radial cell size	—
ΔRe	Reynolds number difference	—
Δt^n	Temporal distance	s
ΔT	Observed time interval	s
Δz^+	Dimensionless streamwise cell size	—
$\Delta \varphi^+$	Dimensionless circumferential cell size	—
ε	Dissipation of the smallest eddies	m^2/s^3
ε^h	Homogeneous part of dissipation of the smallest eddies	m^2/s^3
ε^+	Dimensionless dissipation of the smallest eddies	—
$\varepsilon^{h,+}$	Dimensionless homogeneous part of dissipation of the smallest eddies	—
ε_{ij}	Viscous dissipation of Reynolds stress components	m^2/s^3
ε_{ij}^h	Homogeneous fraction of viscous dissipation of Reynolds stress components	m^2/s^3
ε_{res}	Resolved part of dissipation of smallest eddies	m^2/s^3
ε_{SGS}	Subgrid-Scale (SGS) part of dissipation of smallest eddies	m^2/s^3
ζ	Normalized wall-normal Reynolds stress component	—
η	Kolmogorov lengthscale	m
ϑ	Characteristic velocity scale	m/s
θ_i	Fluctuating part of arbitrary flow quantity	—
θ'_i	Residual/Subgrid-Scale (SGS) part of arbitrary flow quantity	—
Θ_i	Arbitrary flow quantity	—
$\bar{\Theta}_i$	Time-averaged arbitrary flow quantity	—
$\tilde{\Theta}_i$	Spatially-filtered arbitrary flow quantity	—

Symbol	Description	Unit
Θ_M	Angle	$^\circ$
κ	Von Karaman constant	—
κ_{eddy}	Wavenumber of turbulent eddies	m
λ	Flow characteristic ratio	—
μ	Dynamic viscosity	kg/m/s
ν	Kinematic viscosity	m ² /s
ν^*	Turbulent viscosity within the diffusion model approach of EBM	m ² /s
ν_{SGS}	Subgrid-Scale (SGS) viscosity	m ² /s
ν_t	Turbulent viscosity	m ² /s
ϱ	Density	kg/m ³
σ	Model constant of diffusion approach	—
τ	Characteristic time scale	s
$\tau_{\text{SGS},ij}$	Subgrid-Scale (SGS) stress tensor	m ² /s ²
τ_w	Wall shear stress	kg/m/s ²
$\tau_{w,y}$	Wall shear stress in inlet direction (reverse T-junction)	kg/m/s ²
τ_η	Kolmogorov timescale	s
ϕ	Arbitrary scalar field	—
ϕ_c	Face-midpoint value of an arbitrary scalar field	—
ϕ_C	Node value of an arbitrary scalar field	—
ϕ_e	East-sided face-midpoint value of an arbitrary scalar field	—
$\vec{\phi}$	Sum of unknown arbitrary scalar functions	—
φ_{bend}	Angle coordinate within the 90°-pipe bend	$^\circ$
φ_{rTJ}	Inlet angle coordinate within the reverse T-junction	$^\circ$

Symbol	Description	Unit
φ_{TJ}	Inner radius angle coordinate within the T-junction	$^{\circ}$
$\varphi_{WSG,out}$	Inner radius angle coordinate within the Water Spider Geometry (WSG)	$^{\circ}$
Φ_{ij}	Pressure redistribution of Reynolds stress components	m^2/s^3
Φ_{ij}^h	High Reynolds number pressure redistribution formulation of Reynolds stress components	m^2/s^3
Φ_{ij}^w	Wall-related pressure redistribution formulation of Reynolds stress components	m^2/s^3
$\Phi_{ij}^{Manceau}$	Wall-related pressure redistribution formulation according to Manceau and Hanjalić (2002)	m^2/s^3
$\Phi_{ij}^{Jakirlic}$	Pressure redistribution formulation according to Jakirlić (1997)	m^2/s^3
ψ_{bend}	Cross-sectional pipe angle coordinate within the 90°-pipe bend	$^{\circ}$
ψ_{rTJ}	Cross-sectional pipe angle coordinate within the reverse T-junction	$^{\circ}$
ψ_{TJ}	Cross-sectional pipe angle coordinate within the T-junction	$^{\circ}$
$\psi_{WSG,in}$	Cross-sectional pipe angle coordinate within the Water Spider Geometry (WSG) inlet section	$^{\circ}$
ω	Specific dissipation rate	$1/s$
ω^h	Homogeneous part of the specific dissipation rate	$1/s$
ω_{total}^h	Total amount of homogeneous part of the specific dissipation rate	$1/s$
ω_{wall}^h	Wall limit of homogeneous part of the specific dissipation rate	$1/s$
Ω_{ij}	Rate of vorticity tensor	$1/s$
$\widetilde{\Omega}_{ij}$	Spatial-filtered rate of vorticity tensor	$1/s$
Ω_{sbr}	Rotation rate of vortex tube	$1/s$

List of Indices - subscripted

Index	Description
(·) _b	Bulk
(·) _{bend}	Related to 90°-pipe bend
(·) _{block}	Related to inner block of a 'O'-grid arrangement
(·) _c	Face of a cell
(·) _c	Curvature of deflection
(·) _{cell}	Cell of a computational grid
(·) _{cores}	Computer cores
(·) _{cr}	Curvature radial
(·) _{crit}	Critical
(·) _{cs}	Cross-section
(·) _{CD}	Cross-diffusion
(·) _{deflection}	Related to deflection
(·) _{Dean}	Related to Dean vortex
(·) _{Diff}	Diffusion
(·) _{DNS}	Direct Numerical Simulation
(·) _e	East-sided face midpoint
(·) _{eddy}	Related to turbulent eddies
(·) _E	East-sided node to node 'P'
(·) _f	Friction
(·) _{filter}	Related to filter procedure of LES framework
(·) _{flux}	Flux of a fluid mechanical quantity
(·) _h	Domain height
(·) _{in}	Related to inlet section of a computational domain
(·) _{inlet}	Related to inlet section of a computational domain

Index	Description
$(\cdot)_{\text{inner}}$	Related to inner radius of (reverse) T-junction
$(\cdot)_k$	Related to turbulent kinetic energy
$(\cdot)_L$	Related to turbulent properties
$(\cdot)_{\text{max}}$	Maximal
$(\cdot)_{\text{mean}}$	Mean over cross-section
$(\cdot)_{\text{min}}$	Minimum
$(\cdot)_n$	Wall-normal
$(\cdot)_{\text{necking}}$	Related to necking section of a computational domain
$(\cdot)_N$	North-sided node to node 'P'
$(\cdot)_{\text{out}}$	Related to outlet section of a computational domain
$(\cdot)_{\text{outer}}$	Related to outer region of a computational domain
$(\cdot)_{\text{outlet}}$	Related to outlet section of a computational domain
$(\cdot)_p$	Pressure
$(\cdot)_{\text{pre}}$	Related to precursor section of a computational domain
$(\cdot)_P$	Center node 'P'
$(\cdot)_r$	Radial
$(\cdot)_{\text{res}}$	Resolved part
$(\cdot)_{\text{rTJ}}$	Related to reverse T-junction
$(\cdot)_{\text{right}}$	Right-sided
$(\cdot)_{\text{RMS}}$	Root Mean Square
$(\cdot)_s$	Smagorinsky
$(\cdot)_{\text{sbr}}$	Solid body rotation
$(\cdot)_{\text{sp}}$	Saddle point
$(\cdot)_S$	South-sided node to node 'P'
$(\cdot)_{\text{SGS}}$	Subgrid-scale
$(\cdot)_t$	Turbulent
$(\cdot)_{\text{top}}$	Top-sided
$(\cdot)_{\text{total}}$	Total number
$(\cdot)_T$	Related to turbulent quantities
$(\cdot)_{\text{TJ}}$	Related to T-junction

Index	Description
$(\cdot)_{vc}$	Vortex center
$(\cdot)_{vortex}$	Vortex tube-related quantity
$(\cdot)_w$	Related WALE SGS model
$(\cdot)_{wall}$	Related to wall
$(\cdot)_W$	West-sided node to node 'P'
$(\cdot)_{WSG}$	Water spider geometry
$(\cdot)_y$	Wall distance
$(\cdot)_\alpha$	Related to elliptic function
$(\cdot)_\Gamma$	Circulation
$(\cdot)_{\Gamma_1}$	Related to Γ_1 scalar field
$(\cdot)_\varepsilon$	Dissipation rate
$(\cdot)_\eta$	Related to Kolmogorov lengthscale
$(\cdot)_\Theta$	Momentum thickness
$(\cdot)_\lambda$	Related to Taylor micro scale
$(\cdot)_\mu$	Related to turbulent viscosity
$(\cdot)_\tau$	Wall shear stress
$(\cdot)_\phi$	Related to scalar field ϕ
$(\cdot)_\Phi$	Pressure redistribution
$(\cdot)_\omega$	Related to specific dissipation rate
$(\cdot)_\infty$	Farfield

List of Indices - superscripted

Index	Description
$(\cdot)^h$	Homogeneous part
$(\cdot)^n$	Temporal iteration
$(\cdot)^t$	Turbulent
$(\cdot)^w$	Wall
$(\cdot)^*$	Normalized by pipe diameter or related to turbulent diffusion approach
$(\cdot)^+$	Normalized by u_τ

List of Figures

1.1. Schematic illustration of the straight pipe reference test sample (left) and the newly designed reference test sample, denoted as Water Spider Geometry (WSG) (right). Both illustrations are published in Wegst et al. (2002).	3
1.2. Cooling channel configurations in the cylinder head of a realistic internal combustion engine accommodating the valve seat rings according to Reustle (2012) (United States Patent No. US 8,151,743 B2). Interested readers are referred to the original reference (downloadable from https://patents.google.com/patent/US8151743B2) for the explanation of individual positions.	4
2.1. Schematic illustration of the energy spectrum with the eddy energy $E(\kappa_{\text{eddy}})$ depicted over the eddy wave number $\kappa_{\text{eddy}} = 2\pi/l$	12
2.2. Schematic illustration of a simplified, quadrilateral two-dimensional grid with a homogeneous distribution and a cell-orientated arrangement of nodes with the considered cell volume (CV) highlighted in gray. The node and face denotation follows the labeling of a compass.	22
3.1. Schematic illustrations of the WSG, left: sample half with the individual geometries color-coded, right: spatial dimensions of the WSG including inlet section and outlet section. The associated dimensions are listed in Table 3.1.	32

3.2. Thermal response of the dynamic viscosity μ (top) and density ρ (bottom) of MEG/water 50/50 vol.% (squares) according to Sun and Teja (2003). For the interpolation of the experimental data, a polyfit (black solid line) is applied to capture the relevant fluid properties at the reference point $T_{\text{inlet}} = 115 \text{ }^\circ\text{C}$ (red dotted line). 34

3.3. Schematic of the grid structure of a pipe flow configuration according to the so-called *O*-grid arrangement with an octagon-shaped central block. 39

3.4. Computationally obtained friction Reynolds number in relation to its reference DNS value $\text{Re}_\tau/\text{Re}_{\tau,\text{DNS}}$ (top) and calculation time used in relation to calculation time required for the radius ratio $R_{\text{block}}/R = 0.5$ (bottom) over the inner block size ratio R_{block}/R for the pipe flow over the considered Reynolds number range. 41

3.5. Semi-log profiles of the non-dimensional streamwise velocity u^+ (top) as well as the non-dimensional turbulent kinetic energy k^+ and $\overline{u_\tau u_z^+}$ (bottom) over the non-dimensional wall distance $(R - r)^+$ for different inner block size ratios R_{block}/R for $\text{Re}_\tau = 360$ compared to the reference DNS data by El Khoury et al. (2013). 42

3.6. Computationally obtained friction Reynolds number in relation to its reference DNS value $\text{Re}_\tau/\text{Re}_{\tau,\text{DNS}}$ over the streamwise-to-spanwise grid-cell ratio $\Delta z^+/\Delta \varphi^+$ for the pipe flow over the considered Reynolds number range. 44

3.7. Semi-log profile of the non-dimensional streamwise velocity u^+ (top) as well as non-dimensional turbulent kinetic energy k^+ and $\overline{u_\tau u_z^+}$ (bottom) over the non-dimensional wall distance $(R - r)^+$ for different streamwise-to-spanwise grid-cell ratios $\Delta z^+/\Delta \varphi^+$ for $\text{Re}_\tau = 360$ compared to the reference DNS data by El Khoury et al. (2013). 45

3.8. Computationally obtained friction Reynolds number in relation to its reference DNS value $\text{Re}_\tau/\text{Re}_{\tau,\text{DNS}}$ for different non-dimensional pipe section lengths l_{pre}/D for the pipe flow over the considered Reynolds number range. 46

3.9. Semi-log profile of the non-dimensional streamwise velocity u^+ (top) as well as non-dimensional turbulent kinetic energy k^+ and $\overline{u_r u_z}^+$ (bottom) over the non-dimensional wall distance $(R - r)^+$ for different non-dimensional pipe section lengths l_{pre}/D for $\text{Re}_\tau = 360$ compared to the reference DNS data by El Khoury et al. (2013). 47

3.10. Semi-log profiles of the non-dimensional streamwise velocity u^+ over the non-dimensional wall distance $(R - r)^+$ for $\text{Re}_\tau = 360$ predicted by different SGS models - **WALE**, **Smagorinsky** and **dynamic Smagorinsky** models - compared with reference DNS data by El Khoury et al. (2013). In the case of the WALE model, the solid line and the dash-dotted line represent the results obtained at the fine grid by using the constant values $C_w = 0.325$ and $C_w = 0.5$, respectively; the dotted line relates to the coarse-grid LES performed with $C_w = 0.325$ 49

3.11. Semi-log profiles of the non-dimensional Reynolds stress components $\overline{u_i u_j}^+$ over non-dimensional wall distance $(R - r)^+$ for $\text{Re}_\tau = 360$ predicted by different SGS models - **WALE**, **Smagorinsky** and **dynamic Smagorinsky** models - compared with reference DNS data by El Khoury et al. (2013). See caption of Fig. 3.10 for further information. 50

3.12. Semi-log profiles of the non-dimensional dissipation rate ε^+ over non-dimensional wall distance $(R - r)^+$ for $\text{Re}_\tau = 360$ predicted by different SGS models - **WALE**, **Smagorinsky** and **dynamic Smagorinsky** models - compared with reference DNS data by El Khoury et al. (2013). See caption of Fig. 3.10 for further information. 52

3.13. Modeled-to-total turbulence kinetic energy ratio k_{SGS}/k (top) and modeled-to-total dissipation rate ratio $\varepsilon_{\text{SGS}}/\varepsilon$ (bottom) over non-dimensional wall distance $(R - r)^+$ for $\text{Re}_\tau = 360$ characterizing the results obtained by different SGS models (**WALE**, **Smagorinsky** and **dynamic Smagorinsky**). 53

3.14. Profiles of the ratio $\Delta_{\text{filter}}/\eta$ (top) and Δ_{max}/η (bottom) over the non-dimensional wall distance $(R-r)^+$ for $\text{Re}_\tau = 360$ characterizing the results obtained by different SGS models (WALE, Smagorinsky and dynamic Smagorinsky). See caption of Fig. 3.10 for further information. 54

3.15. Normalized energy spectrum of the streamwise velocity component $E(\kappa_{\text{eddy}})/(\varepsilon\nu^5)^{1/4}$ over normalized wavenumber $\kappa_{\text{eddy}}\eta$ for $\text{Re}_\tau = 360$ characterizing the results obtained by different SGS models (WALE, Smagorinsky and dynamic Smagorinsky). See caption of Fig. 3.10 for further information. 55

3.16. Semi-log plot of the non-dimensional streamwise velocity component u^+ (top left), non-dimensional Reynolds stress components $\overline{u_i u_j}^+$ (bottom left & right) and viscous dissipation rate of the turbulent kinetic energy ε^+ (top right) over non-dimensional wall distance $(R-r)^+$ for the Reynolds numbers $\text{Re}_{\text{deflection}} = 7200, 10500$ and 14000 , respectively, friction Reynolds numbers $\text{Re}_\tau = 238, 331$ and 428 59

3.17. Modeled-to-total turbulent kinetic energy ratio k_{SGS}/k (top left), modeled-to-total viscous dissipation rate ratio $\varepsilon_{\text{SGS}}/\varepsilon$ (top right) and ratio Δ_{max}/η over the non-dimensional wall distance $(R-r)^+/\text{Re}_\tau$ (bottom left) for the Reynolds numbers $\text{Re}_{\text{deflection}} = 7200, 10500$ and 14000 , respectively, friction Reynolds numbers $\text{Re}_\tau = 238, 331$ and 428 . The normalized energy spectrum of the streamwise velocity component $E(\kappa_{\text{eddy}})/(\varepsilon\nu^5)^{1/4}$ over normalized wavenumber $\kappa_{\text{eddy}}\eta$ are also depicted for the considered Reynolds numbers (bottom right). 60

3.18. Schematic illustration of the computational domain including the main and precursor regions as well as the dimensionless coordinates $y_{\text{bend}}^* = y_{\text{bend}}/D$, φ_{bend} and $z_{\text{bend}}^* = z_{\text{bend}}/D$ 64

3.19. Streamwise velocity u_z/U_b and turbulence intensity $u_{z,\text{RMS}}/U_b$ at $z_{\text{bend}}^* = z_{\text{bend}}/D = 0.67$ and 1.5 for $\text{Re}_b = 14000$ compared to the experimental data by Kalpakli Vester et al. (2016) and Sattarzadeh Shirvan (2011). 66

-
- 3.20. Time-averaged velocity magnitude U/U_b (upper or left) and turbulent kinetic energy k/U_b^2 (lower or right) within the $y - z$ -symmetry plane and selected cross-sections for $Re_b = 7200$. The visualized data are derived from averaging over the symmetry planes. 68
- 3.21. Time-averaged streamwise u_z/U_b and curvature-radial u_{cr}/U_b velocity at selected positions within the $y - z$ -symmetry plane (top) and in the perpendicular plane, which coincides with the pipe symmetry axis $r/R = 0$ (bottom) for the considered Reynolds numbers. The spatial evolution of the vortex centers are presented by symbols and the pipe bend region is highlighted in gray. The pipe center is marked by a red dash-dotted line. 70
- 3.22. Time-averaged iso-contours of the pressure coefficient $C_p = (p - p_{\text{mean}})/(0.5 \rho U_b^2)$ (left half) and velocity magnitude U/U_b (right half) with the streamlines within the pipe bend at $\varphi_{\text{bend}} = 60^\circ$ (top) and $z_{\text{bend}}^* = 1.5$ (bottom) for $Re_b = 7200$. p_{mean} is the mean pressure within the cross-section. The visualized data are derived from averaging over the symmetry planes. 75
- 3.23. Distribution of the surface pressure coefficient ($C_p = (p - p_{\text{mean}})/(0.5 \rho U_b^2)$) on the side pipe bend wall over the circumferential angle range from $\psi_{\text{bend}} = -90^\circ$ (corresponding to inner wall radius $r/R = -1$) to $\psi_{\text{bend}} = 90^\circ$ (corresponding to outer wall radius $r/R = 1$) for selected deflection angles φ_{bend} between $0^\circ - 90^\circ$ for the three Reynolds numbers considered. p_{mean} is the mean pressure averaged over the corresponding cross-section. 76
- 3.24. Development of the friction coefficient $C_f = \tau_w/(0.5 \rho U_b^2)$ at the inner ($\psi_{\text{bend}} = -90^\circ$; solid lines) and outer ($\psi_{\text{bend}} = 90^\circ$, dashed lines) deflection radius within the pipe bend for all three considered Reynolds numbers. 78
- 3.25. Time-averaged turbulent kinetic energy k/U_b^2 (left half) and velocity magnitude U/U_b (right half) with the streamlines at the location $z_{\text{bend}}^* = 0.5$ for $Re_b = 7200$. The vortex center is highlighted by magenta-colored symbols. The visualized data are derived from averaging over the symmetry planes. 80
-

3.26. Time-averaged turbulent kinetic energy k/U_b^2 at selected positions within the $y - z$ -symmetry plane (top) and in the plane perpendicularly, which coincides with the pipe symmetry axis $r/R = 0$ (bottom) for considered Reynolds numbers. The spatial evolution of the vortex centers are presented by symbols and the pipe bend region is highlighted in gray. The pipe center is marked by a red dash-dotted line. 81

3.27. Vorticity Γ_{Dean} (solid line) and a normlized vorticity by bulk velocity Γ_{Dean}/U_b (dotted line) of the Dean vortex (top) and vortex Reynolds number to Dean number ratio Re_F/De (bottom) depicted over the deflection angle φ_{bend} and the outlet coordinate z_{bend}^* for the considered Reynolds numbers (color-coded). The spatial life-cycle of the secondary vortex structures are highlighted in gray. 85

3.28. Illustration of the computational domain ($y - z$ - and $z - x$ -symmetry plane) including the T-junction and precursor region. R describes the pipe radius, R_c the radius of the rounded inner radius and φ_{TJ} its angle, $l_{\text{inlet}} = l_{\text{outlet}} = 8 D$ the inlet and outlet length, $l_{\text{pre}} = 2.5 D$ the precursor length, ψ_{TJ} the outlet angle and s_{TJ}^* its coordinate. 93

3.29. Block-structured hexahedral grid of the T-junction. Only every fourth cell is shown to highlight the grid structure. 94

3.30. Time-averaged velocity magnitude U/U_b and inplane streamlines within the $x - z$ - and $y - z$ -symmetry planes as well as selected cross-sections (CS1: $y_{\text{TJ}}^* = y_{\text{TJ}}/D = 0.64$, CS2: $y_{\text{TJ}}^* = 1.14$, CS3: $y_{\text{TJ}}^* = 2.14$). Latter also depict the turbulent kinetic energy k/U_b^2 . The depiction lines of Fig. 3.36 are marked by dotted magenta lines. and vortex centers by magenta squares. The visualized data are derived from averaging over the symmetry planes. 95

- 3.31. Enlarged sectional view of the $x - z$ -symmetry plane with the iso-contours of the velocity magnitude field U/U_b and the corresponding in-plane streamlines depicted. The depiction lines for Fig. 3.33 are marked by dotted magenta lines. Saddle points in the flow are marked by a circle, vortex center according to the Γ_1 -criterion by a square and an saddle-point-related wall impingement by a triangle. The visualized data are derived from averaging over the symmetry planes. 97
- 3.32. Pressure coefficient related to outlet pressure $C_p = (p - p_{\text{outlet}}) / (0.5\rho U_b^2)$ (top) and friction coefficient $C_f = \tau_w / (0.5\rho U_b^2)$ (bottom) over $s_{\text{TJ}}^* = s_{\text{TJ}}/D$ within the $x - z$ -symmetry plane. 99
- 3.33. Normalized wall-normal u_n/U_b and tangential velocity u_t/U_b extractions (top) and normalized turbulent kinetic energy k/U_b^2 extractions (bottom) according to dashed lines in Fig. 3.31. **Red dotted line** represents the solid body rotation velocity u_{sbr}/U_b . 101
- 3.34. Enlarged view of the inner radius of the T-junction within a slight offset to the $y - z$ -symmetry plane with the two dimensional velocity divergence $\frac{\partial v}{\partial y} + \frac{\partial w}{\partial z}$ displayed in color as well as the inplane streamlines. The visualized data are derived from the averaging over the symmetry planes. 104
- 3.35. Pressure coefficient related to outlet pressure $C_p = (p - p_{\text{outlet}}) / (0.5\rho U_b^2)$ (top) and friction coefficient $C_f = \tau_w / (0.5\rho U_b^2)$ (bottom) along the T-junction radius over φ_{TJ} within the $y - z$ -symmetry plane. 105
- 3.36. Normalized wall-normal u_n/U_b and tangential velocity u_t/U_b extractions (top) and normalized kinetic turbulent energy k/U_b^2 extractions (bottom) according to magenta dotted lines at the cross-section in Fig. 3.30. The position of the vc are represented by magenta squares. 107
- 3.37. Evolution of the vortex tube pair radius related to the pipe radius r_{vortex}/R (top) and its circulation Γ (bottom) along $y_{\text{TJ}}^* = y_{\text{TJ}}/D$ in the outlet section. Vortex tube radius is detected by the Γ_2 criterion according to Graftieaux et al. (2001) with a threshold of $\pi/2$ and search window size of 11. 110

- 3.38. Friction coefficient $C_f = \tau_w / (0.5\rho U_b^2)$ along selected lines in the outlet section over $y_{TJ}^* = y_{TJ}/D$. The solid lines corresponds to the magnitude of the friction coefficient at the intersection between the counter-wall and the $y-z$ -symmetry plane ($\psi_{TJ} = 0^\circ$, red), the extension of the considerations in Figure 3.35 bottom ($\psi_{TJ} = 180^\circ$, green) and the bottom of the outlet section ($\psi_{TJ} = 90^\circ$, blue). For the latter, the components in outlet direction (dashed line) and circumferential direction (dotted line) are depicted. The end of the inner radius curvature is marked by a black dotted line ($y_{TJ}^* = 0.64$). 111
- 3.39. Illustration of the computational domain ($x-z$ -symmetry plane) of the reverse T-junction. φ_{rTJ} describes the inlet angle and $s_{rTJ}^* = s_{rTJ}/D$ the outlet coordinate. 117
- 3.40. Illustration of the computational domain ($y-z$ -symmetry plane) including the reverse T-junction and both precursor regions. R_c describes the inner radius, $l_{inlet} = l_{outlet} = 8D$ the inlet and the outlet length, $l_{pre} = 2.5D$ the precursor length, ψ_{rTJ} the outlet angle and $s_{rTJ}^* = s_{rTJ}/D$ the outlet coordinate. 118
- 3.41. Iso-contours of the velocity magnitude U/U_b within the $x-y$ -plane (bottom left), the $x-z$ - (top) and $y-z$ -symmetry plane (bottom right) of the reverse T-junction with the inplane mean streamlines. The coordinates $y_{rTJ}^* = y_{rTJ}/D$ and $s_{rTJ}^* = s_{rTJ}/D$ are marked for clarity. The locations of cross-sections shown in Fig. 3.42 are marked with CS1 ($s_{rTJ}^* = 0.0$), CS2 ($s_{rTJ}^* = 0.5$) and CS3 ($s_{rTJ}^* = 1.5$). The visualized data is derived from averaging over the symmetry planes. 120
- 3.42. Normalized velocity magnitude U/U_b and turbulent kinetic energy k/U_b^2 on selected cross-sections in the outlet section (CS1 ($s_{rTJ}^* = 0.0$), CS2 ($s_{rTJ}^* = 0.5$) and CS3 ($s_{rTJ}^* = 1.5$)) with the inplane mean streamlines. For clarification of the spatial location of the cross-sections within the reverse T-junction, see Fig. 3.41. The visualized data are derived from averaging over the symmetry planes. 122

- 3.43. Top: y_{rTJ}^* -friction coefficient $C_{f,y} = \tau_{w,y} / (0.5\rho U_b^2)$ depicted along the inlet coordinate y_{rTJ}^* for selected inlet circumferential angles φ_{rTJ} . Bottom: y_{rTJ}^* -velocity component u_y/U_b over pipe radius for selected inlet angles φ_{rTJ} at $y_{rTJ}^* = 0.13$. The blue dotted line indicates the zero crossing of the velocity profiles. The position of the velocity profiles corresponds to the magenta dotted lines in Fig. 3.44. 126
- 3.44. Flow type $\lambda = (|S_{ij}| - |\Omega_{ij}|) / (|S_{ij}| + |\Omega_{ij}|)$ visualized on $y_{rTJ}^* = 0.13$ plane with the symmetrical S_{ij} and asymmetrical part Ω_{ij} of the velocity gradient tensor. The visualized data derived from averaging over the symmetry planes. 127
- 3.45. Top: Vorticity Γ of a single vortex tube over the outlet coordinate s_{rTJ}^* . Bottom: Friction coefficient $C_f = \tau_w / (0.5\rho U_b^2)$ depicted for different outlet angles ψ_{rTJ} over the outlet coordinate s_{rTJ}^* 129
- 3.46. Normalized wall tangential u_t/U_b (solid line) and normal velocity u_n/U_b (dotted line) (top) and normalized turbulent kinetic energy k/U_b^2 (bottom) depicted for selected cross-sections in the outlet section ($s_{rTJ}^* = 0.0, 0.5$ and 1.5) according to magenta dotted lines in Fig. 3.42. The corresponding vc is highlighted by magenta colored squares. 131
- 3.47. Friction coefficient $C_f = \tau_w / (0.5\rho U_b^2)$ (top) and pressure coefficient $C_p = (p - p_{outlet}) / (0.5\rho U_b^2)$ and its derivative $\partial C_p / \partial s_{rTJ}^*$ (bottom) over the outlet coordinate s_{rTJ}^* along the intersection of the wall with the $y - z$ -symmetry plane. The outlet pressure p_{outlet} is applied as the reference pressure for global comparability. The region of the inner radius curvature is highlighted in gray. 134
- 3.48. Turbulent kinetic energy k/U_b^2 in the $y - z$ -symmetry plane of the reverse T-junction with the inplane mean streamlines. The locations of cross-sections shown in Fig. 3.42 are marked with CS1 ($s_{rTJ}^* = 0.0$), CS2 ($s_{rTJ}^* = 0.5$) and CS3 ($s_{rTJ}^* = 1.5$). The visualized data are derived from averaging over the symmetry planes. 135

- 3.49. Computational domain of WSG including inlet and outlet section as well as precursor region. The experimental pressure measurement point is highlighted by a red circle. 141
- 3.50. Time-averaged velocity magnitude U/U_b (top) and turbulent kinetic energy k/U_b^2 (bottom) as well as time-averaged inplane streamlines within the WSG $y - z$ -symmetry plane as well as the T-junction outlet (red dotted line) and reverse T-junction outlet (magenta dotted line). For comparison, the isolated T-junction and isolated reverse T-junction results within the corresponding planes are additionally shown. The visualized data are derived from averaging over the symmetry planes. . . 143
- 3.51. Normalized streamwise velocity u^+ (top) and turbulent kinetic energy k^+ (bottom) along the WSG inflow pipe radius $(R - r)^+$ within the WSG inlet (black line). For comparison, the profiles at the identical positions within the isolated T-junction (circle) are also depicted. 145
- 3.52. Friction coefficient $C_f = \tau_w / (0.5\rho U_b^2)$ (top) and pressure coefficient $C_p = (p - p(s_{\text{WSG,in}}^* = 2)) / (0.5\rho U_b^2)$ (bottom) over the WSG inlet coordinate $s_{\text{WSG,in}}^*$ for different WSG inlet angles $\psi_{\text{WSG,in}}$ in comparison to the isolated T-junction consideration (symbols). Specific positions are highlighted by dotted colored lines (inlet isolated T-junction, end necking, inlet WSG sample, inlet T-junction). 146
- 3.53. Friction coefficient $C_f = \tau_w / (0.5\rho U_b^2)$ within the WSG $y - z$ -symmetry plane along the T-junction inner radius (top) and the pipe-curved counter wall (bottom). The results of the isolated T-junction (circles) are depicted for comparison. Comparable plots and associated discussion can be found in Figures 3.35 bottom and 3.38. 149
- 3.54. Chemically cleaned, heated sided half-sample after a 96-hour test with $T_{\text{inlet}} = 115 \text{ }^\circ\text{C}$ and $\dot{V} = 2.2 \text{ l/min}$ with view on the $y - z$ -symmetry plane. Initial position of surface degradation is marked around the inlet of the second deflection. The picture of the half-sample originates from Klink and Wegt (2021). . . . 150

-
- 3.55. Iso-contours of the time-averaged velocity magnitude U/U_b (left) and turbulent kinetic energy k/U_b^2 (right) with the time-averaged inplane streamlines within $y-z$ -symmetry plane for the isolated deflection (Chapter 3.5) as well as the first and second deflections of the WSG. The visualized data are derived from averaging over the symmetry planes. 151
- 3.56. Iso-contours of the time-averaged velocity magnitude U/U_b (top) and turbulent kinetic energy k/U_b^2 (bottom) with the time-averaged inplane streamlines within selected cross-sections for the isolated deflection (Chapter 3.5) as well as the first and second deflections of the WSG. The visualized data are derived from averaging over the symmetry planes. 155
- 3.57. Comparison of the isolated deflection (black lines) discussed in Chapter 3.5 with the first (blue lines) and second deflections (red lines) of the WSG in terms of pressure coefficient $C_p = (p - p(\varphi_{\text{bend}} = 0^\circ)) / (0.5 \rho U_b^2)$ (top) and friction coefficient $C_f = \tau_w / (0.5 \rho U_b^2)$ (bottom) for different circumferential angles ψ_{bend} ($\psi_{\text{bend}} = 0$ corresponds to the inner radius of the deflections) along φ_{bend} 158
- 3.58. Cross-sectional wall-normal u_n and tangential velocity u_t (middle) and turbulent kinetic energy k/U_b^2 (bottom) from pipe center $r/R = 0$ to pipe wall ($r/R = 1$) along blue extraction line (top, $\psi_{\text{bend}} = 90^\circ$) for selected positions between the first and second deflection as illustrated in the top-sided sketch (CS1 ... 5). The depicted data are derived from averaging over the symmetry planes. 159
- 3.59. Time-averaged velocity magnitude U/U_b (left) and turbulent kinetic energy k/U_b^2 (right) on the inlet cross-section of the reverse T-junction within the WSG (left, highlighted with a darkgreen dotted line in Fig. 3.50). For comparison, the associated fields of the isolated reverse T-junction (see Chapter 3.7) are also depicted on the inlet cross-section (right). The visualized data are derived from averaging over the symmetry planes. 162

- 3.60. Time-averaged velocity magnitude U/U_b (top) and turbulent kinetic energy k/U_b^2 (bottom) on the $x - z$ -symmetry plane of the reverse T-junction within the WSG and the isolated consideration. The $y - z$ -symmetry plane is highlighted by a black dashed line and the outlet of the reverse T-junction by a magenta dotted line (see also Fig. 3.50). The visualized data derived from averaging over the symmetry planes. 165

- 3.61. Time-averaged velocity magnitude U/U_b (top) and turbulent kinetic energy k/U_b^2 (bottom) as well as time-averaged inplane streamlines within selected cross-sections downstream of the reverse T-junction within the WSG. The visualized data are derived from averaging over the symmetry planes. 167

- 3.62. Friction $C_f = \tau_w / (0.5\rho U_b^2)$ (top) and pressure coefficient $C_p = (p - p(s_{\text{WSG,out}}^* = 3.0)) / (0.5\rho U_b^2)$ (bottom) along the outlet coordinate $s_{\text{WSG,out}}^*$ within the intersection of the wall and the $y - z$ -symmetry plane in comparison to the isolated consideration (circles). The region of the inner radius curvature is highlighted in gray and the corresponding friction coefficient is depicted enlarged over the inner radius angle $\varphi_{\text{WSG,out}}$ 169

- 4.1. Elliptic blending function $f_\Phi = \alpha^3$ (solid) and elliptic function α (dotted line) for channel flow with $\text{Re}_\tau = 395$ (black lines) and $\text{Re}_\tau = 5200$ (blue lines) along channel height y^+ predicted by EBM. 190

- 4.2. Reynolds-stress components in linear (top) and double logarithmic scaling (bottom) for channel flow with $\text{Re}_\tau = 395$ along channel height y^+ predicted by EBM (solid line). The DNS data by Moser et al. (1999) are depicted for comparison (symbols). 191

- 4.3. Gradient-production term $P_{\varepsilon,3}$ for channel flow with $\text{Re}_\tau = 395$ along channel height y^+ predicted by EBM (solid line). The DNS data by Mansour et al. (1988) are depicted for comparison (circle). 193

4.4. Top: Homogeneous ω^h (solid line) and entire specific dissipation rate ω (dotted line) for channel flow with $Re_\tau = 395$ along channel height y^+ predicted by EBM (solid line). The DNS data by Moser et al. (1999) are depicted for comparison (symbols). Bottom: Total viscous dissipation rate ε and its homogeneous (ε^h) and non-homogeneous ($0.5 \nu \partial^2 k / (\partial x_l \partial x_l)$) parts (in accordance to Eq. (4.2)) for channel flow with $Re_\tau = 395$ along channel height y^+ predicted by EBM (solid line). The DNS data by Moser et al. (1999) are depicted for comparison (symbols). 194

4.5. Turbulent diffusion D_{ij}^t components for channel flow with $Re_\tau = 395$ along channel height y^+ predicted by EBM (solid lines). The DNS data by Moser et al. (1999) are depicted for comparison (symbols). 195

4.6. Regions with positive (red) and negative (blue) axial velocities in the periodic hill configuration at $Re_h = 10600$ (top) and 37000 (bottom) illustrating the effect of the adopted diffusion model on the flow behavior at the separation and reattachment points. 197

4.7. β -blending function for channel flow with $Re_\tau = 395$ (solid line) and 5200 (dotted line) along channel height y^+ predicted by EBM. Its maximum possible value of $\beta_{max} = 0.25$ is denoted by a dashed line. 198

4.8. Top: Profile of the model structure parameter $C_\mu = [\overline{uv} / (\partial U / \partial y)] (k / \varepsilon^2)$ for channel flow with $Re_\tau = 395$ along channel height y^+ predicted by EBM (solid lines). The DNS data by Moser et al. (1999) are depicted for comparison (circles). Bottom: Length-scale (Eq. 4.14) normalized by the channel height (L_{ν_t} / h) for channel flow with $Re_\tau = 395$ along channel height y^+ predicted by EBM (solid lines). The corresponding Kolmogorov length-scale L_η (dashed line), Taylor lengthscale L_λ (dotted line) and turbulent lengthscale L_L (dashed-dotted line) are illustrated for completeness. 200

- 4.9. top: Predicted channel friction coefficient $C_f = \tau_w / (0.5\rho U_b^2)$ depicted over the bulk Reynolds number range $Re_b = U_b h / \nu$ by EBM (squares) in comparison with the DNS data by Moser et al. (1999) and Lee and Moser (2015) (circles) as well as an empirical correlation by R. B. Dean (1978) (solid line). bottom: Normalized velocity profiles u^+ in channel flows with $Re_\tau = 180$ up to 5200 depicted over dimensionless wall distance y^+ predicted by EBM (solid line). The DNS data by Moser et al. (1999) and Lee and Moser (2015) (circles) and the logarithmic law (dotted line) with $\kappa = 0.41$ and $B = 5.5$ are depicted for comparison. 202
- 4.10. Top: The von Kàrmàn constant $\kappa = (y^+ \partial u^+ / \partial y^+)^{-1}$ depicted over dimensionless wall distance y^+ within channel flows from $Re_\tau = 180$ up to 5200 predicted by EBM (solid line). The DNS data by Moser et al. (1999) and Lee and Moser (2015) (circles) and the equilibrium law with $\kappa = 0.41$ and $B = 5.5$ are depicted for comparison. Bottom: Homogeneous dissipation rate $\varepsilon^{h,+}$ over dimensionless wall distance y^+ within channel flows from $Re_\tau = 180$ up to 5200 predicted by EBM (solid line). The DNS data by Moser et al. (1999) and Lee and Moser (2015) (circles) are depicted for comparison. 204
- 4.11. Reynolds stress intensity components $\bar{u}^+ = \sqrt{\bar{u}u}/u_\tau$ (top) and $\bar{v}^+ = \sqrt{\bar{v}v}/u_\tau$ (bottom) for channel flows with $Re_\tau = 180$ up to 5200 predicted by EBM (solid line). The DNS data by Moser et al. (1999) and Lee and Moser (2015) (circles) are depicted for comparison. 206
- 4.12. Reynolds stress intensity $\bar{w}^+ = \sqrt{\bar{w}w}/u_\tau$ (top) and component $\bar{w}v^+ = \bar{w}v/u_\tau$ (bottom) for channel flows with $Re_\tau = 180$ up to 5200 predicted by EBM (solid line). The DNS data by Moser et al. (1999) and Lee and Moser (2015) (circles) are depicted for comparison. 207
- 4.13. Normalized semi-log plots of the velocity profiles u^+ for pipe flows with $Re_\tau = 180$ up to 1000 predicted by EBM (solid line). The DNS data by El Khoury et al. (2013) (circles) and the logarithmic law (dotted line) with $\kappa = 0.41$ and $B = 5.5$ are depicted for comparison. 209

- 4.14. Reynolds stress intensity components $\overline{u_z^+} = \sqrt{\overline{u_z u_z}}/u_\tau$ (top) and $\overline{u_r^+} = \sqrt{\overline{u_r u_r}}/u_\tau$ (bottom) for pipe flows with $Re_\tau = 180$ up to 1000 predicted by EBM (solid line). The DNS data by El Khoury et al. (2013) (circles) are depicted for comparison. 211
- 4.15. Reynolds stress intensity component $\overline{u_\varphi^+} = \sqrt{\overline{u_\varphi u_\varphi}}/u_\tau$ (top) and shear component $\overline{u_r u_z^+} = \overline{u_z u_r}/u_\tau$ (bottom) for pipe flows with $Re_\tau = 180$ up to 1000 predicted by EBM (solid line). The DNS data by El Khoury et al. (2013) (circles) are depicted for comparison. 212
- 4.16. Top: Friction coefficient of a zero-pressure-gradient boundary layer $C_f = \tau_w / (0.5\rho U_\infty^2)$ predicted by EBM (solid line). Reference data in terms of DNS simulation (circles) by Schlatter and Örlü (2010) and LES simulation (squares) by Eitel-Amor et al. (2014) are depicted for comparison. Bottom: Streamwise velocity evolution $u^+ = u/u_\tau$ within a zero-pressure-gradient boundary layer depicted over normalized wall distance $y^+ = yu_\tau/\nu$ at $Re_\Theta = 2000, 4000$ and 8200 predicted by EBM (solid line). Reference data in terms of DNS (circles) by Schlatter and Örlü (2010) and LES (squares) by Eitel-Amor et al. (2014) as well as the equilibrium law with $\kappa = 0.41$ and $B = 5.5$ are depicted for comparison. 214
- 4.17. Streamwise $\overline{u^+} = \sqrt{\overline{uu}}/u_\tau$ (top) and wall-normal Reynolds stress evolution $\overline{v^+} = \sqrt{\overline{vv}}/u_\tau$ (bottom) within a zero-pressure-gradient boundary layer depicted over normalized wall distance $y^+ = yu_\tau/\nu$ at $Re_\Theta = 2000, 4000$ and 8200 predicted by EBM (solid line). Reference data in terms of DNS (circles) by Schlatter and Örlü (2010) and LES (squares) by Eitel-Amor et al. (2014) are depicted for comparison. 215
- 4.18. Spanwise $\overline{w^+} = \sqrt{\overline{ww}}/u_\tau$ (top) and shear Reynolds stress evolution $\overline{wv^+} = \overline{wv}/u_\tau^2$ (bottom) within a zero-pressure-gradient boundary layer depicted over normalized wall distance $y^+ = yu_\tau/\nu$ at $Re_\Theta = 2000, 4000$ and 8200 predicted by EBM (solid line). Reference data in terms of DNS (circles) by Schlatter and Örlü (2010) and LES (squares) by Eitel-Amor et al. (2014) are depicted for comparison. 217

4.19. Enlarged visualisation of the iso-contours of the streamwise velocity u/U_∞ and the streamlines around the rounded backstep predicted by EBM. 219

4.20. Friction coefficient $C_f = \tau_w / (0.5\rho U_\infty^2)$ depicted along the streamwise coordinate x/R_{\max} predicted by EBM (solid line) in comparison to the DNS data by Massa and Colombo (2021) (circles). 221

4.21. Streamwise velocity component normalized by the farfield velocity u/U_∞ (top) and friction velocity $u^+ = u/u_\tau$ at selected positions within the TC01 case ($x/R_{\max} = 0, 1, 2, 3, 4$) along the domain height y/R_{\max} (top) and y^+ (bottom) predicted by the EBM (solid line) in comparison to the DNS data by Massa and Colombo (2021) (circles) as well as the log law (dotted line). 223

4.22. Turbulent kinetic energy normalized by the farfield velocity k/U_∞^2 (top) and friction velocity $k^+ = k/u_\tau^2$ at selected positions within the TC01 case ($x/R_{\max} = 0, 1, 2, 3, 4$) along the domain height y/R_{\max} (top) and y^+ (bottom) predicted by the EBM (solid line) in comparison to the DNS data by Massa and Colombo (2021) (circles). 224

4.23. Reynolds shear stress component normalized by the farfield velocity \overline{uv}/U_∞^2 (top) and friction velocity $\overline{uv}^+ = \overline{uv}/u_\tau^2$ at selected positions within the TC01 case ($x/R_{\max} = 0, 1, 2, 3, 4$) along the domain height y/R_{\max} (top) and y^+ (bottom) predicted by the EBM (solid line) in comparison to the DNS data by Massa and Colombo (2021) (circles). 225

4.24. Enlarged visualisation of the iso-contours of the streamwise velocity u/U_∞ and the streamlines around the right-angled step predicted by EBM. 227

4.25. Bottom friction coefficient $C_f = \tau_w / (0.5\rho U_\infty^2)$ (top) and pressure coefficient $C_p = (p - p(x/h = 37.5)) / (0.5\rho U_\infty^2)$ (bottom) of the backward facing step with $Re_h = 36000$ calculated by EBM (solid line) in comparison to the reference data by Driver and Seegmiller (1985) (circles). 228

4.26. Streamwise velocity u/U_∞ (top) and Reynolds stress component \overline{uu}/U_∞^2 (bottom) depicted over the channel height y/h of the backward facing step with $Re_h = 36000$ calculated by EBM (solid line) in comparison to the reference data by Driver and Seegmiller (1985) (circles).	229
4.27. Reynolds stress component \overline{vv}/U_∞^2 (top) and \overline{uv}/U_∞^2 (bottom) depicted over the channel height y/h of the backward facing step with $Re_h = 36000$ calculated by EBM (solid line) in comparison to the reference data by Driver and Seegmiller (1985) (circles).	230
4.28. Iso-contours of the mean streamwise velocity u/U_{inflow} and corresponding streamlines in the periodic hill flow at $Re_h = 10600$ (top) and $Re_h = 37000$ (bottom).	233
4.29. Skin friction coefficient $C_f = \tau_w / (0.5\rho U_{inflow}^2)$ development at the lower hill-shaped wall for $Re_h = 10600$ (black solid line) and $Re_h = 37000$ (blue solid line) predicted by EBM. Reference data by Breuer et al. (2009) (LES, $Re_h = 10600$, triangles) and Rapp (2008) (Experiment, $Re_h = 37000$, fulfilled black square) are depicted for comparison.	234
4.30. Streamwise velocity u/U_{inflow} (top) and streamwise Reynolds stress component $\overline{uu}/U_{inflow}^2$ (bottom) profiles at selected streamwise positions ($x/h = 0.05, 0.5, 1.0, 2.0, 3.0, 4.0, 5.0, 6.0, 7.0$ and 8.0) depicted over the flow domain height y/h predicted by EBM for $Re_h = 10600$ (black line) and $Re_h = 37000$ (blue line). The reference data by Rapp (2008) (black circles and blue squares) and Breuer et al. (2009) (black triangles) are shown for comparison.	237
4.31. Spanwise $\overline{vv}/U_{inflow}^2$ (top) and shear Reynolds stress component $\overline{uv}/U_{inflow}^2$ (bottom) profiles at selected streamwise positions ($x/h = 0.05, 0.5, 1.0, 2.0, 3.0, 4.0, 5.0, 6.0, 7.0$ and 8.0) depicted over the flow domain height y/h predicted by EBM for $Re_h = 10600$ (black line) and $Re_h = 37000$ (blue line). The reference data by Rapp (2008) (black circles and blue squares) and Breuer et al. (2009) (black triangles) are shown for comparison.	238

- 4.32. Iso-contours of streamwise velocity u/U_b at selected cross-sections ($x/h = 0; 2; 5; 8; 12; 15$) for diffuser 1 (left) and diffuser 2 (right) predicted by EBM. The $u/U_b = 0$ surface is illustrated in gray to highlight the separation zone. 239
- 4.33. Friction coefficient $C_f = \tau_w / (0.5\rho U_b^2)$ (top) and pressure coefficient $C_p = (p - p(x/h = 0.05)) / (0.5\rho U_b^2)$ (bottom) development over the streamwise coordinate x/h for both diffuser configurations with $Re_b = 10000$. The EBM results (solid line) are depicted in comparison to the reference data by Ohlsson et al. (2010) (circles) and Cherry et al. (2009) (triangles) 241
- 4.34. Streamwise velocity iso-contour plots for selected cross-sections for diffuser 1 (back solid line) and diffuser 2 (blue solid line) with $Re_b = 10000$ predicted by EBM. The reference DNS data for diffuser 1 by Ohlsson et al. (2010) are depicted for comparison (red solid line). The numbers at the individual velocity iso-contours denote the value of u/U_b 242
- 4.35. Streamwise velocity u/U_b (top) and Reynolds stress component \bar{u}_{RMS}/U_b (bottom) profiles at selected streamwise positions depicted across the duct height y/h for diffuser 1 (solid line) and diffuser 2 (dotted line) with $Re_b = 10000$. The experimental (square, Cherry et al., 2008) and numerical reference data (circles, Ohlsson et al., 2010) are depicted for comparison. . . . 246
- 4.36. Schematic illustration of the WSG with characteristic positions highlighted by magenta dotted lines (1: T-junction inlet; 2: T-junction outlet; 3: 1. deflection inlet; 4: 1. deflection outlet; 5: 2. deflection inlet; 6: 2. deflection outlet; 7: reverse T-junction inlet; 8: reverse T-junction outlet). The inner coordinate $s_{inner}^* = s_{inner}/D$ and its path are introduced by a red marked arrow and a dashed line. 248
- 4.37. Friction coefficient $C_f = \tau_w / (0.5\rho U_b^2)$ and pressure coefficient $C_p = (p - p(s_{inner}^* = 0)) / (0.5\rho U_b^2)$ along the inner coordinate of the WSG $s_{inner}^* = s_{inner}/D$ predicted by EBM (solid lines) and LES (symbols). Characteristic positions are highlighted according to Fig. 4.36. 250

4.38. Velocity magnitude U/U_b (top) and streamwise Reynolds stress component $\sqrt{\overline{uu}}/U_b$ (bottom) over the pipe radius r/R at characteristic positions within the WSG according to Fig. 4.36 predicted by EBM (solid line) and LES (circles).	253
4.39. Wall-normal Reynolds stress component $\sqrt{\overline{vv}}/U_b$ (top) and wall-tangential Reynolds stress component $\sqrt{\overline{ww}}/U_b$ (bottom) over the pipe radius r/R at characteristic positions within the WSG according to Fig. 4.36 predicted by EBM (solid line) and LES (circles).	254
B.1. Iso-contours of the instantaneous velocity magnitude of a channel flow with $Re_\tau = 180$ predicted by the ISEBM.	271
B.2. Streamwise velocity u^+ (top left), Reynolds stress components $\overline{u_i u_j}^+$ (bottom) and modeled to total turbulent kinetic energy ratio $\frac{k_{\text{mod}}}{k_{\text{total}}}$ (top right) depicted over the channel height predicted by EBM (blue solid line), ISEBM (black solid line) and WALE (red solid line). The DNS data by Lee and Moser (2015) are depicted for comparison (symbols).	272

List of Tables

3.1.	Summary of the geometric dimensions of the WSG illustrated in Fig. 3.1 right.	33
3.2.	Complete listing of present pipe Reynolds numbers within the WSG for $T_{\text{inlet}} = 115 \text{ }^\circ\text{C}$ considering the selected volume fluxes \dot{V} . $\text{Re}_b = U_b D / \nu$ denotes the Reynolds number at the WSG inlet, $\text{Re}_{\text{outer}} = U_{b,\text{outer}} D_{\text{outer}} / \nu$ in the outer section and $\text{Re}_{\text{deflection}} = 0.5 U_b D / \nu$ in the deflections.	36
3.3.	Total number of grid cells n_{total} ($k \equiv 10^3$) and computer cores n_{cores} used for computing the pipe flow at five considered friction Reynolds numbers Re_τ	40
3.4.	Grid characteristics for simulating the pipe flow at friction Reynolds number $\text{Re}_\tau = 360$ with respect to the cell numbers ($k \equiv 10^3$) - in total and within the cross-section, n_{total} and n_{cs} , respectively - and the dimensionless grid spacings in radial $\Delta r_{\text{min}}^+, \dots, \text{max}^+$, circumferential $\Delta \varphi^+$ and flow direction Δz^+	48
3.5.	Grid characteristics ($k \equiv 10^3$) for the three pipe Reynolds numbers $\text{Re}_{\text{deflection}} = 7200, 10500, 14000$ in terms of the total and cross-section cell numbers, n_{total} and n_{cs} , respectively, and the dimensionless grid resolution parameters in the radial $\Delta r_{\text{min}}^+, \dots, \text{max}^+$, circumferential $\Delta \varphi^+$ and mean flow directions Δz^+	58
3.6.	Number of grid cell n_{total} (including also the precursor region), for the respective Reynolds Re_b and Dean number De combinations.	65
4.1.	Coefficient constant values in Φ_{ij}^h model term, Eq. (4.6).	188
4.2.	Model constants of the ω^h transport equation	192

4.3. Total number of cells n_{total} for the considered channel flow configurations with bulk Reynolds number Re_b . The predicted friction Reynolds number by DNS $Re_{\tau,\text{DNS}}$ and EBM $Re_{\tau,\text{EBM}}$ are also listed. 201

4.4. Characteristics of the applied grids for the considered pipe flow bulk Reynolds numbers Re_b in terms of the total cell number n_{total} as well as the dimensionless minimal and maximal radial $\Delta r_{\text{min}}^+, \dots, \text{max}$ and circumferential spatial extents $\Delta\varphi^+$ of the cells. The predicted friction Reynolds number by DNS $Re_{\tau,\text{DNS}}$ and EBM $Re_{\tau,\text{EBM}}$ are also listed. 208